

**Theoretical and Experimental Study of Heat Loss and Ice
Accretion for Large Structures on Marine Vessels
and Offshore Structures**

by

© **Alireza Dehghanisani**

A thesis submitted to the School of Graduate Studies in partial fulfillment of the
requirements for the degree of

Doctor of Philosophy

Faculty of Engineering and Applied Science

Memorial University of Newfoundland

December 2017

St. John's

Newfoundland

Abstract

Sea spray icing, or marine icing, is one of the most significant problems for the operation of marine vessels and offshore structures in cold regions and the Arctic. This phenomenon risks the stability of marine vessels and structures as well as the safety of human activities onboard. In this thesis, several issues related to the spray icing phenomena are investigated. Chapter 1 briefly reviews sea spray icing models, along with various experimental, theoretical and numerical approaches, which are used for modeling and prediction of the accumulated ice on marine platforms located in cold seas and ocean regions. In chapter 2, several topics, such as droplet trajectories, flux of seawater spray, liquid water content (LWC), heat balance at the phase interface, and freezing equations are formulated and examined.

The trajectory and cooling process of droplets during flight over marine platforms are investigated and analyzed theoretically in chapter 3. The solidification process of a saline water droplet is studied using semi-analytical techniques in chapter 4. The theoretical prediction of ice accumulation on horizontal and vertical surfaces of marine vessels in cold regions is investigated in chapter 5. An experimental study to measure ice accumulation on vertical marine platform surfaces under various conditions is conducted in chapters 6 and 7. Summary and recommendations for future research are presented in chapter 8.

Chapters 3 to 7 represent the original research in this thesis. Previously, no comprehensive evaluation of ice accumulation on the vertical marine platform surfaces under harsh environmental conditions via empirical measurements had been conducted. To fill the knowledge gap, a number of parameters, such as the weight and thickness of ice accumulation on the plate, relative humidity, the temperature at the front and back of the vertical plate, and the water temperature inside the pipe during the spray icing event for various conditions, as well as the spray mass flux that impacts on the vertical plate for the duration of the spray event were measured (chapter 7). The cooling and freezing processes of water droplets during flight over marine platforms in cold weather conditions were investigated and analyzed. The originality of this study was in the use of a semi-analytical technique to solve an inward moving boundary problem (chapter 4).

Acknowledgements

I would like to express the deepest appreciation to my supervisors, Dr. Yuri S. Muzychka and Dr. Greg F. Naterer, who have the attitude and the substance of great mentors. Without their guidance and persistent help, this dissertation would not have been possible.

I would also like to express my gratitude to Dr. Saeed-Reza Dehghani, Dr. Vali Enjilela, Dr. Scott MacLachlan and Dr. Ronald D. Haynes for their invaluable comments and remarks.

I gratefully acknowledge the financial support from Statoil ASA (Norway), MITACS (IT03198), the Research and Development Corporation of Newfoundland and Labrador (RDC), Petroleum Research of Newfoundland & Labrador (PRNL) (IT03198), and the American Bureau of Shipping (ABS) (207095) for this research.

Last but not the least, I would like to thank my parents. This work could not have been possible without their continuous support and encouragement.

Table of Contents

Abstract	ii
Acknowledgements	iv
Table of Contents	v
List of Tables	ix
List of Figures	xii
Nomenclature	xxv

Chapter 1: Review of Marine Icing Phenomena on Offshore Vessels and

Structures	1
1.1 Introduction	1
1.2 Icing Phenomena	4
1.3 Review of Sea Spray Icing Models	13
1.3.1 Icing Models Before 1980	13
1.3.2 Icing Models between 1980 and 2000	26
1.3.3 Icing Models After 2000	47
1.4 Discussions	58

Chapter 2: Formulation of Sea Spray Icing Phenomena on Offshore

Platforms	64
2.1 Formulation of Marine Icing Models	64

2.1.1 Droplet Trajectories	65
2.1.2 Liquid Water Content (LWC)	68
2.1.2.1 Liquid Water Content in Wind-generated Spray	69
2.1.2.2 Liquid Water Content in Wave-generated Spray	74
2.1.3 Spray Movement	81
2.1.4 Spray Duration	86
2.2 Mass Balance	87
2.3 Heat Balance	91
2.4 Icing Models	99
2.4.1 Simplified Icing Models	99
2.4.2 Advanced Icing Models	102
 Chapter 3: Droplet Trajectory and Thermal Analysis of Impinging Saline	
Spray Flow on Marine Platforms	106
3.1 Droplet Trajectory Formulation	106
3.2 Heat Transfer Formulation	109
3.3 Cooling Process	112
3.4 Results and Discussion	115
3.5 Sensitivity Analysis	125
 Chapter 4: Theoretical Modeling and Analysis of Solidification Process of a	
Saline Water Droplet	131
4.1 Introduction	131

4.2 Model Description	134
4.3 Droplet Cooling and Freezing Processes	136
4.3.1 Liquid Cooling Stage	136
4.3.2 Solidification Stage	137
4.3.3 Solid Cooling Stage	140
4.4 Theoretical Solution Procedure	141
4.5 Results and Discussion	150
Chapter 5: Theoretical Prediction of Ice Accumulation on Horizontal and Vertical Surfaces of Marine Vessels in Cold Regions	158
5.1 Model Description for Horizontal Surfaces	159
5.1.1 Sea Spray Impingement	159
5.1.2 Mass and Heat Balances and Salt Concentration	160
5.1.3 Horizontal Plate without Consideration of Heat Conduction in the Ice Layer	162
5.1.4 Horizontal Plate with Consideration of Heat Conduction in the Ice Layer	172
5.1.4.1 Heat Transfer Formulation	172
5.1.4.2 Results and Discussion	178
5.2 Model Description for Vertical Surfaces	186
Chapter 6: Experimental Arrangement and Procedure for Measurement of Ice Accumulation on Vertical Marine Platform Surfaces	190
6.1 Equipment	190

6.2 Measuring Instruments	197
6.3 Design Factors and Measurements	200
6.4 Spray Mass Flux Measurement	203
Chapter 7: Analysis of Experimental Measurements of Ice Accumulation on Vertical Marine Platform Surfaces	205
7.1 Experimental Results	205
7.2 Discussion	219
Chapter 8: Summary and Recommendations for Future Research	228
References	233
Appendix A: Figures Obtained from Experiments	258

List of Tables

Table 1.1: Distribution of ship icing among the seas and ocean (Efimov, 2012)	2
Table 1.2: Types of ice formation by atmospheric precipitation (Minsk, 1977)	6
Table 1.3: Causes of accumulated ice by different sources (Borisenkov and Panov (1972); Feit (1987))	8
Table 1.4: Reasons of icing of marine vessels (Zakrzewski, 1987)	9
Table 1.5: Classification of icing rate (Lundqvist and Udin, 1977)	19
Table 1.6: Comparison between the original data from Sharapov (1971) and the computed height of splashing seawater on the vessel for the vessel heading of 0° ...	31
Table 1.7: Comparison of the ice accumulation thickness that is obtained from the experimental observations and numerical modeling (Horjen, 2015)	56
Table 2.1: Constant coefficients for third degree of polynomial of the wind velocity defined in Eq. (2.7) (Kato, 2012)	71
Table 2.2: Constant coefficients for fifth degree of polynomial of the wind velocity defined in Eq. (2.8) (Kato, 2012)	72
Table 2.3: The computed amount of wave-generated spray flux at deck level on the Ocean Bounty in Eqs. (2.16) to (2.19) (Forest et al., 2005)	80
Table 2.4: Icing class and rate (Cammaert, 2013)	101
Table 2.5: Forecast of icing rates in past studies (Cammaert, 2013)	102

Table 3.1: Parameter and property values or formulae	116
Table 3.2: Positions and time of water droplets with various sizes throughout the flight duration for the highest height and the moment of impact on the deck	119
Table 3.3: Droplet temperature at the moment of impact on the deck and the time that the droplet begins to freeze for $T_a = -18^\circ C$, $T_{0,w} = 2^\circ C$, $U = 15 m/s$, $S_w = 34\%$, $RH = 80\%$ and various droplet diameters	122
Table 3.4: Comparison of parameters of v_d , Re and C_d at several diameters for the present model and the obtained results by Zarling (1980)	124
Table 3.5: Positions, time and temperature of the droplet at $D = 1$ mm during flight for the maximum height and the moment of impact on the deck	127
Table 5.1: Parameter values	164
Table 5.2: Variations of air temperature and thickness of ice layer at different times for rime icing	183
Table 5.3: Variations of the freezing fraction and ice layer and water film thicknesses for glaze icing at $T_a = 266.1$ K	183
Table 6.1: Relevant characteristics of the solenoid valve and digital timer	197
Table 6.2: Relevant characteristics of the load cells	198
Table 6.3: Relevant specifications of the thermocouple used to record the water temperature inside the pipe	199
Table 7.1: Comparison of the ice weight for two different salinities and temperatures and including at three air velocities	212

Table 7.2: Comparison of the average thickness of ice formation for two different salinities and temperatures and including three air velocities for a 3 hr test	213
Table 7.3: Comparison of the ice weight at $V_{ave,3} \approx 2.65$ m/s, $T_C = -10^\circ\text{C}$, two different salinities and 3 s for the duration of each spray event and 1 min for the period between spray events	218
Table 7.4: Mass flux of water spray that strikes on the vertical plate for the duration of the spray event at three fan speeds	219
Table 7.5: Comparison the quantity of ice accumulation and runoff, as well as the freezing fraction for different conditions and tests	226

List of Figures

Fig. 1.1: View of ice accumulation on deck of a marine vessel (Cammaert, 2013)...	4
Fig. 1.2: View of ice formation on a marine structure (Marine Log Website).....	4
Fig. 1.3: View of splashing of the seawater spray generated from waves on Dutch Coastguard Vessel at the North Sea	7
Fig. 1.4: Mertins' icing charts (Mertins 1968, Jessup, 1985)	14
Fig. 1.5: Comiskey's nomograph for prediction of icing rate (Comiskey, 1976; Jessup, 1985)	15
Fig. 1.6: Nomogram to define the icing rate of small Soviet fishing ships (Kachurin et al., 1974; Jessup, 1985)	17
Fig. 1.7: Relationship between the weight of ice formation, P , which is created on vessel in duration of the icing incident and predicted ice thickness, H' , on the cylindrical shaft, which is computed for the same hydro-meteorological conditions.	18
Fig. 1.8: Formation of ice accumulation with various sizes of water droplets (Tabata et al. (1963) and Ono (1964))	20
Fig. 1.9: Icing severity corresponding to air temperature and wind velocity (Borisenkov and Panov (1972), taken from Japanese data in Tabata et al. (1963))...	21
Fig. 1.10: Distribution of icing on Japanese patrol ships due to course and speed (Tabata, 1969)	22

Fig. 1.11: Relationship between spray intensity and wave course towards the vessel and the vessel speed at (1) 8.5 knots, (2) 7.0 knots, and (3) 5.5 knots (Panov and Moltjanov, 1972)	22
Fig. 1.12: Relationship between the spray intensity and wave course relative to the vessel and wave elevations at (1) 1.0-1.5 m, (2) 2.0-2.5 m, and (3) 3.0-3.5 m (Panov and Moltjanov, 1972)	23
Fig. 1.13: Relationship between the icing, air temperature and wind velocity (Lundqvist and Udin, 1977)	24
Fig. 1.14: Relationship between the icing on vessels, air temperature and wind velocity (Lundqvist and Udin, 1977)	25
Fig. 1.15: Relationship between sea surface temperature and cases with ice accumulation (Lundqvist and Udin, 1977)	25
Fig. 1.16: Comparing the models and empirical measurements for the 30 min tests (Lozowski and Gates, 1985)	28
Fig. 1.17: Comparing the models and empirical measurements for the 120 min tests (Lozowski and Gates, 1985)	28
Fig. 1.18: Comparing the actual accumulation form after 30 min and those predicted via other models (Lozowski and Gates, 1985)	29
Fig. 1.19: Comparing the actual accumulation form after 120 min and those predicted via other models (Lozowski and Gates, 1985)	29

Fig. 1.20: The relation between wind velocity and the greatest height of splashing seawater on the foremast of an MFV for a vessel heading of 0° and different vessel speeds (Zakrzewski et al., 1988)	32
Fig. 1.21: Relationship between vessel speed and the greatest height of splashing seawater on the foremast of a MFV for different wind velocities (Zakrzewski et al., 1988)	32
Fig. 1.22: Relation between vessel heading and the greatest height of splashing seawater on the foremast of an MFV for a vessel heading of 0° and different wind velocities (Zakrzewski et al., 1988)	33
Fig. 1.23: Effect of air temperature on the formation of ice accumulation: (a) $T_a = -15^\circ\text{C}$; (b) $T_a = -10^\circ\text{C}$; (c) $T_a = -5^\circ\text{C}$ and (1) 5 min passed; (2) 10 min passed; (3) 20 min passed (arrow shows flow direction) (Fukusako et al., 1989)	34
Fig. 1.24: Effect of wind velocity on the formation of ice accumulation: (a) $U = 6$ m/s; (b) $U = 10$ m/s; (c) $U = 20$ m/s and (1) 5 min passed; (2) 10 min passed; (3) 20 min passed (arrow shows flow direction) (Fukusako et al., 1989)	36
Fig. 1.25: Effect of water droplets diameter on the formation of ice accumulation: (a) $D = 200 \mu\text{m}$; (b) $D = 900 \mu\text{m}$; (c) $D = 1600 \mu\text{m}$ (arrow shows flow direction) (Fukusako et al., 1989)	36
Fig. 1.26: Effect of water droplet temperature on the formation of ice accumulation: (a) $T_d = -1.4^\circ\text{C}$; (b) $T_d = 0.2^\circ\text{C}$; (c) $T_d = 4^\circ\text{C}$ (arrow shows flow direction) (Fukusako et al., 1989)	37

Fig. 1.27: Effect of the mass flow rate of water droplets on the formation of ice accumulation: (a) mass flow rate of 80 kg/m ² h; (b) mass flow rate of 160 kg/m ² h; (c) mass flow rate of 320 kg/m ² h (arrow shows flow direction) (Fukusako et al., 1989)	37
Fig. 1.28: Sensitivity illustration for (a) air temperature, (b) wind velocity, and (c) water surface salinity. The crossing point is the standard condition (Blackmore and Lozowski, 1994)	41
Fig. 1.29: Sensitivity of the model for (a) significant wave height, (b) water surface salinity, and (c) fetch in standard condition (Blackmore and Lozowski, 1994)	41
Fig. 1.30: Sensitivity of the model for (a) heading angle, (b) vessel speed, and (c) size scaling factor in standard condition (Blackmore and Lozowski, 1994)	42
Fig. 1.31: Evolution of the icicle formation with time	44
Fig. 1.32: Evolution of the icicle formation in the 3-D case with time for a wind velocity of 3 m/s and a supply rate of 10 mg/s	45
Fig. 1.33: Variation of the length growth rate versus air temperature with forced convection for two different amounts of the supply rate: 10 and 20 mg/s and wind velocity of 3 m/s	45
Fig. 1.34: 3-D view of ice accumulation on a hollow hemisphere and a cylinder because of freezing spray	47
Fig. 1.35: A view of marine and pure water icicles (Chung and Lozowski, 2010) ...	48
Fig. 1.36: Estimated ice accumulation rate for the Geosund ship (Shipilova et al., 2012)	49

Fig. 1.37: Ice accumulation rate in the different conditions for the Geosund ship (Shipilova et al., 2012)	50
Fig. 1.38: View of the geometry of a non-horizontal cylinder with a defined 2-D coordinate system (Horjen, 2013)	51
Fig. 1.39: Distribution of the model ice thickness after a 3 hr splashing period of cylinder no. 1 for observation no. 1 at the lower, middle and upper levels (Horjen, 2013, corrected results)	52
Fig. 1.40: Distribution of the model ice thickness after a 3 hr splashing period of cylinder no. 5 for observation no. 1 at the lower, middle and upper levels (Horjen, 2013, corrected results)	52
Fig. 1.41: Distribution of the model ice thickness after a 3 hr splashing period of cylinder nos. 3, 4 and 5 for observation no. 2 at the middle level (Horjen, 2013, corrected results)	53
Fig. 1.42: Ice accumulation rate (mm/hr) on the West Hercules drilling rig for $T_a = -17^\circ\text{C}$, $\psi = 90^\circ$ and $U_{10} = 33$ m/s (Kulyakhtin and Tsarau, 2014)	54
Fig. 1.43: Vertical distribution of model greatest ice thickness on $D = 1.22$ m ($\nu = 70^\circ$) and $D = 1.52$ m ($\nu = 50^\circ$) trusses and estimated greatest ice thickness (from photos by Minsk (1984a)) just after observation 60 (Horjen, 2015)	56
Fig. 2.1: Numerical results of spray cloud movement over an MFV including the maximum wet heights and the maximum extent of spray (Dehghani et al., 2016b)...	67
Fig. 2.2: LWC for the wind spray as a function of the height on top of mean water level (Zakrzewski, 1986b) (From Preobrazhenskii (1973) according to Makkonen	

(1984a))	70
Fig. 2.3: Comparison between various LWC formulae as a function of wave heights (Bodaghkhani et al., 2016)	81
Fig. 2.4: Schematic of sea spray icing and heat balance for vertical components on marine platforms (Dehghani-Sanij et al., 2015)	88
Fig. 2.5: Schematic of sea spray icing and heat balance for horizontal components on marine platforms (Dehghani-Sanij et al., 2016)	88
Fig. 2.6: Variations of surface temperature versus the droplet diameter at different heights (Zarling, 1980)	95
Fig. 3.1: Schematic of sea spray event on a marine vessel	107
Fig. 3.2: Variations of droplet velocity versus time at $U = 15$ m/s and various droplet diameters	117
Fig. 3.3: Pathway of water droplets with various diameters during their flight over the MFV	118
Fig. 3.4: Variations of the droplet's Biot number versus time at various droplet diameters	120
Fig. 3.5: Variations of the water droplet temperature versus time at $T_a = -18^\circ C$, $T_{0,w} = 2^\circ C$, $U = 15$ m/s, $S_w = 34\%$, $RH = 80\%$ and various droplet diameters	121
Fig. 3.6: Heat loss changes versus time at $T_a = -18^\circ C$, $T_{0,w} = 2^\circ C$, $U = 15$ m/s, $D = 1$ mm and $RH = 80\%$	123
Fig. 3.7: Cooling curve for droplets falling from a height of 15 m at $T_a = -18^\circ C$,	

$T_{0,w} = 0^{\circ}\text{C}, U = 0 \text{ m/s}$	125
Fig. 3.8: Variations of the position and velocity of the droplet at different wind velocities and $D = 1 \text{ mm}$	126
Fig. 3.9: Cooling process and the Biot number changes at different (a) wind velocities ($S_b = 34\%$) and (b) salinities ($U = 15 \text{ m/s}$) for $T_a = -18^{\circ}\text{C}$, $T_{0,w} = 2^{\circ}\text{C}$, $D = 1 \text{ mm}$ and $RH = 80\%$	128
Fig. 3.10: Cooling process and the Biot number changes at different (a) initial droplet temperatures ($RH = 80\%$) and (b) relative humidities ($T_{0,w} = 2^{\circ}\text{C}$) for $T_a = -18^{\circ}\text{C}$, $U = 15 \text{ m/s}$, $D = 1 \text{ mm}$ and $S_w = 34\%$	129
Fig. 3.11: Cooling process and the Biot number changes at different ambient air temperatures for $T_{0,w} = 2^{\circ}\text{C}$, $U = 15 \text{ m/s}$, $D = 1 \text{ mm}$, $S_w = 34\%$ and $RH = 80\%$	130
Fig. 4.1: Schematic of the changes of a saline water droplet in freezing conditions during its flight over marine platforms	135
Fig. 4.2: Schematic of the solidification process of a saline water droplet in the second stage	138
Fig. 4.3: Changes of the droplet velocity versus time at a wind velocity of 15 m/s and droplet diameter of 1 mm	152
Fig. 4.4: Water droplet trajectory with a diameter of 1 mm and wind velocity of 15 m/s during its flight on the MFV	153
Fig. 4.5: Comparison of the total time of the droplet freezing for different number of terms of series and dr	154

Fig. 4.6: Droplet cooling and freezing processes: (a) liquid cooling stage, (b) solidification stage, and (c) all stages	156
Fig. 4.7: Variations of the freezing interface position inside the droplet versus time in the solidification stage	157
Fig. 5.1: Schematic illustration of the proposed model for a horizontal plate	160
Fig. 5.2: Changes of the freezing fraction versus air temperature at $v_s = 12.9 m/s$, $U = 20.6 m/s$, $S_w = 34\text{‰}$ and $\alpha = 0^\circ$	165
Fig. 5.3: Changes of the icing intensity per hour versus air temperature at $v_s = 12.9 m/s$, $U = 20.6 m/s$, $S_w = 34\text{‰}$ and $\alpha = 0^\circ$	166
Fig. 5.4: Changes of ice layer and water film thicknesses for two different air temperatures at $v_s = 12.9 m/s$, $U = 20.6 m/s$, $S_w = 34\text{‰}$ and $\alpha = 0^\circ$	167
Fig. 5.5: Changes of ice thickness for different air temperatures at $v_s = 12.9 m/s$, $U = 20.6 m/s$, $S_w = 34\text{‰}$ and $\alpha = 0^\circ$	167
Fig. 5.6: Changes of freezing fraction versus air temperature for different wind velocities at $v_s = 12.9 m/s$, $S_w = 34\text{‰}$, $RH = 80\%$, $L = 1m$ and $\alpha = 0^\circ$	168
Fig. 5.7: Changes of freezing fraction versus air temperature for different salinities at $v_s = 12.9 m/s$, $U = 20.6 m$, $RH = 80\%$, $L = 1m/s$ and $\alpha = 0^\circ$	169
Fig. 5.8: Changes of freezing fraction versus air temperature for different heights at $v_s = 12.9 m/s$, $U = 20.6 m/s$, $S_w = 34\text{‰}$, $RH = 80\%$, $L = 1m$ and $\alpha = 0^\circ$	169
Fig. 5.9: Changes of freezing fraction versus air temperature for different vessel	

speeds at $U = 20.6 \text{ m/s}$, $S_w = 34\text{‰}$, $RH = 80\%$, $L = 1\text{m}$ and $\alpha = 0^\circ$	170
Fig. 5.10: Changes of freezing fraction versus air temperature for different heading angles at $v_s = 12.9 \text{ m/s}$, $U = 20.6 \text{ m/s}$, $S_w = 34\text{‰}$, $RH = 80\%$ and $L = 1\text{m}$	170
Fig. 5.11: Schematic representation of (a) the angle between the vessel heading and the wind/wave direction and (b) the seawater spray flight over a marine vessel.	172
Fig. 5.12: Variations of the freezing fraction versus air temperature at three different times	180
Fig. 5.13: Variations of the freezing fraction versus time for several air temperatures	181
Fig. 5.14: Variations of the ice formation thickness versus time at different air temperatures	182
Fig. 5.15: Variations of the ice layer and water film thicknesses for rime and glaze icing	184
Fig. 5.16: Variations of freezing fraction versus air temperature at two different salinities	185
Fig. 5.17: Variations of freezing fraction versus air temperature at two different wind velocities	185
Fig. 5.18: Comparison of ice layer and water film thicknesses for different models.	186
Fig. 5.19: Variations of the freezing fraction versus air temperature at $v_s = 12.9 \text{ m/s}$, $U = 20.6 \text{ m/s}$, $S_w = 34\text{‰}$ and $\alpha = 0^\circ$	188
Fig. 5.20: Variations of the ice layer thickness versus air temperature at	

$v_s = 12.9 \text{ m/s}$, $U = 20.6 \text{ m/s}$, $S_w = 34\%$ and $\alpha = 0^\circ$	189
Fig. 6.1: Schematic illustration of the experiment with all components	191
Fig. 6.2: Schematic illustration of the vertical plate in detail. Note: all sizes in this figure are in mm	192
Fig. 6.3: Installation of the load cells for measuring ice accretion rates on a vertical plate	193
Fig. 6.4: Schematic illustration of the stand for the vertical plate at different views..	193
Fig. 6.5: Drop size characteristics at (a) $P = 40 \text{ PSI}$ and (b) $P = 100 \text{ PSI}$	194
Fig. 6.6: Characteristics of the fan	195
Fig. 6.7: Stand used underneath the fan	196
Fig. 6.8: Classification of the experiments at various conditions	202
Fig. 6.9: A view of a narrow trapezoidal funnel and a small container	204
Fig. 7.1: Views of ice formation on the vertical plate at $V_{ave,1} \approx 7.85 \text{ m/s}$, $T_C = -10^\circ\text{C}$, $S_w = 0\%$, and the distance of 1.65 m between the fan and the plate	206
Fig. 7.2: Two views of ice accretion on the vertical plate at $V_{ave,3} \approx 2.65 \text{ m/s}$, $T_C = -10^\circ\text{C}$, $S_w = 0\%$, $RH_{ave} = 68.4\%$, including 3 s for the duration of each spray event and 1 min for the period between spray events	214
Fig. 7.3: Changes in (a) the ice weight and (b) temperature at the front and back of the vertical plate versus time at $V_{ave,3} \approx 2.65 \text{ m/s}$, $T_C = -10^\circ\text{C}$, $S_w = 0\%$, $RH_{ave} = 68.4\%$, including 3 s for the duration of each spray event and 1 min for the period between spray events	215
Fig. 7.4: Two views of ice accretion on the vertical plate at $V_{ave,3} \approx 2.65 \text{ m/s}$, $T_C =$	

-10°C, $S_w = 35\%$, $RH_{ave} = 69.6\%$, including 3 s for the duration of each spray event and 1 min for the period between spray events	216
Fig. 7.5: Changes in (a) the ice weight and (b) temperature at the front and back of the vertical plate versus time at $V_{ave,3} \approx 2.65$ m/s, $T_C = -10^\circ\text{C}$, $S_w = 35\%$, $RH_{ave} = 69.6\%$, including 3 s for the duration of each spray event and 1 min for the period between spray events	217
Fig. 7.6: Variations of the water temperature inside the pipe versus time for (a) test (1-1-2-b) and (b) (1-2-1-b)	218
Fig. 7.7: Changes in the ice weight versus time for tests (1-1-1-a) and (1-1-1-b).....	220
Fig. 7.8: Changes in the ice weight versus time for tests (1-1-1-a) and (2-1-1).....	521
Fig. 7.9: Changes in the ice weight versus time for three different fan speeds, $T_C = -20^\circ\text{C}$, $S_w = 35\%$, and the distance of 2.5 m between the fan and the plate.....	222
Fig. 7.10: Changes in the ice weight versus time for two different times of spray event, $T_C = -10^\circ\text{C}$, $S_w = 0\%$, $V_{ave,3} = 2.65$ m/s and the distance of 2.5 m between the fan and the plate	224
Fig. 7.11: Temperature changes at the front and back of the vertical plate versus time for tests (1-1-1-b) and (1-2-1-b)	225
Fig. 7.12: Comparison of the amount of collided water mass and ice accretion on the vertical plate versus time for different conditions	227
Fig. 1.A: Views of ice accretion on the vertical plate for (a) test (1-1-1-a), (b) (1-1-1-b), (c) (1-1-2-a), (d) (1-1-2-b), (e) (1-1-3-a), (f) (1-1-3-b) and (g) (1-1-3-c)	260
Fig. 2.A: Variations of the ice weight versus time on the vertical plate for (a) test	

(1-1-1-a), (b) (1-1-1-b), (c) (1-1-2-a), (d) (1-1-2-b), (e) (1-1-3-a), (f) (1-1-3-b) and (g) (1-1-3-c)	263
Fig. 3.A: Variations of the temperature at the front and back of the vertical plate versus time for (a) test (1-1-1-a), (b) (1-1-1-b), (c) (1-1-2-a), (d) (1-1-2-b), (e) (1-1- 3-a), (f) (1-1-3-b) and (g) (1-1-3-c)	266
Fig. 4.A: Views of ice accretion on the vertical plate for (a) test (1-2-1-a), (b) (1-2- 1-b), (c) (1-2-1-c), (d) (1-2-1-d), (e) (1-2-2-a), (f) (1-2-2-b), (g) (1-2-3-a) and (h) (1-2-3-b)	269
Fig. 5.A: Variations of the ice weight versus time on the vertical plate for (a) test (1-2-1-a), (b) (1-2-1-b), (c) (1-2-1-c), (d) (1-2-1-d), (e) (1-2-2-a), (f) (1-2-2-b), (g) (1-2-3-a) and (h) (1-2-3-b)	273
Fig. 6.A: Variations of the temperature at the front and back of the vertical plate versus time for (a) test (1-2-1-a), (b) (1-2-1-b), (c) (1-2-1-c), (d) (1-2-1-d), (e) (1-2- 2-a), (f) (1-2-2-b), (g) (1-2-3-a) and (h) (1-2-3-b)	277
Fig. 7.A: Views of ice accretion on the vertical plate for (a) test (2-1-1), (b) (2-1-2) and (c) (2-1-3)	279
Fig. 8.A: Variations of the ice weight versus time on the vertical plate for (a) test (2-1-1), (b) (2-1-2) and (c) (2-1-3)	280
Fig. 9.A: Variations of the temperature at the front and back of the vertical plate versus time for (a) test (2-1-1), (b) (2-1-2) and (c) (2-1-3)	282
Fig. 10.A: Views of ice accretion on the vertical plate for (a) test (2-2-1), (b) test (2-2-2-a), (c) (2-2-2-b) and (d) (2-2-3)	283

Fig. 11.A: Variations of the ice weight versus time on the vertical plate for (a) test (2-2-1), (b) (2-2-2-a), (c) (2-2-2-b) and (d) (2-2-3) 285

Fig. 12.A: Variations of the temperature at the front and back of the vertical plate versus time for (a) (2-2-1), (b) (2-2-2-a), (c) (2-2-2-b) and (d) (2-2-3) 287

Nomenclature

A_{eff}	Effective area, m^2
A_s	Surface area of the droplet, m^2
a	Linearization constant, K^3
Bi	Biot number, -
B_s	Shape coefficient, -
b	Ice layer thickness, m
C_d	Droplet drag coefficient, -
c	Specific heat capacity, $J/kg.K$
D	Droplet diameter, m
D_{ab}	Diffusivity of air-water vapour, m^2/s
E	Collision efficiency, -
$e_s(T)$	Saturated vapour pressure, Pa
f_s	Slip factor, -
g	Gravitational acceleration, m/s^2
H_{bow}	Height of vessel bow above surface level, m
H_m	Maximum height of the spray jet, m
h	Height, m, and heat transfer coefficient, $W/m^2.K$
h_s	Significant wave height, m

k	Thermal conductivity, W/m.K
L	Characteristic length, m
l_f	Latent heat of fusion of pure ice, J/kg
l_v	Latent heat of vaporization, J/kg
$\dot{M}_{evap,w}$	Mass flux evaporation, kg/m ² .s
\dot{M}_{ice}	Mass flux of ice formation, kg/m ² .s
$\dot{M}_{runoff,w}$	Mass flux out (runoff), kg/m ² .s
$\dot{M}_{w,t}$	Total flux of sea water spray, kg/m ² .s
\dot{m}_v	Evaporation rate, kg/m ² .s
N_i	Icing intensity per hour, mm/hr
Nu	Nusselt number, -
n	Freezing fraction, -
P	Pressure, Pa
Pr	Prandtl number, -
Q	Heat flux, W/m ²
Re	Reynolds number, -
RH	Relative humidity of the air, %
R_i	Interface radius, m
r	Droplet radius and radial coordinate, m
S	Salinity, ‰
Sc	Schmidt number, -

T	Temperature, °C
T_f	Freezing temperature, °C
T_s	Temperature of the water film at the air-water interface, °C
$T_{0,w}$	Initial temperature of the droplet, °C
t	Time, s
U	Wind velocity, m/s
U_h	Droplet velocity at the moment of impact on the plate, m/s
U_{rw}	Relative velocity of wind to the vessel, m/s
U_{10}	Wind velocity at a height of 10 m above mean sea level, m/s
u_{eff}	Effective velocity, m/s
u^*	Friction velocity, m/s
V_d	Droplet volume, m ³
v_d	Droplet velocity with regard to the ground, m/s
v_s	Vessel speed, m/s
v_{sw}	Vessel speed relative to the waves, m/s
x	Cartesian coordinate and horizontal component of the position vector of droplets with regard to the vessel, m
y	Cartesian coordinate and vertical component of the position vector of droplets with regard to the vessel, m
Greek symbols	
α	Thermal diffusivity, m ² /s

β	Interfacial distribution coefficient, -
γ	Angle between the direction of wind velocity and vessel speed, °
$\gamma_n, \lambda_n, \xi_n$	Eigenvalues, -
δ	Initial travel angle of droplets, °
$\bar{\delta}_t$	Average thickness, m
ε	Emissivity, -
ϵ	Ratio of the molecular weight of water vapour/dry air, -
η	Water film thickness, m
θ	Temperature, °C
μ	Dynamic viscosity, Pa.s
ν	Kinematic viscosity, m ² /s
ρ	Density, kg/m ³
σ	Stefan-Boltzmann constant, W/m ² .K ⁴
τ_s	Duration of sea spray event, s
τ_p	Period between sea spray events, s
τ_w	Significant wave period, s
ω	Liquid Water Content (LWC), kg/m ³

Subscripts

a	Ambient air
b	Brine
C	Cold room

<i>c</i>	Convection
<i>d</i>	Droplet
<i>e</i>	Evaporation
<i>f</i>	Freezing
<i>i</i>	Ice and ice/water interface
<i>m</i>	Maximum
<i>n</i>	Moment of impact on the deck
<i>r</i>	Radiation
<i>w</i>	Water
<i>0</i>	Initial

Chapter 1

Review of Marine Icing Phenomena on Offshore Vessels and Structures¹

1.1 Introduction

The population of the world is growing and will likely reach almost 9 billion people by 2048 (Kreith and Krumdieck, 2013). The development of new renewable energy sources is necessary. Energy supply is a basic requirement for the economic and social development of countries. Oil and gas are still among the major sources of energy worldwide. According to a report by Gautier et al. (2009), approximately 30% of the world's undiscovered natural gas resources and almost 13% of the world's undiscovered petroleum resources may be found in the areas north of the Arctic Circle. The resources, which are typically extracted by offshore structures, are generally around 500 m below the water's surface (Gautier et al., 2009). The exploration and exploitation of oil and gas resources in Arctic regions are both technically difficult and costly because there are many environmental challenges, including the freezing of sea spray and atmospheric precipitation. Efimov (2012) reported that after the increase of offshore operations in the cold areas of Norway and Alaska due to the oil exploration and extraction, the icing

1 . This chapter is based on a review paper that was published in Ocean Engineering (journal).

problems on marine vessels and drilling rigs became a significant important issue and challenge for the oil and gas industry.

Seawater spray and precipitation are the two main sources of icing and ice accumulation in cold seas and ocean regions. Panov (1976) reported that severe ship icing happens mainly in northern regions, such as: the northern coast of Norway and the Kola Peninsula to the Spitsbergen in the Barents sea; in the Northern Atlantic near Canada; in the sea of Okhotsk and in the northern part of the Japan sea; in the Bering sea near the shore of Alaska; and near the Kuril Islands and Kamchatka (Efimov, 2012). Table 1.1 shows the percentage distribution of ship icing among these seas and ocean, which was obtained by Panov (1976) and Vasileva (1971). It should be mentioned that the results obtained by Vasileva (1971) are for the period between 1950 and 1971.

Table 1.1: Distribution of ship icing among the seas and ocean (Efimov, 2012)

Region	Percentage, obtained by Panov (1976)	Percentage, obtained by Vasileva (1971)
Barents and Norwegian Sea	34.5	38.6
Bering Sea	25.5	25.2
Sea of Okhotsk	18.0	19.3
Western Pacific Ocean	10.5	8
Sea of Japan	8.1	6.2
Baltic Sea	2.4	1.9
Black and Azov Seas	1.0	0.8 ¹

1. This percentage is only for the Black Sea

The phenomenon of icing has led to many fishing vessels of small and medium sizes to be lost at sea (Aksyutin, 1979; Fukusako et al., 1989; Guest, 2005; Hay, 1956; Jessup, 1985; Lundqvist and Udin, 1977; Shellard, 1974; Zakrzewski, 1987; Zakrzewski and Lozowski, 1989a) and has adversely affected the stability and movement of small cargo ships (Aksyutin, 1979; Lundquist and Udin, 1977; Zakrzewski, 1987). According to a report by Hay (1956a), sea spray icing had caused the loss of two trawlers, the “Lorella” and the “Roderigo”, in the north coast of Iceland in January 1955. Blackmore and Lozowski (1994) reported that this accident prompted the start of studies on ship icing problems. Hay (1956b) and Lackenby (1960) carried out a serious investigation on icing problems involving trawlers. Sutherby (1951) reported that the icing problems of naval ships were fully known after the Second World War. Shellard (1974) provided a list of the loss of 81 vessels from the winter of 1942 to December 1970 due to icing. Fukusako et al. (1989) reported that sea spray icing caused more than 25 severe accidents for fishing vessels from 1960 to 1987 in the northern winter sea near Hokkaido, Japan. According to a report by Shekhtman (1968), 10 Soviet ships were damaged in the Bering Sea in January 1965 because of instability caused by the accretion of ice. Figure 1.1 illustrates an example of ice accretion due to sea spray icing on a marine vessel. Visual and thermal photos can be used to estimate ice loads on structures (Fazelpour et al., 2016a, 2016b). Figure 1.2 shows accumulated ice on a marine structure in cold weather conditions.



Fig. 1.1: View of ice accumulation on deck of a marine vessel (Cammaert, 2013)



Fig. 1.2: View of ice formation on a marine structure (Marine Log Website)

1.2 Icing Phenomena

Sea spray icing can lead to substantial hazards, including stability problems of marine vessels and safety of a crew in cold seas or ocean regions (Cammaert, 2013; Dehghani-Sanij et al., 2017a; Feit, 1987; Fukusako et al., 1989; Jørgensen, 1982; Jessup, 1985;

Lock, 1972; Lundqvist and Udin, 1977; Rashid et al., 2016; Ryerson, 2008, 2009, 2011; Wiersema et al., 2014). Jessup (1985) expressed that sea spray icing can increase the vessel's weight and lower its freeboard (the distance of the water level from the deck); consequently, icing will raise the center of gravity and decrease the stability. A number of researchers have reported the hazards caused by icing and ice accumulation on marine platforms (Brown and Mitten, 1988; Cammaert, 2013; Jessup, 1985; Jørgensen, 1982; Makkonen, 1989; Nauman and Tyagi, 1985; Ryerson, 2008, 2009, 2011; Schrøder Hansen, 2012). Ryerson (2011) and Cammaert (2013) provided a list of the hazards of the icing phenomena for marine vessels and offshore structures. These hazards are: instability and loss of integrity of marine ships and structures, malfunction of the operational equipment such as winches, derricks and valves as well as communication antennas, slippery handrails, ladders or decks, unusable lifeboats and fire equipment, and the blocking of air vents. Also, the icing problems caused by seawater spray and precipitation for offshore structures were reported by Jørgensen (1982). Risks created by the offshore icing phenomenon are a function of the kind of icing, and how it affects special regions and functions of platforms. The icing phenomenon is not generally a major problem, but the kinds of ice that can be experienced offshore, where it forms, and its physical characteristics have significant impacts on activities and regions of platforms (Ryerson, 2009).

According to a report by Jørgensen (1982), atmospheric icing will be created because of the freezing of freshwater in the form of supercooled drizzle or rain, snow or sleet, supercooled fog, and frost smoke. Saha et al. (2016a) reported on the freezing of saline water droplets on cold plates in different situations. They reported that the size and

salinity of water droplets, as well as the surface temperature of plates, affect the freezing phenomena significantly. Additionally, Ryerson (2011) reported that atmospheric icing can be categorized as (a) glaze ice, which is freezing rain, snow and drizzle, (b) hoar frost resulting from the direct deposition of water vapor as ice crystals, as well as (c) rime ice resulting from supercooled cloud or fog droplets. The author also reported that sleet, which is a type of freezing precipitation, is traditionally not categorized as atmospheric icing. Makkonen (2000) showed that atmospheric icing is a result of freezing either by cloud droplets, raindrops, snow or water vapor. Minsk (1977) reported that ice formation by atmospheric precipitation does not usually contain brine inclusions. Also, three major types of ice can form depending on wind velocity and ambient air temperature: glaze, hard rime and soft rime. Table 1.2 illustrates their properties and occurrence. Moreover, a combination of glaze-hard rime, glaze-wet snow, hard and soft rime, and glaze-soft rime can happen (Minsk, 1977).

Table 1.2: Types of ice formation by atmospheric precipitation (Minsk, 1977)

Type of ice	Appearance	Density (g/cm ³)	Conditions of formation
Glaze	Hard, well-bonded, generally clear homogeneous ice	0.7 - 0.9	Supercooled water droplets at a temperature close to freezing (0 to -3°C) and wind velocities of 1-20 m/s
Hard rime	Hard, granular white or translucent ice growing in the direction of the wind	0.1 - 0.6	Supercooled water droplets at a temperature of -3 to -8°C, wind velocities generally 5-10 m/s
Soft rime	White, opaque, granular ice with delicate structure only loosely bonded, growing in the direction of the wind	0.01 - 0.08	Supercooled water droplets at a temperature of -5 to -25°C and low wind velocity (1-5 m/s)

Wave-generated and wind-generated spray are the two principal sources of sea spray icing or marine icing in cold seas or ocean regions. Wave spray is generated due to the impact of waves on marine vessels and offshore structures. According to Dehghani-Sanij et al. (2015, 2016, 2017a) and Schröder Hansen (2012), wave spray is ordinarily a large source that is typically a short and approximately periodic water flux. Wind spray is generated by sea spray from water droplets that are ejected off whitecaps onto the sea or ocean surface. Wind spray is generally a small source that is a constant water flux (Dehghani-Sanij et al., 2015, 2016, 2017a; Schröder Hansen, 2012). It is not a major factor in many cases of sea spray icing, but it can have a significant impact on the icing of small ships like fishing vessels. Figure 1.3 indicates a cloud of spray by waves on a marine vessel.



Fig. 1.3: View of splashing of the seawater spray generated from waves on Dutch Coastguard Vessel at the North Sea (<https://www.reddit.com/r/GaleWarning/>)

A number of researchers reported that sea spray is a major reason of icing on marine vessels and offshore structures (Aksyutin, 1979; Brown and Roebber, 1985; Cammaert,

2013; Feit, 1987; Itagaki, 1979; Jørgensen, 1982; Kato, 2012; Lozowski et al., 2000; Makkonen, 1984a, 1984b; Minsk, 1977; Shekhtman, 1968; Shellard, 1974; Stallabrass, 1980; Tabata et al., 1963; Zakrzewski, 1986a, 1986b, 1987). Jørgensen (1982) reported that atmospheric icing, alone or together with seawater spray icing, amounts to only 5-10% of the recorded icing events in North Atlantic waters. Cammaert (2013) reported that according to Russian investigations, seawater spray creates approximately 90% of the icing on vessels. According to a report by Minsk (1984), the freezing rain happens only around 4% of the time in the Barents and Chukchi Seas. Borisenkov and Panov (1972) studied more than 2,000 samples of icing on Soviet fishing ships using statistical methods. They showed that the main source of icing is freezing seawater spray (Table 1.3).

Table 1.3: Causes of accumulated ice by different sources
(Borisenkov and Panov (1972); Feit (1987)).

	Spray (%)	Spray with fog, rain or drizzle (%)	Snow (%)	Fog, rain or drizzle (%)
Northern Hemisphere	89.9	6.4	1.1	2.7
Arctic	50.0	41.0	N/A	9.0

The incidents of icing of marine vessels, according to numerous observations by several researchers, are displayed in Table 1.4. From this table, sea spray icing happens more than 80% of the time on marine vessels except for Arctic regions because, according to a report by Aksyutin (1979), sea spray and atmospheric icing includes 50%

and 41% of the icing in these regions, respectively (Table 1.4), but the total number of observations is “unknown” in this report. Cammaert (2013) expressed that the greatest quantity of seawater spray happens up to height of 15 - 20 m above the sea surface, which produces almost 50 to 90% of the accumulated ice on marine vessels. According to the majority of past studies, the splashing of a stationary rig is less intense compared to the splashing of a vessel, and seawater spray seldom carries more than 5 to 10 m over the sea surface (Cammaert, 2013). It should be noted that several researchers, such as Zakrzewski (1987) and Lozowski et al. (2000) ignored wind-generated spray for the modeling, prediction, and calculation of the amount of marine icing.

Table 1.4: Reasons of icing of marine vessels (Zakrzewski, 1987)

Region	Total number of observations	Cause of icing (%)			Reference
		Sea spray	Spray and fog or rain or snow	Other types	
All seas	400	89.0 (82) ¹	7.0 (16) ¹	4.0 (2) ¹	Shekhtman (1968)
North Pacific	3000 ²	89.8	7.5	2.7	Aksyutin (1979)
North Atlantic					
Arctic	Unknown	50.0	41.0	9.0	Aksyutin (1979)
Gulf of St. Lawrence	100	81.0	2.0	17.0	Brown and Roebber (1985)
Scotian Shelf	536	94.2	3.0	2.8	Brown and Roebber (1985)
Grand Banks	100	97.0	2.0	1.0	Brown and Roebber (1985)
NE Newfoundland Shelf	233	95.9	1.4	2.8	Brown and Roebber (1985)
Labrador Sea and Davis Strait	72	86.9	11.1	1.7	Brown and Roebber (1985)

1. Reported cases of fast growth of ice are given in parentheses, if known.

2. Makkonen (1984a) and Shellard (1974) mentioned more than 2000 cases of icing.

Bodaghkhani et al. (2016) reviewed the process of spray cloud formation on the topside of the bows of the vessels due to wave impact. They indicated that sea spray

production consists of several stages of free surface related phenomena such as: wave slamming, air-entrainment process, water sheet formation, water sheet breakup and spray cloud formation. Additionally, they extensively reviewed the methods and phenomena related to these concepts and suggested a pathway for tackling this problem. Droplet-size dependence after primary breakup at the tip of vessels striking a wave was reported by Dehghani et al. (2016a). This study suggested initial velocities and sizes of droplets for a trajectory model related to marine vessels. A sensitivity analysis determines the best injection angle, size-velocity dependence and initial velocity for the case of wave-impact sea spray. Dehghani et al. (2016b) employed the size-velocity dependence to calculate the distribution of size and velocity of droplets in a cloud of spray travelling over a vessel. They showed that very small and very large droplets cannot reach the highest heights on the deck. Small droplets are carried by the wind and large droplets fall on the deck soon after. The results are validated using the maximum height reported in field observations.

Water breakup occurs as a result of the high energy impact of a sea wave on the bow or hull of a vessel. Dehghani et al. (2017a) modeled spray cloud generation considering “bag breakup” and “stripping breakup” phenomena. Breakup phenomena affect the distribution of sizes and velocities of droplets in a spray cloud moving over the deck. For modeling of water impact on a vertical plate, Saha et al. (2016b) conducted a set of experiments, including the impact of water jet on a vertical plate, to determine the water area spread on the plate. They reported on the variation of this area versus water jet velocities and angles.

A number of researchers reported that several parameters have significant influences on the ice accumulation upon marine platforms during a seawater spray event (Blackmore

and Lozowski, 1994; Cammaert, 2013; Fukusako et al., 1989; Guest, 2005; Jørgensen, 1982, 1985; Minsk, 1977; Rashid et al., 2016). These parameters are: (1) environmental factors, including wind velocity, ambient air temperature, droplet temperature, salinity, sea surface temperature, the size and distribution of droplets, relative humidity, characteristics of swell and wind waves (height, period, propagation direction), and sea or ocean states, as well as (2) the characteristics of marine vessels, including the size and design of vessels, vessel speed, and the angle between the vessel heading and wind/wave direction. In addition, sea spray icing can occur once the following environmental factors exist:

(1) *High wind velocity*. When the wind velocity exceeds approximately 9 m/s, impact-generated spray may impinge on marine platform columns and trusses (Horjen and Vefsnmo, 1985).

(2) *Low air temperature*. According to reports by Tabata et al. (1963) and Tabata (1969), ice accumulation begins at an air temperature of -2°C , and the highest growth rate of icing intensity occurs at -17°C , below which the icing rate decreases. Kulyakhtin and Tsarau (2014) reported that the water and its salt content freezes once the brine temperature falls below -23°C . Furthermore, Lundqvist and Udin (1977) reported that the air temperature must go below -2°C for icing to occur in ocean water. Cammaert (2013) stated that, for sea spray, ice accumulation occurs when both the air temperature is under the freezing point of seawater (-2°C), and air-borne brine droplets affect a structure and partially freeze. Some Russian sources reported that once the air temperature is lower than -18°C , spray icing does not occur; the water droplets will freeze in the air during their flight, convert to ice crystals, and will not adhere to components of marine vessels

and offshore structures (Minsk, 1977). However, in reality, there will be many cases of marine icing once the air temperature is below -18°C (Berenbeim, 1969; Minsk, 1977). Several parameters, such as air temperature, salinity, the size of the droplets, wind velocity, relative humidity, the droplet flight time, and the temperature of the seawater surface have substantial effects on the freezing process of water droplets. Moreover, the size of marine vessels and structures is an important factor.

(3) *Low seawater temperature.* Commonly, sea temperature should be less than 5°C for sea spray icing (Cammaert, 2013). According to a report by the US Navy (1988), the critical temperatures of seawater for marine icing are between -2.2 and 8.9°C in the Aleutian Islands, the Gulf of Alaska, the Bering Sea and the Arctic (Cammaert, 2013; Fett et al., 1993; US Navy, 1988). For most Canadian waters, freezing spray seldom occurs once the seawater surface is warmer than 5°C . Also, the temperature of the seawater's surface is generally between -1.7 and 5°C (Dehghani-Sanij et al., 2017a).

Dehghani-Sanij et al. (2017a) reviewed the fundamentals and formulations of the sea spray icing phenomena on marine platforms. They studied several issues, such as: droplet trajectories, the flux of sea spray, liquid water content (LWC), heat balance at the phase interface, and freezing equations. The topics and formulae to be discussed in this study are fundamental to forecast and compute the growth rate of icing as well as obtain the amount of ice accumulation on marine vessels and offshore structures in cold seas and ocean regions. Note that sea spray icing is a complicated phenomenon because seawater cannot entirely freeze. Freezing of the seawater spray leads to the formation of spongy ice, which contains pure ice, brine pockets and air bubbles. Fukusako et al. (1989) expressed that the inclusion of salinity impacts and their time dependence are two

important issues for the sea spray icing phenomenon. It is worth mentioning that the salinity of droplets depends on the droplet sizes and the droplet flight time in the air.

1.3 Review of Sea Spray Icing Models

This section will briefly examine some substantial past developments in modeling and estimating the ice formation caused by seawater spray icing using different experimental, theoretical and numerical approaches. The authors classified the marine icing models into three parts according to the time that the research was conducted: before 1980, between 1980 and 2000, and after 2000.

1.3.1 Icing Models Before 1980

The early studies, which were carried out on the prediction and estimation of the icing rate over marine vessels and structures using semi-quantitative analyses, were mostly experimental methods that included atmospheric and seawater spray freezing. These methods are typically based on graphs, charts and nomograms that are obtained from empirical observations and reported on icing events (Jessup, 1985). For instance, Sawada (1966) presented one set of graphs that illustrate the relationship between icing on vessels, air temperature and wind velocity. The results were derived according to the data obtained from Japanese patrol and fishing vessels. These results will be presented and compared with other results in the following subsection. In another study, Mertins (1968) obtained one set of charts for icing on German trawlers, which were acquired from approximately 400 empirical observations in the Northeast Atlantic (Fig. 1.4). Jørgensen (1985) reported that these charts are valid only for a small range of ship sizes (trawling

operations) and velocities (2 to 5 knots). Figure 1.4 shows the charts obtained by Mertins (1968) for icing on trawlers at low velocities in wind of a Beaufort force ranging from 6 to 12. Comiskey (1976) combined these four graphs into a single nomograph (Fig. 1.5). Berenbeim (1969) expressed that Mertins' icing charts need corrections because they are based on the assumption that there is no icing when the ambient air temperature is below -18°C . Minsk (1977) reported that actual shipboard observations have illustrated that the icing phenomenon can happen for air temperatures as low as -29°C .

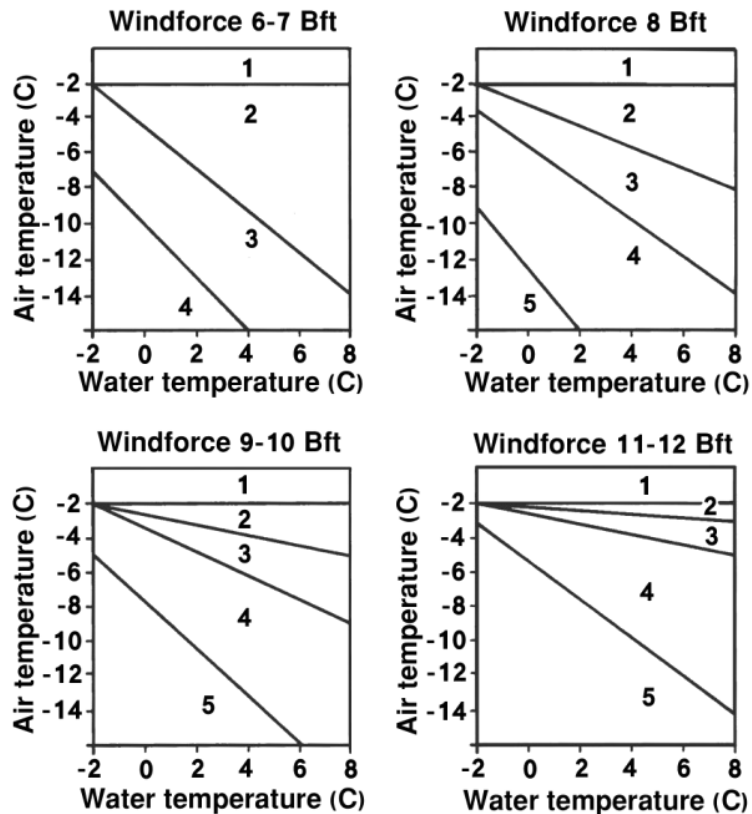


Fig. 1.4: Mertins' icing charts (Mertins 1968, Jessup, 1985). Degree of icing: 1-None, 2-Light (1-3 cm/24hr), 3-Moderate (4-6 cm/24hr), 4-Severe (7-14 cm/24hr), and 5-Very Severe (≥ 15 cm/24hr). Note that in this figure, Bft refers to Beaufort scale.

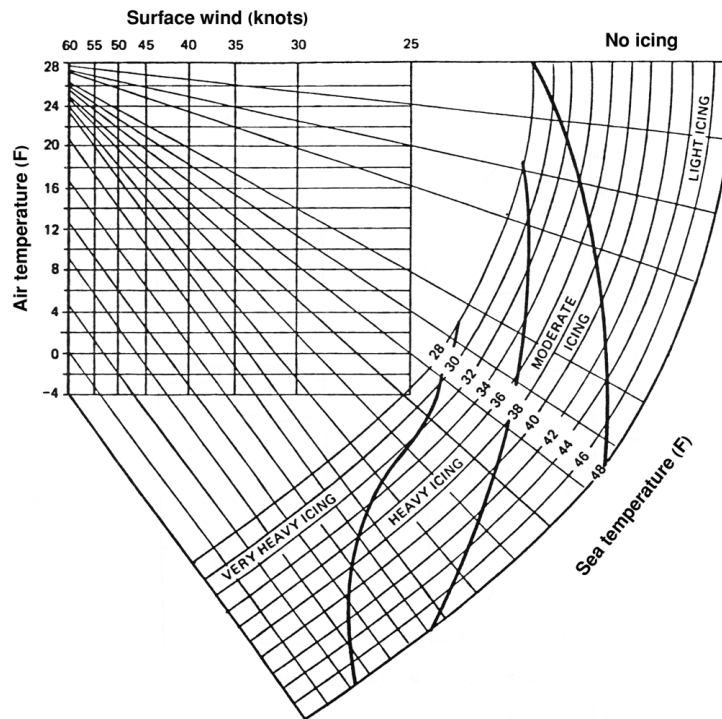


Fig. 1.5: Comiskey's nomograph for prediction of icing rate (Comiskey, 1976; Jessup, 1985). Light: 0.4 to 1.4 inch during 24 hr, Moderate: 1.4 to 2.6 inch during 24 hr, Heavy: 2.6 to 5.7 inch during 24 hr, and Very Heavy 5.7 inch and more during 24 hr

To forecast and estimate the ice accumulation rate on the cylindrical shaft (50 cm diameter) of a small trawler, Kachurin et al. (1974) collected data of many icing incidents that were obtained from Soviet research vessels and Japanese fishing ships. They theoretically modeled the accumulated ice thickness on the shaft, and then compared this thickness with the observed weight of ice accumulation for each of these incidents by considering only wave-generated spray. The following assumptions were used: (1) steady state conditions at the ice-water and air-water interfaces, (2) a wind velocity between 6 and 30 m/s, (3) the main liquid water impingement rate and the droplet temperatures are

not varying in time, (4) the collision efficiency is equal to 1, (5) the thermal conductivity of the shaft is significant compared to the ice and water, and (6) neglecting kinetic energy flux, radiative transfer flux, and viscous heating flux.

Figure 1.6 indicates the results obtained by Kachurin et al. (1974) to specify the rate of icing on small Soviet trawlers. Jessup (1985) explained how the ice accumulation rate can be calculated for a whole vessel by using this nomogram. The comparison between the experimental results and the theoretical predictions is displayed in Fig. 1.7(a). Also, the comparison between the mean amount of the actual icing rate and the predicted icing rate is shown in Fig. 1.7(b). Note that in these graphs, Kachurin et al. (1974) utilized data only for those incidents when the vessel heading was less than or equal to 40° relative to the wind. Thus, the rates of icing illustrate the maximum amount for the related hydro-meteorological conditions.

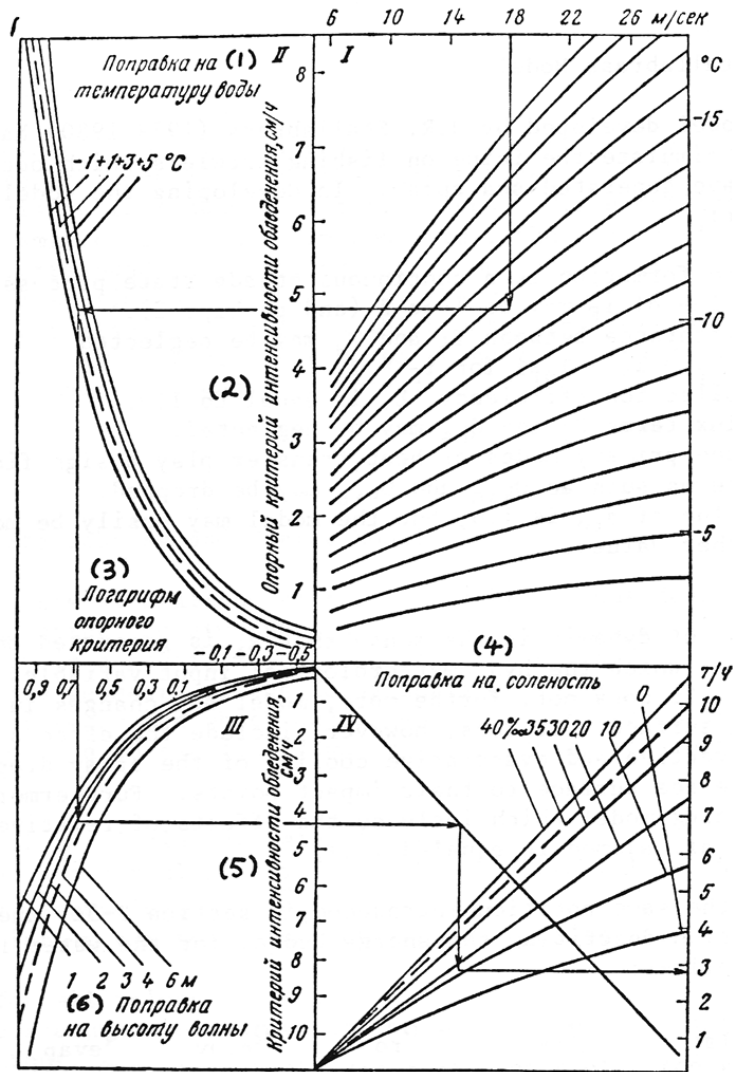


Fig. 1.6: Nomogram to define the icing rate of small Soviet fishing ships (Kachurin et al., 1974; Jessup, 1985). Note: (1) correction factor for water temperature, (2) reference criterion of icing rate (cm/hr), (3) logarithm of reference criterion, (4) correction factor for salinity, (5) criterion of icing rate (cm/hr), and (6) correction factor for wave height.

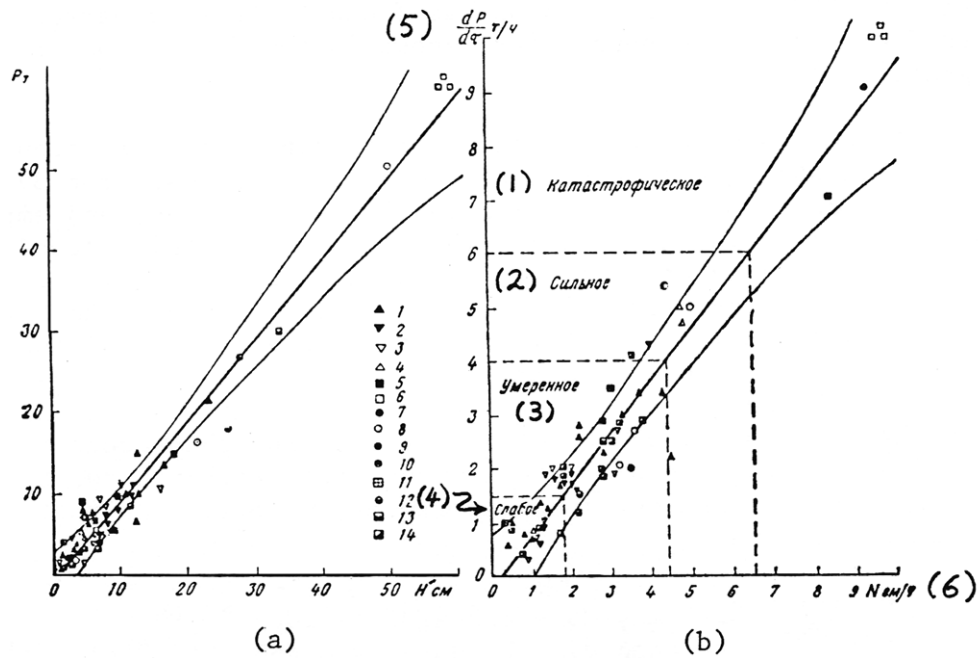


Fig. 1.7: (a) Relationship between the weight of ice formation, P , which is created on vessel in duration of the icing incident and predicted ice thickness, H' , on the cylindrical shaft, which is computed for the same hydro-meteorological conditions, and (b) relationship between the predicted icing rate of the cylindrical shaft, N , and the actual icing rate, dP/dt , from types medium fishing trawler and medium fishing trawler-freezer vessels (Kachurin et al., 1974; Jessup, 1985). Note: (1) Catastrophic, (2) Severe, (3) Moderate, (4) Light, (5) tones/hr, and (6) N

As part of the research conducted by the Swedish Meteorological and Hydrological Institute (SMHI), Lundqvist and Udin (1977) investigated the icing phenomenon and ice accumulation on vessels traveling in the Baltic Sea. SMHI collected icing data and reports in the middle of 1960 from different types of marine vessels in the Baltic. The salinity of this sea was between 15‰ (in the south) and 3‰ (in the north), and the temperature of

the seawater surface was approximately between 0°C in the winter and 20°C in the summer. During the data collection, more than 300 reports were prepared. The total data collection was not homogeneous because the data was collected for several vessel types and tonnages (Lundqvist and Udin, 1977). Table 1.5 illustrates the various classifications of icing rate that were reported by Lundqvist and Udin (1977). Note that measuring the class of icing is not simply achievable, because the amount of ice formation is generally a non-uniform distribution on the marine vessel. Also, several parameters affect the class of icing such as: the vessel’s design and size, the vessel’s course and speed, and the parameters of meteorological and oceanographic conditions.

Table 1.5: Classification of icing rate (Lundqvist and Udin, 1977)

Icing Class	SMHI	WMO² before 1975	WMO from 1975	Mertins (1968)
Light	0.5-2 cm / 12 hrs	0.6-1.2 cm / 12 hrs	1 cm / 3 hrs	1-3 cm / 24 hrs
Moderate	1-3 cm / 4 hrs		1-5 cm / 3 hrs	4-6 cm / 24 hrs
Severe	> 4 cm / 4 hrs	2.5 cm / 4 hrs	6-12 cm / 3 hrs	7-14 cm / 24 hrs
Very Severe			> 12 cm / 3 hrs	≥ 15 cm / 24 hrs

Note: Various classifications have been determined by different researchers

Lundqvist and Udin (1977) considered four main factors to create ice accumulation: (1) sea spray, (2) overflow of water, (3) supercooled fog and raindrops, and (4) snow. Tabata et al. (1963) and Ono (1964) investigated the icing process and the formation of accumulated ice on various parts of the vessel with details. According to Fig. 1.8, the results obtained by Tabata et al. (1963) and Ono (1964) demonstrate that the amount of ice accumulation changes due to the size of droplets and wind velocity. When water droplets are small and the wind velocity is low, all droplets will freeze immediately upon

2. World Meteorological Organization

impact provided the temperature is sufficiently low (Fig. 1.8(a)). For larger water droplets and a higher wind velocity, after the impingement of the droplets on the object, they will not freeze before coming next droplets, so the water film will move downward. Figures 1.8(b) and 1.8(d) illustrate the typical formation of the accumulated ice. With a further increase of droplets, more water can collect on the sides and move downward before freezing (Fig. 1.8(c)). Figure 1.9 shows icing severity with air temperature and wind velocity for two vessel sizes. As illustrated in this figure, the accumulated ice starts to form at air temperature of -2°C , and for vessel sizes of 350 to 450 tonnes, icing happens from a wind velocity of 6 to 8 m/s. Also, by decreasing the air temperature and increasing the wind velocity, severe icing will occur. According to Lundqvist and Udin (1977), ice accretion begins at air temperatures between 0°C and -0.5°C because the salinity of the Baltic Sea is low.

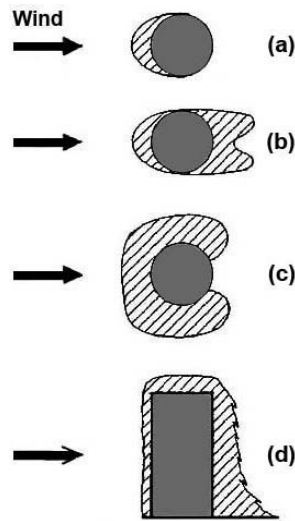


Fig. 1.8: Formation of ice accumulation with various sizes of water droplets (Tabata et al. (1963) and Ono (1964)): (a) small droplets and low wind velocity, and for (b), (c) and (d) larger droplets and stronger wind but with different conditions

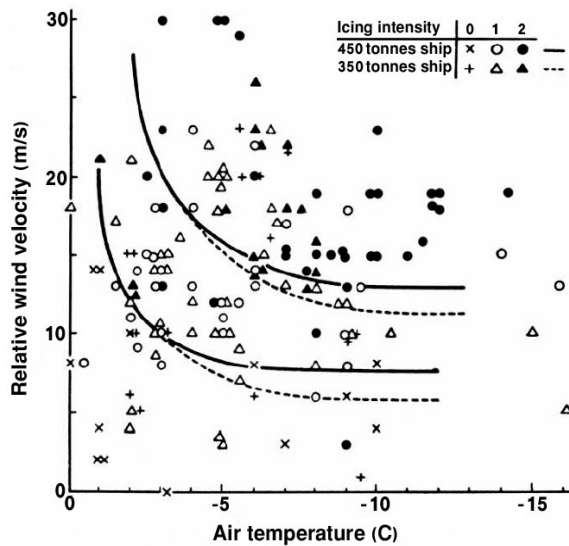


Fig. 1.9: Icing severity corresponding to air temperature and wind velocity (Borisenkov and Panov (1972), taken from Japanese data in Tabata et al. (1963)).

Note that the number of 0, 1, and 2 in this figure refer to no icing, significant icing, and heavy icing, respectively.

According to Lundqvist and Udin (1977), the ice accumulation on various ship decks is caused mostly by large water droplets or washing of the deck by seawater. Additionally, they mentioned that the distribution and the value of ice accumulation on marine vessels are not identical because several parameters have an impact on the icing phenomenon, such as the course and speed of the vessel relative to waves and wind, and the height and length of waves. Figure 1.10 illustrates the rate and distribution of icing on Japanese patrol ships, which were obtained by Tabata (1969) due to field observation. As a result, the rate of icing is higher for angles of vessels heading between 30° and 60° relative to the waves when the traveling vessels pass through the waves. According to field observation, Panov and Moltjanov (1972) reported that the maximum spray intensity

and icing rate occur at angles of vessel heading between 30° and 40° towards the waves for fishing ships (Fig. 1.11). In addition, they reported that the intensity and icing rate will increase when the vessel speed increases at greater angles.

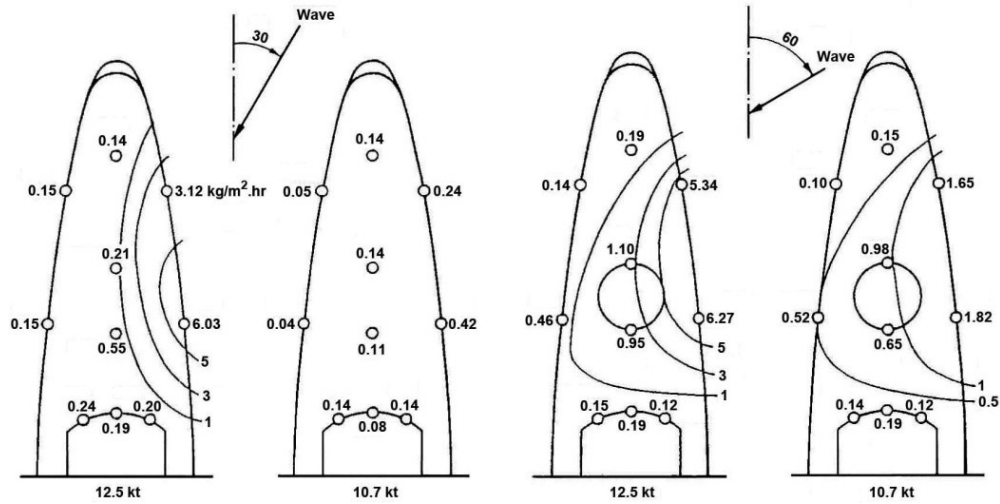


Fig. 1.10: Distribution of icing on Japanese patrol ships due to course and speed (Tabata, 1969)

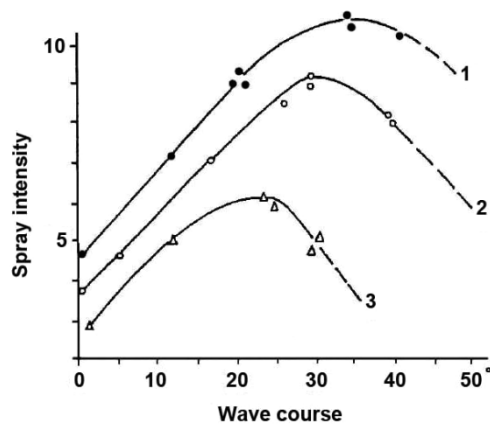


Fig. 1.11: Relationship between spray intensity and wave course towards the vessel and the vessel speed at (1) 8.5 knots, (2) 7.0 knots, and (3) 5.5 knots (Panov and Moltjanov, 1972)

Panov and Moltjanov (1972) discovered a relationship between the intensity of the spray and the course and altitude of waves (Fig. 1.12). According to Fig. 1.12, the major spray intensity is at an angle of 20° between the wave and the vessel's course for a wave elevation between 3 and 3.5 m. However, the highest amount occurs at an angle of approximately 40° at a 1-1.5 m wave elevation. Due to the collection data for wind velocity and air temperature on ice accumulation, Lundqvist and Udin (1977) classified these results as the degree of icing. Figure 1.13 shows the classification of icing on marine vessels for the Baltic Sea. Note that for Fig. 1.13, to obtain the graphs, the course and speed of the vessels are not considered; however, these amounts are important for the classification of icing rate.

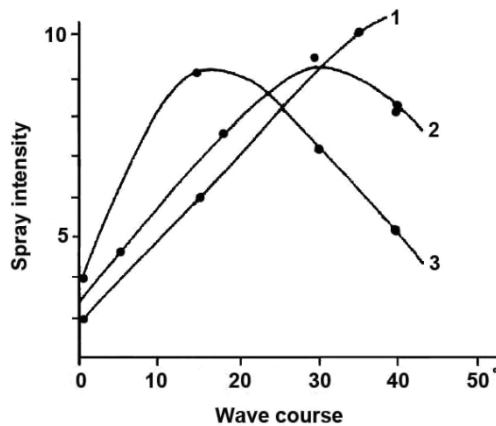


Fig. 1.12: Relationship between the spray intensity and wave course relative to the vessel and wave elevations at (1) 1.0-1.5 m, (2) 2.0-2.5 m, and (3) 3.0-3.5 m (Panov and Moltjanov, 1972)

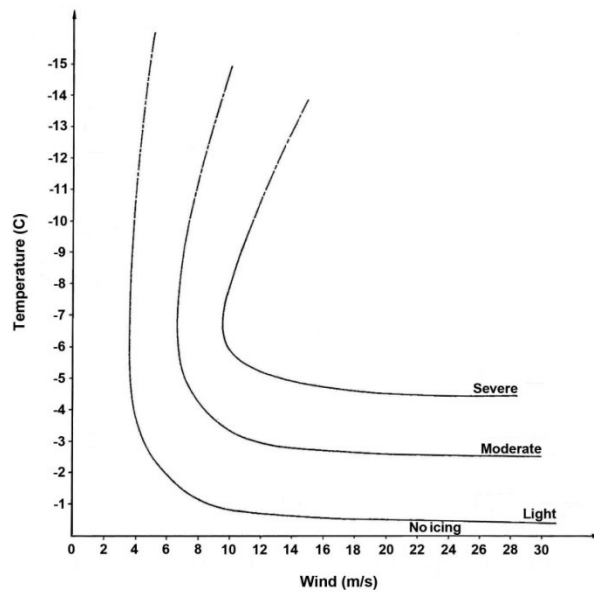


Fig. 1.13: Relationship between the icing, air temperature and wind velocity
(Lundqvist and Udin, 1977)

Figure 1.14 illustrates and compares two different results and graphs from Sawada (1966) and Lundqvist and Udin (1977) relevant to wind velocity and air temperature for ice accretion. According to Fig. 1.14, the main difference between the results obtained by Sawada (1966) and Lundqvist and Udin (1977) is the variation in ocean conditions, particularly salinity, because the salinity of the Baltic Sea is less than all other seas and ocean. Furthermore, the temperature of the sea surface has an impact on the icing phenomenon. Figure 1.15 shows the classification of icing based on the sea surface temperature of the Baltic Sea. As a result, severe and moderate icing happens when the sea surface temperature is less than 2°C and 4°C, respectively. Also, there is no icing when the sea surface temperature is higher than 6°C.

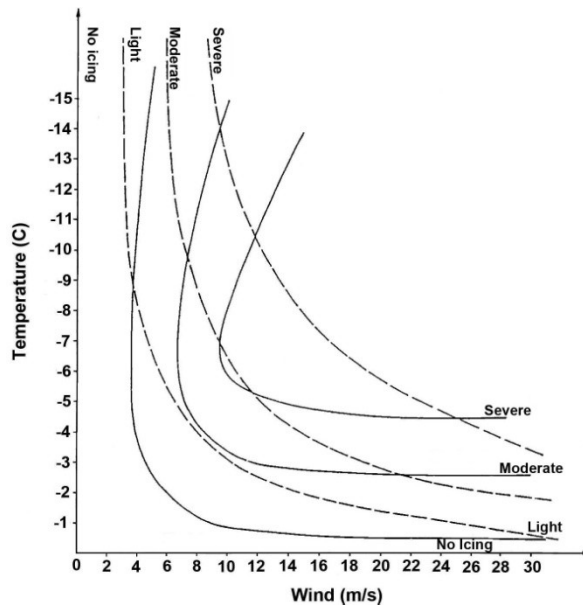


Fig. 1.14: Relationship between the icing on vessels, air temperature and wind velocity (Lundqvist and Udin, 1977). The data from the Baltic Sea are solid curves and ocean conditions are dashed curves (from Sawada (1966))

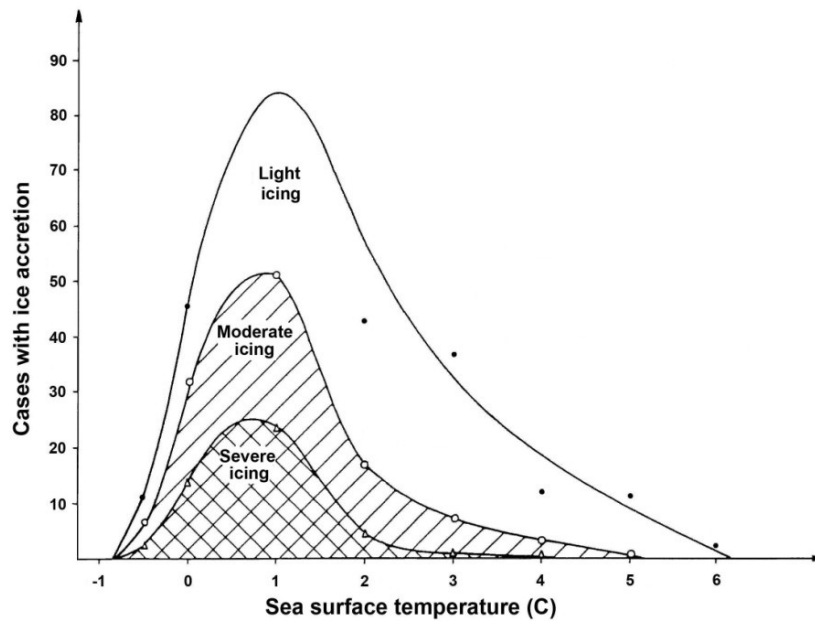


Fig. 1.15: Relationship between sea surface temperature and cases with ice accumulation (Lundqvist and Udin, 1977)

It should be noted that before 1980, a number of researchers in the U.S., the U.S.S.R., Britain, Canada, Iceland, Germany and Japan had investigated several issues relevant to the icing phenomenon and the amount of ice accumulation over marine platforms, especially for small and medium sized vessels, by using different approaches (Lundqvist and Udin, 1977; Minsk, 1977). These issues included: the growth rate and the characteristics of icing, de-icing using different methods, and the estimation of the amount of the accumulated ice during various weather and sea or ocean conditions. Unfortunately, often these studies are not available or are not in English.

1.3.2 Icing Models between 1980 and 2000

Minsk (1984a, 1984b) appraised the ice accumulation processes based on observations and measurements from semi-submersible offshore structures (SEDCO 708), including both marine icing and atmospheric icing. Also, the author described in detail an ice detector for gauging the icing (Minsk, 1984a). Minsk (1984a) measured the atmospheric icing on the derrick using three detectors with elevations of 80, 120, and 180 ft above the deck, and four detectors on the railing and roof of the diving bell storage area, which were almost 20 ft on top of the deck. Moreover, he used special detectors to measure the value of marine icing between the waterline and deck (Minsk, 1984a). The results showed that sea spray icing was the main reason for ice accretion on the semi-submersible structure. Also, the maximum thickness of the ice layer was almost 5 in (or 12.7 cm) on the diagonal cylindrical trusses beneath the rig in the central part of the offshore platform (6 January 1983).

Lozowski and Gates (1985) used analytical and physical approaches to study and compare several icing models for a horizontal and unheated circular cylinder. Each model has used different assumptions for the prediction of ice accretion, particularly in terms of time dependency. For comparison purposes, they tested the models through an icing wind tunnel with the following conditions: (1) spray is freshwater, (2) the diameter of the horizontal cylinder is 2.54 cm, (3) the average volume droplet diameter is 130×10^{-6} m, (4) the LWC are 0.5, 1.0, and 1.5 g/m³, (5) air velocity is 10 m/s, (6) the duration of tests are 30 min and 120 min, and (7) air temperature is -10°C. Figures 1.16 and 1.17 show a comparison for the models and experimental results based on the mass of ice accumulation for 30 min and 120 min tests, respectively. In these figures, the icing process is dry growth, and the freezing fraction is equal to 1. Consequently, assessments of the models show good agreement with the empirical measurements. However, this agreement is lower for the 120 min tests than for the 30 min tests. This may have occurred due to fewer tests compared to the other test series. Also, the distinctions between the shape of models and the actual form are illustrated in Figs. 1.18 and 1.19. As a result, the shape predicted by Lozowski has good agreement with the actual form of the 30 min tests. For the 120 min tests, the shape of models and the actual form varies significantly; however, the stagnation line thickness from Lozowski's model agrees well with experimental results. This occurs primarily because Lozowski's model considers a fixed density while in the actual form, density decreases toward the edge.

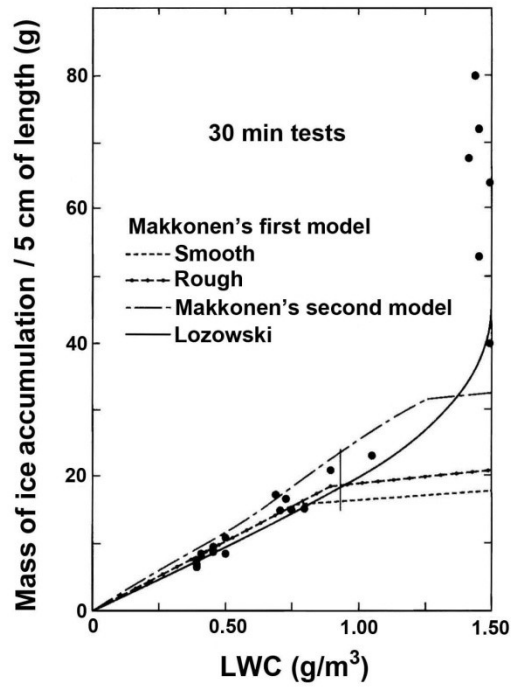


Fig. 1.16: Comparing the models and empirical measurements for the 30 min tests (Lozowski and Gates, 1985)

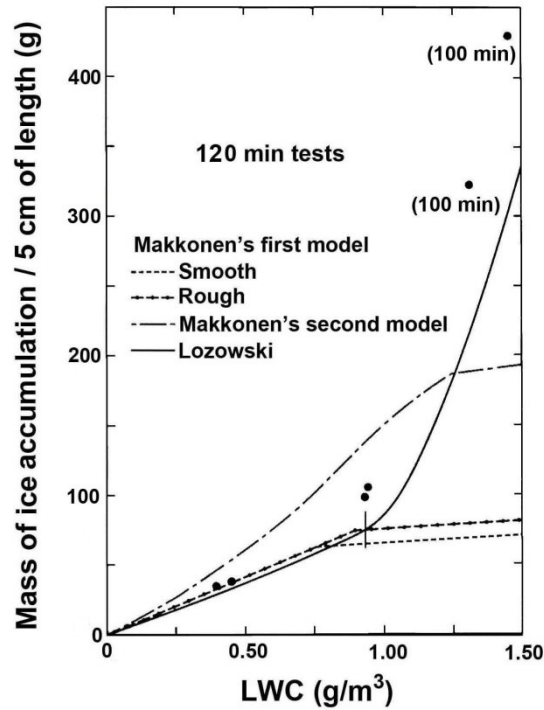


Fig. 1.17: Comparing the models and empirical measurements for the 120 min tests (Lozowski and Gates, 1985)

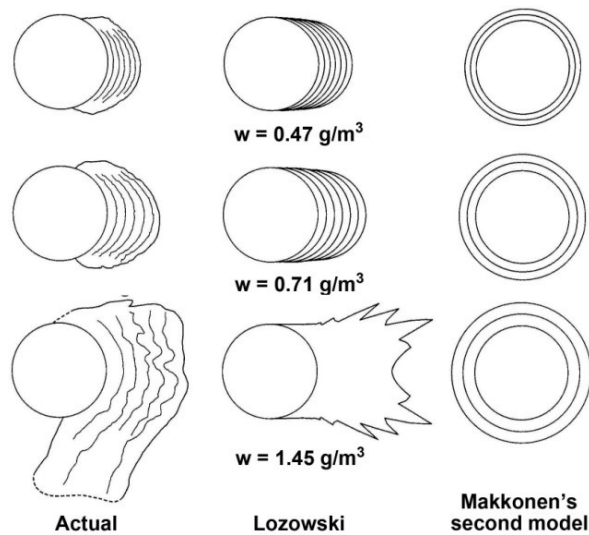


Fig. 1.18: Comparing the actual accumulation form after 30 min and those predicted via other models (Lozowski and Gates, 1985)

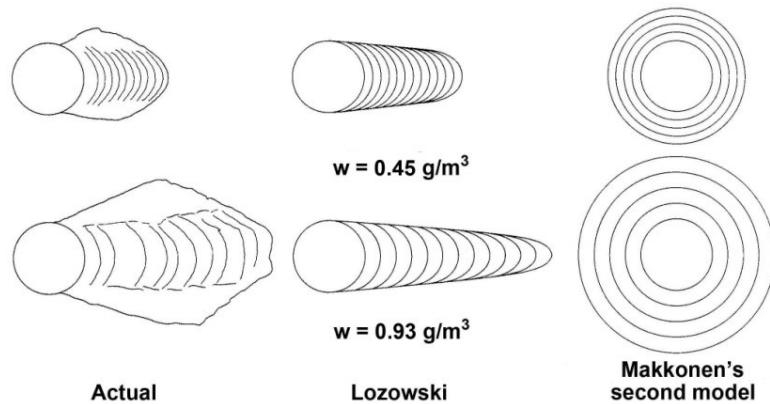


Fig. 1.19: Comparing the actual accumulation form after 120 min and those predicted via other models (Lozowski and Gates, 1985)

In the 1980s, to simulate and estimate the icing phenomenon on offshore structures, two numerical sea spray icing models were developed: (a) “ICEMOD” at the Norwegian Hydrotechnical Laboratory in 1986 and later modified in 1988 (Horjen and Vefsnmo 1986a, 1986b; 1987; Horjen et al., 1988) and (b) “RIGICE” ordered by the Atmospheric

Environment Service of Canada in 1987 (Roebber and Mitten 1987). ICEMOD is a time-dependent marine icing model based on the governing equations for the conservation of mass, heat and concentration of salt for the water film covering the ice surface. The predicted results of the model provide good agreement with field observations and laboratory data (Horjen, 1990). However, this model is limited to solving one-dimensional problems such as, for example, icing along the stagnation line of a vertical cylinder. RIGICE is a stationary model as the time-averaged spray mass flux is used as an input to the model. In addition, the model contained several simplifying assumptions, such as no consideration of droplet cooling during flight and no movement of the brine film. Brown and Horjen (1989) reported a comparison between the two models.

Zakrzewski et al. (1988) studied and evaluated the expanse of the splashing area caused by impinging waves to the ship on a Medium-sized Fishing Vessel (MFV). To simulate the sea spray, a model with a simple geometry has been used to obtain the greatest height of the splashing seawater on top of the deck. To validate the results and the efficiency of the model, the results were compared to the results obtained by Sharapov (1971). For this purpose, they calculated the greatest height of accumulation on the foremast of the MFV with several assumptions: (1) the foremast of the vessel is exactly vertical when the water droplets reach the vessel, (2) wind velocity is constant on the vessel deck and is equal to U_{10} , and (3) the diameter of droplets are identical ($D = 1.25$ mm).

The obtained results for the estimated height, and the measured results by Sharapov (1971) for different wind forces on several parts of the vessel, are shown and compared in Table 1.6. There is good agreement between the computed and observed results. The

authors studied the role of several parameters such as wind velocity, vessel speed, and vessel heading on the greatest vertical height of splashing seawater (Zakrzewski et al., 1988). For this study, the foremast of the vessel has been selected as an obstacle. Figures 1.20 to 1.22 illustrate the effects of different wind velocities, vessel speeds, and headings, respectively. As can be observed in Figs. 1.20 and 1.21, by increasing wind velocity and vessel speed, the greatest height of splashing seawater will increase. Also, the lowest values of the greatest heights of spraying are for a vessel heading of 0° , namely, when the vessel moves directly into the waves. Moreover, the greatest height of spraying are for vessels heading, approximately between 110° and 120° , defined here to be the angle between the vessel and wind velocity vector (Fig. 1.22) (Zakrzewski et al., 1988).

Table 1.6: Comparison between the original data from Sharapov (1971) and the computed height of splashing seawater on the vessel for the vessel heading of 0° . The amounts in parentheses are for the vessel heading of 45° (Zakrzewski et al., 1988)

Wind force in Beaufort and (m/s)	Wind velocity (m/s)	Foremast ¹		Rigging ²	
		Observed	Predicted	Observed	Predicted
5 Beaufort 8.0 – 10.7	8	Up to 5.5 m above deck	4.42	Up to 5.5 m above deck	5.74
	9		5.07		6.26
	10		5.61		6.70
6 Beaufort 10.8 – 13.8	11	Up to 7.9 m above deck	5.85 (6.61)	Up to 7.9 m above deck	6.87 (7.61)
	12		6.21 (7.00)		7.16 (7.80)
	13		6.53 (7.24)		7.42 (7.98)
7 Beaufort 13.9 – 17.1	14	Up to 10.5 m above deck	6.78 (7.47)	Up to 10.5 m above deck	7.60 (8.12)
	15		7.07 (7.74)		7.83 (8.32)
	16		7.35 (7.91)		8.06 (8.48)
	17		7.54 (8.19)		8.21 (8.65)
8 Beaufort 17.2 – 20.7	18	10.5 m above deck	7.86 (8.36)	10.5 m above deck	8.48 (8.85)
	19		7.90 (8.53)		8.59 (9.04)
	20		8.15 (8.75)		8.68 (9.23)
≥ 10 Beaufort	25	10.5 m above deck	8.46 (9.19)	10.5 m above deck	8.90 (9.64)
	28		8.98 (9.58)		9.00 (9.81)
≥ 24.5	30	10.5 m above deck	9.30 (9.81)	10.5 m above deck	9.60 (10.02)
	32		9.65 (10.11)		9.92 (10.12)

1. Height equal to 10.5 m (location 11.0 m from the vessel bow),

2. Height equal to 10.5 m (location assumed to be $x = 11.0$ m and $y = -2.50$ m)

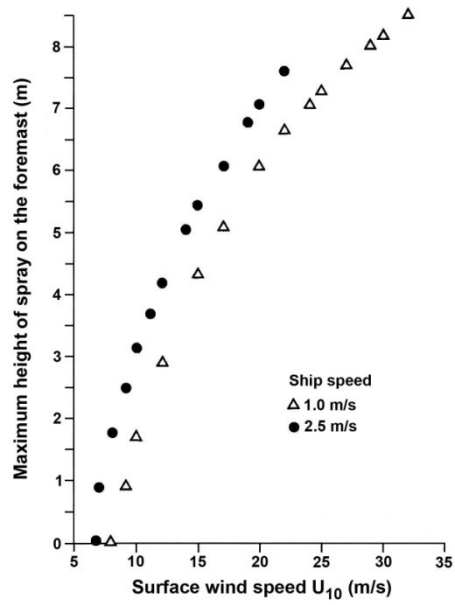


Fig. 1.20: The relation between wind velocity and the greatest height of splashing seawater on the foremast of an MFV for a vessel heading of 0° and different vessel speeds (Zakrzewski et al., 1988)

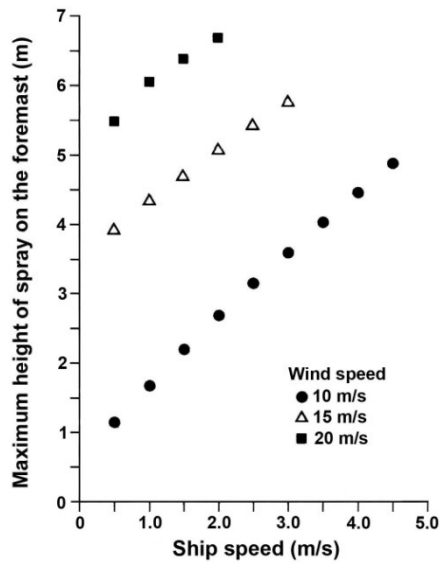


Fig. 1.21: Relationship between vessel speed and the greatest height of splashing seawater on the foremast of a MFV for different wind velocities (Zakrzewski et al., 1988)

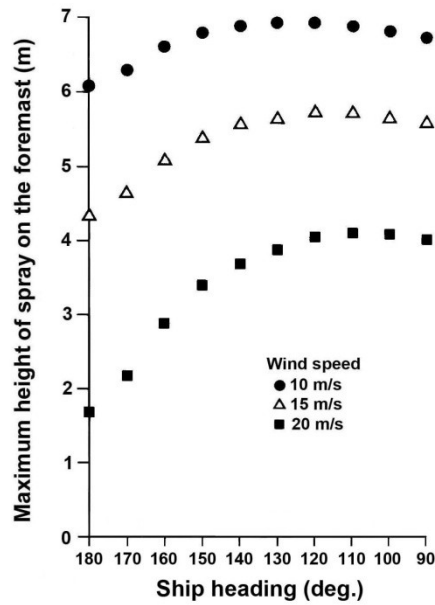


Fig. 1.22: Relation between vessel heading and the greatest height of splashing seawater on the foremast of an MFV for a vessel heading of 0° and different wind velocities (Zakrzewski et al., 1988)

Fukusako et al. (1989) experimentally studied the specifications of sea spray icing on a horizontal, circular cylinder exposed to cold airflow and sea spray. They measured several parameters such as wind velocity, air temperature, the diameter of water droplets, the initial temperature of water droplets, and mass flow rate of water droplets for different conditions. To obtain experimental measurements, Fukusako et al. (1989) used a sea spray icing wind tunnel with refrigeration. It should be noted that in this empirical investigation, the average diameters of water droplets were 200 μm, 900 μm, and 1600 μm and the salinity was 33‰. Figure 1.23 illustrates the effect of air temperature on sea spray icing over a horizontal cylinder for the following conditions: a wind speed of 6.0 m/s, an initial water droplet temperature of -1.4°C, a water droplet diameter of 200 μm,

and a mass flow rate of impinging water droplets of $80 \text{ kg/m}^2\text{h}$. According to this figure, the ice accretion on the upper sector of the horizontal cylinder increases with lower air temperatures as splashing time elapses. In addition, for higher air temperatures, the ice accretion was smaller, and icicles were created in the bottom sector of the cylinder.

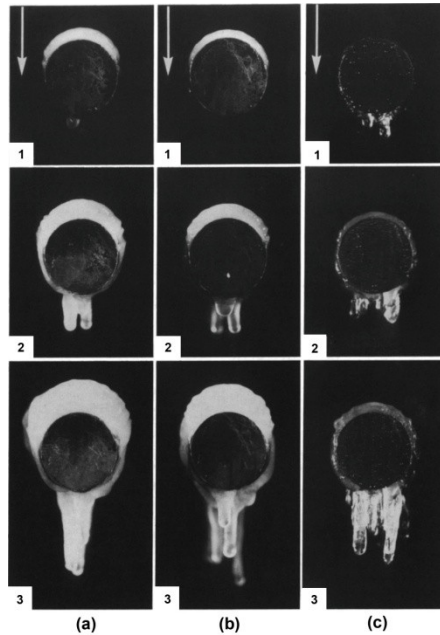


Fig. 1.23: Effect of air temperature on the formation of ice accumulation: (a) $T_a = -15^\circ\text{C}$; (b) $T_a = -10^\circ\text{C}$; (c) $T_a = -5^\circ\text{C}$ and (1) 5 min passed; (2) 10 min passed; (3) 20 min passed (arrow shows flow direction) (Fukusako et al., 1989)

Figure 1.24 represents the effect of wind speed on the marine icing phenomenon over a horizontal circular cylinder for an initial water droplet temperature of -1.4°C , an air the water droplet diameter of $200 \mu\text{m}$, a mass flow rate of water droplet of $240 \text{ kg/m}^2\text{h}$, and an air temperature of -15°C . As a result, the forms of ice accretion at wind speeds higher than 10 m/s were considerably different relative to the ice formed at a wind speed at 6

m/s. Furthermore, for wind speeds more than 10 m/s, some of the water droplets will freeze after hitting the cylinder and forming ice accretion, and the other water droplets will scatter into the airflow. For $U = 6$ m/s, some of the water droplets will freeze to create an ice layer, but some of them cannot freeze. These droplets will form icicles. The other water droplets will distribute in the airflow.

Figure 1.25 demonstrates the effect of water droplet diameters on ice accumulation for a wind speed of 6 m/s, a mass flow rate of water droplets of $240 \text{ kg/m}^2\text{h}$, an initial water droplet temperature of -1.4°C , and an air temperature of -15°C . As can be observed in this figure, after 20 min of sea spray, for $D = 200 \text{ }\mu\text{m}$ the ice formation on the cylinder surface seems to be glassy. For $D = 900 \text{ }\mu\text{m}$, the surface of the ice formation is significantly lumpy. However, for $D = 1,600 \text{ }\mu\text{m}$, the formation of ice accretion is totally different, so that it tends to vanish adjacent to the stagnation point on the cylinder surface. This occurs because by increasing the size of water droplets, the droplet temperature arriving at the surface of the cylinder increases. Fukusako et al. (1989) calculated that the temperature of water droplets for $D = 200 \text{ }\mu\text{m}$, $900 \text{ }\mu\text{m}$, and $1600 \text{ }\mu\text{m}$ are -7.8°C , -2.1°C , and -1.7°C , respectively. Moreover, by increasing the size of droplets, the kinetic energy of the water droplets will increase (Fukusako et al., 1989).

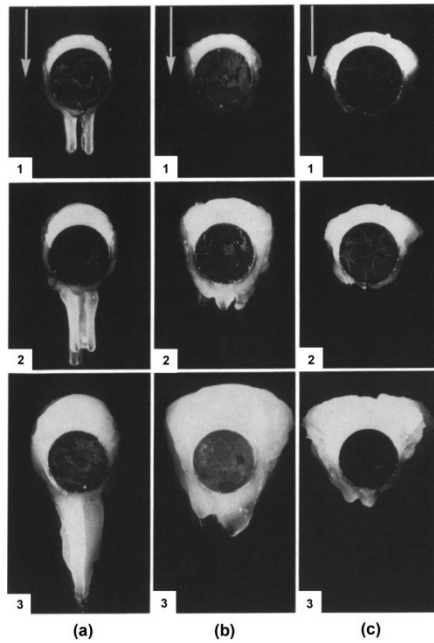


Fig. 1.24: Effect of wind velocity on the formation of ice accumulation: (a) $U = 6$ m/s; (b) $U = 10$ m/s; (c) $U = 20$ m/s and (1) 5 min passed; (2) 10 min passed; (3) 20 min passed (arrow shows flow direction) (Fukusako et al., 1989)

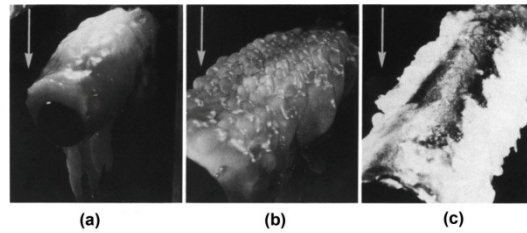


Fig. 1.25: Effect of water droplets diameter on the formation of ice accumulation: (a) $D = 200$ μm ; (b) $D = 900$ μm ; (c) $D = 1600$ μm (arrow shows flow direction) (Fukusako et al., 1989)

The effect of initial water droplet temperature on the formation of ice accretion for $U = 6$ m/s, $T_a = -15^\circ\text{C}$, $D = 200$ μm , and the mass flow rate of a water droplet of 240 $\text{kg}/\text{m}^2\text{h}$ is indicated in Fig. 1.26. As a result, the surface of ice accumulation is completely even

once the temperature of the water droplet is low, and it is uneven when the temperature of the droplet increases. Figure 1.27 indicates the effect of the mass flow rate of water droplets on sea spray icing over a horizontal cylinder for $U = 6$ m/s, $T_a = -15^\circ\text{C}$, $T_d = -1.4^\circ\text{C}$ and $D = 200$ μm . As can be seen in this figure, different morphologies of ice accretion formation on the cylinder are almost identical. However, for larger mass flow rates of water droplets, the icicles will tend to increase at the bottom of the cylinder (Fukusako et al., 1989). Additionally, despite a doubling in the amount of mass flow rate of water droplets, the thickness of ice accretion increases no more than approximately 40% on the horizontal cylinder.

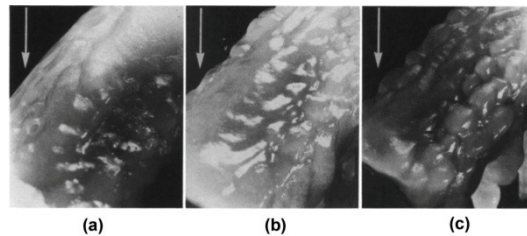


Fig. 1.26: Effect of water droplet temperature on the formation of ice accumulation:

(a) $T_d = -1.4^\circ\text{C}$; (b) $T_d = 0.2^\circ\text{C}$; (c) $T_d = 4^\circ\text{C}$ (arrow shows flow direction)

(Fukusako et al., 1989)

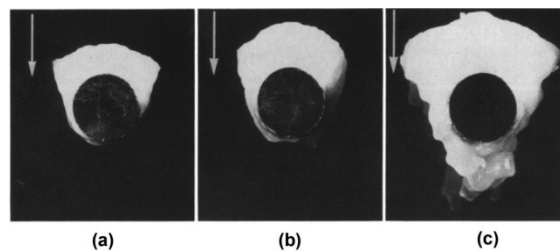


Fig. 1.27: Effect of the mass flow rate of water droplets on the formation of ice accumulation: (a) mass flow rate of 80 $\text{kg}/\text{m}^2\text{h}$; (b) mass flow rate of 160 $\text{kg}/\text{m}^2\text{h}$; (c) mass flow rate of 320 $\text{kg}/\text{m}^2\text{h}$ (arrow shows flow direction) (Fukusako et al., 1989)

Ryerson (1995) measured the seawater spray and ice accumulation on a large US Coast Guard cutter in the North Pacific Ocean and the Bering Sea during February and March, 1990. The results obtained by Ryerson (1995) can be summarized as follows.

- (1) The average duration of a seawater spray event was 2.73 s, so that a maximum and a minimum length time were 5.57 s and 0.47 s, respectively.
- (2) Droplet number concentration was in the range of almost 2.0×10^5 to 3.0×10^5 drops.m⁻³ for 39 sampled spray events; however, most of the seawater spray events were in the lower end of the concentration range. Note that droplet number concentration is the number of droplets per unit volume of spray cloud.
- (3) The size of water droplets was between 14 μm and 7700 μm, and the average size was 295 μm.
- (4) The average median volume droplet diameter (MVDD) was 1094 μm, so that it ranged from 169 to 6097 μm for single spray events.
- (5) The LWC for the sea spray cloud was between 1.1 and 1,162.9 g/m³, so that the average amount was 64.1 g/m³.
- (6) The minimum and maximum amounts of seawater spray flux on vessel decks per spray event for the 37 single-splash events were 5.22×10^{-4} and 18.62 kg/m² event.
- (7) In the February event, thicknesses of the ice layer were in the range of 3.0 cm on the forecastle deck to 0.4 cm on the 01 level deck surface. Also, for vertical surfaces, the ice layer thicknesses were in the range of 2.9 cm on the front and sides of the 5-in gun to 1.7 cm on the forward bulkhead, and the ultrasonic range finders showed ice thicknesses from 0.2 to 0.4 cm on the 02 level bulkhead. In the March event, ice layer thicknesses were 3.4 cm and 0.4 cm on the forecastle deck and the 01 level deck,

respectively. The thicknesses of the ice layer for vertical surfaces were 2.3 cm on the sides of the 5-in gun, 0.4 cm on the forward bulkhead, and lower than 0.2 cm on the 02 level bulkheads as gauged by the range finders.

(8) Throughout the icing event in the month of February, the average amounts of ice accretion thicknesses on vertical and horizontal surfaces were 2.2 cm and 2.6 cm, respectively. Also, for the duration of the March icing event, the mean value of ice layer thicknesses on the horizontal and vertical surfaces were 2.0 cm and 1.5 cm, respectively.

It should be noted that the figures that show forward bulkhead, 01 level deck and 02 level bulkhead, are not clear in the paper of Ryerson (1995).

Blackmore and Lozowski (1994) introduced two heuristic models for the sea spray icing phenomenon on marine vessels, which are supercooled and nucleated models. They developed a heat balance for seawater spray-airflow to compute the spray ice accumulation rate for one of these models: (1) the supercooling of sea spray and (2) the nucleation of sea spray. For modeling and analyzing the models, the authors reported all details in their investigation (Blackmore and Lozowski, 1994). To validate the models, a group of 60 icing events was selected for the Zakrzewski and Lozowski (1989b) data collection. The sensitivity of Blackmore and Lozowski's heuristic model with supercooling spray (BL(S)) was studied for a Soviet MFV specified under a standard condition, including (Blackmore and Lozowski, 1994): an air temperature of -10°C , a water surface temperature of 1°C , a wind velocity of 20 m/s, a vessel speed of 1 m/s, a heading angle of 180° , a seawater salinity of 35‰, and a significant wave height of 6 m.

The BL(S) model sensitivity to the air temperature, wind velocity, and water surface temperature is illustrated in Fig. 1.28. The figure shows that the wind velocity and the air temperature are effective parameters. Figure 1.29 demonstrates that the BL(S) model's sensitivity to significant wave height and fetch can be noteworthy and analogous to the effect of air temperature and wind velocity. Furthermore, a horizontal line plotted on Fig. 1.29 for a specific model icing rate shows the underlying, fully developed fetch-wave height correlation utilized in the model. The icing rate represents a very small sensitivity to water surface salinity relative to wave height or fetch, as well as a reduction in the icing rate because of rising salinity. Figure 1.30 indicates the sensitivity of the model icing rate to the heading angle, vessel speed, and the size scaling factor. As a result, the heading angle has a significant effect on the icing rate. Moreover, the ship speed for a Soviet MFV is restricted to approximately 2.5 m/s for the conditions determined; this means that the icing rate is restricted according to the ship speed. Also, the icing rate is very sensitive to scaling factors lower than 1, so that the maximum amount of the scaling factors is between 0.3 and 0.4. The result for the ice growth rate is the same as the icing rate. To analyze the sensitivity of ice growth rate to ship size, the size scaling factor was multiplied by the characteristic linear magnitudes of an MFV. In general, the model shows that a water surface temperature based on limitations made to marine icing is not realistic.

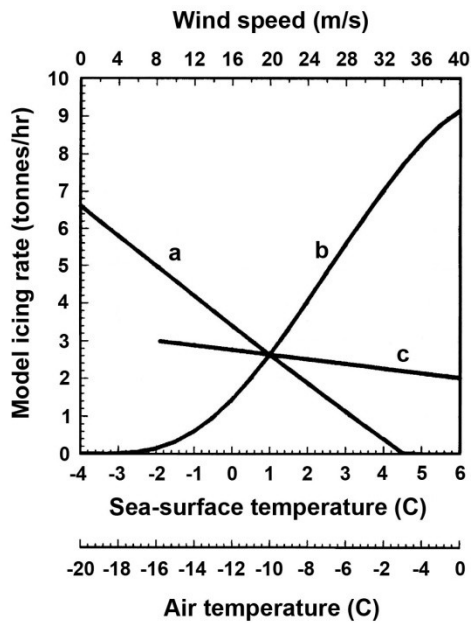


Fig. 1.28: Sensitivity illustration for (a) air temperature, (b) wind velocity, and (c) water surface salinity. The crossing point is the standard condition

(Blackmore and Lozowski, 1994)

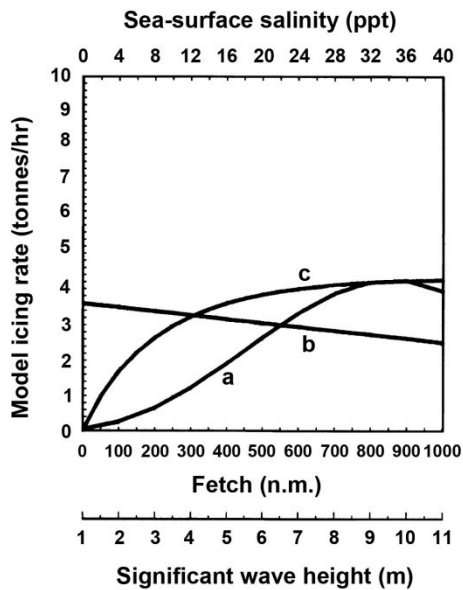


Fig. 1.29: Sensitivity of the model for (a) significant wave height, (b) sea-surface temperature, and (c) fetch in standard condition (Blackmore and Lozowski, 1994)

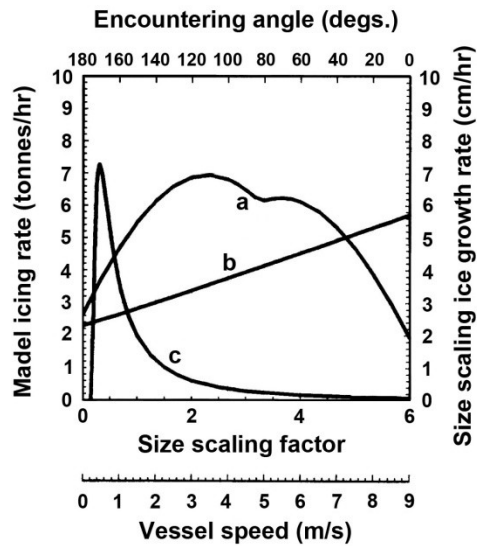


Fig. 1.30: Sensitivity of the model for (a) heading angle, (b) vessel speed, and (c) size scaling factor in standard condition (Blackmore and Lozowski, 1994)

Lozowski et al. (1996) and Blackmore and Lozowski (1998) conducted experimental tests and derived theoretical models related to spongy ice. Lozowski et al. (1996) tested the rate of ice accretion and evaluated the sponginess of ice created by freshwater spray in a wind tunnel. The liquid fraction of the experiments varies from 32% to 47%. Blackmore and Lozowski (1998) proposed a theoretical model for sponginess of freshwater ice accretion. The model is based on the growth rate of the dendrites and their spacing. The most challenging part of these studies was the existence of an analogy between the sponginess of freshwater and salt water.

Lozowski et al. (2000) collected and studied numerical simulations of the marine icing phenomena. In addition, they briefly reviewed the history of marine icing computer models and explained in detail the two new approaches to superstructure icing modeling: 2-D and 3-D morphogenetic icing models. Note that these models were useful tools for

predicting the ice growth. They are called “morphogenetic” since the ice structure shapes are specified mainly by water particle motion (in the air and on the icing surface) and the freezing process. This means that the structure of ice can expand (especially a suspended ice structure) and this has little similarity compared to the surface on which they are formed. As a result, the modeled structure is disordered. Also, two different initial conditions can lead to two ice accumulations, which are generally the same structure, but different in formation and properties.

Figure 1.31 illustrates an instance of the formation evolution of five icicles in the 2-D case. Even curves have been fitted to the real surface that is separate. In this figure, the total simulation time was 120 min. For every 40 min, forms were represented. As a result, sometimes the surfaces collided. The ensuing ribs were a result of the accidental nature of the model. To show the stochastic nature of the model, two simulations with the same model parameters have been located in Fig. 1.31(e), to the right and the same as in Fig. 1.31(d). Also, Fig. 1.31 displays that for all cases, by increasing the heat flux, the icicle mass and cross-section have increased. Moreover, by increasing heat flux, the length of an icicle can increase or decrease (Lozowski et al., 2000). In another 2-D survey, Lozowski et al. (2000) studied a slab-symmetrical model of ice accumulation on a horizontal cylinder in vertical impact freezing spray conditions in gentle airflows.

For the 3-D case, Lozowski et al. (2000) surveyed the formation of icicles and ice accumulation on a hollow hemisphere and a cylinder. Szilder and Lozowski (1995) investigated the 3-D icicle model with all details and obtained relationships for the freezing probability and shedding parameter based on the ambient macroscopic conditions (Lozowski et al., 2000). Figure 1.32 indicates the variations of icicle formation

in the 3-D case based on air temperature. To better visualize, the shadow of the components varies after each of three successive 3 min time intervals. This occurs because the majority of the droplets will freeze near the tip of the icicle, instead of along the walls. Thus, the form of the icicle is slightly more cylindrical than in the 2-D model (compare Fig. 1.31). Figure 1.33 demonstrates the effect of air temperature on the length growth rate for two different amounts of the supply rate: 10 mg/s and 20 mg/s. In this figure, the solid curves are multinomial fits to the model predictions. As a result, by reducing air temperature, the length growth rate will increase.

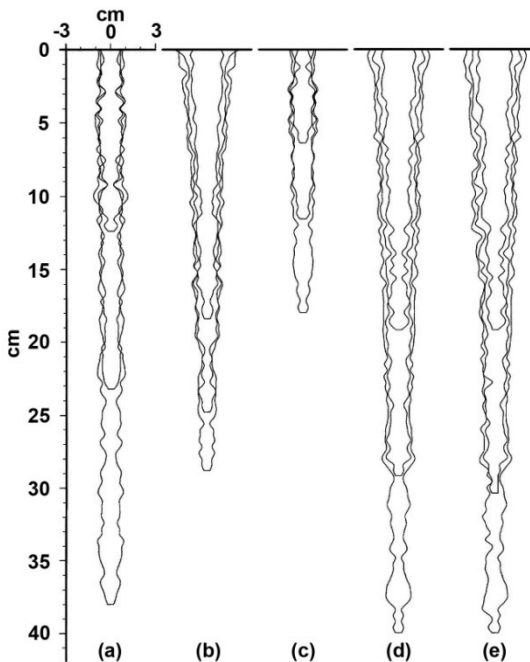


Fig. 1.31: Evolution of the icicle formation with time. The amounts of the liquid supply rate and heat flux from the icicle surface: (a) 15 mg/s and 40 W/m^2 ; (b) 15 mg/s and 400 W/m^2 ; (c) 30 mg/s and 40 W/m^2 ; (d) 30 mg/s and 400 W/m^2 ; (e) identical to (d), but profiles from two various simulations are collocated (Lozowski et al., 2000)

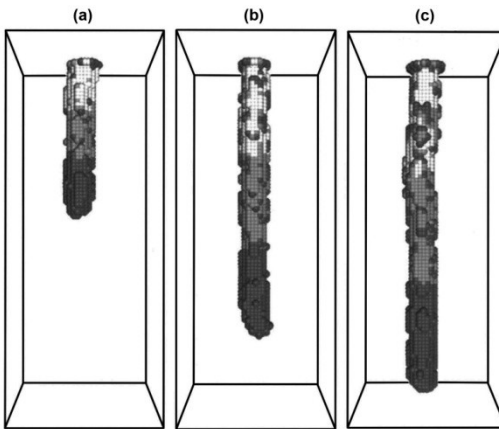


Fig. 1.32: Evolution of the icicle formation in the 3-D case with time for a wind velocity of 3 m/s and a supply rate of 10 mg/s. The total simulation time was 9 min and various shadows were applied to illustrate three successive 3 min intervals. The height and width of the box are 10 cm and 4 cm, respectively. Also, the air temperature is: (a) -5°C , (b) -10°C , and (c) -15°C (Lozowski et al., 2000)

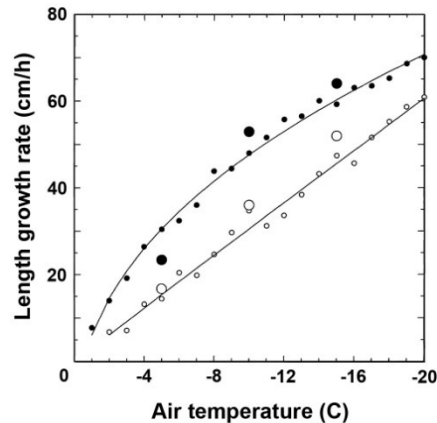


Fig. 1.33: Variation of the length growth rate versus air temperature with forced convection for two different amounts of the supply rate: 10 and 20 mg/s and wind velocity of 3 m/s. The experimental results are displayed with large circles and the model predictions with small circles. The two solid curves are multinomial fits to the model predictions. ● is for 10 mg/s and ○ is for 20 mg/s (Lozowski et al., 2000)

Szilder and Lozowski (1995) explained the 3-D icing model and how it can be used for two different conditions: accumulations on a non-rotating cylinder, and a hemisphere in freezing spray conditions without airflow (Lozowski et al., 2000). These simulations were carried out based on the microscopic model parameters instead of the macroscopic ambient conditions. Figure 1.34(a) illustrates a 3-D form of the ice accumulation simulation on a hemisphere, with a total spray equivalent depth of 4 mm, and a freezing probability of 0.05% and a shedding parameter of 2,000. As a result, almost 89% of the water droplet's collision will freeze on the platform as icicles (three icicles can be observed in Fig. 1.34(a)). Moreover, if the simulation continues with an extra 4 mm of splashing, three new icicles will form and the previous icicles will grow only slightly (Lozowski et al., 2000).

Finally, with extra splashing time, the icicles will grow in length, but their number will be constant. Figure 1.34(b) shows a 3-D view of ice accumulation on a horizontal cylinder with identical conditions for the hemisphere. The distribution of icicle length is almost uniform, and approximately 88% of the colliding water droplets are converted to ice accumulation (Lozowski et al., 2000).

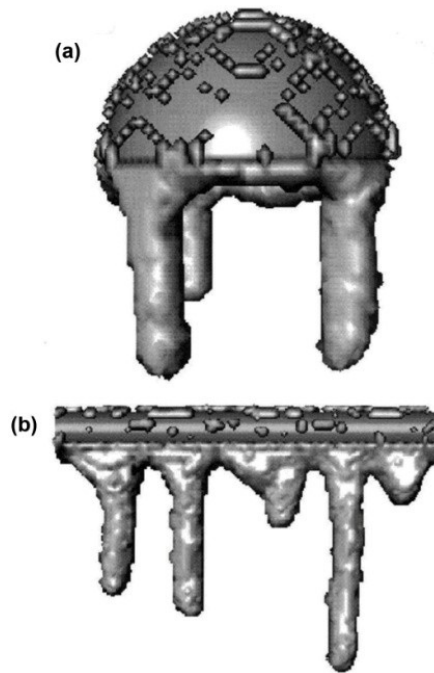


Fig. 1.34: 3-D view of ice accumulation on a hollow hemisphere and a cylinder because of freezing spray, (a) Total spray tantamount depth is 4 mm; freezing probability 0.05%; shedding parameter 2000; internal and external hemisphere radius 15 mm and 20 mm, respectively, (b) Total spray tantamount depth is 12 mm; freezing probability 0.05%; shedding parameter 2000; cylinder diameter 10 mm; cylinder length 100 mm
(Lozowski et al., 2000)

1.3.3 Icing Models After 2000

Chung and Lozowski (2010) numerically and experimentally investigated and developed a new model of marine icicle growth. According to Fig. 1.35, empirical results illustrated that the manner of growth of marine icicles is distinct from pure water icicles under identical conditions, as the marine icicles are shorter and broader. Figure 1.35 represents three of the obtained icicles. As shown in this figure, two features separate

marine icicles from pure water icicles: the salt water icicles have a milky appearance and pronounced ribs (Chung and Lozowski, 2010). Also, by comparing the numerical model and the form obtained by the experimental method, it can be observed that they have the same behaviour but the resulting shapes are slightly different. Moreover, when the growth rate of icing is low, the maximum errors occur at higher temperatures for the numerical method.

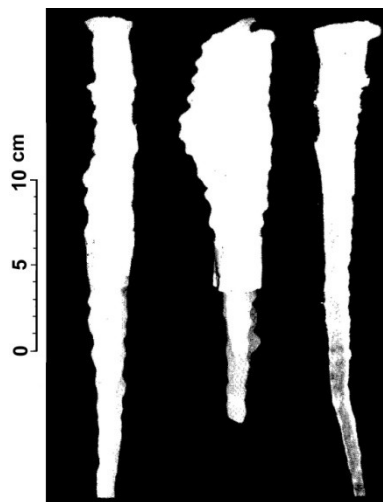


Fig. 1.35: A view of marine and pure water icicles (Chung and Lozowski, 2010)

Shipilova et al. (2012) investigated the physical details of the sea spray icing process and simulated this phenomenon on two different supply vessels types (Skandi Mongstad and Geosund). To compute and forecast the ice accumulation on the vessels, they studied the influence of the temperature of water droplets, wind velocity and air temperature on the icing growth rate. In addition, Shipilova et al. (2012) compared the simulation results with the empirical measurements for the validation of the proposed model. Both supply ships have a length of almost 100 m with the bridge in the front of the main deck. Also,

the Geosund has a more complex superstructure with a helicopter deck above the bridge. By considering several assumptions, the authors obtained the simulation results using the RNG $k-\varepsilon$ method with FLUENT-ANSYS software.

The icing rate on the Geosund for the whole vessel is represented in Fig. 1.36 for two varying cases: (1) the temperature of water droplets is equal to air temperature, and (2) the temperature of the water droplets is identical to the seawater temperature, $+5^{\circ}\text{C}$. As a result, by increasing the wind velocity and decreasing the temperature of water droplets, the icing rate will increase. Figure 1.37 displays the icing rate on both the whole and individual parts of the Geosund ship for two cases: $T_d = T_a$ and $T_d = T_w$. Note that the real temperature of the water droplets must be between T_a and T_w . According to this figure, by increasing the wind velocity and reducing the size of water droplets and air temperature, the ice accumulation rate will increase. Water droplets will freeze faster with a smaller size, a lower temperature, and a higher wind velocity. Also, the predicted results by Shipilova et al. (2012) showed that the larger amount of water droplets hitting the surface does not produce a higher ice accumulation rate.

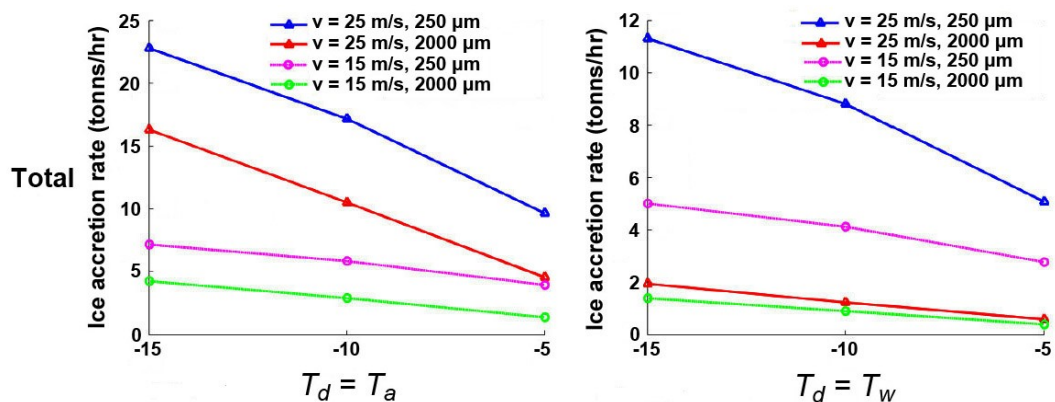


Fig. 1.36: Estimated ice accumulation rate for the Geosund ship (Shipilova et al., 2012)

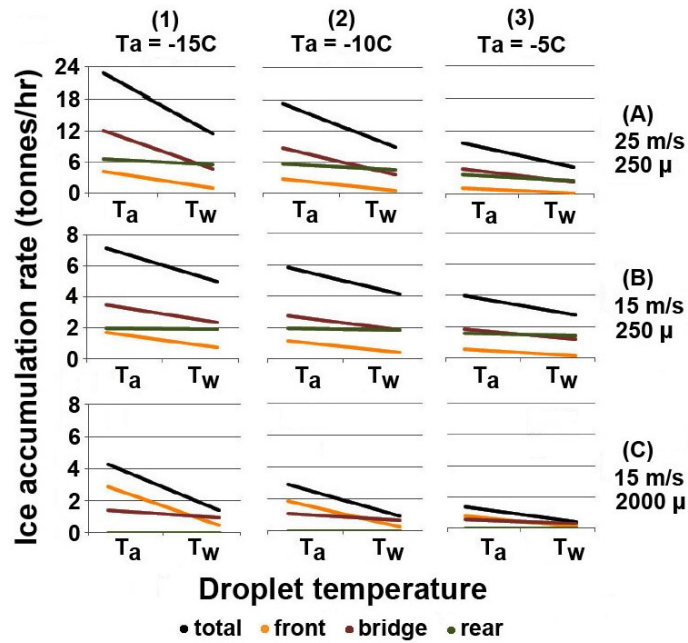


Fig. 1.37: Ice accumulation rate in the different conditions for the Geosund ship
(Shipilova et al., 2012)

ICEMOD2 is an extension of the original one-dimensional model ICEMOD to 2-D motion of the water film when inertia terms are neglected (Horjen, 2013). ICEMOD2 was used for cylinders with different diameters situated on a marine vessel or structure. The author compared the numerical results with actual empirical results for vertical cylinders located on the observation ship, “Endre Dyrøy”. In order to analyze and compute the sea spray icing phenomenon and ice accumulation, Horjen (2013) considered a non-horizontal cylinder for a defined 2-D coordinate system (Fig. 1.38). In Fig. 1.38, ice accumulation on the upwind side of the cylinder between the points S_1 and S_2 is considered. To determine the numerical results, a finite difference method (FDM) was

used assuming that the temperature and salt mixing over the water film layer was uniform.

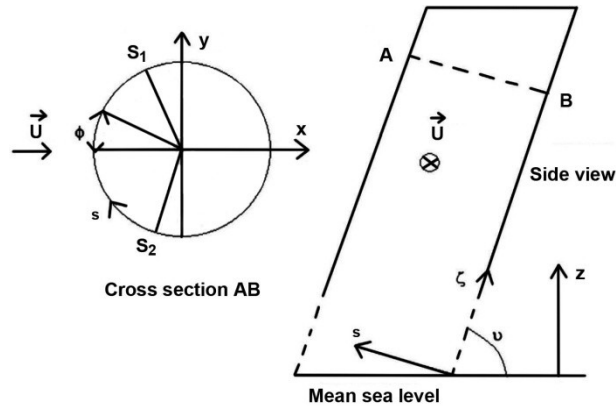


Fig. 1.38: View of the geometry of a non-horizontal cylinder with a defined 2-D coordinate system (Horjen, 2013).

To validate the results, Horjen (2013) used two different observations, which were acquired on March 13, 1985, at 08.00-11.00 hr (no. 1) and 11.00-14.00 hr (no. 2). He obtained the horizontal distribution of the ice layer thickness in 5 cylinder elements for observation no. 1. The results were for the lower, middle and upper parts of each cylinder. For example, Figs. 1.39 and 1.40 show the distribution of model ice thickness for two different cylinder elements, respectively. As a result, the distribution of ice thickness along the cylinder's surroundings is even and symmetrical around the stagnation line for all 5 elements. The apex of the angles on the horizontal surface is on the cylinder axis (Horjen, 2013). Figure 1.41 displays the horizontal distribution of the ice layer thickness for three various cylinder elements and observation no. 2, which is only for the middle level. As a result, the distribution of ice thickness along the cylinder is even and symmetrical around the stagnation line. The shape of the predicted ice profile is not only

a function of the spray mass flux, but also a result of the cylinder diameter (Horjen, 2013). It should be noted that Figs. 1.39-1.41 are somewhat different from the corresponding diagrams in Horjen (2013) as a result of a change in the data program (personal communication with Horjen).

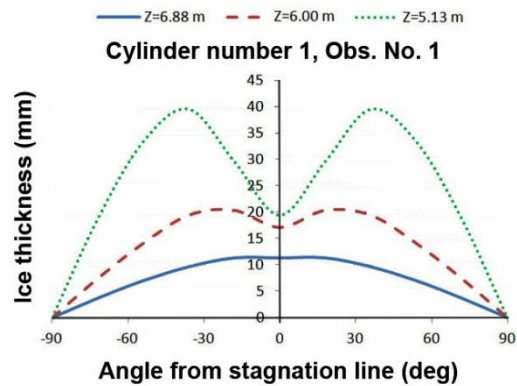


Fig. 1.39: Distribution of the model ice thickness after a 3 hr splashing period of cylinder no. 1 for observation no. 1 at the lower, middle and upper levels (Horjen, 2013, corrected results)

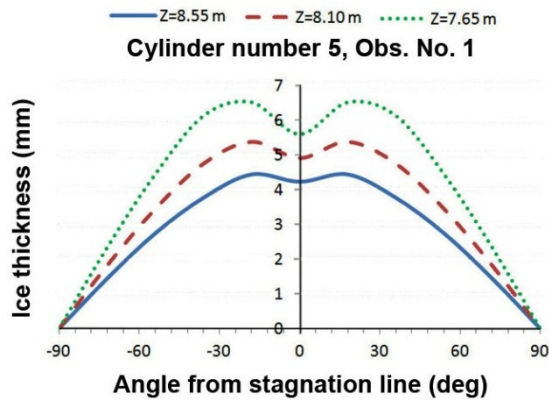


Fig. 1.40: Distribution of the model ice thickness after a 3 hr splashing period of cylinder no. 5 for observation no. 1 at the lower, middle and upper levels (Horjen, 2013, corrected results)

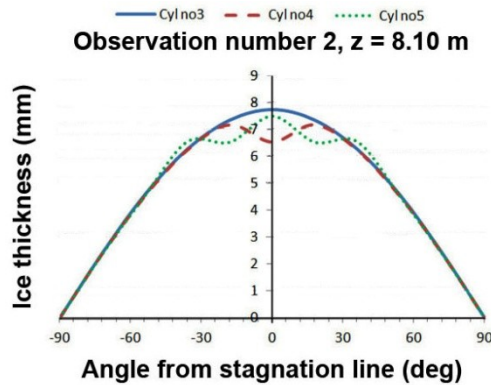


Fig. 1.41: Distribution of the model ice thickness after a 3 hr splashing period of cylinder nos. 3, 4 and 5 for observation no. 2 at the middle level (Horjen, 2013, corrected results)

Kulyakhtin and Tsarau (2014) developed a 3-D time-dependent model of sea spray icing on a drilling rig by employing the MARICE solver. In the MARICE solver, experimental formulae are used to determine the amount of splashing seawater. The benefit of the MARICE solver is the usage of computational fluid dynamics (CFD) to compute the heat transfer, turbulent airstream motion, and trajectories of the water droplets around the entire geometry of the structure (Kulyakhtin and Tsarau, 2014; Kulyakhtin et al., 2012; Nakakita et al., 2010). Also, the model of the brine film dynamics and freezing is suitable for any arbitrary surface (Kulyakhtin and Tsarau, 2014). MARICE estimates ice accumulation based on the input parameters, such as the structure geometry and meteorological and oceanographic data (metocean) (Kulyakhtin and Tsarau, 2014).

To obtain the ice accumulation rate from the MARICE solver, they selected a semi-submersible drilling rig in the Norwegian offshore sector. In this study, three harsh environmental conditions were chosen from the metocean design basis by Gaches et al.

(2013) for the Johan Castberg field. These conditions are (Kulyakhtin and Tsarau, 2014): (a) $T_a = -9^\circ\text{C}$ and $U_{10} = 33$ m/s, (b) $T_a = -17^\circ\text{C}$ and $U_{10} = 33$ m/s, and (c) $T_a = -17^\circ\text{C}$ and $U_{10} = 20$ m/s; with 0° , 30° , 45° and 90° orientations of the structure versus the wind. The angle between the line that connects the centre of the structure with the rescue boats and the upwind direction is called the orientation angle. The intensity of turbulence in the air was assumed as 10%, and the relative humidity as 80% (Kulyakhtin and Tsarau, 2014). The wave height and wave period were determined through the fifth-degree polynomials of U_{10} , which is presented by Zakrzewski (1986a).

Figure 1.42 illustrates the distribution of ice accumulation on the drilling rig for $T_a = -17^\circ\text{C}$, $\psi = 90^\circ$ and $U_{10} = 33$ m/s. According to this figure, the ice accumulation increased exclusively on the Pontoons. Furthermore, the ice layer increased rapidly near the corners where the heat transfer was greater because of accelerated airstream. The structure portions had a complex influence on the heat transfer to different elements of the structure. Also, Aft Pontoons were in the shadow of Front Pontoons for $\psi = 90^\circ$ (Kulyakhtin and Tsarau, 2014). Due to the increased heat transfer, ice accumulation on the Aft Pontoons was greater compared to the Front Pontoons.

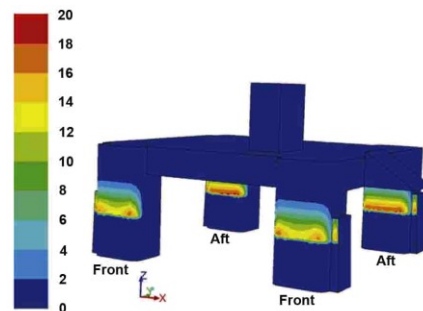


Fig. 1.42: Ice accumulation rate (mm/hr) on the West Hercules drilling rig for $T_a = -17^\circ\text{C}$, $\psi = 90^\circ$ and $U_{10} = 33$ m/s (Kulyakhtin and Tsarau, 2014)

Horjen (2015) modeled and analyzed the ice accumulation of an offshore drilling rig for two different structures, a corner column and a truss, that were exposed to impact-generated spray using an extension of ICEMOD2 called ICEMOD2.1, which includes the effect of inertia terms in the momentum equations. To validate the results of the modeling, Horjen (2015) compared the numerical results with the field data (Brown et al., 1988; Brown and Horjen, 1989) that was obtained from the drilling rigs “SEDCO 708” and “SEDCO 709”.

For instance, Fig. 1.43 indicates the numerical results for the diagonal truss for $\nu = 70^\circ$ and $\phi = 36^\circ$ (see Fig. 1.38). The figure also compares these results with the field data that is obtained just after observation 60. It should be noted that the SEDCO 708 icing event, which includes 60 observations, is reported in Appendix A of the paper that was published by Horjen (2015). Figure 1.43 shows good agreement between the results. Additionally, according to this figure, the model thickness is greater above a height of 4.5 *m* compared to the estimated thickness (0–6 cm). Table 1.7 illustrates and compares the predicted results and the empirical observations for the thickness of ice accumulation. As shown in this table, the largest ice thicknesses of the model are up to 29% lower or higher compared to estimated amounts, whereas the heights of the greatest ice thicknesses are not much different from the estimated amounts that are obtained by photos.

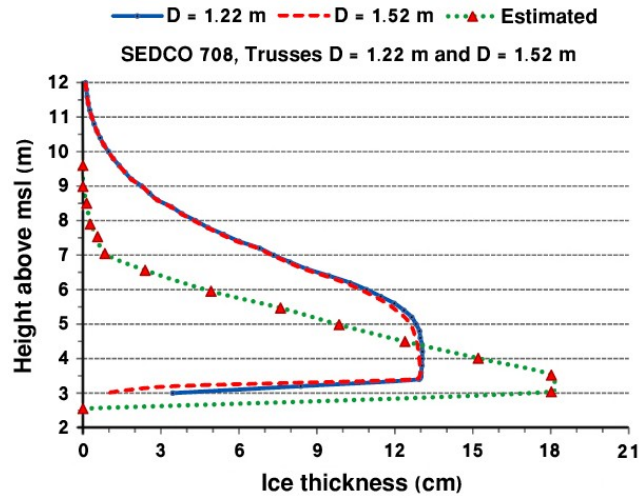


Fig. 1.43: Vertical distribution of model greatest ice thickness on $D = 1.22$ m ($v = 70^\circ$) and $D = 1.52$ m ($v = 50^\circ$) trusses and estimated greatest ice thickness (from photos by Minsk (1984a)) just after observation 60 (Horjen, 2015).

Note that msl is an acronym referring to mean sea level

Table 1.7: Comparison of the ice accumulation thickness that is obtained from the experimental observations and numerical modeling (Horjen, 2015)

Icing event	Icing object	Max. thickness (cm)		Height of max. thickness (m)		Max. height of icing (m)	
		Model	Obs.	Model	Obs.	Model	Obs.
SEDCO 708	Corner column, $D = 9.15$ m	9.7	7.5	5.0	4.0	~12.0	9.0
	70° truss, $D = 1.22$ m	13.1	18.0 ¹	4.0-4.4	3.5 ¹	~12.0	9.0
	50° truss, $D = 1.52$ m	13.0	18.0 ¹	3.6-3.8	3.5 ¹	~12.0	9.0
SEDCO 708	Corner column, $D = 9.15$ m	11.5	10.0	2.5	3.5	~5.5	7.0
	70° truss, $D = 1.22$ m	15.3	15.0	2.0	2.0	~5.4	7.0
	50° truss, $D = 1.52$ m	15.2	-	2.0	-	~5.4	-

1. Type of truss for ice thickness observations was not distinguished.

A new approach to calculate the ice accumulation of periodic sea spray was proposed by Kulyakhtin et al. (2016). This approach considers heat transfer through the ice layer and the substrate (aluminum). They used the enthalpy from the heat conduction equation

and derived a formula for the transient thickness of the brine layer on the accumulated ice. Experiments were conducted considering different period of the spray from 31.9 s to 147.8 s while the air temperature varies from -5°C to -8.4°C . They compared conductive solutions, non-conductive solutions and experimental results. The numerical and experimental results have an overall difference of less than 25% when the conduction model was used. The authors reported that the error can occur because of assuming the liquid fraction in dendritic ice accumulation as a constant. Governing equations of transient heat conduction through a substrate of spongy ice have been developed and examined by Deghani et al. (2017b). They reported that the rate of heat transfer is strongly dependent on the salinity of brine-spongy ice.

The International Maritime Organization (IMO) developed an international code, called Polar Code, and applied it to all vessels operating in Polar areas from January 2017 (IMO, 2016). This code enables better safety of vessels' operation and crews aboard them, as well as identifying the hazards existing in Polar areas in order to preserve the Polar environment. The risks of harsh environmental conditions that will affect vessels operating in polar areas, such as operation in low air temperature, high latitude and ice as well as icing conditions are considered in the Polar Code.

A new Marine Icing Model for the Norwegian Coast Guard, which is called MINCOG, was developed by Samuelsen et al. (2017). To validate the predicted icing rates by MINCOG, the measured data from a large coast guard ship type was employed. Additionally, Samuelsen et al. (2017) used different field data in the MINCOG, and they compared the obtained results. In this model, to compute the sea spray flux, two experimentally-derived formulations from Borisenkov et al. (1975) and Horjen et al.

(1986) were utilized. The aim of MINCOG is to predict the rates of icing in three main classifications: light, moderate, and severe when the ice accretion is reported from the vessel. Note that the marine icing models based on numerical simulations are computationally intensive; therefore, they cannot be employed for icing forecasting.

1.4 Discussions

Modeling, analyzing and estimating the icing rate and the amount of accumulated ice on marine vessels and structures are complex and challenging (Fukusako et al., 1989; Horjen, 1983a, 1990, 2013, 2015; Jessup, 1985; Kulyakhtin and Tsarau, 2014; Kulyakhtin et al., 2016; Lozowski et al., 1996; Lozowski et al., 2000; Makkonen, 1984a, 1984b, 1989; Szilder and Lozowski, 1995; Zakrzewski, 1987, Zakrzewski et al., 1988), because several issues and phenomena must be considered, such as: characteristics of swell and wind waves, sea spray frequency, the trajectory and distribution of water droplets, heat losses, mass fluxes, salt concentration and salt rejection during the freezing process. Despite several studies that have been carried out on sea spray icing, some of which are explained briefly in the third section, the procedures for modeling and simulating the growth rate and amount of ice accumulation on complex marine platforms need further research and development. This does not mean that the past studies conducted during the last decades were not significant and efficient. To improve the quality and accuracy of sea spray icing models, various issues need to be further addressed, including: (1) collecting field data with complete details, (2) obtaining a better understanding of the fundamental physical processes that are involved in sea spray icing, and (3) modeling and simulating the marine icing models with the use of more accurate and realistic approaches.

(1) *Data acquisition.* To develop and validate the predicted sea spray icing models for various marine platforms using different approaches, the lack of reliable data is quite evident. Jessup (1985) reported that although there is a considerable volume of data for small ships like fishing trawlers, the data is mostly sketchy, such that important details about the data are not available. Another significant point is that there are rarely sufficient and accurate observations for other kinds of marine ships and structures. For instance, as mentioned in subsection 1.3.3, Horjen (2015) compared the numerical results for the modeling of two different structures of a drilling rig with the field data that was obtained from *photos* by Minsk (1984a) of drilling rigs “SEDCO 708” and “SEDCO 709”. Efimov (2012) expressed that the first information that was obtained about ship icing was presented by fishermen and marine explorers; such information is normally inaccurate and not optimal for model comparison. According to a report by Minsk (1977), some Russian sources reported that sea spray icing will not happen at temperatures below -18°C . Actual shipboard observations have revealed that icing can occur at temperatures as low as -29°C .

The use of a cold room or cold wind tunnel is a useful way to obtain the experimental results by using scale models of the different marine structures, like the experimental results of Fukusako et al. (1989) that is illustrated in subsection 1.3.2. However, creating the actual manners like the existing conditions in the cold seas and ocean regions is difficult in a cold room or cold wind tunnel. So there is a need to collect more accurate field data with complete details, such as environmental factors, sea or ocean conditions, and measuring the ice thickness for different marine structures during the sea spray icing events.

(2) *Physical processes in the formation of ice.* To create more realistic simulations of the sea spray icing models and obtain more accurate results, a better understanding of the physical processes that are involved in marine icing is crucial. As mentioned in the previous section, the researchers considered a number of assumptions to simplify their modeling processes, like Horjen (2013, 2015), Kulyakhtin and Tsarau (2014), Shipilova et al. (2012), Blackmore and Lozowski (1994), and Lozowski and Gates (1985). However, these processes are complicated and numerous. Some of the physical processes are expressed as follows.

(i) The more accurate measurement or prediction of the weather and sea or ocean conditions. Several parameters, such as ambient air temperature, wind velocity, relative humidity, sea surface temperature, salinity, and wind direction have an influence on the freezing process. These parameters are variable during the sea spray icing events.

(ii) The process of sea spray formation due to wave impact and wind, as well as spray frequency. The liquid water content (LWC) and droplet size distribution that are generated by waves and wind are a function of several factors, such as the characteristics of swell and wind waves (height, period and propagation direction), wind velocity, and the types of marine structures. Several researchers like Preobrazhenskii (1973), Itakagi (1979, 1984), Horjen (1983a), Horjen and Vefsnmo (1984), and Jones and Andreas (2012) obtained the various formulae to compute the LWC of wind spray. In addition, a number of investigators, such as Kachurin et al. (1974), Stallabrass (1980), Borisenkov et al. (1975), Horjen and Vefsnmo (1984), Horjen (1990), Brown and Roebber (1985), Zakrzewski (1986a), Forest et al. (2005), and Lozowski et al. (2000) found the different formulae to estimate the LWC of wave spray. By using these formulae, the LWC can be

obtained only as an approximate amount; however, they are valid for some special marine vessels or structures.

(iii) The forecasting of the trajectory and analysis of the freezing process of saline water droplets. Ryerson (1995) reported that the range of droplet diameters was between 14 and 7700 μm for 39 sea spray events. Also, for fixed marine structures, Jones and Andreas (2009) reported that the radius drop range, which are produced by wind, were from 0.5 to 500 μm . The droplet size has a considerable impact on the droplet velocity, the motion trajectory, and collision efficiency (Makkonen, 2000). The modeling and analysis of the droplet freezing process are important to determine the configuration (water or ice) and the temperature of droplets at the moment of impact. Several forces affect the motion of a water droplet during its flight onto marine platforms, including: gravity, air drag, buoyancy, and accelerating body forces (Fu et al., 2006; Lorenzini and Saro, 2013; Macdonald and McCartney, 1987; Pearcey and Hill, 1956); however, often researchers consider only gravity and air drag forces.

(iv) The influence of salinity of the spray droplets and the accreted ice on the physical processes that are involved in ice accumulation. Salinity has an impact on the supercooling of droplets, thermodynamics at the icing surface, and the ice properties (Jessup, 1985), such as the thermal conductivity, density, specific heat capacity, strength, and adhesion to substrate, as well as the freezing temperature. As described in the previous section, the ice accretion layer includes pure ice, brine pockets and air bubbles that are called spongy ice (Blackmore et al., 2002; Makkonen, 1987). The modeling and analysis of the spongy ice and also salt rejection phenomena are challenging (Blackmore et al., 2002; Fukusako et al., 1989; Terwilliger and Dizon, 1970; Makkonen, 1987).

(v) The computation of a more accurate heat transfer coefficient on different marine structural surfaces. The heat transfer coefficient plays an important role in determining the convection and evaporation heat fluxes. A number of researchers have suggested several formulae to estimate the heat transfer coefficient for different configurations, such as Rohsenow and Choi (1961), Livingood and Hrycak (1973), Achenbach (1977), Jones (1996), Lozowski et al. (1983), Makkonen (1985), and Lozowski et al. (2000). However, these formulae calculate an approximate value.

(vi) The fluid mechanics and thermodynamics of the runback and runoff processes. Jessup (1985) expressed that these processes are affected by gravity, turbulent interaction between the water film and the wind field, as well as by the shape of the icing surface.

(vii) The study of influences generated by the complex geometry of typical marine platforms on physical processes.

(3) *Marine icing modeling*: As illustrated in the previous section, all sea spray icing models were obtained by considering various assumptions, especially in the theoretical and numerical modeling (Blackmore and Lozowski, 1994; Chung and Lozowski, 2010; Horjen, 2013, 2015, Kulyakhtin and Tsarau, 2014, Lozowski and Gates, 1985; Shipilova et al., 2012; Szilder and Lozowski, 1995; Zakrzewski et al., 1988). To improve the simulation of the marine icing models and obtain more accurate results, more investigations are required in the physics of the different processes and the use of various methods of modeling and considering more realistic conditions. Some of these investigations are expressed as follows.

(i) All of the different time dependent aspects in creating the accumulated ice must be considered in the models.

(ii) Considering conduction heat transfer in the accumulated ice layer. Kulyakhtin (2014) reported that existing marine icing models, such as ICEMOD, RIGICE04, and MARICE ignore conduction heat transfer in the formed ice layer. However, Kulyakhtin et al. (2016) theoretically showed that heat conduction has an important role in the formation of the accumulated ice. Conduction heat transfer depends on the distribution of ice salinity, which is not well understood.

(iii) Performing more accurate studies on spongy ice and the properties of ice accumulation.

(iv) Most investigations of sea spray icing are performed for cylindrical components on marine platforms, although few studies have been carried out on the planar components. Modeling and analysis of the various types of marine structures, such as large structures, complex geometry, and stationary or moving structures are also needed. To increase the safety and stability of marine vessels and structures, one approach is to reduce the amount of accumulated ice on them. More accurate modeling, prediction and analysis of the icing phenomenon can help to mitigate the ice formation. Another approach is the use of anti-/de-icing techniques. Ryerson (2009) and Rashid et al. (2016) categorized and reported these techniques.

Chapter 2

Formulation of Sea Spray Icing Phenomena on Offshore Platforms¹

In this chapter, the sea spray icing phenomenon on marine platforms is reviewed to better understand, model and analyze the phenomenon in cold seas and ocean regions. For the formulation of marine icing models, several issues such as droplet trajectories, liquid water content (LWC), spray movement, and spray duration are investigated in section 2.1. To model the sea spray icing on marine platforms, a mass balance is presented in section 2.2. The water droplets impinging on marine platforms will freeze because of several different heat fluxes. These heat fluxes are described in section 2.3. Some simplified icing models and also more advanced icing models are explained in section 2.4.

2.1 Formulation of Marine Icing Models

In order to analyze and model the marine icing phenomenon as well as to obtain the amount of ice accretion, the following issues will be examined: droplet trajectories, liquid water content (LWC), spray movement, and spray duration.

1. This chapter is based on a review paper that was published in Ocean Engineering (journal).

2.1.1 Droplet Trajectories

As mentioned in chapter 1, a cloud of seawater spray is generated by two main but different causes, which are wave spray and wind spray. In other words, water droplets with different sizes are produced by wind blowing droplets off whitecaps at the water surface, as well as by the impact of waves on marine vessels or structures (Dehghani-Sanij et al., 2015, 2016). Furthermore, wind spray is fundamentally formed by two mechanisms (Zakrzewski, 1986b): (1) the direct whipping of wave crests through the wind, and (2) the bursting of air bubbles at the water surface. The second mechanism generally seems to be the major source of the wind spray.

According to a report by Jones and Andreas (2009), for fixed marine structures, three different types of droplets are generated by the wind (Monahan, 1986; Monahan et al., 1983): (1) small film droplets, ranging from 0.5 to 50 μm in radius, (2) jet droplets, ranging from 1 to 100 μm in radius, and (3) spume droplets (or spindrift), ranging from 20 to 500 μm in radius. Based on empirical measurements by Ryerson (1995) on a large US Coast Guard cutter in the North Pacific Ocean and the Bering Sea, by measuring roughly 7,000 water droplets, the range of droplet diameters for 39 spray events were from 14 to 7700 μm . In these spray events, the mean median volume diameter was 1094 μm and they ranged from 169 to 6097 μm for single spray events (Ryerson and Gow, 2000a, 2000b).

As droplets move over marine platforms, the larger droplets tend to fall out of the spray cloud because of gravity; however, there is a balance between gravity and wind so that larger droplets are kept aloft at higher wind speeds. Lozowski et al. (2000) have expressed relationships for droplet trajectory and droplet cooling. They assumed that the

water droplets are spherical, and coalescence and break-up are omitted. Yoon and Ettema (1993) investigated the effects of non-spherical droplets on both the drag coefficient and the collision efficiency. These results showed that the drag coefficient is changed by 35%, and the variation of collision efficiency is lower than 1%. Therefore, the effects of non-spherical droplets can be ignored. Also, for all the droplets, evaporative cooling has been considered. The effect of evaporation on droplet mass depends on the droplet size (Lewis and Schwarz, 2004). This effect on wind generated spray is substantial because the size of the droplets is small. The effect of evaporation for large droplets is not important, and it can be neglected. Horjen (1990) obtained analytical solutions of the droplet size, temperature and salinity history for the water droplets during flight.

Kulyakhtin and Løset (2011) numerically and semi-analytically studied the effects of relative humidity on seawater spray temperatures during flight. The results for a constant air temperature and wind velocity indicated that by increasing the Liquid Water Content (LWC), the relative humidity of the ambient air will increase. Additionally, the variations in humidity had insignificant effects on the temperature of the water droplet. Moreover, for lower LWC, the temperature difference is directly related to the relative humidity of the ambient air. The thermal and evaporative effects of the seawater spray droplets with a radius between 0.5 μm and 500 μm were investigated by Andreas (1990). The results illustrated that the relative humidity of ambient air has an insignificant impact on the thermal characteristics of sea spray droplets. In addition, the temperature difference between the airflow and seawater has a small effect on the evaporative process. The equilibrium diameter of a water droplet was found to be about one-half of the diameter at its formation for a relative humidity of 80%.

Dehghani et al. (2016a) analyzed the trajectory of water droplets from the impingement of waves on a ship. The results showed that the distributions of the size and velocity of droplets in front of the ship are the most important factors to estimate the droplet trajectories and the LWC. Also, there is an inverse dependence between the size and velocity of the water droplets, such that the droplets with small sizes have high-speed and vice versa. In another study, Dehghani et al. (2016b) numerically investigated the distribution of sizes and velocities of water droplets upon a medium-size fishing vessel (MFV). They illustrated that both the biggest and smallest water droplets will not reach the highest height of the sea spray cloud. However, the water droplets with medium sizes (2.4 to 3.8 mm diameters) can reach the highest height. Figure 2.1 shows the numerical results of size distributions of droplets over a Medium-sized Fishing Vessel (MFV), where D represents droplet diameters.

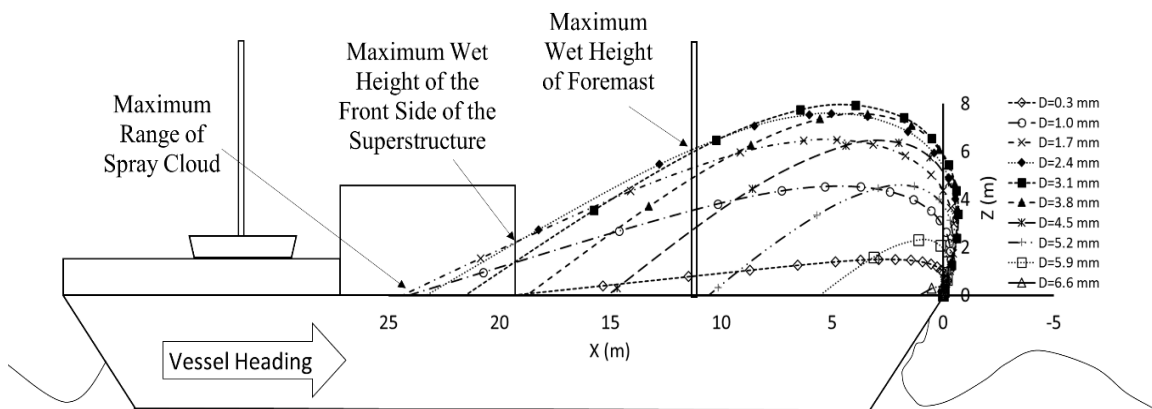


Fig. 2.1: Numerical results of spray cloud movement over an MFV including the maximum wet heights and the maximum extent of spray (Dehghani et al., 2016b)

The trajectory and cooling process of the water droplets during flight over marine platforms are investigated in the next chapter.

The total mass flux of seawater spray, $\dot{M}_{w,t}$, during a seawater splashing event is obtained by the following formula:

$$\dot{M}_{w,t} = \dot{M}_{w,wind} + \dot{M}_{w,wave} \quad (t < \tau_s) \quad (2.1)$$

where τ_s is the duration of the spray event. The amount of the total mass flux of seawater spray reaching an object located on a marine platform per unit area and unit time for wind and wave spray is obtained by (Chaine and Skeates, 1974; Paulin, 2008):

$$\dot{M}_{w,t} = B_s E U_{rs} [\omega(z)_{wind} + \omega(z)_{wave}] \quad (2.2)$$

Here, B_s is the shape coefficient, E is the collision efficiency, U_{rs} is the spray/wind velocity relative to the object, and ω is the Liquid Water Content (LWC). These parameters will be explained in the following sections. Note that Eq. (2.2) is only valid for a surface placed normal to the free wind velocity vector and it is the mean value for the upwind side of the structure.

2.1.2 Liquid Water Content (LWC)

The LWC is the measure of the mass of the water in a spray cloud per unit amount of dry air. The LWC in a seawater spray event is an important parameter to calculate the amount of total flux of sea spray, as is the vertical distribution of LWC. A number of researchers (Borisenkov et al., 1975; Forest et al., 2005; Horjen, 1983a; Horjen and Vefsnmo, 1984; Jones and Andreas, 2012; Kachurin et al., 1974; Lozowski et al., 2000;

Preobrazhenskii, 1973; Zakrzewski, 1986a, 1986b, 1987) obtained the LWC for wave spray and/or wind spray by different relations. These relations will be described in the following sections.

2.1.2.1 Liquid Water Content in Wind-generated Spray

To compute the LWC for wind-generated spray, several models have been proposed.

(a) *Preobrazhenskii (1973)*.

In order to calculate the vertical distribution of the LWC for wind spray, Preobrazhenskii (1973) suggested the following formula for wind flow over the fetch (Kato, 2012; Preobrazhenskii, 1973; Zakrzewski, 1986b):

$$\omega(z) = \omega_0 \exp\left(-\psi\left(z - \frac{h_s}{2}\right)\right) \quad (2.3)$$

where z is the height above the mean water level, h_s is the significant wave height, and ω_0 and ψ are constants experimentally selected for different wind velocities, which are (Preobrazhenskii, 1973; Zakrzewski, 1986b):

$$\omega_0 = 10^{-7} \text{ (kg/m}^3\text{)} \text{ and } \psi = 0.35 \text{ for moderate winds } (U_{10} = 7 - 12 \text{ m/s)}$$

$$\omega_0 = 10^{-5} \text{ (kg/m}^3\text{)} \text{ and } \psi = 1 \text{ for strong winds } (U_{10} = 15 - 25 \text{ m/s)}$$

Eq. (2.3) is obtained based on experimental measurements. Figure 2.2 shows the vertical distribution of spray water content, while Eq. (2.3) represents by two linear lines.

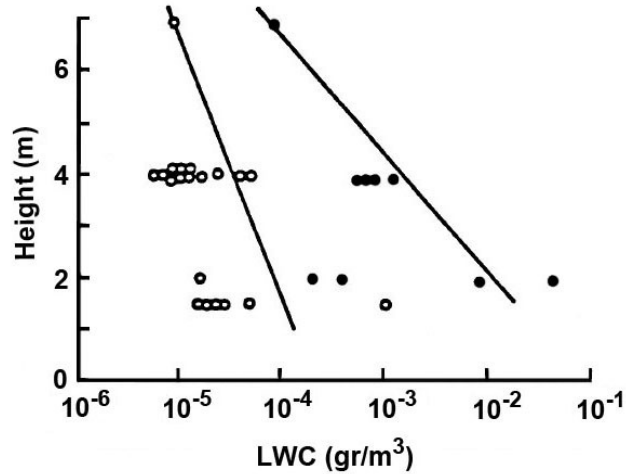


Fig. 2.2: LWC for the wind spray as a function of the height on top of mean water level (Zakrzewski, 1986b) (From Preobrazhenskii (1973) according to Makkonen (1984a)).

Note that the two graphs shown in this figure refer to two different ranges of wind velocities: left line is for moderate winds (7-12 m/s) and right line is for strong winds (15-25 m/s)

(b) Itakagi (1979, 1984).

To determine the distribution of the LWC for wind spray, Itakagi (1979, 1984) expressed the equation below (Zakrzewski, 1986b):

$$\omega = 1.30818 \times 10^{-4} A(U_{10}) \quad (2.4)$$

where $A(U_{10})$ is a third-degree polynomial at wind velocity U_{10} , which is defined as follows (Itakagi, 1979, 1984; Zakrzewski, 1986b):

$$A(U_{10}) = -53.5173 + 11.3119 U_{10} - 0.7934 U_{10}^2 + 0.01864 U_{10}^3 \quad (2.5)$$

Using Eqs. (2.4) and (2.5), the LWC is determined at any known wind velocity at a reference height of 10 m, but the vertical profile of spray is not specified.

(c) Horjen (1983a).

According to Horjen (1983a), the vertical distribution of the LWC can be approximately written as follows:

$$\omega(z) = 6.3185 \times 10^{-5} A(U_{10}) \frac{h_s(U_{10})}{z^2} \quad (2.6)$$

where $A(U_{10})$ is specified by Eq. (2.5) in units of m^{-1} and h_s is the significant wave height, which can be obtained by the following formulae (Horjen, 1983a; Zakrzewski, 1986b; Kato, 2012):

$$h_s(U_{10}) = B_0 + B_1 U_{10} + B_2 U_{10}^2 + B_3 U_{10}^3 \quad (2.7)$$

or

$$h_s(U_{10}) = B_0 + B_1 U_{10} + B_2 U_{10}^2 + B_3 U_{10}^3 + B_4 U_{10}^4 + B_5 U_{10}^5 \quad (2.8)$$

Here, B_0 to B_5 are constant coefficients, which are defined by Tables 2.1 and 2.2 for a known fetch. Note that these relationships are only valid for wind velocity up to 32.4 m/s.

Table 2.1: Constant coefficients for third degree of polynomial of the wind velocity defined in Eq. (2.7) (Kato, 2012)

Fetch (n.m.)	B_0	B_1	B_2	B_3
100	6.05709×10^{-2}	2.89125×10^{-2}	2.54698×10^{-2}	-4.89792×10^{-4}
200	4.21968×10^{-1}	-7.75092×10^{-2}	3.46928×10^{-2}	-5.72020×10^{-4}
300	1.28311	-2.26480×10^{-2}	4.19756×10^{-2}	-6.05377×10^{-4}
400	6.09959×10^{-1}	-1.32694×10^{-1}	3.87922×10^{-2}	-5.44265×10^{-4}
500	5.59229×10^{-1}	-1.34134×10^{-1}	4.03976×10^{-2}	-5.73259×10^{-4}

Table 2.2: Constant coefficients for fifth degree of polynomial of the wind velocity defined in Eq. (2.8) (Kato, 2012)

Fetch (n.m.)	B_0	B_1	B_2	B_3	B_4	B_5
100	8.68869×10^{-1}	-4.41178×10^{-1}	1.16227×10^{-1}	-7.87593×10^{-3}	2.62150×10^{-4}	-3.34401×10^{-6}
200	-7.71688×10^{-1}	2.71899×10^{-1}	1.07151×10^{-2}	-8.30642×10^{-4}	5.99481×10^{-5}	-1.20460×10^{-6}
300	-2.31314	5.96961×10^{-1}	-1.71261×10^{-3}	-1.75507×10^{-3}	1.32954×10^{-4}	-2.40288×10^{-6}
400	4.86322×10^{-1}	-3.41913×10^{-1}	1.14635×10^{-1}	-8.51850×10^{-3}	3.24417×10^{-4}	-4.49695×10^{-6}
500	6.55261×10^{-1}	-3.78443×10^{-1}	1.11329×10^{-1}	-7.55389×10^{-3}	2.75507×10^{-4}	-3.75483×10^{-6}

(d) Horjen and Vefsnmo (1984).

Horjen and Vefsnmo (1984) described a relationship to compute the vertical distribution of the LWC based on Preobrazhenskii's (1973) empirical field data for severe winds, which is given by (1986b):

$$\omega(z) = \omega_0 \left(\frac{U_{10}}{U_0} \right)^{3.8} \exp\left(\frac{H}{2} - z \right) \quad (2.9)$$

where $\omega_0 = 9.45 \times 10^{-6}$ (kg/m³), $U_{10} > 15$ m/s, and $U_0 = 15$ m/s.

(e) Jones and Andreas (2012).

Jones and Andreas (2012) used two experimental relationships to calculate the seawater spray droplet concentrations near the sea or ocean surface for wind velocities ranging from 0 to 28.8 m/s. They studied and developed all previous relationships. These relationships are as follows (Jones and Andreas, 2012; Schröder Hansen, 2012):

$$\frac{d\omega(r,z)}{dr} = \rho_w \left(\frac{4}{3} \pi r^3 \right) \left(\frac{z}{h} \right)^{-\frac{v_g(r)}{ku_* f_s}} \begin{cases} \frac{7 \times 10^4 U_{10}^2}{r} \exp\left(-\frac{1}{2} \left[\frac{\ln(r/0.3)}{\ln 2.8} \right]^2 \right) , & \text{if } U_{10} < 19 \text{ m/s} \\ \frac{30 U_{10}^4}{r} \exp\left(-\frac{1}{2} \left[\frac{\ln(r/0.3)}{\ln 4} \right]^2 \right) , & \text{if } U_{10} \geq 19 \text{ m/s} \end{cases} \quad (2.10)$$

where r is the droplet radius, ρ_w is the density of seawater, k is the Von Kármán constant, f_s is the slip factor, u^* is the friction velocity, and h is the height which is specified as the upper limit of the source region for spray droplet generation. For $U_{10} < 19$ m/s, $h = 1$ m and for $U_{10} \geq 19$ m/s, $h = 0.5 h_s$ where h_s is the significant wave height. The function $v_g(r)$ is the terminal fall velocity of the droplets. Here, v_g is specified as a positive amount, therefore the minus sign is kept. The fall velocity function is given by (Andreas, 1990):

$$v_g(r) = \frac{2r^2 g}{9v_a \left[1 + 0.158 \left(\frac{2rv_g}{v_a} \right)^{2/3} \right]} \left(\frac{\rho_w}{\rho_a} - 1 \right) \quad (2.11)$$

Here, g is the acceleration of gravity ($g = 9.81$ m/s²), v_a is the air kinematic viscosity, and ρ_a is the air density. According to Andreas (1990), Eq. (2.11) is solved by Newton's method. Since the equation is indeterminate for $v_g < 0$ and its derivative is indeterminate for $v_g \leq 0$, using Newton's method may be problematic.

In order to estimate friction velocity and wind profile, an algorithm of Andreas et al. (2008) is used. Applying this algorithm is difficult because the algorithm itself is complicated. Schröder Hansen (2012) described the algorithm, stating where all the needed equations, parameters and references may be found. Consequently, the vertical distribution of the LWC of the wind spray can be written as (Schröder Hansen, 2012):

$$\omega(z) = \int_{r_{min}}^{r_{max}} E \frac{d\omega(r, z)}{dr} dr \quad (2.12)$$

If $U_{10} < 19$ m/s, the maximum droplet radius assumed to contribute to icing is 100 μm and if $U_{10} \geq 19$ m/s, it is 200 μm . The minimum droplet radius assumed to contribute to icing is 5 μm (Jones and Andreas, 2012; Schröder Hansen, 2012).

It should be mentioned that comparing the different formulae to estimate the LWC of wind spray is not fruitful. In other words, the parameters and conditions for these formulae are different. For instance, Eq. (2.4) is only a function of wind velocity but Eqs. (2.3), (2.6), and (2.9) are functions of wind velocity, height above the mean water level, and significant wave height or wave height. Eq. (2.10) is a function of wind velocity, height above the water's surface, significant wave height, and droplet radius. It seems that the formula obtained by Jones and Andreas (2012) gave more accurate results, because they considered almost all parameters needed for two different conditions of wind velocity in the range of 0 to 28.8 m/s.

2.1.2.2 Liquid Water Content in Wave-generated Spray

As mentioned in chapter 1, wave spray is the major cause of marine icing. To calculate of the LWC for wave-generated spray, several formulae have been proposed.

(a) *Kachurin et al. (1974)*.

The simple formula for a ship is suggested by Kachurin et al. (1974). This formula is just a function of wave height, which is written as follows (Kachurin et al., 1974; Zakrzewski, 1987):

$$\omega = \zeta H \tag{2.13}$$

where H is the wave height and ζ is a constant. This constant is 10^{-3} kg/m⁴ for vessel headings $0 \pm 40^\circ$ and wind velocity between 6 and 8 knots (Kachurin et al., 1974; Stallabrass, 1980; Zakrzewski, 1987). Stallabrass (1980) developed Eq. (2.13) in the icing model according to the formula below:

$$\omega = 1.7 \times 10^{-4} H \quad (2.14)$$

The author calculated that the LWC is one sixth of Eq. (2.13). This result was a considerable improvement upon the relationship of Kachurin et al. (1974) with observed results.

(b) Borisenkov et al. (1975).

Borisenkov et al. (1975) obtained an empirical formula for the vertical distribution of the LWC by waves based on field data for an MFV in the Sea of Japan as follows (Borisenkov and Pchelko, 1975):

$$\omega = 2.36 \times 10^{-5} \exp(-0.55 h) \quad (2.15)$$

where h is the altitude of an object over the deck of MFV, and the freeboard height of the MFV is 2.5 m. The units of above equation are the volume of water in a unit volume of air. The MFV moves into the waves with an angle of 90° - 110° and a speed of 5-6 knots. Also, the wind velocity is reported as 10-12 m/s. This model is applicable for a particular type of ship under certain sea conditions, and cannot be employed to compute the vertical distribution of LWC for various types of ships and sea conditions (Bodaghkhani et al., 2016).

(c) *Horjen and Vefsnmo (1984) and Horjen (1990, 2013, 2015)*.

Horjen and Vefsnmo (1984) suggested the formula below for the time-averaged spray cloud LWC for an offshore drilling rig.

$$\omega = 0.1 H \exp(H - 2z) \quad (2.16)$$

where H is the wave height and z is the height over the mean seawater level. Horjen (1990, 2013, 2015) has developed several other expressions for the spray mass flux.

(d) *Brown and Roebber (1985)*.

A relationship for vertical distribution of the LWC for offshore structures was obtained by Brown and Roebber (1985) as follows (Forest et al., 2005):

$$\omega = 4.6 \exp\left(-\left(\frac{2z}{h_s}\right)^2\right) \quad (2.17)$$

where h_s is the root-mean-square wave height.

(e) *Zakrzewski (1986a)*.

Zakrzewski (1986a) found a formula to calculate the vertical distribution of the LWC for an MFV, which is given by:

$$\omega = 6.1457 \times 10^{-5} H v_{sw}^2 \exp(-0.55 h) \quad (2.18)$$

where H is the wave height and can be computed by Eq. (2.7) or (2.8) for a known fetch and wind velocity, and v_{sw} is the vessel speed relative to the waves.

(f) *Forest et al. (2005)*.

Forest et al. (2005) estimated a relationship for the vertical distribution of the LWC for one single seawater spray event on an offshore structure, which is defined as:

$$\omega = 1.35 h_s^2 \exp(-0.53 z) \quad (2.19)$$

where h_s is the significant wave height. Note that the above formula is derived from spraying data at one site only.

(g) *Lozowski et al. (2000)*.

In order to calculate the vertical distribution of the LWC in the spray jet for the ship, Lozowski et al. (2000) expressed the formula below based on results from Zakrzewski (1986b). This formula is given by:

$$\omega(z) = 6.1457 \times 10^{-5} h_s v_{sw}^2 \exp\left(-\frac{(z - H_{bow})}{1.82}\right) \quad (2.20)$$

where H_{bow} is the height of the bow above the surface level. Here, a coordinate system has been used where $z = 0$ at the water surface. The vessel speed relative to the waves, v_{sw} , is given by (Aksyutin, 1979; Schröder Hansen, 2012; Zakrzewski, 1986b, 1987):

$$v_{sw} = \frac{g}{2\pi} \tau_w + v_s \cos(\pi - \alpha) \quad (2.21)$$

Here, τ_w is the significant wave period, v_s is the vessel speed, g is the gravitational acceleration, and α is the angle between the vessel heading and the wind/wave direction. For α to be equal to 0° , the vessel goes into the waves directly, and when α is 180° , the vessel passes the waves.

The spray jet (in the form of a thin liquid sheet) is assumed to start at the top of the bow and develop symmetrically along both sides of the vessel to a distance x_e , which is estimated with the following formula (Lozowski et al., 2000):

$$x_e = 2.0 h_s + 0.04 v_{sw}^2 - 10.0 \quad (2.22)$$

If x_e is negative, there is no spray jet. The maximum height of the spray jet may be approximated by (Lozowski et al., 2000):

$$H_m = h_s + \frac{v_{sw}^2}{2g} \quad (2.23)$$

In the above formula, the term $\frac{v_{sw}^2}{2g}$ is based on the assumption that the ejection velocity of the droplets is approximately equal to the vessel speed relative to the waves and also air drag on the water droplets can be neglected (Lozowski et al., 2000). Note that the spray jets do not occur in every vessel-wave collision (Aksyutin, 1979; Horjen and Carstens, 1990; Lozowski et al., 2000; Panov, 1976; Schröder Hansen, 2012). The duration of a spray event is calculated by the following formula (Zakrzewski, 1987):

$$\tau_s = \frac{C v_{sw} h_s}{U_{10}^2} \quad (2.24)$$

In the above relationship, C is an experimental constant, which depends on two main factors: the dimensions and configuration of the vessel hull (Zakrzewski, 1987). According to Lozowski et al. (2000), the parameter C is 10 for a USCGC patrol vessel when it is assumed that a spray event is generated for every fourth wave collision. Furthermore, according to Zakrzewski (1987), the parameter C is equal to 20.62 as a result of spray jet creation by every second wave on a fishing trawler (Lozowski et al., 2000).

A principal factor in determining wave spray icing is spray frequency. According to Lozowski et al. (2000), it is assumed that a spray event is generated once for every fourth wave collision on a large whaling ship. Also, Zakrzewski (1987) reported that the spray

jet is created by every second wave on a fishing trawler (Lozowski et al., 2000). Horjen (2015) expressed that the mechanism of spray generation is completely distinct for a semi-submersible drill rig and marine vessel. Based on several observations, two experimental relationships to calculate significant wave height and period are obtained for Norwegian waters. To determine h_s , the following relationship can be employed (Horjen, 2015, 2013; Jørgensen, 1985):

$$h_s = 0.752 U_{10}^{0.723} \quad (2.25)$$

Also, for calculating τ_w the relationship below is applied (Horjen, 1990, 2013, 2015):

$$\tau_w = 6.161 h_s^{0.252} \quad (2.26)$$

Note that Horjen (2015) considered that every significant wave generates spray for his numerical modeling on an offshore structure. A total time period between spray events is computed by (Aksyutin, 1979; Lozowski et al., 2000):

$$\tau_p = \frac{g \tau_w^2}{2\pi v_{sw}} \quad (2.27)$$

This relationship is based on the assumption that every significant wave encounter produces spray. Forest et al. (2005) surveyed and compared the amount of the wave-generated spray flux density using Eqs. (2.16) to (2.19) (Table 2.3). For this purpose, they used the climate and geometric conditions for calculations and estimations of the sea spray icing on the semi-submersible drilling rig Ocean Bounty, in Cook Inlet, Alaska. During the marine icing event, the mean wind velocity, U , was 45 m/s from 290° to 300°, and the average significant wave height, h_s , was 3.8 m (Forest et al., 2005). According to Table 2.3, the values obtained from Eqs. (2.16) to (2.19) for wave-generated spray flux

are different because these equations are obtained for distinct weather parameters and spray generation mechanisms. As a result, the results obtained by Forest et al. (2005) are closer to the observations, because they used the data collected from the observations to determine the results by Eq. (2.19).

Table 2.3: The computed amount of wave-generated spray flux at deck level on the Ocean Bounty in Eqs. (2.16) to (2.19) (Forest et al., 2005)

Source of spray flux amount	Wave spray flux density (kg/ m².hr)
Spray flux measured on Ocean Bounty (Forest et al., 2005)	5 – 10 (between 10 and 15 m)
Horjen and Vefsnmo (1984)	2.56 × 10 ⁻⁷ (15 m) 5.67 × 10 ⁻³ (10 m)
Brown and Roebber (1985)	6.37 × 10 ⁻²² (15 m) 6.95 × 10 ⁻⁷ (10 m)
Zakrzewski (1987)	2.82 (15 m) 44.0 (10 m)
Forest et al. (2005)	1.15 (15 m) 16.35 (10 m)

Bodaghkhani et al. (2016) compared several formulae of the LWC, as obtained by different researchers for conditions of $v_s = 10$ m/s, $\tau_w = 15$, $\alpha = 0^\circ$, and $z-h = 5$. Figure 2.3 shows this comparison. It should be mentioned that the comparison of the results obtained by different formulae to compute the LWC of wave spray is not useful, because several factors such as weather conditions and the spray producing mechanisms, applications for marine vessels and offshore structures are completely different.

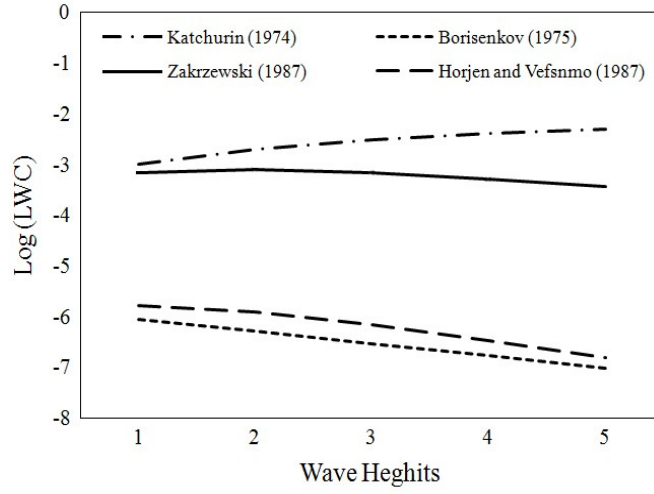


Fig. 2.3: Comparison between various LWC formulae as a function of wave heights (Bodaghkhani et al., 2016)

2.1.3 Spray Movement

Zakrzewski (1987) obtained the spray velocity relative to the object located on an MFV, as follows:

$$U_{rs} = \sqrt{U^2 + v_s^2 - 2U \cdot v_s \cos \gamma} \quad (2.28)$$

where U is the spray velocity, v_s is the vessel speed, and γ is the angle between the direction of spray velocity and vessel speed that is measured in the clockwise direction.

The spray/wind velocity before impinging on the object has two components: (1) the velocity in the horizontal direction, U_h , and (2) the velocity in the vertical direction, U_z . It can be calculated by the following formula (Zakrzewski, 1987):

$$U = \sqrt{U_h^2 + U_z^2} \quad (2.29)$$

For 3-D cases, the size of the angle between vectors of wind velocity and vessel speed is defined by (Zakrzewski, 1987):

$$\gamma = \text{Arc cos} \left(\frac{U_x V_x + U_y V_y + U_z V_z}{\sqrt{U_x^2 + U_y^2 + U_z^2} \sqrt{V_x^2 + V_y^2 + V_z^2}} \right) \quad (2.30)$$

Here, subscripts x , y , and z for vectors of wind velocity and vessel speed refer to their components in the x , y , and z directions, respectively.

According to Horjen (1983a, 1983b), the shape coefficient or factor is $2/\pi$ for cylindrical components and 1 for planar components. Collision, or collection, efficiency is an important parameter for computing the growth rate of ice accumulation on marine platforms during icing conditions. The range of collision efficiency, E , is between 0 and 1. When a water droplet departs from the water's surface with the airflow to an icing object located on the marine platform, its trajectory is specified through two forces: aerodynamic drag and inertia (Makkonen, 2000). Also, these forces define how the trajectories deviate from the flow stream around the object. As a result, large water droplets tend to collide with the object when inertial forces prevail over aerodynamic drag forces; these droplets do not deflect considerably, although it is possible that the small droplets deviate from their direction relative to the object. Note that some droplets, after hitting the object, may not freeze and will become runoff.

According to Makkonen (2000), the wind velocity, the size of water droplets, and the dimensions of the object located on marine platforms have significant effects on the collision efficiency and the amount of inertia and drag forces. Also, determining the value of collision efficiency is very complex because (Makkonen, 2000; Silveira et al., 2003): (1) the sizes of water droplets in the cloud spray are different and (2) solving the equations of water droplet trajectory and finding the impingement locations is difficult.

Stallabrass (1980) suggested two approximate formulae to compute collision efficiency for vertical structures (cylinders or plates) as follows:

$$E = \frac{\zeta - 3200}{\zeta + 27000} \text{ (if } \zeta \geq 3200 \text{) and } E = 0 \text{ (if } \zeta < 3200 \text{) for cylinders} \quad (2.31)$$

$$E = \frac{\zeta - 2800}{\zeta + 11700} \text{ (if } \zeta \geq 2800 \text{) and } E = 0 \text{ (if } \zeta < 2800 \text{) for rectangular plates} \quad (2.32)$$

where the dimensionless parameter ζ is obtained by:

$$\zeta = \frac{U_r^{0.6} D^{1.6}}{L} \quad (2.33)$$

Here, U_r is the relative wind velocity adjacent to the object, D is the water droplet diameter, and L is the characteristic length of the object (cylinder diameter or body width). For $U_r = 3-60$ m/s, $D = 20-1000$ μm , and $L = 0.03-1$ m (cylinder) and $L = 0.03-3$ m (plate), Stallabrass (1980) derived these relationships to obtain collision efficiency (Stallabrass, 1980; Zakrzewski, 1986b, 1987). The collision efficiency for the horizontal plates can be considered equal to 1. Also, if the amount of wind velocity in the vertical direction is negligible, the relative wind velocity can be obtained by the following relationship (Zakrzewski, 1987):

$$U_r = \sqrt{U^2 + v_s^2 + 2U \cdot v_s \cos \alpha} \quad (2.34)$$

A number of researchers found a formula to estimate the collision efficiency for circular cylinders (Cansdale and McNaughton, 1977; Langmuir and Blodgett, 1946; Lozowski et al., 1983; Makkonen, 1984a). Langmuir and Blodgett (1946) have proposed the following formula to calculate collision efficiency (Finstad et al., 1988):

$$E = 0.466 [\log(8 K_0)]^2, \quad 0.125 < K_0 < 1.1 \quad (2.35)$$

$$E = \frac{K_0}{K_0 + \frac{\pi}{2}}, K_0 > 1.1 \quad (2.36)$$

$$E = \frac{K}{K + \frac{\pi}{2} \times 0.112 Re^{0.63} + 0.75 \times 10^{-4} Re^{1.38}}, E > 0.5 \quad (2.37)$$

where the Stokes number, K (the proportion of the inertia force and drag force acting on the water droplet (Horjen, 2013)), and the parameter of K_0 are (Finstad et al., 1988; Langmuir and Blodgett, 1946):

$$K = \frac{\rho_w D^2 U}{9 \mu_a D_c} \quad (2.38)$$

$$K_0 = 0.125 + \frac{(K - 0.125)}{1 + 0.0967 Re^{0.6367}} \quad (2.39)$$

Here, ρ_w is the density of the droplet (assumed to be as the density of seawater), μ_a is the air dynamic viscosity, D is the droplet diameter, and D_c is the cylinder diameter. Also, Re is the cylinder free flow Reynolds number ($Re = \frac{\rho_a U D}{\mu_a}$) and ρ_a is the air density.

To determine the collection efficiency, Lozowski et al. (1983) derived the formula below (Finstad et al., 1988):

$$E = 0.489 [\log(8 K_0)]^{1.978}, 0.125 < K_0 < 0.9 \quad (2.40)$$

$$E = \frac{K_0}{K_0 + \frac{\pi}{2}}, K_0 > 0.9 \quad (2.41)$$

In the equations above, the parameters of K and K_0 can be calculated by Eqs. (2.38) and (2.39). Cansdale and McNaughton (1977) expressed the following relationships for obtaining collision efficiency (Finstad et al., 1988):

$$E = 0.53 [\log(8 K_0)]^{1.8} \quad , 0.125 < K_0 < 1.1 \quad (2.42)$$

$$E = \frac{K_0^{1.1}}{K_0^{1.1} + 1.223} \quad , K_0 > 1.1 \quad (2.43)$$

where

$$K_0 = \frac{K}{1 + 0.087 Re^{(0.76 Re^{-0.027})}} \quad (2.44)$$

Also, the relationships for the collection efficiency were obtained by Makkonen (1984) as follows (Finstad et al., 1988):

$$E = 0.5 [\log(8 K_0)]^{1.6} \quad , 0.125 < K_0 < 0.8 \quad (2.45)$$

$$E = \frac{K_0^{1.1}}{K_0^{1.1} + 1.426} \quad , K_0 > 0.8 \quad (2.46)$$

In the equations above, the parameter of K_0 is defined by Eq. (2.44).

According to Panov (1976), the collision efficiency may be considered equal to 1 for water droplet diameters much larger than 1 mm (Stallabrass, 1980; Zakrzewski, 1987). Also, Finstad et al. (1988) and Horjen (2013) expressed that the amount of collision efficiency is equal to 1 when the Stokes number is more than approximately 1,000. When the Stokes number is less than 1,000, the amount of collision efficiency must be calculated.

2.1.4 Spray Duration

According to Zakrzewski (1987), the duration of direct splashing of an object located on an MFV during a single seawater spray event is obtained by:

$$\Delta t = \tau_s - \tau_f \quad (2.47)$$

where τ_s is the total duration of the seawater spray cloud habitation on top of the vessel and τ_f is the time of seawater spray flight to the surface of the object, which is obtained approximately by the following formula (Zakrzewski, 1987):

$$\tau_f = \frac{x}{\sqrt{U_{10}^2 + v_s^2 - 2U_{10} \cdot v_s \cos(\pi - \alpha)}} \quad (2.48)$$

where x is the distance of spray movement downwind (relative to a moving ship) in the ambient air to a known object.

Zakrzewski (1987) reported that the amount of the mass flux of seawater spray on an object located on a marine platform per unit area for wave spray during a single spraying event is given by:

$$\dot{M}_{w,wave} = E U_{rs} \omega(z)_{wave} \Delta t \quad (2.49)$$

The total amount of ice accretion on marine platforms depends on the frequency of splashing (Efimov, 2012; Panov, 1971). The splashing frequency is a function of the relative wave period, namely, the encounter frequency between waves and the marine platform hull. The frequency of spraying can be expressed by the following experimental correlation (Efimov, 2012; Panov, 1976; Zakrzewski, 1987):

$$m = 15.78 - 18.04 \exp\left(-\frac{4026}{\tau_k}\right) \quad (2.50)$$

where τ_k is the wave encounter period. According to Borisenkov and Panov (1972), the frequency of spraying depends on wave height, speed of wave diffusion, and heading angle. The wave encounter period, τ_k , can be calculated by the time between two wave crests or with the following formula (Zakrzewski, 1987).

$$\tau_k = \frac{\lambda}{1.25 \sqrt{\lambda} - v_s \cos(\pi - \alpha)} \quad (2.51)$$

Here, λ is the wave length. By using linear theory, the wavelength of significant surface waves is given by:

$$\lambda = \frac{g \tau_w^2}{2\pi} \quad (2.52)$$

where τ_w is the significant wave period (see Eq. (2.26)). The equation above is valid for deep water waves (depth > wavelength/2).

2.2 Mass Balance

In order to compute the ice layer thickness and water film thickness, a mass balance is applied. After generating wave spray and wind spray, the sea spray mass flux is transferred using the relative wind velocity and impact components located on the marine vessels and structures (Dehghani-Sani et al., 2015, 2016). Figures 2.4 and 2.5 show the mechanism of the ice accumulation process on vertical and horizontal components. According to these figures, the seawater droplets hit the surface of a cold body and cool further to freezing. The segment that does actually freeze on collision is called the freezing fraction, n , and the remaining fraction ($1-n$) is brine film. It should be noted that

the freezing fraction is between 0 and 1. For horizontal components the brine film remains on the ice accretion layer but for vertical and inclined components, there is a runoff at the bottom of the brine film.

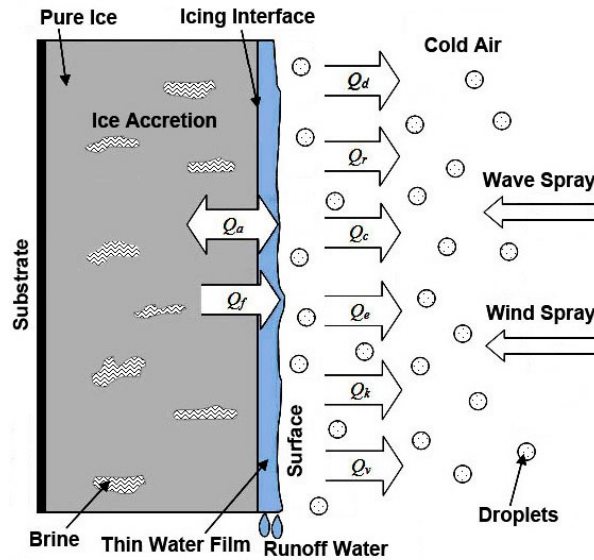


Fig. 2.4: Schematic of sea spray icing and heat balance for vertical components on marine platforms (Dehghani-Sanij et al., 2015)

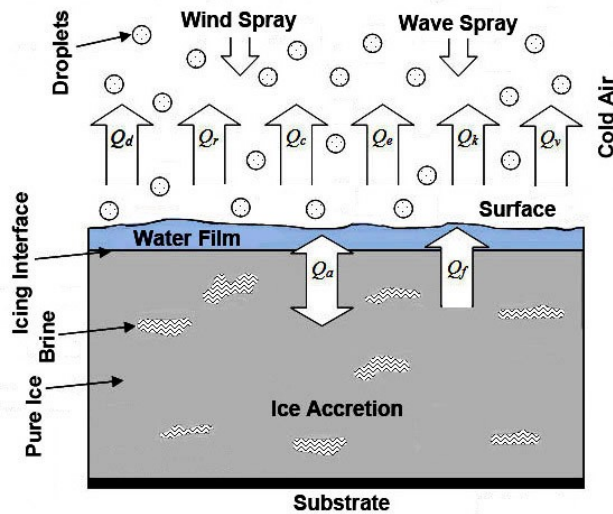


Fig. 2.5: Schematic of sea spray icing and heat balance for horizontal components on marine platforms (Dehghani-Sanij et al., 2016)

By employing a mass balance for vertical and horizontal components, the equations below can be obtained (Dehghani-Sanij et al., 2015, 2016).

$$\dot{M}_{w,t} = \dot{M}_{ice} + \dot{M}_{runoff,w} + \dot{M}_{evap.,w} \quad (\text{Vertical components}) \quad (2.53)$$

$$\dot{M}_{w,t} = \dot{M}_{ice} + \dot{M}_{water} + \dot{M}_{evap.,w} \quad (\text{Horizontal components}) \quad (2.54)$$

Here, \dot{M}_{ice} is the mass flux of ice formation on the plate and $\dot{M}_{evap.,w}$ is the mass flux of evaporation. For vertical components $\dot{M}_{runoff,w}$ is the mass flux out (runoff), and for horizontal components \dot{M}_{water} is the mass flux of water on the ice accretion layer. Estimation of \dot{M}_{ice} can be determined by the following formula (Dehghani-Sanij et al., 2016):

$$\dot{M}_{ice} = n \dot{M}_{w,t} = \rho_i \frac{db}{dt} \quad (2.55)$$

where n is the freezing fraction, ρ_i is the density of ice accretion, including entrapped brine and air, and $\frac{db}{dt}$ is the time derivative of b , or ice layer thickness. The mass flux of evaporation, $\dot{M}_{evap.,w}$ is assumed to be negligible (Schröder Hansen, 2012; Myers et al., 2002; Myers and Charpin, 2004).

For horizontal components, the mass flux of water on the ice accretion layer, \dot{M}_{water} is written as follows (Dehghani-Sanij et al., 2016):

$$\dot{M}_{water} = (1 - n) \dot{M}_{w,t} = \rho_b \frac{d\eta}{dt} \quad (2.56)$$

where ρ_b is the density of brine and $\frac{d\eta}{dt}$ is the time derivative of η , or water film thickness.

For dry-growth icing (rime), n is equal to 1, and for wet-growth icing (glaze), n is less than 1. In addition, the ice thickness growth rate per hour is computed by (Kato, 2012):

$$N_i = 3.6 \times 10^6 \frac{\dot{M}_{ice}}{\rho_i} = 3.6 \times 10^6 \frac{n \dot{M}_{w,t}}{\rho_i} \quad (2.57)$$

where N_i is in units of $\frac{mm}{hr}$.

In the marine icing phenomenon, the salinity of seawater has an impact in the formation of ice accretion on marine vessels and offshore structures. However, according to model studies by Stallabrass (1980), the icing rate changes insignificantly when the spray salinity varies between 30‰ and 35‰. Some part of the water droplets will freeze after impinging on the object located on a marine platform, and the other part will remain to form a water film on the surface of the ice formation. Therefore, the value of salinity in seawater spray is important in specifying the growth rate of the icing phenomenon and thickness of the ice layer and water film. Jørgensen (1982) reported that icing begins at higher temperatures when salinity is lower (Ryerson and Gow, 2000a).

Makkonen (1987) and Horjen (1990) have investigated and developed models for the entrapment of salt in the accreted ice at an icing front. For a stationary icing model with no brine film movement the following two formulae were derived by Makkonen (1978):

$$S_b = \frac{I}{I - (1 - \beta)n} S_w \quad (2.58)$$

$$S_i = \frac{\beta}{I - (1 - \beta)n} S_w \quad (2.59)$$

where S_w is the salinity of the seawater spray and β is the interfacial distribution coefficient or the relative amount of entrapped brine in the ice accretion. Since the model of Horjen (1990) is fully time-dependent, Eq. (2.58) is not valid in his model. It may, however, be shown that using the same assumptions as in the model of Makkonen (1978) the differential equation of brine film salinity is reduced to Eq. (2.58) (with a small addition due to evaporative mass transport). In Eqs. (2.58) and (2.59), Makkonen (1987) considered the parameter of β equal to 0.26, Horjen (1990) reported β equal to 0.34, and Horjen (2013, 2015) assumed β equal to 1/3. Also, Makkonen (2010) theoretically determined a new value of 0.30 for ice. The temperature of the icing surface (the water film on the surface), T_s , is a function of the salinity of the water film, S_b . The temperature of the water film at the air-water interface can be calculated by (Makkonen, 1987):

$$T_s = -54.0 S_b - 600 S_b^3 \quad (2.60)$$

In the equation above, T_s is in units of °C. The salinity of the water film is always higher than the salinity of the water spray (Kulyakhtin and Tsarau, 2014).

2.3 Heat Balance

In order to forecast and estimate the growth rate of the icing phenomenon and ice accumulation as well as to compute the freezing fraction, the heat balance for the thermodynamic process is required. When water droplets affect the components located on marine vessels and offshore structures, they freeze due to various heat fluxes. According to Figs. 2.4 and 2.5, these heat fluxes are: (1) convection (losing energy), Q_c ; (2) evaporation (losing energy), Q_e ; (3) heat capacity of the impinging water droplets

(losing energy), Q_d ; (4) radiant heat flux (losing energy), Q_r ; (5) kinetic energy of incoming droplets (gaining energy), Q_k ; (6) viscous aerodynamic heating (gaining energy), Q_v ; (7) release of latent heat (gaining energy), Q_f , and (8) heat flux by conduction, Q_a . A number of researchers have surveyed the thermodynamics of the icing and thermal problem (Blackmore and Lozowski, 1994; Blackmore et al., 2002; Chung and Lozowski, 2010; Horjen, 1983b, 2013; Horjen and Vefsnmo, 1985; Jones, 1996; Kato, 2012; Kulyakhtin and Løset, 2011; Kulyakhtin and Tsarau, 2014; Lozowski and Gates, 1985; Lozowski et al., 1983; Lozowski et al., 2000; Makkonen, 1986, 2000; Myers and Hammond, 1999; Naterer, 2011; Szilder et al., 1988). In the following descriptions, the heat fluxes have been studied individually. Note that water flow has an effect on the heat balance (Myers and Hammond, 1999).

- *Convection Heat Flux*

Sensible heat flux between the freezing surface and the surrounding airflow or heat loss by convection is written as follows:

$$Q_c = h_c (T_s - T_a) \quad (2.61)$$

Here, T_s is the temperature of the water film at the air-water interface, T_a is the air temperature, and h_c is the heat transfer coefficient. The heat transfer coefficient is determined by body geometry, length, Reynolds number, and Prandtl number. The heat transfer coefficient is given by:

$$h_c = \frac{Nu k_a}{L} \quad (2.62)$$

where k_a is the thermal conductivity of air, L is the characteristic length of the component, which is the diameter for cylindrical components and the maximum dimension along the

direction of the relative wind velocity for planar components (Lozowski et al., 2000), and Nu is the Nusselt number that according to Lozowski et al. (2000), is equal to:

$$Nu = \begin{cases} 0.036 Pr^{0.33} Re^{0.80} & (\text{planar components}) \\ 3.0 Re^{0.50} & (\text{cylindrical components}) \end{cases} \quad (2.63)$$

Here, Pr is the Prandtl number for the airflow and Re is the Reynolds number of the component, which is as follows:

$$Re = \frac{U_{rs} L}{\nu_a} \quad (2.64)$$

where ν_a is the air kinematic viscosity. According to Rohsenow and Choi (1961), for a flat plate (or for planar components), in a turbulent flow parallel to the surface, an average heat transfer coefficient over a length L can be given by the following formula:

$$h_c = 0.037 \frac{k_a}{L} Pr^{0.33} Re^{0.8} \quad (2.65)$$

To calculate the Nusselt number or the convective heat transfer coefficient, some researchers suggested several formulae (Achenbach, 1977; Jones, 1996; Livingood and Hrycak, 1973; Lozowski et al., 1983; Makkonen, 1985).

- *Evaporation Heat Flux*

Evaporative heat loss to the surrounding airflow is obtained by (Bergman et al., 2011):

$$Q_e = h_c \left(\frac{Pr}{Sc} \right)^{0.63} \frac{\varepsilon l_v}{P c_a} (e_s(T) - RH \cdot e_s(T_a)) = C (e_s(T) - RH \cdot e_s(T_a)) \quad (2.66)$$

Here, Sc is the Schmidt Number, ε is the ratio of molecular weights of water vapour and dry air, P is the atmospheric air pressure, l_v is latent heat of vaporization for water at the surface temperature, c_a is the specific heat capacity of dry air at constant pressure, RH is

the relative humidity of the air, and $e_s(T)$ is the saturated water pressure, which has been linearized by (Myers, 2001):

$$e_s(T) \approx E_0 + e_0 T \quad (2.67)$$

where $e_0 = 27.03$ Pa/K and $E_0 = -6803$ Pa. The relationship above is accurate to within 8% over the range between 257 and 73.15 K (Myers, 2001). It should be noted that the salinity has an impact on evaporation although it is generally negligible.

- *Heat Loss Due to Incoming Water Droplets*

The heat flux of the impinging water droplets to the equilibrium surface temperature is defined as (Kulyakhtin and Tsarau, 2014):

$$Q_d = \dot{M}_{w,wave} c_w (T_s - T_{d,wave}) + \dot{M}_{w,wind} c_w (T_s - T_{d,wind}) \quad (2.68)$$

where c_w is the specific heat capacity of the water, $T_{d,wave}$ and $T_{d,wind}$ are the droplet temperatures of the wave spray and the wind spray immediately prior to impingement, respectively. The droplet diameters in the wind spray are usually small, measuring less than 100 μm (Kulyakhtin and Tsarau, 2014). Therefore, the temperature of the droplets will generally reach the air temperature in less than 0.1 s (Andreas, 1990). Furthermore, the temperature of the droplets in the wave spray is between the air temperature and the seawater temperature, because the droplet diameters are mostly larger (1-2 mm) (Kulyakhtin and Tsarau, 2014).

Zarling (1980) modeled and analyzed a single water droplet by ignoring the temperature gradients in the droplet. The author considered convection, evaporation, and radiation heat transfer between the air and the droplet surface, and assumed that the heat and mass transfer coefficients and the fluid physical properties were constant. Figure 2.6

shows the surface temperature variations for different droplet diameters. The initial temperature of the droplets was 0°C, and the temperature of the ambient air was -18°C. In addition, the sizes of droplets were from 0.5 mm to 6.5 mm.

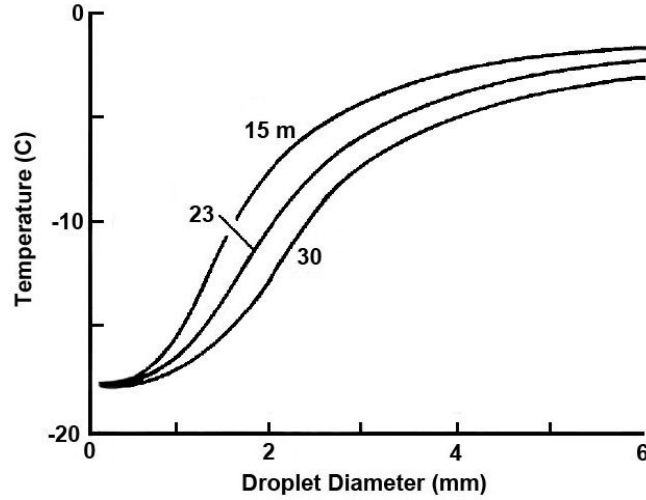


Fig. 2.6: Variations of surface temperature versus the droplet diameter at different heights (Zarling, 1980)

Thus, Eq. (2.79) can be written approximately as follows:

$$Q_d = \dot{M}_{w,t} c_w (T_s - T_d) \quad (2.69)$$

According to Stallabrass (1980), the temperature of water droplets can be calculated through an iterative procedure. For this purpose, the first droplet temperature, T_d , is set as the same as the seawater temperature, T_w , and then the factor allowing for evaporation becomes:

$$X_t = 1 + 0.622 \frac{l_v}{P c_a} \frac{e_a - e_w}{T_a - T_w} \quad (2.70)$$

A new value of T_d can be derived by (Kato, 2012; Stallabrass, 1980):

$$T_d = T_a + (T_w - T_a) \exp \left[- \frac{6 Nu k_a}{\rho_w c_w D^2} X_t \tau \right] \quad (2.71)$$

where Nu is the droplet Nusselt number, τ is the droplet flight time and D is the droplet diameter. This procedure was repeated until the successive value of the T_d differed by less than an arbitrary amount.

- *Radiant Heat Flux*

Heat transfer by radiation exchange can be divided into long-wave and short-wave. Heat loss because of long-wave radiation is obtained by the following formula (Chung and Lozowski, 2010; Lozowski et al., 2000):

$$Q_r = \sigma (\varepsilon_s T_s^4 - \varepsilon_a T_a^4) = \sigma a (T_s - T_a) \quad (2.72)$$

where σ is the Stefan-Boltzmann constant, ε_a and ε_s are the emissivity of airflow and the icing surface, respectively, and also a is a linearization constant and approximates linearly the black body radiation heat exchange between the icing surface and the airflow. The emissivity of both are considered to be 1 (emissivity of ice is 0.98 and of water is 0.96 (Incropera and DeWitt, 1985)). According to Kulyakhtin and Tsarau (2014) and Kulyakhtin et al. (2013), the long wave radiation is less than 9% of convection heat flux, Q_c , under typical weather conditions. Often researchers like Kulyakhtin and Tsarau (2014) neglected the effect of the short wave radiation, but some researchers like Jones (1996) have considered the effect, for example of freezing rain.

According to Jones (1996), the radiation fluxes of long-wave and short-wave are opposite in sign and analogous in magnitude; however, there is no radiation flux of short-wave at night, when the air temperature is comparatively cold and the radiation flux of

long-wave comparatively large. Both are small in magnitude compared to the convection and evaporation heat fluxes, but large in magnitude compared to the kinetic energy of incoming droplets and viscous aerodynamic dissipation.

- *Kinetic Energy of Incoming Droplets*

The heat flux due to the conversion of water droplets' kinetic energy into heat is calculated approximately by (Lozowski et al., 1983):

$$Q_k = \frac{I}{2} \dot{M}_{w,t} U_{rs}^2 \quad (2.73)$$

where U_{rs} is the spray/wind velocity relative to the object. In Eq. (2.73), it is assumed that the water droplets are impacting at the velocity of ambient air, after which all of their kinetic energy is dissipated to heat. Since this flux is usually small, the error for this assumption is approximately negligible (Lozowski et al., 1983).

- *Aerodynamic Heating*

The heat flux due to viscous aerodynamic heating is specified by (Lozowski et al., 1983):

$$Q_v = \frac{h_c r_c U_{rs}^2}{2 c_a} \quad (2.74)$$

where r_c is the local recovery factor along the cylinder surface, expressed by (Lozowski et al., 1983; Seban, 1960):

$$r_c = 0.75 + 0.25 \cos 2\theta \quad (2.75)$$

Here, θ is the collision angle. For a cylinder, the local recovery factor is equal to 0.79 (Makkonen, 2000). This flux describes the adiabatic heating because of the air

compressibility at higher speeds and viscous heating inside the boundary layer (Bottyan, 2011; Lozowski et al., 1983).

- *Latent Heat Flux*

The latent heat flux, because of freezing of a certain fraction of the impinging water, is estimated by (Horjen, 1990):

$$Q_f = l_f (1 - \beta) \dot{M}_{ice} = l_f \rho_i (1 - \beta) \frac{db}{dt} \quad (2.76)$$

where l_f is the latent heat of fusion of pure ice and $l_f (1 - \beta)$ is the latent heat of fusion of the saline ice accumulation (Makkonen, 1987). The parameter of β is the interfacial distribution coefficient, and can be defined as follows:

$$\beta = \frac{S_i}{S_b} \quad (2.77)$$

where S_i is salinity of ice accretion and S_b is the salinity of brine. Note that β is also the ratio of the mass of brine occluded in the ice and total ice mass near the icing surface.

- *Conduction Heat Flux*

The heat flux by conduction to or from the icing surface through the underlying structure in the water film and the ice layer, respectively, are determined per unit area by the following formulas (Myers, 2001; Brakel et al., 2007; Myers and Hammond, 1999).

$$Q_{a,b} = -k_b \nabla T_b \quad (2.78)$$

$$Q_{a,i} = -k_i \nabla T_i \quad (2.79)$$

where k_b is the thermal conductivity of brine, k_i is the thermal conductivity of the ice formation, T_b is the temperature in the water film, and T_i is the temperature in the ice

layer. Kulyakhtin (2014) and Kulyakhtin et al. (2016) reported that neglecting the heat conduction within the ice accretion layer is reasonable for only two different cases: “marine icing produced by continuous seawater spray” and “freshwater icing”, but for periodic seawater spray it is not acceptable. In addition, current marine icing models like ICEMOD, RIGICE04, and MARICE do not consider the effect of the heat conduction inside the ice layer (Kulyakhtin, 2014).

It should be noted that normally, Q_v is considerable at the high speeds characteristic of aircraft flight and the Q_k is generally small (Lozowski et al., 1983). Thus, they are often neglected. By using the heat balance at the air-water interface and at the ice-water interface, the freezing fraction, n , can be calculated. The freezing fraction is between 0 and 1. When n is equal to 1, all water droplets will freeze when they impinge on the object.

2.4 Icing Models

2.4.1 Simplified Icing Models

The icing intensity is evaluated through the rate of growth of ice on a marine vessel or structure during one hour. Simplified models are based on visual measurements or weather severity factors (Efimov, 2012). The main environmental factors that affect sea spray icing are: wind velocity, U , air temperature, T_a , and seawater temperature, T_w . Thus, the weather severity factor is defined by the following formula (Efimov, 2012; Young et al., 2011):

$$S = U(T_a + T_w) \quad (2.80)$$

Borisenkov and Panov (1972) and Panov (1976) obtained a formula to calculate the icing intensity, which is written as follows (Lundqvist and Udin, 1977):

$$I = \chi \frac{(T_i - T_d) + 2.6 \left(\frac{l_v}{P} \right) (e_{T_a} - e_{T_i})}{l_i + c_i (T_a - T_i) + c_w (T_i - T_d)} \quad (2.81)$$

Here, χ is the heat transfer coefficient that is a function of the wind velocity and the shape of the surface exposed to the icing, T_i is the temperature of ice accretion, T_d is the temperature of water droplets in the atmospheric cloud or in the sea spray that is a function of the temperature of air and water, as well as the flight time and size of droplets, P is the standard atmospheric pressure at the water surface, l_v is the latent heat of vaporization, e_{T_a} is the saturated vapour pressure for air temperature, e_{T_i} is the saturated vapour pressure for temperature of ice accretion, l_i is the latent heat of ice accretion, c_i and c_w are the specific heat capacity of ice and water, respectively, and T_a is the temperature of air. Eq. (2.81) predicts the icing intensity for an area of 1 cm² perpendicular to the spray. The equation was derived using a heat balance on the surface exposed to the icing and it can be employed for sea spray and atmospheric icing (Efimov, 2012).

To predict sea spray icing on marine vessels and structures, the following formula has been suggested by Overland et al. (1986) and Overland (1990):

$$PPR = \frac{U (T_{f,w} - T_a)}{1 + \varphi (T_w - T_{f,w})} \quad (2.82)$$

Here, U is the wind velocity, $T_{f,w}$ is the freezing point of seawater (generally -1.7°C or -1.8°C (Guest, 2005)), T_a is the air temperature, T_w is the seawater-surface temperature,

and ϕ is the experimental constant (0.4 according to Overland et al. (1986) and 0.3 by Overland (1990)). According to Makkonen et al. (1991), Eq. (2.82) is based on an incorrect heat balance. Assuming a constant value for ϕ is not correct. Table 2.4 illustrates the predicted icing classes and rates for ships of 20 to 75 m in length, which are moving into the wind.

Table 2.4: Icing class and rate (Cammaert, 2013)

PPR	< 0	0-22.4	22.4-53.3	53.3-83.0	> 83.0
Icing Class	None	Light	Moderate	Heavy	Extreme
Icing Rates (cm/hour)	0	< 0.7	0.7-2.0	2.0-4.0	> 4.0
(inches/hour)	0	< 0.3	0.3-0.8	0.8-1.6	> 1.6

The icing rates in Table 2.5 are a simplified guide. Real icing rates are a function of vessel characteristics, cold soaking, and exposure to sea spray (Guest, 2005). In another classification, the forecast and assessment of icing rates by several researchers are shown in Table 2.5. These models have the following assumptions (Cammaert, 2013):

- (1) no change in the geometry of ship;
- (2) no changes of properties of sea spray;
- (3) assumption of steady state, and
- (4) thermally limited scenarios.

Table 2.5: Forecast of icing rates in past studies (Cammaert, 2013)

	Light	Moderate	Heavy or Severe	Very Severe, extreme, very heavy	Extreme
Overland et al. (1986)	< 0.7	0.7-2.0	> 2.0		-
Overland (1990)	< 0.7	0.7-2.0	2.0-4.0	> 4.0	-
Lundqvist and Udin (1977)	0.04-0.17	0.25-0.75	> 1.0	-	-
Sawada (1968)	< 0.5	0.5-2.0	> 2.0	-	-
Kachurin et al. (1974)	-	-	1.8	4.2	-
Mertins (1968)	0.04-0.125	0.17-0.25	0.29-0.58	> 0.625	-
Wise and Comiskey (1980)	0.09-0.21	0.21-0.42	0.42-0.63	0.63-1.06	> 1.06

2.4.2 Advanced Icing Models

In order to predict and analyze marine icing on a structure due to a time-variable spray mass flux, a set of differential equations must be solved based on the conservation of mass, heat and salt for the water film are as follows (Horjen, 1990, 2013):

$$\frac{\partial X}{\partial t} + \nabla_t \cdot (V_b X) = \dot{M}_{w,t} - \dot{M}_{ice} + \dot{M}_{evap,w} \quad (2.83)$$

$$c_b X \left(\frac{\partial}{\partial t} + V_b \cdot \nabla_t \right) T_b = Q + (1 - \beta) l_f \dot{M}_{ice} \quad (2.84)$$

$$\frac{X}{S_b} \left(\frac{\partial}{\partial t} + V_b \cdot \nabla_t \right) S_b = \dot{M}_{ice} (1 - \beta) - \dot{M}_{w,t} \left(1 - \frac{S_w}{S_b} \right) + \dot{M}_{evap,w} \quad (2.85)$$

where $X \equiv \rho_b \eta$ is the local brine mass per unit area, Q is the total heat flux to the water film (which can be calculated by heat balance at the air-water interface and at the ice-water interface), c_b is the specific heat capacity of brine (at constant pressure), T_b is the brine temperature, V_b is the brine velocity, and ∇_t is the differential operator in the tangential direction (i.e., along the direction that the brine moves in).

To estimate the brine temperature, T_b , the following approximate relations may be used (Assur, 1968):

$$T_b = -\frac{a S_b}{1 - 10^{-3} S_b}, \quad S_b < 125\text{‰} \quad (2.86)$$

$$T_b = -\frac{b S_b}{1 - 10^{-3} S_b} + c, \quad 125\text{‰} \leq S_b < 230\text{‰} \quad (2.87)$$

Here, $a = 5.4113 \times 10^{-2} \text{ }^\circ\text{C}$, $b = 9.7007 \times 10^{-2} \text{ }^\circ\text{C}$ and $c = 6.0533 \text{ }^\circ\text{C}$.

From Eqs. (2.83) and (2.85), the two-dimensional differential equations for the conservation of mass and salt of the water film may be written as follows (Horjen, 2013):

$$\frac{\partial X}{\partial t} + \frac{\partial}{\partial s}(U_b X) + \frac{\partial}{\partial \zeta}(W_b X) = \dot{M}_{w,t} - \dot{M}_{ice} + \dot{M}_{evap,w} \quad (2.88)$$

$$\frac{\partial Y}{\partial t} + \frac{\partial}{\partial s}(U_b Y) + \frac{\partial}{\partial \zeta}(W_b Y) = \dot{M}_{w,t} S_w - \beta \dot{M}_{ice} \frac{Y}{X} \quad (2.89)$$

where

$$X = \rho_b \eta, \quad Y = \rho_b \eta S_b \quad (2.90)$$

The parameters of s and ζ are the icing surface curvilinear coordinates. For an inclined cylinder, the s -axis is along the cylinder perimeter (including ice accumulation) and the ζ -axis is upwards and parallel to the cylinder axis (Horjen, 2013). In Eqs. (2.88) and (2.89), U_b and W_b are the velocity of water film in the s -direction and ζ -direction, respectively. The icing intensity is obtained from Eqs. (2.84) and (2.85) using the equilibrium sea-ice phase condition (Eqs. (2.86) or (2.87)) (Horjen, 1990):

$$\dot{M}_{ice} = \frac{\left(1 - \frac{S_w}{S_b}\right) \dot{M}_{w,t} + \dot{M}_{evap,w} - \frac{F(S_b)}{l_f} Q}{(1 - \beta)(1 + F(S_b))} \quad (2.91)$$

where

$$F(S_b) = K_0 \frac{(1 - 10^{-3} S_b)^2}{S_b} \quad (2.92)$$

$$K_0 = \frac{l_f}{(a c_b)} \approx 1.46 \times 10^3, \quad (S_b < 125) \quad (2.93)$$

$$K_0 = \frac{l_f}{(b c_b)} \approx 8.16 \times 10^2, \quad (125 \leq S_b < 230) \quad (2.94)$$

The brine film velocity, V_b , for flat and vertical geometries, can be determined by the following formula (Horjen, 1990, 2013):

$$V_b = -0.264 \frac{g}{\rho_b \mu_b} X^2 \quad (2.95)$$

where ρ_b is the brine density and μ_b is the dynamic viscosity of brine. The variations of brine density can be estimated approximately linearly with the salinity water film as follows (Horjen, 2013):

$$\rho_b = 1000 + 0.8 S_b \quad (2.96)$$

Kulyakhtin and Tsarau (2014) as well as Myers and Charpin (2004) expressed the following differential equation for the mass conservation of the water film as Eq. (2.94).

$$\rho_b \frac{\partial \eta}{\partial t} + \rho_b \nabla \cdot (V_b \eta) = \dot{M}_{w,t} - \rho_i \frac{\partial b}{\partial t} \quad (2.97)$$

Here, $\frac{d\eta}{dt}$ is the time derivative of η , $\frac{db}{dt}$ is the time derivative of b , and $\nabla \cdot ()$ is the divergence operator. In Eq. (2.97), the velocity of the water film is determined through the balance of the viscous forces resisting gravity (lubrication theory), which is equal to (Kulyakhtin and Tsarau 2014; Myers, 1998):

$$V_b = \left[-\frac{\eta^2}{3\nu_w} \left(\mathbf{g} \cdot \mathbf{s}_1 + \frac{\partial \eta}{\partial s_1} \mathbf{g} \cdot \mathbf{s}_3 \right), -\frac{\eta^2}{3\nu_w} \left(\mathbf{g} \cdot \mathbf{s}_2 + \frac{\partial \eta}{\partial s_2} \mathbf{g} \cdot \mathbf{s}_3 \right) \right] \quad (2.98)$$

where ν_w is the kinematic viscosity of water, s_1 and s_2 are the surface coordinates in the major directions and s_3 is the vector normal to the surface. They assumed that there was no wind shear stress on the water film. Also, they considered that gravity is the only major driving force in sea spray icing (Kulyakhtin and Tsarau 2014). As a result, the gravity reduces total mass of the ice on the structure, while the wind stress has an effective role in the ice distribution of the surface. Also, they omitted the effect of the air/water surface tension in Eq. (2.97) (Kulyakhtin and Tsarau 2014).

Kulyakhtin and Tsarau (2014) have presented a generalization of the differential equation of salt conservation (Eq. (2.89)) by considering the difference in salinity of wind-generated and impact-generated droplets at the moment of impact (assuming brine film density constant):

$$\rho_b \frac{\partial (\eta S_b)}{\partial t} + \rho_b \nabla_s \cdot (V_b \eta S_b) = (S_{w,wind} \dot{M}_{w,wind} + S_{w,wave} \dot{M}_{w,wave}) - \rho_i \frac{\partial b}{\partial t} (\beta S_b) \quad (2.99)$$

where $S_{w,wind}$ and $S_{w,wave}$ are the salinities of wind spray and wave spray, respectively. The salinity of wave spray, $S_{w,wave}$, is equal to the seawater salinity. According to Andreas (1990), a droplet diameter at formation is equal to twice the equilibrium diameter and also the salinity of each droplet is 8 times higher than the seawater salinity at a relative humidity of 80% (Andreas, 1990; Kulyakhtin and Tsarau, 2014).

Chapter 3

Droplet Trajectory and Thermal Analysis of Impinging Saline Spray Flow on Marine Platforms¹

The modeling and analysis of the trajectory and cooling process of droplets is important for many engineering applications. For instance, to predict and estimate the amount of ice accumulation on marine vessels and offshore structures, the thermal behavior and pathway of water droplets need to be determined. Figure 3.1 illustrates the formation of sea spray from waves and wind, and the movement of a spray cloud on a marine vessel.

3.1 Droplet Trajectory Formulation

To study the thermal behaviour and predict the trajectory and cooling process of the water droplets, the velocity of droplets must be computed for the time period of their flight over marine platforms. Dehghani et al. (2016b) found that the water droplets with different sizes and velocities, which are generated by wave-impact sea spray, will have

1. This chapter is based on two papers. One of them was presented at the International Conference of Ocean, Offshore and Arctic Engineering in Trondheim, Norway in 2017 and another was published in Ocean Engineering (journal).

various trajectories and attain various positions on marine vessels. However, the geometry of the vessel and the position of different objects on the deck are important.

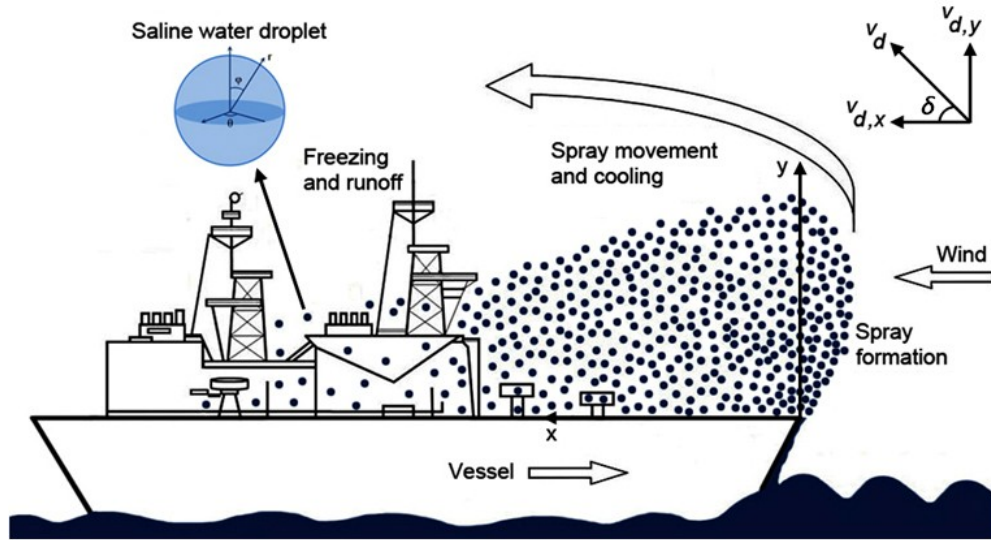


Fig. 3.1: Schematic representation of sea spray on a marine vessel

Several factors such as drag force, droplet size, wind velocity, gravity, and the initial droplet velocity have a significant role in the droplet's path (Dehghani et al., 2016b; Dehghani-Sanij et al., 2017d). By considering the air drag and gravity forces, the motion of the droplet is governed by (Lozowski et al., 2000):

$$\frac{d\vec{v}_d}{dt} = -\frac{3}{4} \frac{C_d}{D} \frac{\rho_a}{\rho_d} |\vec{v}_d - \vec{U}| (\vec{v}_d - \vec{U}) - \vec{g} \left(\frac{\rho_a}{\rho_d} - 1 \right) \quad (3.1)$$

where v_d is the droplet velocity with regard to the ground, t is the time, C_d is the droplet's drag coefficient, D is the droplet's diameter, ρ_a is the density of the air, ρ_d is the density of the droplet (assumed to be equal to the density of seawater), g is the gravitational

acceleration, and U is the wind velocity. The droplet's drag coefficient can be calculated by (Clift et al., 1978):

$$C_d = \begin{cases} \frac{24.0}{Re} , & Re \leq 1 \\ \frac{24.0}{Re} (1 + 0.15 Re^{0.687}) , & 1 < Re \leq 1000 \\ 0.44 , & Re > 1000 \end{cases} \quad (3.2)$$

Here, Re is the droplet's Reynolds number. The parameter of Re can be defined by:

$$Re = \frac{D u_{eff}}{\nu_a} , \quad u_{eff} = |\vec{v}_d - \vec{U}| \quad (3.3)$$

where u_{eff} is the effective velocity and ν_a is the kinematic viscosity of the air. Dehghani et al. (2016a, 2016b) determined the initial velocity of water droplets with various sizes after the droplet breakup stage at the front edge of the MFV. They reported that the initial velocities for the water droplets with a diameter close to zero and a diameter of 7 mm are 60 m/s and 0, respectively. There is approximately a linear inverse relationship between these droplet diameters and initial velocities. By combining Eqs. (3.1)-(3.3) and solving these equations using a numerical time stepping method, the droplet velocity with regard to the ground can be estimated.

To specify the position of the pathway of water droplets during flight over marine platforms, the following equations can be used.

$$\frac{d^2x}{dt^2} = -\frac{3}{4} \frac{C_d}{D} \frac{\rho_a}{\rho_d} \left(\frac{dx}{dt} - U_{rw} \right) \sqrt{\left(\frac{dx}{dt} - U_{rw} \right)^2 + \left(\frac{dy}{dt} \right)^2} \quad (3.4)$$

$$\frac{d^2y}{dt^2} = g \left(\frac{\rho_a}{\rho_d} - 1 \right) - \frac{3}{4} \frac{C_d}{D} \frac{\rho_a}{\rho_d} \left(\frac{dy}{dt} \right) \sqrt{\left(\frac{dx}{dt} - U_{rw} \right)^2 + \left(\frac{dy}{dt} \right)^2} \quad (3.5)$$

Here, x and y are the components of the positions of droplets with regard to the vessel and U_{rw} is the relative velocity of wind to the vessel. In this study, evaporation heat transfer in the cooling process of the droplets is considered, but the influence of evaporation on the droplet mass is neglected. The mass of evaporated water from the droplets is insignificant compared to the original mass of the droplets. To solve Eqs. (3.4) and (3.5), the initial conditions are given as follows:

$$x(t=0)=0 \quad (3.6)$$

$$\left. \frac{dx}{dt} \right|_{t=0} = v_{d0,x} = v_{d0} \cos \delta \quad (3.7)$$

$$y(t=0)=0 \quad (3.8)$$

$$\left. \frac{dy}{dt} \right|_{t=0} = v_{d0,y} = v_{d0} \sin \delta \quad (3.9)$$

where v_{d0} is the initial droplet velocity and δ is the initial travel angle of the water droplets.

3.2 Heat Transfer Formulation

The water droplet is cooled and supercooled due to convection, evaporation, and radiation heat transfer to the airstream. The heat loss by convection to the ambient air can be found by (Lozowski et al., 2000):

$$Q_c = h_c (T_d - T_a) \quad (3.10)$$

$$h_c = \frac{Nu k_a}{D} \quad (3.11)$$

$$Nu = 2.0 + 0.6 Pr^{0.33} Re^{0.5} \quad (3.12)$$

Here, h_c is the convection heat transfer coefficient of the water droplet, T_d is the droplet temperature, T_a is the air temperature, k_a is the thermal conductivity of the air, Nu is the droplet's Nusselt number, and Pr is the Prandtl number of the airflow. The parameter of Pr can be computed by (Bergman et al., 2011):

$$Pr = \frac{\mu_a}{\rho_a \alpha_a} \quad (3.13)$$

where α_a is the air thermal diffusivity, and μ_a is the air dynamic viscosity that is defined by (Tracy et al., 1980):

$$\mu_a = \mu_o \left[\frac{T_o + 120}{T + 120} \left(\frac{T}{T_o} \right)^{1.5} \right] \quad (3.14)$$

Here, $\mu_o = 1.8325 \times 10^{-5}$ Pa.s, $T_o = 296.16$ K and $T = (T_a + 273.15)$ K. In addition, the parameter of ρ_a can be given by (Tracy et al., 1980):

$$\rho_a = \frac{P}{287.04(T_a + 273.15)} \quad (3.15)$$

where P is the atmospheric air pressure and the air temperature, T_a , in units of °C.

The heat loss by evaporation with the ambient air can be obtained by (Bergman et al., 2011):

$$Q_e = h_c \left(\frac{Pr}{Sc} \right)^{0.63} \frac{\epsilon l_v}{P c_a} (e_s(T) - RH \cdot e_s(T_a)) = C (e_s(T) - RH \cdot e_s(T_a)) \quad (3.16)$$

Here, Sc is the droplet's Schmidt number, ϵ is the ratio of the molecular weight of water vapour and dry air, l_v is latent heat of vaporization of water, c_a is the specific heat capacity of dry air at a constant pressure, RH is the relative humidity of the air, and $e_s(T)$ is the

saturated vapour pressure that is linearized by Eq. (2.67). The droplet's Schmidt number is given by (Bergman et al., 2011):

$$Sc = \frac{\mu_a}{\rho_a D_{ab}} \quad (3.17)$$

Here, D_{ab} is the air-water vapour diffusivity.

The heat loss by long-wave radiation can be calculated by:

$$Q_r = \varepsilon \sigma (T_d^4 - T_a^4) \quad (3.18)$$

where ε is the droplet emissivity and σ is the Stefan-Boltzmann constant. For simplification of the above equation, the radiation heat transfer coefficient of the droplet, h_r , can be used. Thus:

$$h_r = \varepsilon \sigma (T_d^2 + T_a^2) (T_d + T_a) \quad (3.19)$$

According to a report by Zarling (1980), when the temperature differences are small, the radiation heat transfer coefficient can be approximated as a constant, or by using the following expression:

$$h_r = \varepsilon \sigma (T_{0,w}^2 + T_a^2) (T_{0,w} + T_a) \quad (3.20)$$

Here, $T_{0,w}$ is the initial temperature of the water droplet. Hence, Eq. (3.18) can be written as follows:

$$Q_r = h_r (T_d - T_a) \quad (3.21)$$

Several assumptions will be used in order to simplify and solve the problem. First, the water droplet has a spherical shape during the entire trajectory. This is a reasonable approximation for small droplet diameters (Gao et al., 2000). McDonald (1954) reported that droplets with small sizes (1 mm in diameter and less) have a spherical shape in flight.

Also, the shape of large droplets is mostly controlled via “surface tension, hydrostatic pressure, and external aerodynamic pressure”. Second, the initial temperature of the water droplet equals the temperature of the water’s surface. Third, the temperature within the droplet is uniform. Fourth, the wind velocity is uniform and in the horizontal direction.

3.3 Cooling Process

Hindmarsh et al. (2003) reported that by assuming the uniform temperature within the droplet the obtained results illustrate a good agreement with the empirical results. Yao and Schrock (1976) investigated the cooling of free falling droplets. They considered both the temperature gradient and uniform temperature inside the droplet. The results showed that considering conduction heat transfer in the model leads to longer cooling times relative to a uniform temperature. Furthermore, the average difference between the obtained results was 11%. Therefore, neglecting the temperature gradient within the water droplet is a reasonable assumption. The droplet’s Biot number can confirm the accuracy of this assumption.

The governing equation for the cooling process of droplets by considering convection, evaporation, and radiation heat loss from the droplet’s surface to the ambient air is given by:

$$\rho_b c_b \frac{d(V_d T_d)}{dt} = - A_s (Q_c + Q_e + Q_r) \quad (3.22)$$

where ρ_b is the density of brine, c_b is the specific heat capacity of brine, V_d is the droplet volume, and A_s is the surface area of the droplet. The parameters of V_d and A_s , respectively, are:

$$V_d = \frac{4}{3} \pi r_d^3 \quad (3.23)$$

and

$$A_s = 4 \pi r_d^2 \quad (3.24)$$

Here, r_d is the droplet radius. The brine density, ρ_b , can be calculated by Eq. (2.96).

Kuwahara (1938) obtained an experimental correlation to estimate the specific heat capacity of seawater at 0°C and atmospheric pressure that is equal to:

$$c_b = 1.005 - 0.004136 S_b + 0.0001098 S_b^2 - 0.000001324 S_b^3 \quad (3.25)$$

Here, the parameter of c_b is in units of Cal/gr°C. Based on a study conducted by Assur (1958), Forest et al. (2005) found a more accurate formula between the droplet salinity, S_b , and the freezing temperature, T_f , for three temperature regions. For the first region is:

$$T_f = -54.1126 \left(\frac{S_b}{1 - S_b} \right), \quad -7.7 \leq T_f \leq 0^\circ C \text{ and } 0 \leq S_b \leq 124.7\text{‰} \quad (3.26)$$

for the second region is:

$$T_f = \frac{0.063 - 1.063 S_b}{0.01031(1 - S_b)}, \quad -23 \leq T_f < -7.7^\circ C \text{ and } 124.7 < S_b \leq 230.8\text{‰} \quad (3.27)$$

and for the third region is:

$$S_b = \frac{3.3136 \times 10^{-4} T_f^2 + 0.01524 T_f + 0.4752}{3.3136 \times 10^{-4} T_f^2 + 0.01524 T_f + 1.4752}, \quad (3.28)$$

$$-36 \leq T_f < -23^\circ C \text{ and } 230.8 < S_b \leq 262.5\text{‰}$$

The parameter of S_b is a fraction when employed in the above formulae.

The salinity of large water droplets, which is generated by the wave spray, is only somewhat greater compared to the seawater salinity owing to evaporation (Horjen, 1990,

2013). However, for very small water droplets created by wind spray as well as for long distance flight, the droplet salinity is higher than the seawater surface salinity (Horjen, 1990, 2013; Kulyakhtin and Tsarau, 2014). In this study, it is considered that the droplet salinity, S_b , equals the seawater salinity, S_w , when the droplet diameter is equal to or greater than 0.5 mm.

The volume of a droplet will decrease because of evaporation, so the changes in the droplet's radius, r_d , can be obtained by (Sadafi et al., 2014, 2015; Mezhericher et al., 2008):

$$(4\pi r_d^2) \frac{dr_d}{dt} = -\frac{\dot{m}_v}{\rho_b} \quad (3.29)$$

where \dot{m}_v is the evaporation rate from the droplet's surface to the ambient air and can be defined by (Horjen, 2013):

$$\dot{m}_v = \frac{Q_e}{l_v} A_s \quad (3.30)$$

By substituting Eqs. (3.23), (3.24) and (3.29) into Eq. (3.22), the equation below will be obtained:

$$\frac{dT_d}{dt} = \left[\frac{3\dot{m}_v}{4\pi\rho_b r_d^3} \right] T_d - \frac{3}{\rho_b c_b r_d} (Q_c + Q_e + Q_r) \quad (3.31)$$

By combining Eqs. (3.10), (3.16), (3.21), and (3.29)-(3.31), the temperature within the droplet can be determined during its flight over marine platforms.

To consider a uniform temperature across the droplet, the lumped capacitance approximation must hold. This approximation can be made when the following condition is satisfied (Bergman et al., 2011):

$$Bi = \frac{h \left(\frac{r_d}{3} \right)}{k_b} \leq 0.1 \quad (3.32)$$

where h is the heat transfer coefficient, Bi is the droplet's Biot number and k_b is the thermal conductivity of brine. The parameter of k_b can be calculated by (Lange and Forke, 1952; Pringle et al., 2007):

$$k_b = 0.523 + 0.013 T_b \quad (3.33)$$

Here, T_b is the brine temperature. It should be noted that the temperature variations, by assuming a uniform temperature within the droplet, are only a function of time.

3.4 Results and Discussion

Problem parameters and properties for case studies are shown in Table 3.1. In order to analyze the thermal behaviour and predict the cooling process of water droplets, a Matlab code (version R14) was employed to solve the governing equations. The theoretical results are obtained for an MFV with an overall length of 45 m, following Zakrzewski (1986) who reported that the overall length for MFVs is between 40 and 50 m. It is assumed that (a) the MFV goes directly into the waves and wind, so a spray cloud will form in front of the bow, and also (b) the sea spray is not dense, so water droplets do not affect each other; hence, the trajectory of the droplet can be employed for every droplet separately.

Table 3.1: Parameter and property values or correlations

Parameter	Value or correlation	Units	References
c_a	1005	J/kg.K	Eng. Toolbox, 2017; Tracy et al., 1980
D_{ab}	$2.227 \times 10^{-5} \left(\frac{T_a + 273}{273} \right)^{1.81}$	m ² /s	ASHRAE Handbook, 1977; Karlekar and Desmond, 1977
k_a	$0.024577 + 9.027 \times 10^{-5} T_a$	W/m°C	ASHRAE Handbook, 1977; Karlekar and Desmond, 1977
l_v	2.27×10^6	J/kg	Eng. Toolbox, 2017
P	10^5	Pa	
RH	80	%	
S_w	34	‰	
$T_{0,w}^*$	0	°C	
v_s	6.17	m/s	
α_a	$\frac{l}{(57736 - 585.78 T_a)}$	m/s ²	ASHRAE Handbook, 1977; Karlekar and Desmond, 1977
δ^{**}	110	°	Dehghani et al., 2016a
ε	0.95	-	Guglielmini and Pisoni, 2001; Lorenzini and Saro, 2013
ϵ	0.622	-	Kato, 2012; Makkonen, 1989
v_a	$\frac{l}{(80711.7 - 766.15 T_a)}$	m ² /s	Zarling, 1980
ρ_d	1027	kg/m ³	Eng. Toolbox, 2017
σ	5.67×10^{-8}	W/m ² K ⁴	

* The temperature of seawater surface is generally between -1.7 and 5°C (Environment and Climate Change, Met 101)

** See Cartesian coordinate system in Fig. 3.1

Figure 3.2 shows the changes of the droplet velocity (v_d) over time at a wind velocity of 15 m/s and different diameters throughout the droplet flight over the MFV. As illustrated in Fig. 3.2, the smaller droplets have greater initial velocities and the bigger droplets have lower initial velocities. Additionally, with increasing time, the droplet

velocity will decrease until attaining the lowest value. This point is the highest height of the droplet during its flight. Then, with increasing time, the droplet velocity will increase until it reaches the terminal velocity. From this figure, smaller droplets will reach the terminal velocity faster compared to bigger droplets. For example, the droplet with a diameter of 0.5 mm will reach the terminal velocity after approximately 0.5 s, whereas the water droplet with a diameter of 6 mm reaches the terminal velocity after around 5 s.

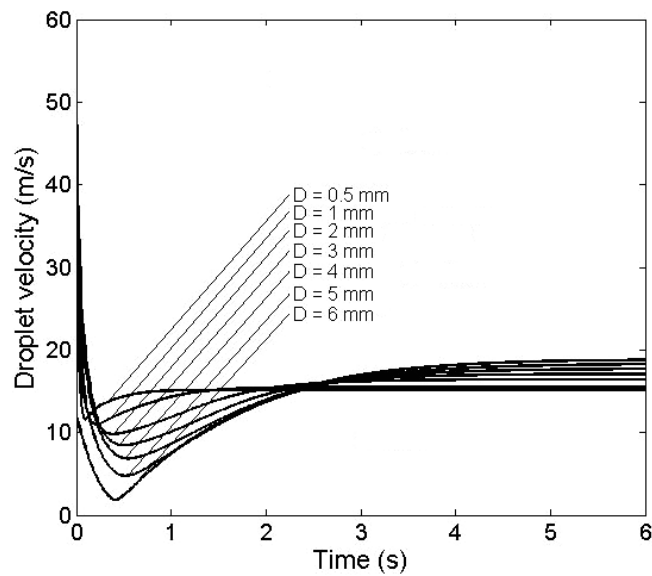


Fig. 3.2: Variations of droplet velocity versus time at $U = 15$ m/s and various droplet diameters

Figure 3.3 shows the trajectory and position of droplets during their flight over the MFV. As illustrated in Fig. 3.3, the droplets will depart in the same direction of the MFV for a very short time after formation in the front of the tip of the bow, and then turn back towards the deck. Table 3.2 indicates the maximum height of the droplets during flight (y_m), the horizontal distance from the tip of the bow up to the position of highest height

(x_m), time for the droplet to reach the maximum height (t_m), as well as the horizontal position (x_n) and time (t_n) of droplets with different sizes at the moment of impact on the deck. As a result from Fig. 3.3 and Table 3.2, the droplets with sizes approximately between 1 and 3 mm can attain the maximum positions at the moment of impact on the deck. Also, the maximum heights in the flight duration occur for droplets with diameters from 2 to 4 mm. The water droplets with larger sizes drop to the deck faster because of the higher gravity force. For instance, the maximum height and position at the moment of impact on the deck for the droplet with a diameter of 6 mm is 1.871 m and 10.258 m, respectively. According to Fig. 3.2 and Table 3.2, the droplet with a diameter of 6 mm will reach the terminal velocity after approximately 5 s, whereas the time at the moment of impact on the deck is equal to 1.121 s. This means that the larger droplets will fall on the deck before attaining their terminal velocity.

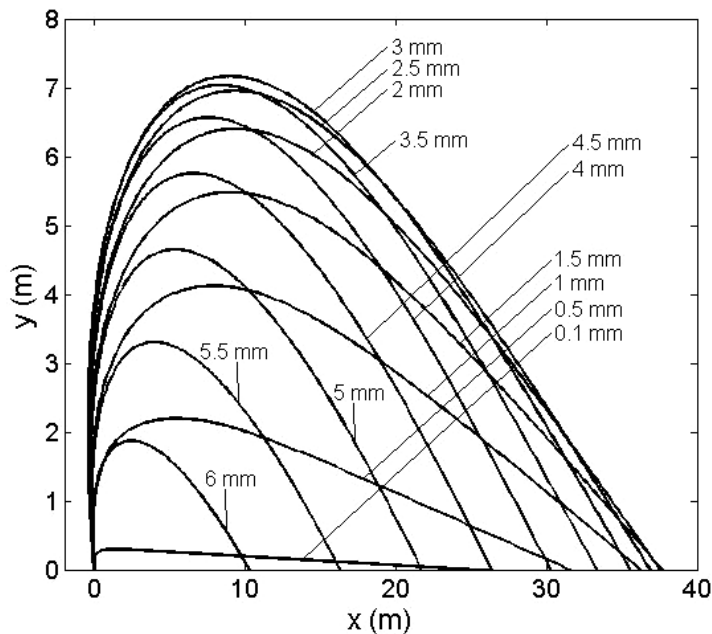


Fig. 3.3: Pathway of water droplets with various diameters during their flight over the MFV

Table 3.2: Positions and time of water droplets at the highest height and the moment of impact on the deck for various sizes

D (mm)	y_m (m)	x_m (m)	t_m (s)	x_n (m)	t_n (s)
0.1	0.295	1.463	0.08	24.936	1.189
0.5	2.194	5.501	0.35	31.534	1.593
1	4.119	7.880	0.56	36.243	1.949
1.5	5.480	9.031	0.70	37.666	2.146
2	6.401	9.385	0.79	37.519	2.259
2.5	6.954	9.318	0.85	36.872	2.335
3	7.164	9.005	0.89	35.553	2.362
3.5	7.035	8.466	0.91	33.342	2.335
4	6.562	7.600	0.90	30.278	2.252
4.5	5.755	6.479	0.87	26.390	2.108
5	4.649	5.315	0.80	21.725	1.898
5.5	3.303	3.955	0.70	16.290	1.606
6	1.871	2.460	0.55	10.258	1.121

The highest height for small droplets is low (Fig. 3.3). For example, the maximum height of droplet with a diameter of 0.1 mm is 0.295 m. As illustrated in Fig. 3.3, the maximum heights in the flight duration over the MFV occur for the water droplets with medium sizes. In these sizes, the droplets are not heavy enough to be affected by gravity and not fast and large enough to be stopped by the drag force. Also, the maximum heights occur at the horizontal distance between 1 and 10 m from the tip of the bow. The theoretical approach to determine the droplet pathways, which are shown in Fig. 3.3, have good agreement with the results of Dehghani et al. (2016b).

Figure 3.4 illustrates the changes of the droplet's Biot number over time for different droplet diameters. From this figure, for conditions of $T_a = -18^\circ\text{C}$, $T_{0,w} = 2^\circ\text{C}$, $U = 15$ m/s, $S_w = 34\%$ and $RH = 80\%$ when the droplet diameter is up to 1.1 mm, considering a uniform temperature within the droplet is a reasonable approximation, because the

droplet's Biot number is lower than 0.1 except at initial times. When the droplet diameter is larger than 1.1 mm, there is a temperature gradient inside the water droplet but it is not significant. For instance, for the droplet diameter of 6 mm, the Biot number is lower than 0.5. This means that the temperature gradient within the droplet is relatively small. A Biot number lower than 0.5 will likely be a reasonable approximation to assume a uniform temperature across the droplet with induced motion.

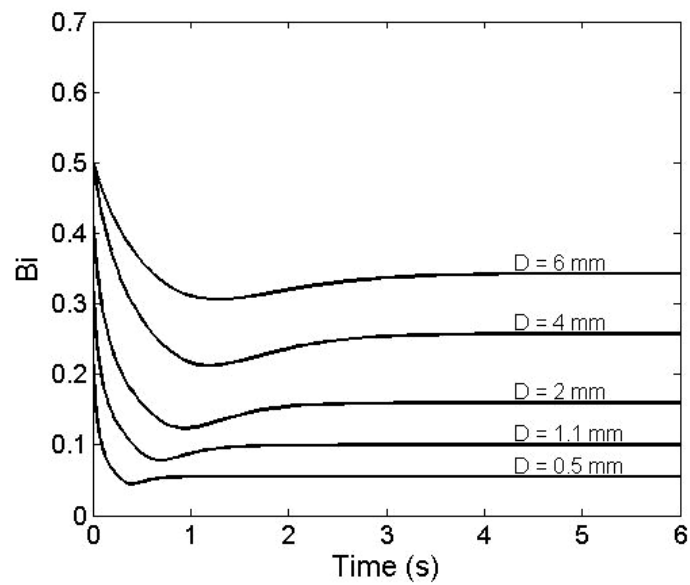


Fig. 3.4: Variations of the droplet's Biot number versus time at various droplet diameters

Figure 3.5 shows the changes of water droplet temperature over time at different diameters until the moment of droplet impact on the deck of the MFV. Table 3.3 indicates the time that the saline water droplets with different sizes start to freeze (t_f) and the temperature of the droplets at the moment of their impact on the deck (T_n). Note that the equilibrium freezing temperature, T_f , is equal to -1.9°C at a salinity of 34‰. From Fig. 3.5 and Table 3.3, the small droplets, which are smaller than 0.5 mm in diameter, will freeze

before impinging on the deck. Andreas (1990) reported that the temperature of the small droplets (lower than 0.1 mm in diameter) will attain the temperature of ambient air in under 0.1 s. The large droplets, which are bigger than 4 mm, do not freeze before colliding on the deck. For the droplets with medium sizes, a part of the droplet will freeze before impacting on the deck. For instance, with a diameter of 3 mm the droplet temperature is equal to -4.2°C at the moment of impact on the deck. This means that an ice shell will form on the surface of the droplet after the freezing temperature is reached and will grow towards the centre of the droplet.

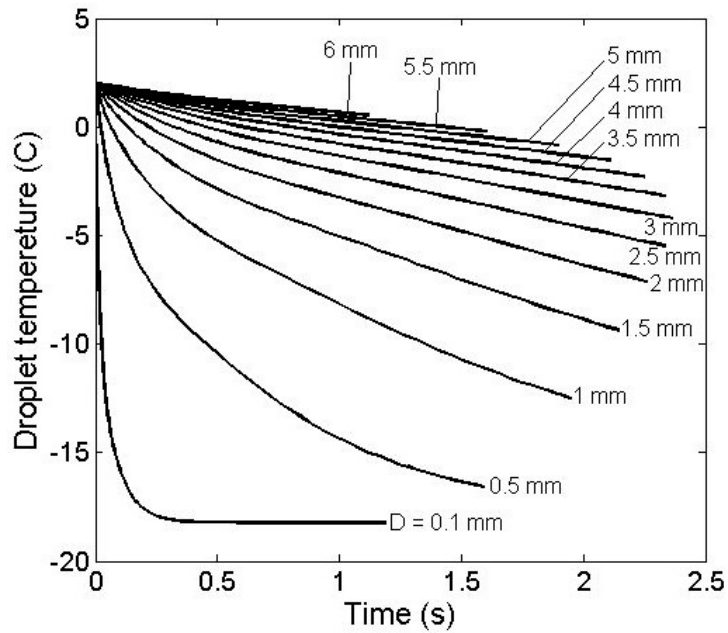


Fig. 3.5: Variations of the water droplet temperature versus time at

$$T_a = -18^{\circ}\text{C}, T_{0,w} = 2^{\circ}\text{C}, U = 15\text{ m/s}, S_w = 34\%, RH = 80\%$$

and various droplet diameters

Table 3.3: Droplet temperature at the moment of impact on the deck and the time that the droplet begins to freeze for $T_a = -18^\circ\text{C}$, $T_{0,w} = 2^\circ\text{C}$, $U = 15\text{ m/s}$, $S_w = 34\text{‰}$, $RH = 80\%$

and various droplet diameters

D (mm)	t_f (s)	T_n ($^\circ\text{C}$)
0.1	3.452×10^{-3}	-18.00
0.5	49.22×10^{-3}	-16.59
1.0	0.1653	-12.50
1.5	0.3447	-9.36
2.0	0.5931	-7.12
2.5	0.9120	-5.48
3	1.2720	-4.20
3.5	1.6350	-3.17
4.0	2.004	-2.29
4.5	2.369	-1.53
5	2.735	-0.85
5.5	3.103	-0.19
6.0	3.470	0.35

Figure 3.5 and Table 3.2 illustrate that the droplet size and the time of droplet flight are important factors in the cooling process. Also, another notable factor for the prediction of the cooling and freezing of water droplets in cold seas and ocean regions is the size of marine vessels. It is possible that the water droplets freeze before reaching the objects on marine platforms, although the different parameters, such as the droplet size, wind velocity, vessel speed, droplet salinity, ambient air temperature, relative humidity, and the initial droplet temperature have an impact on the cooling process. Additionally, it is possible that the water droplets pass over a vessel.

Figure 3.6 displays the changes in heat loss including convection, evaporation and radiation for the droplet cooling process over time at $D = 1\text{ mm}$ during flight on the MFV.

From this figure, the effects of convection and evaporation heat transfer in the droplet cooling process are significant; however, the influence of convection during the cooling process is almost two times more than the magnitude of evaporation. In addition, the influence of radiation heat transfer in the droplet cooling process is negligible. The reduction of the droplet size due to evaporation during flight is very small. For example, for conditions of $D = 1 \text{ mm}$, $T_a = -18^\circ\text{C}$, $T_{0,w} = 2^\circ\text{C}$, $U = 15 \text{ m/s}$, $S_b = 34\%$, and $RH = 80\%$, the droplet diameter reduction is equal to $25.8 \text{ }\mu\text{m}$.

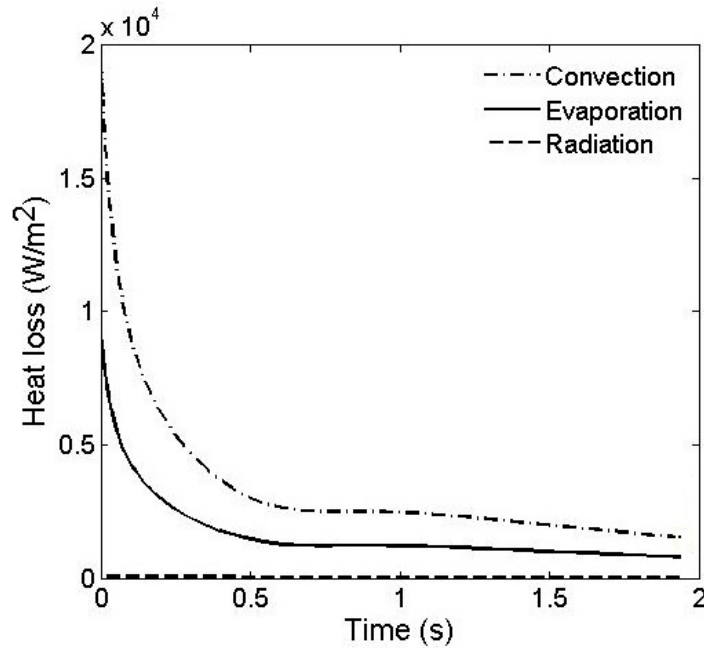


Fig. 3.6: Heat loss changes versus time at $T_a = -18^\circ\text{C}$, $T_{0,w} = 2^\circ\text{C}$, $U = 15 \text{ m/s}$, $D = 1 \text{ mm}$ and $RH = 80\%$

The theoretical results with past results obtained by Zarling (1980), where the droplet was freshwater and had a free fall at low air temperatures were compared. By considering $S_b = 0\%$, $T_a = -18^\circ\text{C}$, $T_{0,w} = 0^\circ\text{C}$, $U = 0 \text{ m/s}$, and different droplet diameters, the results

are examined and evaluated. Table 3.4 shows and compares the droplet velocity (v_d), the droplet's Reynolds number (Re) and the droplet's drag coefficient (C_d) at various diameters of the water droplet for the present model and the obtained results by Zarling (1980). As can be seen from this table, the difference between the results is small.

Table 3.4: Comparison of parameters of v_d , Re and C_d at several diameters for the present model and the obtained results by Zarling (1980)

		Zarling (1980)	Present model
$D = 0.50$ (mm)	v_d (m/s)	2.07	2.03
	Re	87	95
	C_d	1.129	1.159
$D = 1.27$ (mm)	v_d (m/s)	4.54	4.51
	Re	477	481
	C_d	0.583	0.596
$D = 2.54$ (mm)	v_d (m/s)	6.95	7.55
	Re	1463	1611
	C_d	0.495	0.425

The temperature of the water droplet at various diameters for three different conditions is illustrated in Fig. 3.7. There is good agreement between the predicted results and past obtained results by Zarling (1980). Additionally, when the droplet diameters are very small, the droplet temperature is close to the ambient air temperature, whereas for large water droplets, the temperature is higher. For example, when the diameter is more than 3 mm, the droplet temperature is greater than -5°C (Fig. 3.7). It should be noted that a difference between the results may be due to the predicted radiation heat loss, decrease in the size of the droplet due to evaporation, and/or the use of different formulae to obtain parameters and properties.

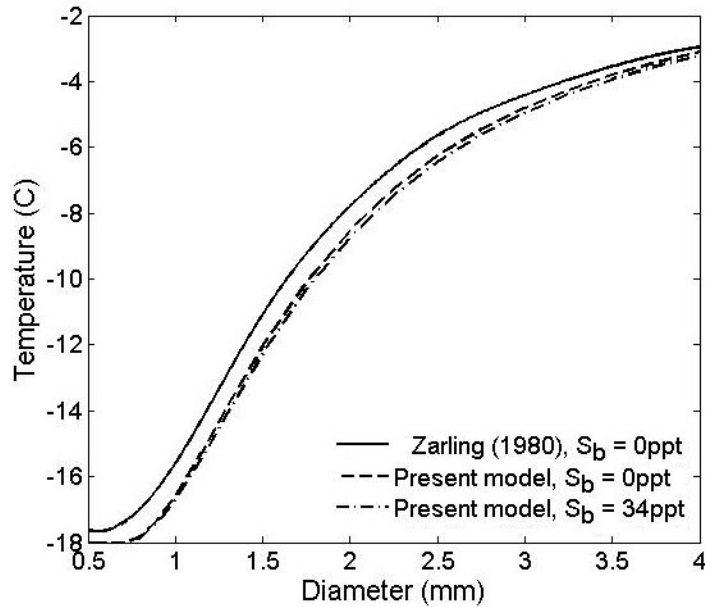


Fig. 3.7: Cooling curve for droplets falling from a height of 15 m
at $T_a = -18^\circ\text{C}$, $T_{\theta,w} = 0^\circ\text{C}$, $U = 0 \text{ m/s}$

3.5 Sensitivity Analysis

A sensitivity analysis is carried out to determine the effects of the various parameters on the trajectory and cooling process of saline water droplets as well as the droplets' Biot number. During each study, one parameter is variable, whereas the other parameters are kept constant. A droplet diameter of 1 mm is selected for the sensitivity analysis because (a) its Biot number is less than 0.1 during flight except at initial times, so a uniform temperature inside the droplet is a reasonable approximation, and (b) the droplet with this size can more likely retain its spherical shape during flight.

Horjen and Vefsnmo (1985) reported that waves can be generated and impacted by marine platforms when the wind velocity increases more than 9 m/s. Figure 3.8 shows the changes in the position and velocity of the droplet at $D = 1 \text{ mm}$ for different wind

velocities during flight over the MFV. As a result, by increasing the wind velocity, the droplet velocity and drag force will increase, so the maximum height of droplet flight will decrease but the horizontal position of the droplet at the moment of impact on the deck will increase (Table 3.5). As illustrated in Fig. 3.8 and Table 3.5, for a wind velocity equal to 25 m/s, the droplet passes over the MFV because x_n is equal to 51.6 m. Thus, wind velocity plays an important role in the droplet trajectories.

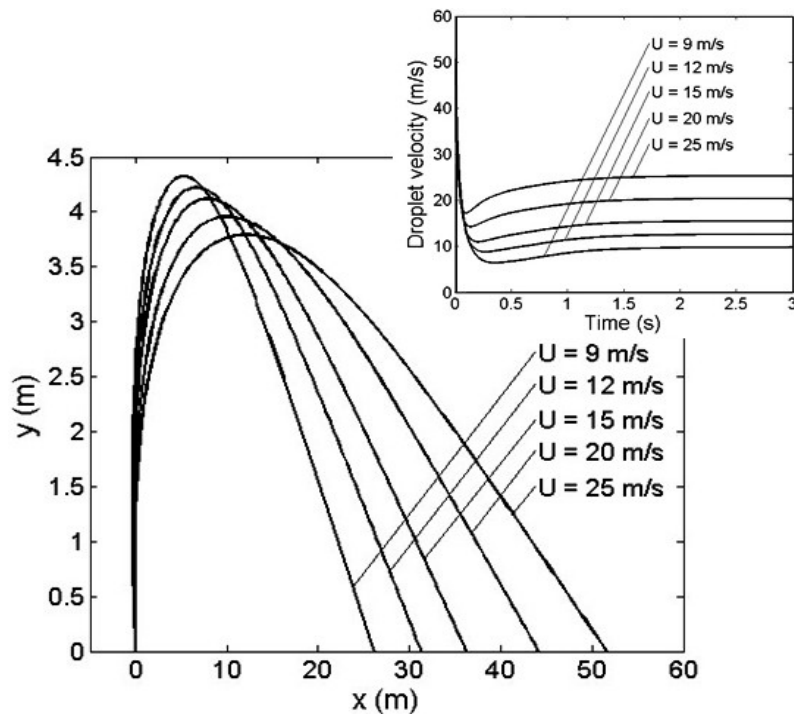
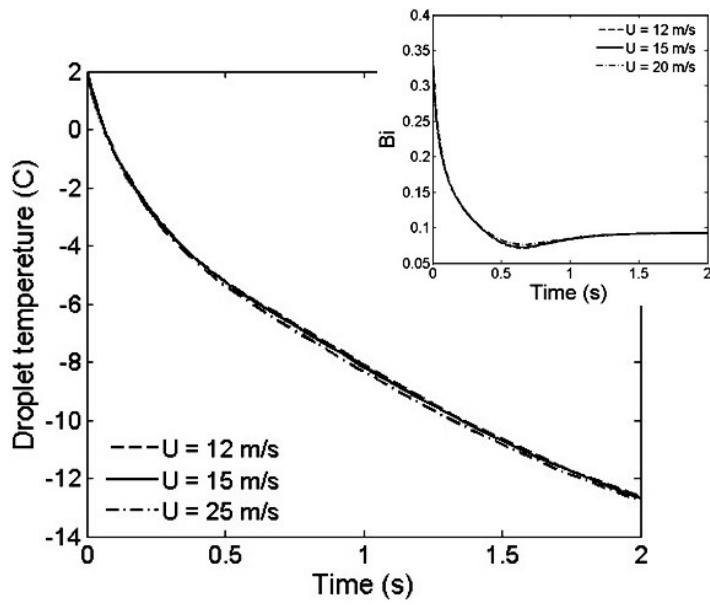


Fig. 3.8: Variations of the position and velocity of the droplet at different wind velocities and $D = 1$ mm

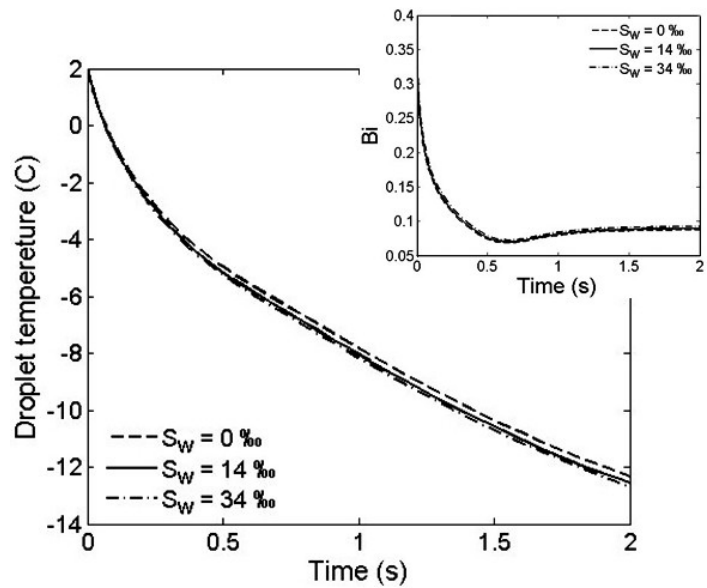
Table 3.5: Positions, time and temperature of the droplet at $D = 1$ mm during flight
for the maximum height and the moment of impact on the deck

	U (m/s)	y_m (m)	x_m (m)	t_m (s)	x_n (m)	t_n (s)	T_n ($^{\circ}\text{C}$)
$D = 1$ (mm)	9	4.322	5.257	0.58	26.118	2.017	-12.66
	12	4.221	6.591	0.57	31.272	1.983	-12.58
	15	4.119	7.880	0.56	36.243	1.949	-12.50
	20	3.954	10.09	0.55	44.141	1.894	-12.36
	25	3.792	11.94	0.53	51.562	1.839	-12.21

Figure 3.9 indicates the influence of wind velocity and droplet salinity on the cooling process and the droplet's Biot number. As illustrated from this figure, wind velocity and salinity have a slight impact on the cooling process and the Biot number. The influence of the initial temperature of the water droplet and the relative humidity on the cooling process as well as the Biot number is shown in Fig. 3.10. From this figure, the initial droplet temperature has a substantial impact on the cooling process. However, this parameter has an insignificant impact on the Biot number. The effect of relative humidity on the cooling process is small, and the effect of this parameter on the Biot number is negligible.



(a)

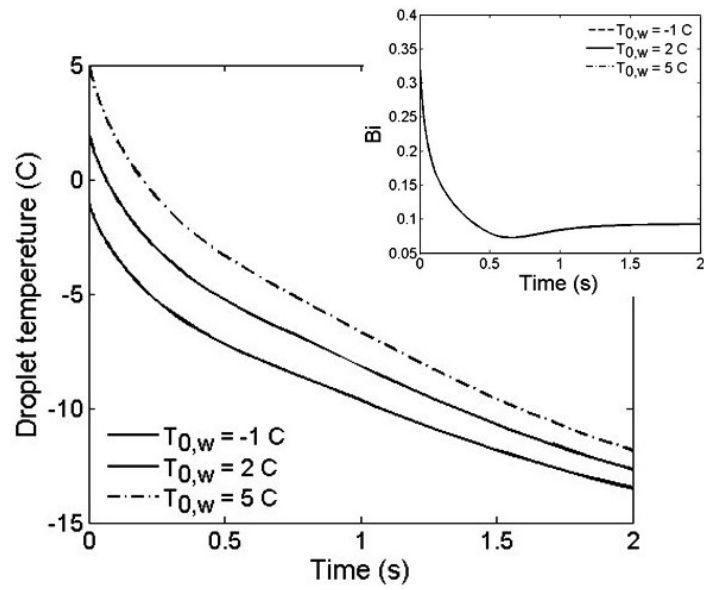


(b)

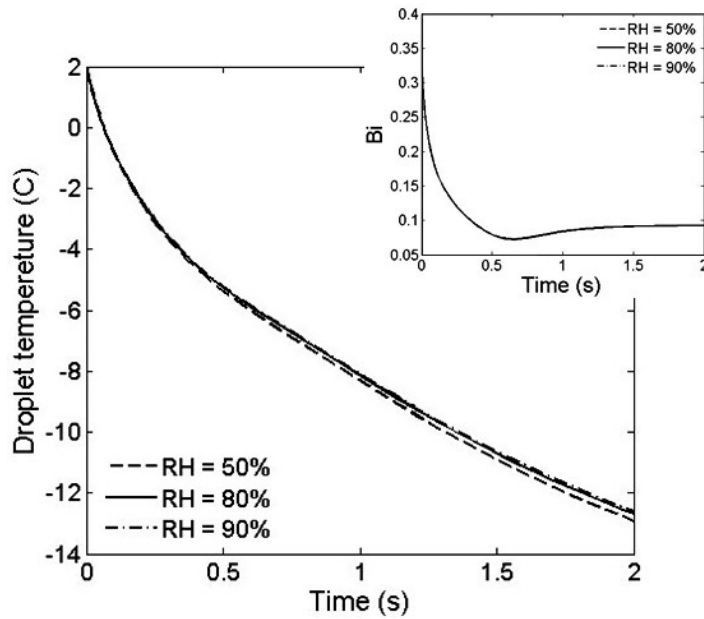
Fig. 3.9: Cooling process and the Biot number changes at different (a) wind velocities

($S_b = 34$ ‰) and (b) salinities ($U = 15$ m/s) for $T_a = -18^\circ\text{C}$, $T_{0,w} = 2^\circ\text{C}$, $D = 1$ mm

and $RH = 80\%$



(a)



(b)

Fig. 3.10: Cooling process and the Biot number changes at different (a) initial droplet temperatures ($RH = 80\%$) and (b) relative humidities ($T_{0,w} = 2$ °C) for

$$T_a = -18^\circ\text{C}, U = 15\text{ m/s}, D = 1\text{ mm and } S_w = 34\%$$

Figure 3.11 illustrates the influence of ambient air temperature on the cooling process and the droplet's Biot number. In this figure, the ambient air temperature has a significant impact on the cooling process, although the effect of this parameter on the Biot number is negligible. As a general result, the parameters of the droplet size, ambient air temperature, and initial droplet temperature have a significant impact on the cooling process during droplet flight.

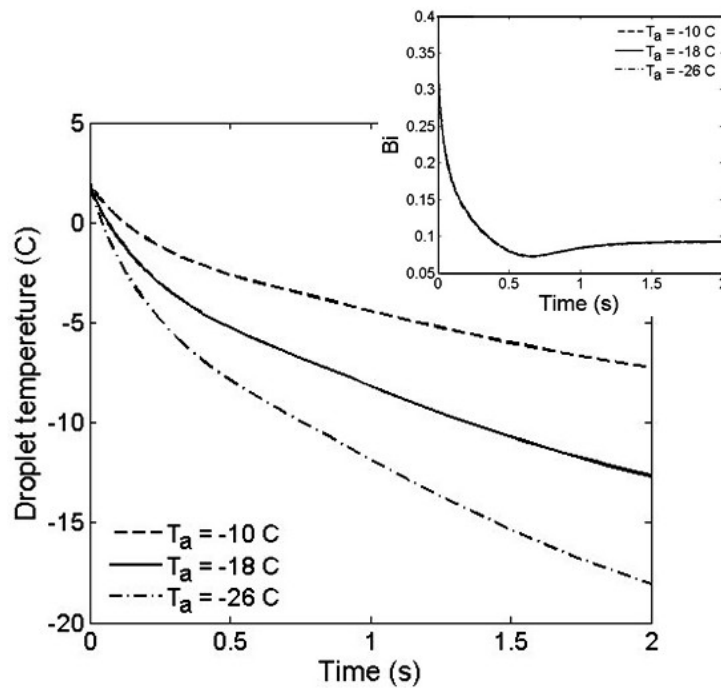


Fig. 3.11: Cooling process and the Biot number changes at different ambient air temperatures for $T_{0,w} = 2^{\circ}\text{C}$, $U = 15\text{ m/s}$, $D = 1\text{ mm}$, $S_w = 34\%$ and $RH = 80\%$

Chapter 4

Theoretical Modeling and Analysis of Solidification Process of a Saline Water Droplet¹

4.1 Introduction

Solidification and melting processes have a wide range of practical applications for materials science and engineering. Some of these applications are (Chan and Tan, 2006; Gupta and Arora, 1992; Hill and Kucera, 1983; Li and Barber, 1989; Parang et al., 1990; Tabakova et al., 2010): thermal energy storage systems, freezing foods, crystal growth, laser glazing, ice formation on power cables, marine platforms and aircraft during flights, the processes of casting metals and alloys as well as welding, groundwater freezing, low-temperature biology, and medicine. The trajectory and also the cooling and freezing processes of water droplets in cold regions are the most important issues for modeling and prediction of the sea spray icing phenomena on marine vessels and offshore structures (Bodaghkhani et al., 2016; Dehghani et al., 2016a, 2016b; Dehghani-Sanij et al., 2015, 2016, 2017a, 2017b).

1. This chapter is based on a paper that was submitted to International Journal of Heat and Mass Transfer.

The solidification process of the water droplets in cold weather conditions corresponds with the phase change from the liquid to solid. The phase change, or Stefan problem, is one of the moving boundary problems associated with a time-dependency, which is non-linear and cannot be solved analytically. Thus, numerical and approximate methods can be employed to solve these types of problems. Neumann found the exact solution for the one-dimensional phase change problem of solidification in a semi-infinite region that is not initially at the fusion temperature (Carslaw and Jaeger, 1959). Neumann's solution led to very few exact similarity solutions. Note that similarity solutions for some conditions, such as finite domains, two phases present initially, non-uniform initial temperatures, and boundary temperatures that are arbitrary functions of time cannot be used to find the exact solution (Krzewinski and Tart, 1985). Schulze et al. (1983) expressed that approximate methods are commonly not accurate for short times. Hindmarsh et al. (2003) reported that several numerical techniques have been formulated by a number of researchers for solving the moving boundary problems. These numerical techniques with proper references are listed in the following: (1) "Temperature formulation", Murray and Landis (1959), (2) "Enthalpy formulation", Voller (1985), (3) "Heat balancing integral methods", Caldwell and Chan (2000), (4) "Equivalent heat capacity method", Bonacina (1973), (5) "Crystal growth method", Wang and Matthys (1992), and (6) "Most recently developed thermodynamic formulation called the phase field method", Wheeler and Ahmad (1995).

A number of researchers have employed the perturbation technique (or the method of strained coordinates) to find the inward spherical solidification by using a major assumption, which is a low Stefan number (Feuillebois et al., 1995; Gupta, 1987; Gupta and Arora, 1992; Hill and Kucera, 1983; Huang and Shih, 1975; Li and Barber, 1989;

Milanez and Boldrini, 1988; Pedroso and Domoto, 1973a, 1973b; Riley et al., 1974; Seeniraj and Bose, 1982; Weinbaum and Jiji, 1977; Yan and Huang, 1974). In other words, the perturbation method can be used when the sensible heat is negligible compared to the latent heat, namely, the Stefan number tends to be zero. Additionally, these researchers compared the results obtained from the perturbation method with the numerical results, which were acquired by different approaches. As a result, the perturbation solution for a small value of the Stefan number is approximately accurate (Pedroso and Domoto, 1973a). It should be noted that the researchers considered different assumptions to solve the inward spherical freezing using the perturbation technique. Some of these assumptions are: (1) thermophysical properties are constant (Gupta, 1987; Gupta and Arora, 1992; Hill and Kucera, 1983; London and Seban, 1943; Pedroso and Domoto, 1973a, 1973b; Parang et al., 1990; Seeniraj and Bose, 1982; Weinbaum and Jiji, 1977; Yan and Huang, 1974), (2) considering the equal value for densities of liquid and solid phases (Feuillebois et al., 1995; Gupta and Arora, 1992; Tabakova et al., 2010), and (3) the freezing temperature is invariable and the liquid will be presumed to be at the freezing temperature (Pedroso and Domoto, 1973a).

Tabakova et al. (2010) studied the freezing process of a spherical droplet by considering two different stages: “recalescence” and a phase change process to/from solidification. To analyze and solve the problem, they used two distinct methods: (a) the technique of matched asymptotic expansions for a small Stefan number as well as an arbitrary Biot number, and (b) the numerical approach for an arbitrary Stefan number by employing the enthalpy method. The results showed that there is a good agreement between the two methods. Feuillebois et al. (1995) considered three various possible

situations to create ice accretion in the recalescence stage, which are: (1) at the centre of the droplet, (2) with uniform distribution of the ice formed within the droplet randomly, and (3) at the outside surface of the droplet.

Hindmarsh et al. (2004) experimentally and numerically investigated the temperature behaviour of a solidification food solution droplet. They considered five different stages for the solidification of the droplet, which are respectively (Hindmarsh et al., 2004): “(1) liquid cooling and supercooling, (2) nucleation, (3) recalescence, (4) freezing, and (5) solid cooling or tempering.” In another study, Hindmarsh et al. (2003) analyzed the freezing process of a suspended water droplet using numerical and experimental methods. They studied both the outward and inward moving boundaries during the solidification process of the droplet. Results showed that the outward solidification model predicted shorter freezing times compared to the inward solidification model.

4.2 Model Description

To analyze and predict the cooling and freezing processes of a saline water droplet during flight on marine platforms, two situations can be considered: (1) a uniform temperature across the droplet, and (2) heat conduction or a temperature gradient within the droplet. In this study, three different stages during the cooling and freezing processes, when there is a temperature gradient inside the water droplet, are considered. In the first stage, or liquid cooling stage, the droplet is fully liquid and its volume will decrease because of evaporation from the droplet’s surface. The second stage, or solidification stage, will begin when the surface temperature reaches the freezing temperature, then an ice shell will form on the surface of the droplet. A number of experimental investigations

have illustrated that the solidification in the droplets generally occurs from the surface by forming a frozen shell towards the centre of the droplets (Chan and Tan, 2006; Gao et al., 2000; Hindmarsh et al., 2003; Tagami et al., 1999). Hence, an inward freezing for the spherical saline water droplet is considered. In the third stage, or solid cooling stage, the droplet and its salt content will freeze completely. In fact, a brine-spongy ice will form, which contains pure ice, brine pockets and air bubbles. Figure 4.1 displays the variations of a saline water droplet in the different stages for freezing conditions when the droplet flies over a marine vessel or an offshore structure.

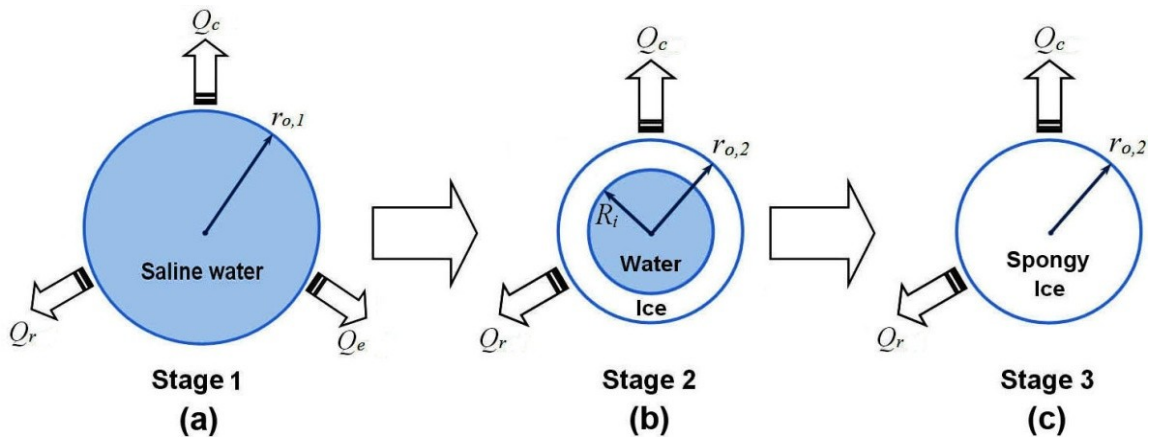


Fig. 4.1: Schematic of the changes of a saline water droplet in freezing conditions during its flight over marine platforms

In this chapter, the droplet trajectory and heat transfer models are the same as sections 3.1 and 3.2, respectively. It should be noted that a number of assumptions will be employed in order to simplify and solve the problem, which are: (1) the droplet has a spherical shape during the entire trajectory, (2) the droplet's shape is axisymmetric, so it can be described by the spatial coordinate r , (3) the direction of the aerodynamic drag is

exactly opposite of the direction of velocity during flight, (4) the initial temperature of the droplet in a spray event is equal to the temperature of the water's surface, (5) the coordinate origin is at the center of the droplet, (6) the properties of ice formation, such as the thermal conductivity, density and the specific heat capacity, are uniform in the ice formation, and (7) the velocity of wind is uniform and in the horizontal direction.

4.3 Droplet Cooling and Freezing Processes

By ignoring the directional forces for all stages, because these forces are small (Ranz and Marshall, 1952; Sadafi et al., 2015), the governing equation in the spherical coordinates can be written as:

$$\frac{\partial(\rho c T)}{\partial t} = \frac{1}{r^2} \frac{\partial}{\partial r} \left(k r^2 \frac{\partial T}{\partial r} \right), \quad 0 \leq r \leq r_d \quad (4.1)$$

where ρ is the density, c is the specific heat capacity, k is the thermal conductivity, T is the temperature, and r is the radial coordinate. To solve Eq. (4.1) for each stage, the boundary and initial conditions are needed. These boundary and initial conditions will be explained in the following sections.

4.3.1 Liquid Cooling Stage

According to Fig. 4.1(a), the boundary condition at the center of the saline water droplet is:

$$\left. \frac{\partial T_w}{\partial r} \right|_{r=0} = 0 \quad (4.2)$$

Also, by considering conduction heat transfer within the droplet as well as convection, evaporation and radiation heat transfer between the droplet's surface and the ambient air, and assuming the average value for the convection heat transfer coefficient of the droplet, h_c , another boundary condition is:

$$\left. \frac{\partial T_w}{\partial r} \right|_{r=r_{o,l}} = G_2 - G_1 T_w(r = r_{o,l}) \quad (4.3)$$

where the coefficients of G_1 and G_2 are defined as:

$$G_1 = \frac{(h_c + h_r + C e_0)}{k_b} \quad (4.4)$$

$$G_2 = \frac{[(h_c + h_r + C RH e_0) T_a + C E_0 (RH - 1)]}{k_b} \quad (4.5)$$

The initial condition for the first stage is:

$$T_w(r, 0) = T_{0,w} \quad (4.6)$$

The variations in the droplet's radius during the liquid cooling stage can be determined by solving Eqs. (3.29)-(3.30). It is assumed that the change of the droplet's volume in the first stage is negligible.

4.3.2 Solidification Stage

As mentioned in section 4.2, when the temperature of the droplet's surface reaches the freezing temperature, the first particles of ice form on the top and bottom surfaces (when the droplet moves in the horizontal direction) because of higher wind velocity and then grow to cover other portions. Subsequently, the ice shell will be created on the surface of the droplet. Throughout the solidification stage, the internal liquid progressively varies

from water to ice, and the latent heat of fusion must be transferred to the ambient air via the ice shell. The ice growth inside the droplet is similar to a dendritic form at a microscopic scale (Makkonen, 2010). It is assumed that the growth of the ice shell within the droplet is uniform during the solidification stage; however, in reality, there are different shapes of freezing. Figure 4.2 illustrates the freezing process of the water droplet in the second stage.

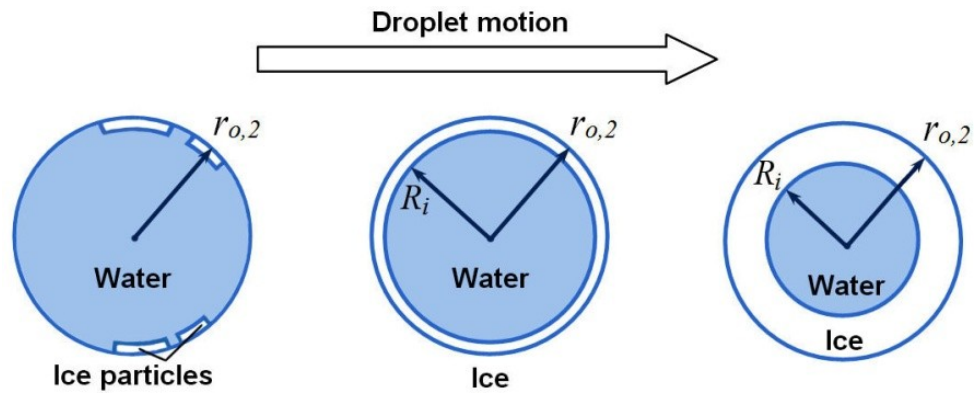


Fig. 4.2: Schematic of the solidification process of a saline water droplet in the second stage

In accordance with Fig. 4.1(b), the boundary conditions for the water and ice shell are:

$$\frac{\partial T_w}{\partial r} \Big|_{r=0} = 0 \quad (4.7)$$

$$-k_i \frac{\partial T_i}{\partial r} \Big|_{r=r_{o,2}} = (h_c + h_r) [T_i(r = r_{o,2}) - T_a] \quad (4.8)$$

$$T_w(R_i, t) = T_i(R_i, t) = T_f \quad (4.9)$$

where T_f is the freezing temperature at the water-ice interface and the subscripts w and i refer to the water and ice shell, respectively. Note that the evaporation from the droplet's surface in the second stage is negligible.

By applying a phase change or Stefan condition at the ice-water interface, the following equation can be obtained:

$$\rho_i l_f (1 - \beta) \frac{dR_i}{dt} = k_i \left. \frac{\partial T_i}{\partial r} \right|_{r=R_i} - k_b \left. \frac{\partial T_w}{\partial r} \right|_{r=R_i} \quad (4.10)$$

Here, l_f is the latent heat of fusion of pure ice, $l_f (1 - \beta)$ is the latent heat of fusion of the saline ice formation (Makkonen, 1987) and β is the interfacial distribution coefficient. Note that the radius of the freezing interface, R_i , is a function of time, which is variable between 0 and the radius of the droplet in the solidification stage.

The initial conditions for the water and ice shell, respectively, are:

$$T_w(r, 0) = T_l \quad (4.11)$$

$$T_i(r = r_{o,2}, 0) = T_f \quad (4.12)$$

where T_l is the temperature obtained from the liquid cooling stage at the freezing time, t_f . In the above equation, the freezing temperature, T_f , for three temperature regions can be obtained according to Eqs. (3.26)-(3.28).

The salinity has an effect on several parameters, such as density, thermal conductivity, specific heat capacity, and freezing temperature. Andreas (1990) reported that the salinity of seawater spray will increase due to evaporation and the equilibrium radius of a water droplet is one-half of the radius at formation for a relative humidity of 80%. Kulyakhtin and Tsarau (2014) expressed that the salinity of the water droplet, which is created by

wave spray, is equal to the seawater salinity, but the salinity of the droplet, which is produced by wind spray, is higher compared to the seawater salinity. Schwerdtfeger (1963) reported that the highest amount of salt in unfrozen water is equal to 237‰ when the temperature is -17°C. Horjen (2013) expressed that the droplet salinity for large water droplets, impact-generated sea spray, is only slightly higher than the seawater surface salinity because of evaporation during flight. However, for water droplets with small sizes (about 0.1 mm) and also long flight distances, the difference between the droplet salinity and seawater salinity is significant. In this study, it is assumed that the droplet salinity, S_b , equals the seawater salinity, S_w , when the droplet diameter is equal to or greater than 0.5 mm.

4.3.3 Solid Cooling Stage

With regards to Fig. 4.1(c), the boundary and initial conditions for the solid cooling stage are:

$$\left. \frac{\partial T_i}{\partial r} \right|_{r=0} = 0 \quad (4.13)$$

$$-k_i \left. \frac{\partial T_i}{\partial r} \right|_{r=r_{o,2}} = (h_c + h_r) [T_i(r = r_{o,2}) - T_a] \quad (4.14)$$

$$T_i(r = r_{o,2}, 0) = T_2 \quad (4.15)$$

where T_2 is the temperature obtained from the solidification stage at the solid time, t_s . In this stage, like the second stage, the evaporation from the droplet's surface is neglected.

4.4 Theoretical Solution Procedure

To determine the temperature distribution inside the water droplet in the liquid cooling and solid cooling stages, an analytical technique can be employed. By using the separation of variables method (Ozisik, 2000), the solution for the temperature distribution in the liquid cooling stage is obtained as follows:

$$T_w(r, t) = \frac{G_2}{G_1} + \sum_{n=1}^{\infty} A_n \frac{\sin(\lambda_n r)}{r} \exp(-\alpha_b \lambda_n^2 t) \quad (4.16)$$

where α_b is the thermal diffusivity of brine, which is given by:

$$\alpha_b = \frac{k_b}{\rho_b c_b} \quad (4.17)$$

and A_n is a coefficient, which is defined by:

$$A_n = \frac{\left(T_{0,w} - \frac{G_2}{G_1} \right) \left[\frac{1}{\lambda_n^2} \sin(\lambda_n r_{o,l}) - \frac{r_{o,l}}{\lambda_n} \cos(\lambda_n r_{o,l}) \right]}{\frac{r_{o,l}}{2} - \frac{1}{4\lambda_n} \sin 2(\lambda_n r_{o,l})} \quad (4.18)$$

The eigenvalues, λ_n , can be calculated from the roots of the following transcendental equation:

$$\tan(\lambda_n r_{o,l}) = \frac{\lambda_n}{\left(\frac{1}{r_{o,l}} - G_1 \right)} \quad (4.19)$$

To estimate the density of brine, ρ_b , Eq. (2.96) is used. The thermal conductivity of brine, k_b , can be computed by Eq. (3.33). In Eq. (3.33) the brine temperature, T_b , can be calculated by Eq. (2.86)-(2.87). To determine the specific heat capacity of seawater, c_b , Eq. (3.25) is employed.

In the solidification stage, there is a phase change condition, or a Stefan type condition. Hence, a semi-analytical technique for solving the moving boundary problem inside the water droplet is utilized. In this technique, the semi-discretization method in time and the separation of variables method in radial direction will be used. Therefore, the temperature distribution in the water and the ice shell will be specified.

In order to homogenize the boundary conditions in the water, a temperature excess, $\theta_w = T_w - T_f$, is used. Thus, the governing equation leads to:

$$\frac{1}{r^2} \frac{\partial}{\partial r} \left(r^2 \frac{\partial \theta_w}{\partial r} \right) = \frac{1}{\alpha_w} \frac{\partial \theta_w}{\partial t}, \quad 0 \leq r < R_i \quad (4.20)$$

which is subject to:

$$\left. \frac{\partial \theta_w}{\partial r} \right|_{r=0} = 0 \quad (4.21)$$

$$\theta_w(R_i, t) = 0 \quad (4.22)$$

$$\theta_w(r, 0) = T_i - T_f \quad (4.23)$$

By applying the separation of variables method in r -direction, the following solution can be obtained.

$$\theta_w(r) = \sum_{n=1}^{\infty} B_n \frac{\sin\left(\frac{n\pi}{R_i} r\right)}{r} \quad (4.24)$$

In addition, the time approximation below can be used at any time.

$$\frac{\partial \theta_w}{\partial t} = \frac{\theta_w(r, t_k) - \theta_w(r, t_k - \Delta t)}{\Delta t} \quad (4.25)$$

where

$$\theta_w(r, t_k) = \sum_{n=1}^{\infty} B_{n,k} \frac{\sin\left(\frac{n\pi}{R_i^k} r\right)}{r} \quad (4.26)$$

and

$$\theta_w(r, t_k - \Delta t) = \sum_{n=1}^{\infty} B_{n,k-1} \frac{\sin\left(\frac{n\pi}{R_i^{k-1}} r\right)}{r} \quad (4.27)$$

Also, Eq. (4.22) can be written as follows:

$$\theta_w(r, t_k) = \theta_w(r, t_k - \Delta t) + \Delta t \frac{\alpha_w}{r^2} \frac{\partial}{\partial r} \left(r^2 \frac{\partial \theta_w}{\partial r} \right) \quad (4.28)$$

By substituting Eqs. (4.26) and (4.27) into Eq. (4.28), the following relationship can be obtained.

$$\sum_{n=1}^{\infty} \left(1 + \Delta t \alpha_w \left(\frac{n\pi}{R_i^k} \right)^2 \right) B_{n,k} \frac{\sin\left(\frac{n\pi}{R_i^k} r\right)}{r} = \sum_{n=1}^{\infty} B_{n,k-1} \frac{\sin\left(\frac{n\pi}{R_i^{k-1}} r\right)}{r} \quad (4.29)$$

By multiplying $\frac{\sin\left(\frac{m\pi}{R_i^k} r\right)}{r}$ in the above relationship and integrating from 0 to R_i^k , the

coefficient of $B_{m,k}$ can be determined as follows:

$$B_{m,k} = \sum_{n=1}^{\infty} B_{n,k-1} \frac{R_i^{k-1}}{\pi \left(1 + \Delta t \alpha_w \left(\frac{m\pi}{R_i^k} \right)^2 \right)} \left\{ \frac{1}{(n R_i^k - m R_i^{k-1})} \sin\left(\pi \left(\frac{n R_i^k - m R_i^{k-1}}{R_i^{k-1}} \right) \right) \right. \\ \left. - \frac{1}{(n R_i^k + m R_i^{k-1})} \sin\left(\pi \left(\frac{n R_i^k + m R_i^{k-1}}{R_i^{k-1}} \right) \right) \right\} \quad (4.30)$$

To calculate the coefficient of $B_{m,k}$ the initial condition must be applied. By using the initial condition, the coefficient of $B_{m,1}$ can be defined as follows:

$$B_{m,l} = \left(T_f - \frac{G_2}{G_1} \right) \left[\frac{2R_i^l}{m\pi} (-1)^m \right] + \sum_{n=1}^{\infty} A_n \frac{1}{R_i^l} \left\{ \frac{1}{\left(\lambda_n - \frac{m\pi}{R_i^l} \right)} \sin \left(\left(\lambda_n - \frac{m\pi}{R_i^l} \right) R_i^l \right) \right. \\ \left. - \frac{1}{\left(\lambda_n + \frac{m\pi}{R_i^l} \right)} \sin \left(\left(\lambda_n + \frac{m\pi}{R_i^l} \right) R_i^l \right) \right\} \exp \left(-\alpha_b \lambda_n^2 t_f \right) \quad (4.31)$$

where R_i^l is the radius of water at start of the solidification stage and is equal to $r_{o,2}$. By computing $B_{m,l}$ from Eq. (4.31), the coefficient of $B_{m,k}$ will be estimated. Consequently, the solution for the temperature distribution in the water can be determined as follows:

$$\theta_w(r, t_k) = \sum_{m=1}^{\infty} B_{m,k} \frac{\sin \left(\frac{m\pi}{R_i^k} r \right)}{r} \quad (4.32)$$

To find the temperature distribution in the ice shell, the semi-analytical solution procedure will be utilized in the same manner as used with water. To homogenize the boundary conditions in the ice shell, a temperature excess, $\theta_i = T_i - (a + br)$, is used. By using the homogeneous boundary conditions, the parameters of a and b can be calculated. Thus, these parameters are equal to:

$$a = T_f - \frac{(T_a - T_f)R_i}{\left[r_{o,2} - R_i + \left(\frac{k_i}{h_c + h_r} \right) \right]} \quad (4.33)$$

$$b = \frac{(T_a - T_f)}{\left[r_{o,2} - R_i + \left(\frac{k_i}{h_c + h_r} \right) \right]} \quad (4.34)$$

The governing equation for the ice shell can be written as follows:

$$\frac{1}{r^2} \frac{\partial}{\partial r} \left(r^2 \frac{\partial \theta_i}{\partial r} \right) + \frac{2b}{r} = \frac{1}{\alpha_i} \frac{\partial \theta_i}{\partial t}, \quad R_i \leq r \leq r_{o,2} \quad (4.35)$$

which is subject to:

$$-k_i \frac{\partial \theta_i}{\partial r} \Big|_{r=r_{o,2}} = (h_c + h_r) \theta_i(r = r_{o,2}) \quad (4.36)$$

$$\theta_i(R_i, t) = 0 \quad (4.37)$$

$$\theta_i(r_{o,2}, 0) = 0 \quad (4.38)$$

By applying the separation of variables method in r -direction, the solution below can be found.

$$\theta_i(r) = \sum_{n=1}^{\infty} C_n \left[\frac{\cos(\gamma_n r)}{r} - \cot \text{an}(\gamma_n R_i) \frac{\sin(\gamma_n r)}{r} \right] \quad (4.39)$$

In the above relationship, γ_n is the eigenvalues that can be calculated from the roots of the following transcendental equation:

$$\tan(\gamma_n r_{o,2}) = \frac{\left(\frac{h_c + h_r}{k_i} \right) r_{o,2} - (\gamma_n r_{o,2}) \cot \text{an}(\gamma_n R_i) - 1}{\left[\left(\frac{h_c + h_r}{k_i} \right) r_{o,2} \cot \text{an}(\gamma_n R_i) - \cot \text{an}(\gamma_n R_i) + (\gamma_n r_{o,2}) \right]} \quad (4.40)$$

By employing the time approximation for any time, Eq. (4.35) can be written as follows:

$$\theta_i(r, t_k) - \Delta t \frac{\alpha_i}{r^2} \frac{\partial}{\partial r} \left(r^2 \frac{\partial \theta_i}{\partial r} \right) = \frac{2\alpha_i \Delta t b}{r} + \theta_i(r, t_k - \Delta t) \quad (4.41)$$

where

$$\theta_i(r, t_k) = \sum_{n=1}^{\infty} C_{n,k} \left[\frac{\cos(\gamma_{n,k} r)}{r} - \cot \text{an}(\gamma_{n,k} R_i^k) \frac{\sin(\gamma_{n,k} r)}{r} \right] \quad (4.42)$$

and

$$\theta_i(r, t_k - \Delta t) = \sum_{n=1}^{\infty} C_{n,k-1} \left[\frac{\cos(\gamma_{n,k-1} r)}{r} - \cot \text{an}(\gamma_{n,k-1} R_i^{k-1}) \frac{\sin(\gamma_{n,k-1} r)}{r} \right] \quad (4.43)$$

By substituting Eqs. (4.42) and (4.43) into Eq. (4.41), the following relationship can be obtained.

$$\begin{aligned} \sum_{n=1}^{\infty} (I + \Delta t \alpha_i \gamma_{n,k}^2) C_{n,k} \left[\frac{\cos(\gamma_{n,k} r)}{r} - \cot \text{an}(\gamma_{n,k} R_i^k) \frac{\sin(\gamma_{n,k} r)}{r} \right] &= \frac{2 \alpha_i \Delta t b}{r} + \\ \sum_{n=1}^{\infty} C_{n,k-1} \left[\frac{\cos(\gamma_{n,k-1} r)}{r} - \cot \text{an}(\gamma_{n,k-1} R_i^{k-1}) \frac{\sin(\gamma_{n,k-1} r)}{r} \right] & \end{aligned} \quad (4.44)$$

By multiplying $\left[\frac{\cos(\gamma_{m,k} r)}{r} - \cot \text{an}(\gamma_{m,k} R_i^k) \frac{\sin(\gamma_{m,k} r)}{r} \right]$ in Eq. (4.44) and integrating

from R_i^k to $r_{o,2}$, the coefficient of $C_{m,k}$ can be determined as follows:

$$C_{m,k} = \frac{I}{(I + \Delta t \alpha_i \gamma_{m,k}^2) I_1} \left[2 \alpha_i \Delta t b I_2 + \sum_{n=1}^{\infty} C_{n,k-1} I_3 \right] \quad (4.45)$$

In the above equation, the coefficients I_1 , I_2 and I_3 are acquired from appropriate relationships, which are:

$$\begin{aligned} I_1 &= \frac{I}{2} (r_{o,2} - R_i^k) + \frac{I}{4 \gamma_{m,k}} [\sin 2(\gamma_{m,k} r_{o,2}) - \sin 2(\gamma_{m,k} R_i^k)] + \frac{I}{2 \gamma_{m,k}} \cot \text{an}(\gamma_{m,k} R_i^k) \\ & \quad [\cos 2(\gamma_{m,k} r_{o,2}) - \cos 2(\gamma_{m,k} R_i^k)] + \cot \text{an}^2(\gamma_{m,k} R_i^k) \\ & \quad \left\{ \frac{I}{2} (r_{o,2} - R_i^k) - \frac{I}{4 \gamma_{m,k}} [\sin 2(\gamma_{m,k} r_{o,2}) - \sin 2(\gamma_{m,k} R_i^k)] \right\} \end{aligned} \quad (4.46)$$

$$\begin{aligned} I_2 &= \frac{I}{\gamma_{m,k}} [\sin(\gamma_{m,k} r_{o,2}) - \sin(\gamma_{m,k} R_i^k)] + \frac{I}{\gamma_{m,k}} \cot \text{an}(\gamma_{m,k} R_i^k) \\ & \quad [\cos(\gamma_{m,k} r_{o,2}) - \cos(\gamma_{m,k} R_i^k)] \end{aligned} \quad (4.47)$$

$$\begin{aligned} I_3 &= E_1 - \cot \text{an}(\gamma_{m,k} R_i^k) E_2 - \cot \text{an}(\gamma_{n,k-1} R_i^{k-1}) E_3 + \cot \text{an}(\gamma_{n,k-1} R_i^{k-1}) \\ & \quad \cot \text{an}(\gamma_{m,k} R_i^k) E_4 + T_f E_5 - T_f \cot \text{an}(\gamma_{m,k} R_i^k) E_6 \end{aligned} \quad (4.48)$$

where

$$E_1 = \frac{I}{2(\gamma_{n,k-1} - \gamma_{m,k})} \left[\sin(\gamma_{n,k-1} - \gamma_{m,k}) r_{o,2} - \sin(\gamma_{n,k-1} - \gamma_{m,k}) R_i^{k-1} \right] \\ + \frac{I}{2(\gamma_{n,k-1} + \gamma_{m,k})} \left[\sin(\gamma_{n,k-1} + \gamma_{m,k}) r_{o,2} - \sin(\gamma_{n,k-1} + \gamma_{m,k}) R_i^{k-1} \right] \quad (4.49)$$

$$E_2 = -\frac{I}{2(\gamma_{n,k-1} + \gamma_{m,k})} \left[\cos(\gamma_{n,k-1} + \gamma_{m,k}) r_{o,2} - \cos(\gamma_{n,k-1} + \gamma_{m,k}) R_i^{k-1} \right] \\ + \frac{I}{2(\gamma_{n,k-1} - \gamma_{m,k})} \left[\cos(\gamma_{n,k-1} - \gamma_{m,k}) r_{o,2} - \cos(\gamma_{n,k-1} - \gamma_{m,k}) R_i^{k-1} \right] \quad (4.50)$$

$$E_3 = -\frac{I}{2(\gamma_{n,k-1} + \gamma_{m,k})} \left[\cos(\gamma_{n,k-1} + \gamma_{m,k}) r_{o,2} - \cos(\gamma_{n,k-1} + \gamma_{m,k}) R_i^{k-1} \right] \\ - \frac{I}{2(\gamma_{n,k-1} - \gamma_{m,k})} \left[\cos(\gamma_{n,k-1} - \gamma_{m,k}) r_{o,2} - \cos(\gamma_{n,k-1} - \gamma_{m,k}) R_i^{k-1} \right] \quad (4.51)$$

$$E_4 = \frac{I}{2(\gamma_{n,k-1} - \gamma_{m,k})} \left[\sin(\gamma_{n,k-1} - \gamma_{m,k}) r_{o,2} - \sin(\gamma_{n,k-1} - \gamma_{m,k}) R_i^{k-1} \right] \\ - \frac{I}{2(\gamma_{n,k-1} + \gamma_{m,k})} \left[\sin(\gamma_{n,k-1} + \gamma_{m,k}) r_{o,2} - \sin(\gamma_{n,k-1} + \gamma_{m,k}) R_i^{k-1} \right] \quad (4.52)$$

$$E_5 = \left[\frac{R_i^{k-1}}{\gamma_{m,k}} \sin(\gamma_{m,k} R_i^{k-1}) + \frac{I}{\gamma_{m,k}^2} \cos(\gamma_{m,k} R_i^{k-1}) \right] - \\ \left[\frac{R_i^k}{\gamma_{m,k}} \sin(\gamma_{m,k} R_i^k) + \frac{I}{\gamma_{m,k}^2} \cos(\gamma_{m,k} R_i^k) \right] \quad (4.53)$$

$$E_6 = \left[-\frac{R_i^{k-1}}{\gamma_{m,k}} \cos(\gamma_{m,k} R_i^{k-1}) + \frac{I}{\gamma_{m,k}^2} \sin(\gamma_{m,k} R_i^{k-1}) \right] - \\ \left[-\frac{R_i^k}{\gamma_{m,k}} \cos(\gamma_{m,k} R_i^k) + \frac{I}{\gamma_{m,k}^2} \sin(\gamma_{m,k} R_i^k) \right] \quad (4.54)$$

It should be noted that due to the initial condition, the coefficient of $C_{m,1} = 0$. By computing the coefficient of $C_{m,k}$, the solution for the temperature distribution in the ice shell can be found as follows:

$$\theta_i(r, t_k) = \sum_{m=1}^{\infty} C_{m,k} \left[\frac{\cos(\gamma_{m,k} r)}{r} - \cot \text{an}(\gamma_{m,k} R_i^k) \frac{\sin(\gamma_{m,k} r)}{r} \right] \quad (4.55)$$

To determine the interface radius, R_i , and the temperature distribution in the water and ice shell, the Stefan condition at the ice-water interface will be used. By taking the derivative from Eqs. (4.32) and (4.55) and substituting these equations in the Stefan condition (Eq. (4.10)), the equation below will be obtained:

$$\rho_i l_f (1 - \beta) \frac{R_i^k - R_i^{k-1}}{\Delta t} = k_i \sum_{m=1}^{\infty} C_{m,k} \left[-\frac{(\gamma_{m,k} R_i^k) \sin(\gamma_{m,k} R_i^k) + \cos(\gamma_{m,k} R_i^k)}{(R_i^k)^2} - \cot \text{an}(\gamma_{m,k} R_i^k) \right. \\ \left. \frac{(\gamma_{m,k} R_i^k) \cos(\gamma_{m,k} R_i^k) - \sin(\gamma_{m,k} R_i^k)}{(R_i^k)^2} \right] - k_b \sum_{m=1}^{\infty} B_{m,k} \left[\frac{m\pi}{(R_i^k)^2} (-1)^m \right], \quad R_i^k \leq R_i^{k-1} \quad (4.56)$$

To solve the above relationship, an iterative procedure will be required. This iterative procedure is as follows:

(1) Guessing R_i^k ; for the first time-step of the solidification stage, R_i^2 will be guessed.

(2) Computing $T_w(r, t_k)$ and $T_i(r, t_k)$.

(3) Checking the Stefan condition:

(a) If the right hand side of Eq. (4.56) is equal to the left hand side of Eq. (4.56), the guessed quantity for R_i^k is correct, so return back to stage (1) to guess the new quantity of R_i^k for the next time-step.

(b) If the right hand side of Eq. (4.56) is not equal to the left hand side of Eq. (4.56), the procedure (1) to (3) must be repeated.

(4) Reaching R_i^k to the center of the droplet, so the problem is solved.

In the solid cooling stage, by employing the separation of variables method, the solution for the temperature distribution is expressed as follows:

$$T_i(r, t) = T_a + \sum_{n=1}^{\infty} D_n \frac{\sin(\xi_n r)}{r} \exp(-\alpha_i \xi_n^2 t) \quad (4.57)$$

where α_i is the thermal diffusivity of ice formation, which is given by:

$$\alpha_i = \frac{k_i}{\rho_i c_i} \quad (4.58)$$

and D_n is a coefficient, which is defined by:

$$D_n = \frac{\int_0^{r_{o,2}} T_2(r, t_s) \sin(\xi_n r) r dr - T_a \left[\frac{1}{\xi_n^2} \sin(\xi_n r_{o,2}) - \frac{r_{o,2}}{\xi_n} \cos(\xi_n r_{o,2}) \right]}{\frac{r_{o,2}}{2} - \frac{1}{4\xi_n} \sin 2(\xi_n r_{o,2})} \quad (4.59)$$

The eigenvalues, ξ_n , can be calculated from the roots of the following transcendental equation:

$$\tan(\xi_n r_{o,2}) = \frac{\xi_n}{\left(\frac{1}{r_{o,2}} - \frac{(h_c + h_r)}{k_i} \right)} \quad (4.60)$$

The density of ice formation, ρ_i , can be computed by (Cox and Weeks 1983; Horjen, 2013):

$$\rho_i = \begin{cases} \frac{(1 - v'_a)}{\frac{1}{\rho_{i,p}} - \beta \left(\frac{1}{\rho_{i,p}} - \frac{1}{\rho_b} \right)}, & S_b < 125\% \\ \frac{(1 - v'_a)}{\frac{1}{\rho_{i,p}} - \beta S_b \frac{P_3(T_b)}{Q_3(T_b)}}, & S_b \geq 125\% \end{cases} \quad (4.61)$$

where v'_a is the volume fraction of air in the ice (in this study considered equal to 0), $\rho_{i,p}$ is the density of pure ice, and the parameters of $P_3(T_b)$ and $Q_3(T_b)$ are two third degree polynomials of the brine temperature, as follows (Cox and Weeks 1983; Horjen, 2013):

$$\begin{cases} P_3(T_b) = 8.903 \times 10^{-2} - 1.763 \times 10^{-2} T_b - 5.33 \times 10^{-4} T_b^2 - 8.801 \times 10^{-6} T_b^3 \\ Q_3(T_b) = -4.732 \times 10^3 - 2.245 \times 10^4 T_b - 6.397 \times 10^2 T_b^2 - 10.74 T_b^3 \end{cases} \quad (4.62)$$

To calculate the thermal conductivity of ice, Maykut and Untersteiner (1971) suggested the following formula:

$$k_i = 2.03 + 0.117 \frac{S_i}{T} \quad (4.63)$$

where S_i is the salinity of ice formation. It should be noted that Fichet and Maqueda (1997) considered a constant thermal conductivity of sea ice equal to 2.03 W/m.K. The specific heat capacity of ice, c_i , can be determined by (Ono, 1967):

$$c_i = 0.505 + 0.0018 T + 4.3115 \frac{S_i}{T^2} \quad (4.64)$$

To estimate the temperature in Eqs. (4.63) and (4.64), it is assumed that the temperature is equal to T_f .

4.5 Results and Discussion

To solve the governing equations and obtain the cooling and solidification processes as well as temperature distribution within the droplet, several parameters and properties are employed. Some of these parameters can be determined by the formulae presented in the previous sections and Table 3.1. The other parameters used in the modeling of the droplet processes are $l_f = 3.34 \times 10^5$ J/kg (Schröder Hansen, 2012), $T_{\theta,w} = 2^\circ\text{C}$, $U = 15$ m/s, $\beta =$

0.34 (Horjen, 2013, 2015; Karlekar and Desmond, 1977) and $\rho_{i,p} = 917 \text{ kg/m}^3$ (Brakel et al., 2007; Pringle et al., 2007). A Matlab code (version R14) was used in order to perform the calculations.

According to a past study by Zakrzewski (1986), the overall length of MFVs is from 40 to 50 m. In this study, an MFV with an overall length of 45 m is selected. In order to simplify the problem, it is considered that: (a) the MFV moves directly into the wind and waves, such that a spray cloud will form in front of the MFV (Fig. 3.1); (b) a water droplet diameter of 1 mm is chosen to analyze its thermal behaviour as a droplet with this size can keep its spherical shape throughout flight. According to a report by McDonald (1954), small droplets (1 mm in diameter and lower) have a spherical shape during flight.

Figure 4.3 illustrates the variations of droplet velocity (v_d) over time at a wind velocity of 15 m/s when the water droplet is moving on the MFV. From the figure, the droplet velocity at primary time is high because of its high initial velocity. With increasing time, the velocity of the droplet will decrease until reaching its lowest amount. This point is the maximum height of the droplet in the flight duration. Afterwards, with increasing time, the velocity of the droplet will increase until it attains the terminal velocity. As observed in Fig. 4.3, the water droplet with a diameter of 1 mm will attain a terminal velocity after approximately 1.2 s. Figure 4.4 indicates the pathway and position of the water droplet ($D = 1 \text{ mm}$) throughout its flight over the MFV. As shown in Fig. 4.4, the water droplet will depart in the same direction of the MFV for a very short time after formation at the edge of the vessel, and then turn back towards the deck. Additionally, the highest height of the droplet in the flight duration is equal to 4.12 m as well as the horizontal position and time

of the droplet at the moment of impact on the deck are equal to 36.24 m and 1.95 s, respectively. As a result from Figs. 4.3 and 4.4, the water droplet with a diameter of 1 mm attains the terminal velocity before impacting on the deck. Indeed, there is a rivalry between drag and gravity forces to specify the droplet trajectory during its flight over the MFV. The theoretical result in defining the trajectory of the droplet, which is illustrated in Fig. 4.4, has good agreement with the results obtained by Dehghani et al. (2016b).

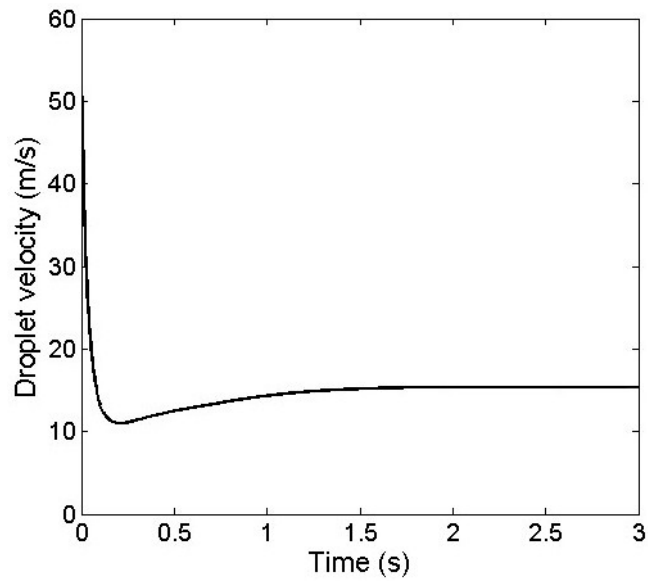


Fig. 4.3: Changes of the droplet velocity versus time at a wind velocity of 15 m/s and droplet diameter of 1 mm

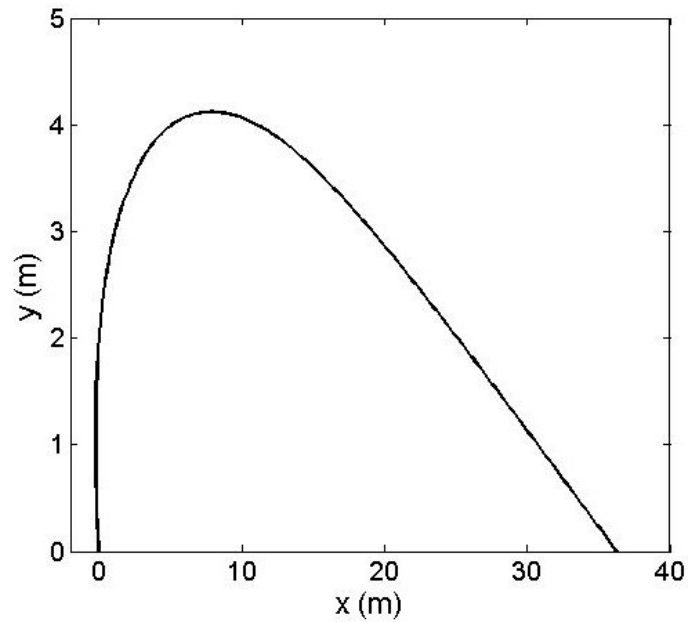


Fig. 4.4: Water droplet trajectory with a diameter of 1 mm and wind velocity of 15 m/s during its flight on the MFV

In order to find the results for the solidification stage and reduce the number and time of computations, the problem is solved for a different number of terms of series and dr (Fig. 4.5). As illustrated in this figure, the difference between the results after 6 terms of series is very small, so to obtain the results with good accuracy, 9 terms of the series are considered. Also, by decreasing dr , more accurate results are obtained. Hence, to reduce the time of computations, dr equaling 0.01 is considered.

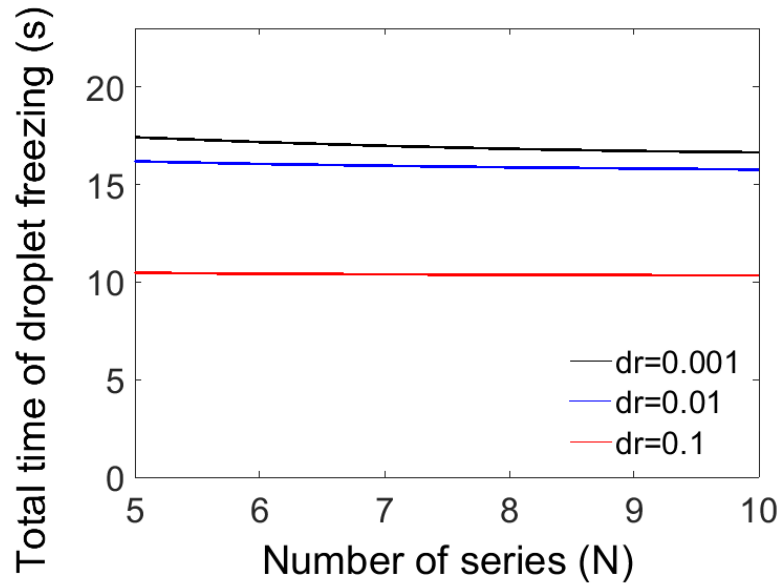
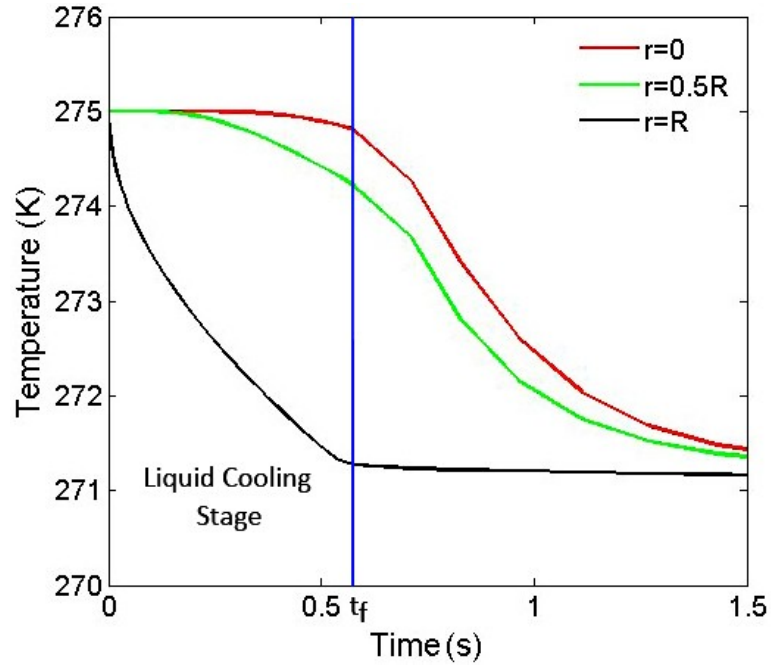


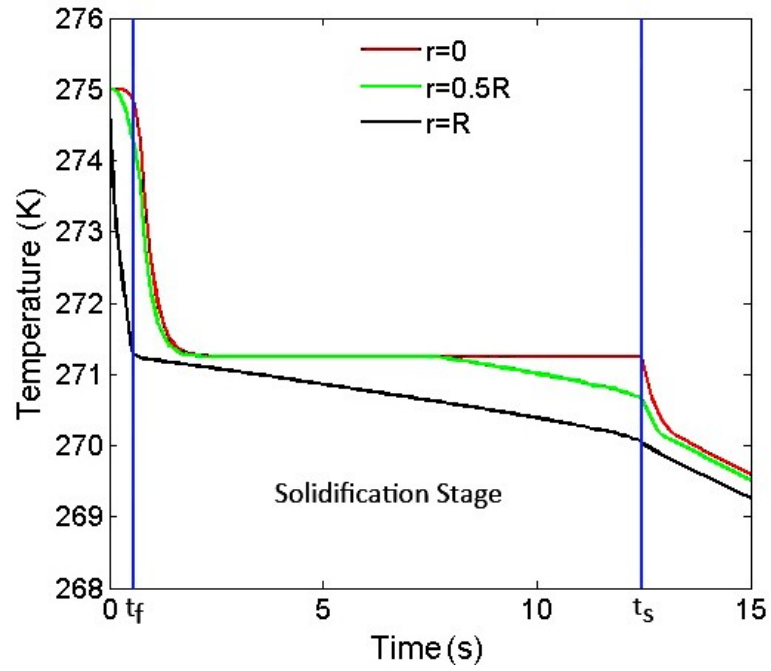
Fig. 4.5: Comparison of the total time of the droplet freezing for different number of terms of series and dr

Figure 4.6 shows the temperature changes over time for the droplet cooling and freezing processes at three different positions: the center ($r = 0$), middle ($r = 0.5R$), and the surface ($r = R$) of the water droplet. As illustrated in Fig. 4.6(a), the liquid cooling stage is very short so that t_f is equal to 0.57 s. Furthermore, the variations of temperature in this stage are non-linear, and the temperature of the droplet's center is close to the initial droplet temperature. The first ice particles will create on the surface of the water droplet until the droplet's surface temperature attains the freezing temperature. Then, an ice shell forms on the surface, and it moves towards the centre of the droplets. Fig. 4.6(b) indicates the solidification stage that is between the freezing time ($t_f = 0.57$ s) and solid time ($t_s = 12.43$ s). In addition, when the temperature of the droplet's center reaches the

freezing temperature, the change of temperature at the center of the droplet is linear until the end of this stage.



(a)



(b)

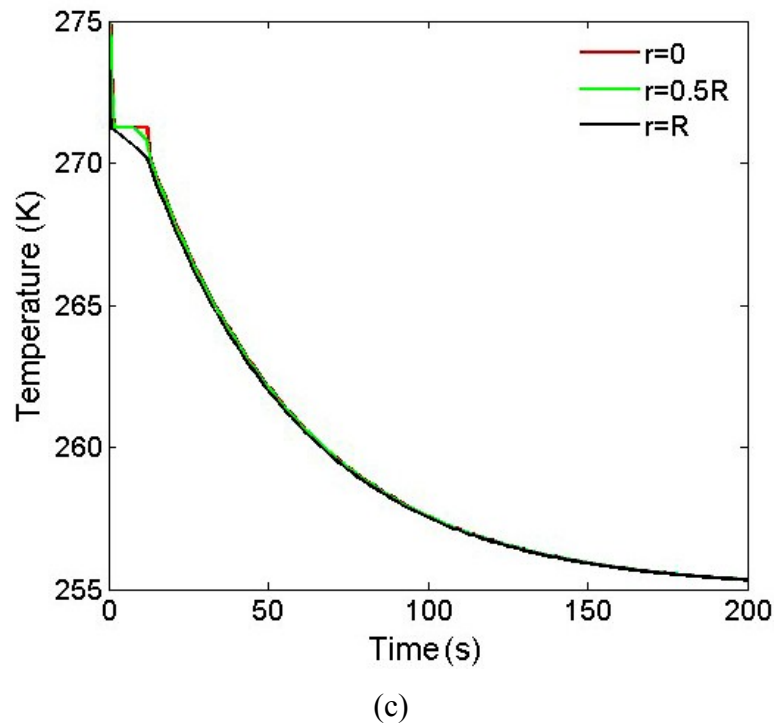


Fig. 4.6: Droplet cooling and freezing processes: (a) liquid cooling stage,
 (b) solidification stage, and (c) all stages

After the solidification stage, the solid cooling stage will begin, such that the whole droplet and its salt content will freeze completely at this stage. As illustrated in Fig. 4.6(c), the droplet temperature will attain the ambient air temperature after approximately 200 s. Also, the temperature changes in this stage are non-linear. According to Fig. 4.6, there are no nucleation and recalescence stages in the droplet freezing process. This is likely because of the salinity, high wind velocity, and insufficient supercooling to create spontaneous crystal nucleation. The trend of the droplet freezing, as shown in Fig. 4.6, is similar to the results obtained by Hindmarsh et al. (2003, 2004).

According to Fig. 4.6, the temperature of the surface and center of the water droplet at the moment of impact on the deck are equal to -2.1°C and -1.9°C , respectively. Figure 4.7 shows the changes in the position of the freezing interface from the droplet's surface over time in the solidification stage. The radius of the freezing interface, R_i , at the moment of impact on the deck (1.95 s) is equal to 0.43 mm. This means that the thickness of the ice shell on the droplet's surface is equal to 0.07 mm, and 14% of the droplet's volume is ice.

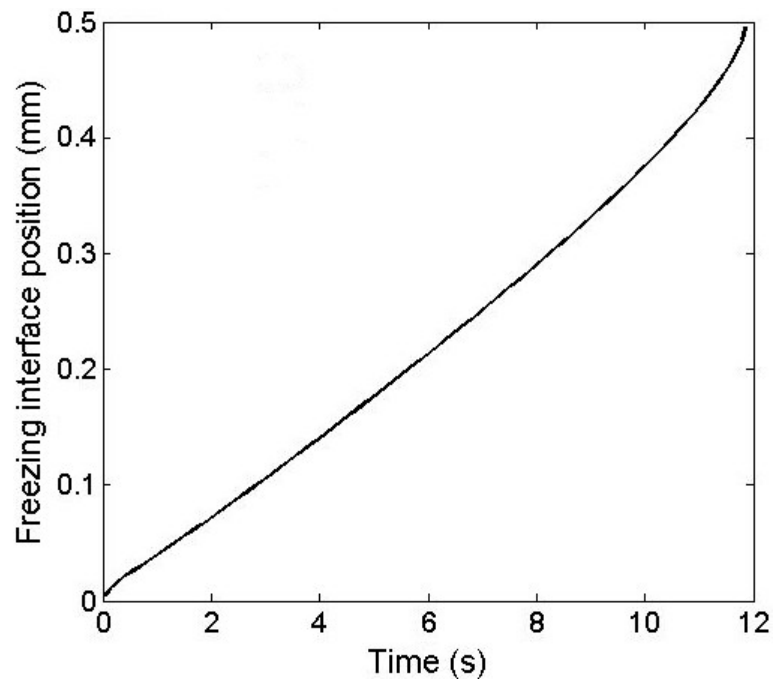


Fig. 4.7: Variations of the freezing interface position inside the droplet versus time in the solidification stage

Chapter 5

Theoretical Prediction of Ice Accumulation on Horizontal and Vertical Surfaces of Marine Vessels in Cold Regions¹

In this chapter, the amount of ice accumulation on horizontal and vertical surfaces of marine vessels during the sea spray icing event is investigated theoretically. For this purpose, predictive models are developed to determine the freezing fraction and thickness of the ice formation layer on horizontal and vertical icing plates. This chapter is divided into two main parts. In the first part, the ice accretion on a horizontal plate is predicted using two different approaches: (a) neglecting heat conduction inside the accumulated ice layer and (b) considering conduction heat transfer within the ice formation layer. A sensitivity analysis is performed to obtain the effects of the various parameters on the freezing fraction for the horizontal icing surfaces. In the second part, the ice accretion on a vertical plate is forecasted by assuming that the heat conduction through the ice layer is negligible.

1. This chapter is based on three papers. Two of them were presented at the International Conference of OMAE2015 in St John's, Canada and OMAE2016 in Busan, South Korea. Further, another was published in Heat Transfer Research (journal).

5.1 Model Description for Horizontal Surfaces

The prediction and assessment of the icing rate and the quantity of ice accumulation on marine platforms is a challenging and complex problem because marine weather conditions change substantially. Some researchers have made different assumptions to compute the growth rate of ice on marine vessels and structures by various theoretical and numerical methods. One of these assumptions is to neglect atmospheric icing, since freezing owing to sea spray is the main cause of icing phenomena in cold seas and ocean regions (Aksyutin, 1979; Brown and Roebber, 1985; Cammaert, 2013; Dehghani-Sanij et al., 2017a, 2017b; Makkonen, 1984; US Navy, 1988; Shekhtman, 1968; Shellard, 1974; Tabata et al., 1963; Zakrzewski, 1986, 1987). Another common assumption is that wave spray is regarded as being periodic for sea spray events.

To predict and analyze the icing phenomenon on horizontal surfaces of marine platforms, a typical horizontal plate from the superstructure of a supply vessel is investigated. Figure 5.1 shows a schematic of the proposed problem with associated heat fluxes. Beyond for the estimation of the ice growth rate on marine platforms, the determination of the trajectory and velocity of water droplets is an important issue in the icing phenomena, which is described in chapter 3.

5.1.1 Sea Spray Impingement

As mentioned in chapter 1, sea spray has two principal but distinct sources: wave-induced spray and wind-induced spray. Thus, the total mass flux of seawater spray ($\dot{M}_{w,t}$) during a spray event can be computed by Eq. (2.1). In this equation, the LWC of wind

spray and wave spray can be calculated from Eqs. (2.12) and (2.20), respectively. Note that the collision efficiency for a horizontal plate can be considered equal to 1 (Dehghani-Sanij et al., 2016, 2017a). To obtain $\dot{M}_{w,t}$, all details and formulae needed are given in chapter 2.

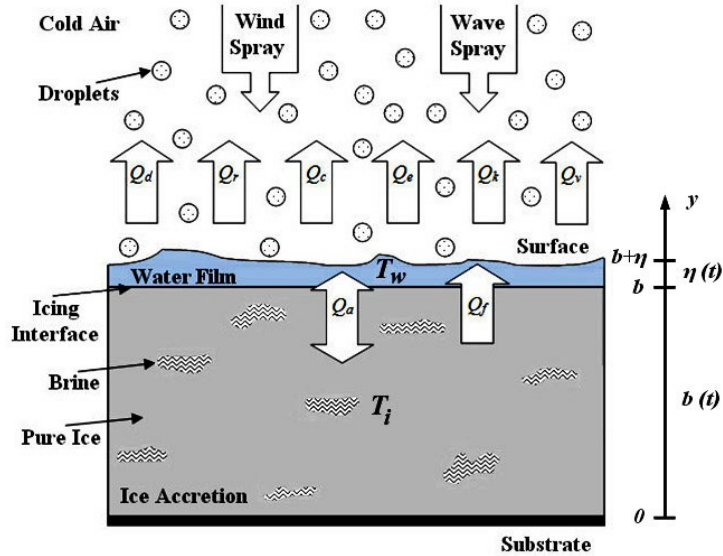


Fig. 5.1: Schematic illustration of the proposed model for a horizontal plate

5.1.2 Mass and Heat Balances and Salt Concentration

A mass balance is used in order to estimate the ice layer and water film thicknesses. According to Fig. 5.1, by employing the mass balance for the horizontal plate, Eq. (2.54) can be obtained. In this equation, the mass flux of ice formation on the plate (\dot{M}_{ice}) and the mass flux of water film on the ice accumulation layer (\dot{M}_{water}) can be determined from Eqs. (2.55) and (2.56), respectively. Moreover, U_{rs} for the horizontal plate is the droplet velocity at the moment of impact on the plate. It should be noted that the details and formulae required for defining the mass fluxes are reported in section 2.2. Also, the

ice thickness growth rate per hour, or icing intensity per hour, can be computed by Eq. (2.57).

According to Fig. 5.1, there are several heat fluxes present in the icing process. These heat fluxes are described in all details in section 2.3. The salinity of sea or ocean water is an important factor in the growth rate of marine icing. According to Makkonen (1987) and Szilder et al. (1995), during the freezing of a water film with a salinity of S_b , the ice formation can entrap only a part of the salt, namely βS_b , and the remainder will be rejected in the solution. Therefore, the salinity of the water film is related to the freezing temperature as follows (Schwerdtfeger, 1963):

$$S_b = \begin{cases} -0.0182 T_f, & \text{if } 0^\circ\text{C} \geq T_f > -8.2^\circ\text{C} \\ 0.149 - 0.01(T_f + 8.2), & \text{if } -8.2^\circ\text{C} \geq T_f > -23^\circ\text{C} \end{cases} \quad (5.1)$$

where T_f is the freezing temperature in units of $^\circ\text{C}$. In Eq. (5.1), the absolute value of brine salinity is used. Based on studies conducted by Horjen (2013, 2015), to calculate the salinity of the water film for a stationary icing model with no convective movement of the brine film is adopted by the following formula:

$$S_b = \frac{\dot{M}_{water} S_w}{\dot{M}_{water} + \dot{M}_{evap.w} + \frac{(Q_t + Q_i)}{l_f}} \quad (5.2)$$

where Q_i is the conduction heat flux through the ice formation layer at the water-ice interface and Q_t is the net heat flux in the brine film at the air-water interface, which is equal to (Horjen, 2013):

$$Q_t = Q_c + Q_e + Q_d + Q_r \quad (5.3)$$

By neglecting $\dot{M}_{evap.w}$, and from Eq. (2.76) and Eq. (5.2), after simplification, Eq. (2.58) can be obtained to estimate the salinity of the water film. Furthermore, the salinity of the ice formation can be computed by Eq. (2.59).

5.1.3 Horizontal Plate without Consideration of Heat Conduction in the Ice Layer

A number of past studies assumed that conduction heat transfer inside the ice formation layer was negligible, and therefore neglected it (Dehghani-Saniij et al., 2016; Horjen, 1990, 2013, 2015; Kulyakhtin and Tsarau, 2014; Lozowski et al., 2000; Makkonen, 1987, 2010). Additionally, the heat fluxes from the air-water interface are conducted by the water film to the freezing interface (water-ice). Heat conduction is a major heat transfer mechanism in the water film, and the temperature gradient is assumed to be linear when the water film thickness is less than 3 mm (Kulyakhtin and Tsarau, 2014; Myers and Charpin, 2004).

As illustrated in Fig. 5.1, Q_a is the conduction heat flux and Q_f is the latent heat flux due to the freezing of a certain fraction of the impinging water. The latent heat flux is represented by Eq. (2.76). For a 1-D case, the conduction heat flux in the water film is expressed by:

$$Q_{a,w} = -k_w \frac{T_s - T_f}{\eta} \quad (T_s < T_f) \quad (5.4)$$

where k_w is the thermal conductivity of the brine, T_f is the freezing temperature of brine at the water-ice interface, η is the thickness of water film and T_s is the temperature of the water film at the air-water interface (Eq. (2.60)).

By taking the heat balance at the air-water interface and ignoring Q_v and Q_k , the formula can be written as:

$$\frac{T_s - T_f}{\eta} = -\frac{Q_c + Q_e + Q_d + Q_r}{k_w} = A_r - B_r T_s \quad (5.5)$$

Here, A_r and B_r are coefficients independent of the water film temperature. They are defined as:

$$A_r = \frac{[(h_c + C e_0 RH + \dot{M}_{w,t} c_w + \sigma a) T_a + C E_0 (RH - 1)]}{k_w} \quad (5.6)$$

$$B_r = \frac{[h_c + C e_0 + \dot{M}_{w,t} c_w + \sigma a]}{k_w} \quad (5.7)$$

By using the heat balance at the ice-water interface, the following equation is obtained:

$$l_f \rho_i (1 - \beta) \frac{db}{dt} = -k_w \frac{T_s - T_f}{\eta} \quad (5.8)$$

Also, by combining equations (5.5) and (5.8), the formula can be written as follows:

$$l_f \rho_i (1 - \beta) \frac{db}{dt} = -k_w (A_r - B_r T_s) \quad (5.9)$$

In the above equation, T_s is in units of Kelvin. By substituting $\frac{db}{dt} = \frac{n \dot{M}_{w,t}}{\rho_i}$ in equation (5.9) and solving it, the freezing fraction, n , can be determined.

To solve the governing equations as well as determine the freezing fraction and the thickness of the ice layer, several specified parameters and transport properties have been used. Table 5.1 illustrates the parameters used for the modeling of a typical horizontal plate with impinging water droplets.

Table 5.1: Parameter values

Parameter	Value	Units	References
a	8.1×10^7	K^3	(Chung and Lozowski, 2010; Lozowski et al., 2000)
B_s	1 for plate	-	(Horjen, 1983; Zakrzewski, 1987)
c_a	1005	J/kg.K	(Tracy et al., 1980; Eng. Toolbox, 2016)
c_w	3.93×10^3	J/kg.K	(Schröder Hansen, 2012)
f_s	1	-	(Jones and Andreas, 2012)
H_{bow}	4	m	-
k	0.40	-	(Kulyakhtin and Tsarau, 2014)
k_a	0.0243	W/m.K	(Eng. Toolbox, 2017)
k_w	0.58	W/m.K	(Eng. Toolbox, 2017)
L	1	m	-
l_f	3.34×10^5	J/K	(Green and Perry, 2008)
l_v	2.27×10^6	J/K	(Green and Perry, 2008)
P	10^5	Pa	-
Pr	0.720	-	(Eng. Toolbox, 2017)
RH	80	%	(Jones and Andreas, 2012; Schröder Hansen, 2012)
Sc	0.595	-	(Kato, 2012)
S_w	34	‰	(Schröder Hansen, 2012)
U	20.6	m/s	(Borisenkov and Panov, 1972; Lozowski et al., 2000)
v_s	12.9	m/s	(Lozowski et al., 2000)
z	10	m	-
α	0	°	(Lozowski et al., 2000)
β	1/3	-	(Horjen, 2013, 2015)
γ	180	°	-
ε	0.622	-	(Kato, 2012; Makkonen, 1989)
v_a	1.33×10^{-5}	m^2/s	(Eng. Toolbox, 2017)
ρ_w	1027	Kg/m^3	(Schröder Hansen, 2012)
ρ_i	900	Kg/m^3	(Jones and Andreas, 2012; Kulyakhtin and Tsarau, 2014)
σ	5.67×10^{-8}	$\text{W/m}^2 \cdot \text{K}^4$	-

Figure 5.2 shows the variations in the freezing fraction with air temperature. As can be seen in this figure, when the air temperature goes down to -1°C , ice accretion begins. The freezing fraction, n , is equal to 1 at the air temperature of -12.6°C . Also, the changes of freezing fraction are non-linear. The variations of icing intensity per hour, N_i , versus air temperature are demonstrated in Fig. 5.3. These variations from -1°C to -12.6°C can be divided into 3 parts. The first part is almost linear between -1°C and -4°C . The second part, from -4°C to -10°C , is non-linear. The last part is approximately linear between -10°C and -12.6°C . The highest growth rate of icing is near $T_a = -7^{\circ}\text{C}$, after which the icing rate decreases. Furthermore, the manner of change in the freezing fraction and the icing intensity is identical.

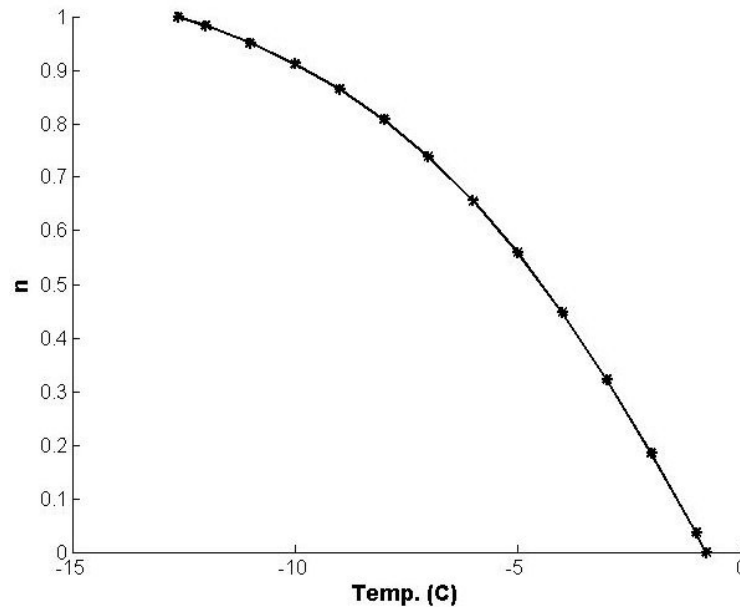


Fig. 5.2: Changes in the freezing fraction versus air temperature at

$$v_s = 12.9 \text{ m/s}, U = 20.6 \text{ m/s}, S_w = 34\text{‰} \text{ and } \alpha = 0^{\circ}$$

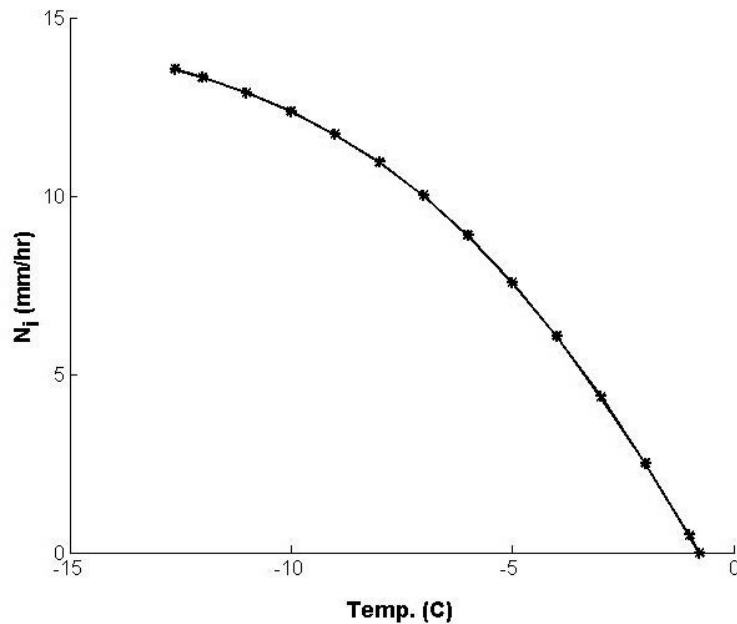


Fig. 5.3: Changes in the icing intensity per hour versus air temperature at

$$v_s = 12.9 \text{ m/s}, U = 20.6 \text{ m/s}, S_w = 34\text{‰} \text{ and } \alpha = 0^\circ$$

Figure 5.4 indicates the variations of ice and water film thicknesses over time for the freezing fraction of 0.739 and an air temperature of -7°C , as well as for the freezing fraction of 1 and an air temperature of -12.6°C . As can be observed in this figure, the ice layer and water film thicknesses are 2.00 cm and 0.62 cm, respectively. The variations of the ice layer thickness over time at different air temperatures are displayed in Fig. 5.5. One can observe that the changes of ice formation thickness over time are nearly linear because, in this study, the average amounts of wind spray and wave spray have been considered for a seawater spray event. In other words, there is a stationary icing model. Additionally, all parameters such as air temperature, vessel speed, wind velocity and salinity are constant during the event.

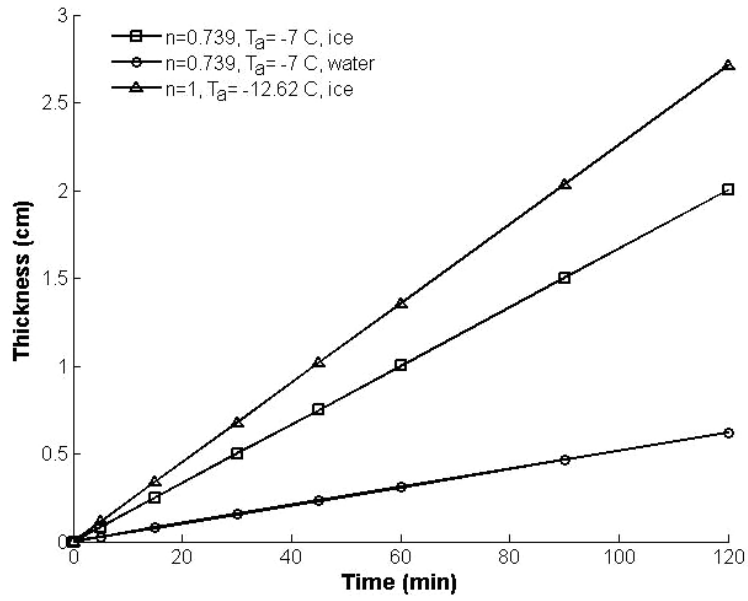


Fig. 5.4: Changes in ice layer and water film thicknesses for two different air temperatures at $v_s = 12.9 \text{ m/s}$, $U = 20.6 \text{ m/s}$, $S_w = 34\text{‰}$ and $\alpha = 0^\circ$

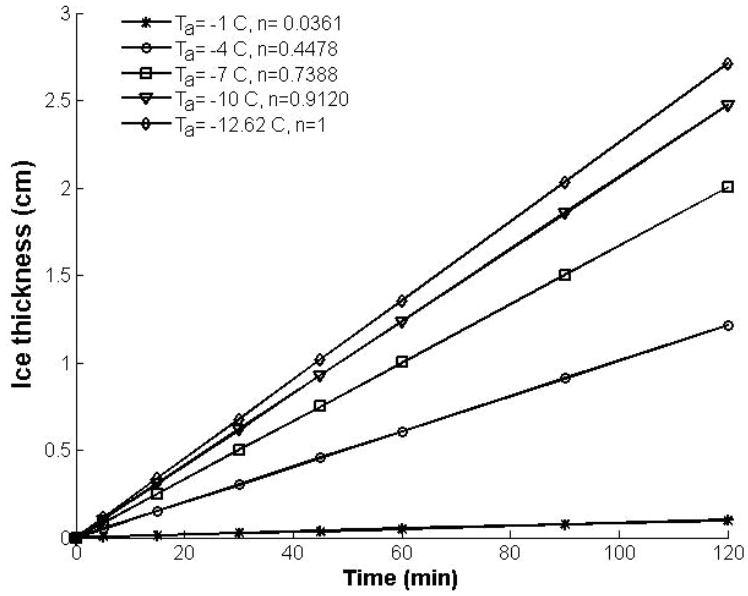


Fig. 5.5: Changes in ice thickness for different air temperatures at $v_s = 12.9 \text{ m/s}$, $U = 20.6 \text{ m/s}$, $S_w = 34\text{‰}$ and $\alpha = 0^\circ$

According to Table 5.1, often parameters are approximately fixed during the sea spray icing event, but some parameters are not constant. The variable parameters affect the freezing fraction, but among these parameters, some of them have a significant impact on the freezing fraction, such as wind velocity, U , vessel speed, v_s , air temperature, T_a , spray water salinity, S_w , height from the water's surface, z , and the angle between the vessel heading and the wind/wave direction, α . Figures 5.6 to 5.10 show the effects of wind velocity, salinity of the water spray, height from the water's surface, vessel speed and the angle between vessel heading and wind/wave direction, respectively, when other parameters are constant.

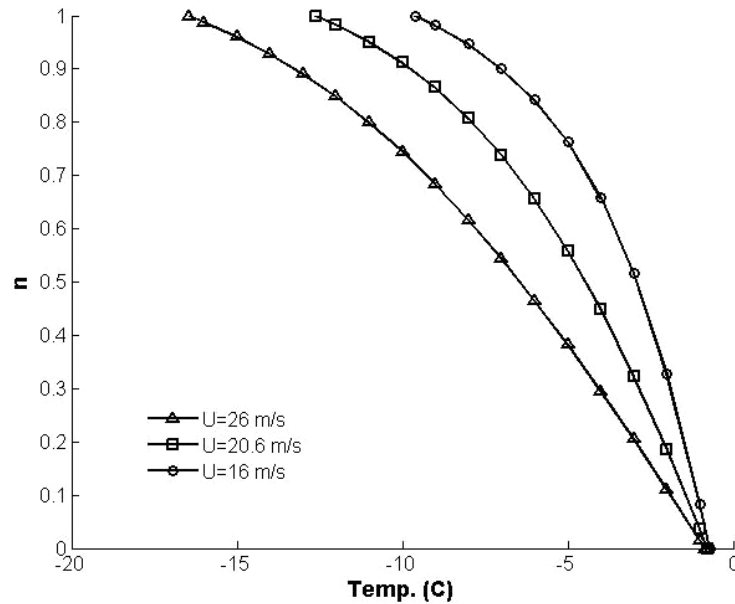


Fig. 5.6: Changes in freezing fraction versus air temperature for different wind velocities

at $v_s = 12.9 \text{ m/s}$, $S_w = 34\%$, $RH = 80\%$, $L = 1 \text{ m}$ and $\alpha = 0^\circ$

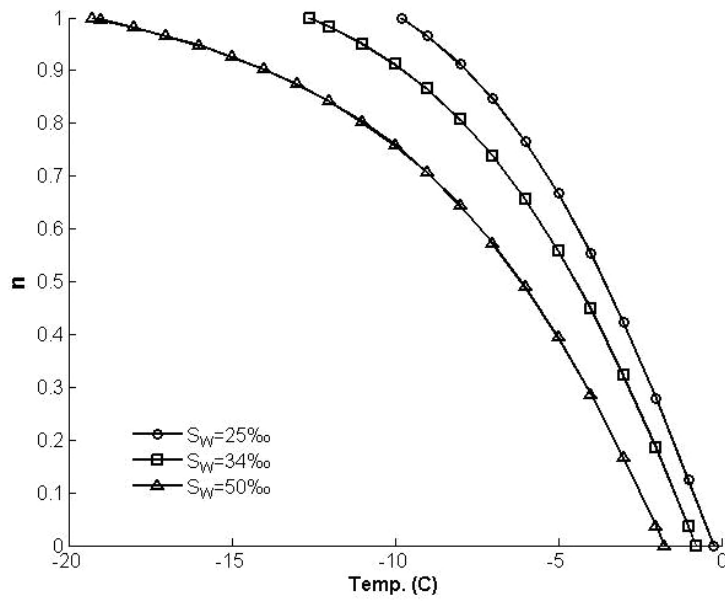


Fig. 5.7: Changes in freezing fraction versus air temperature for different salinities at

$$v_s = 12.9 \text{ m/s}, U = 20.6 \text{ m}, RH = 80\%, L = 1 \text{ m/s and } \alpha = 0^\circ$$

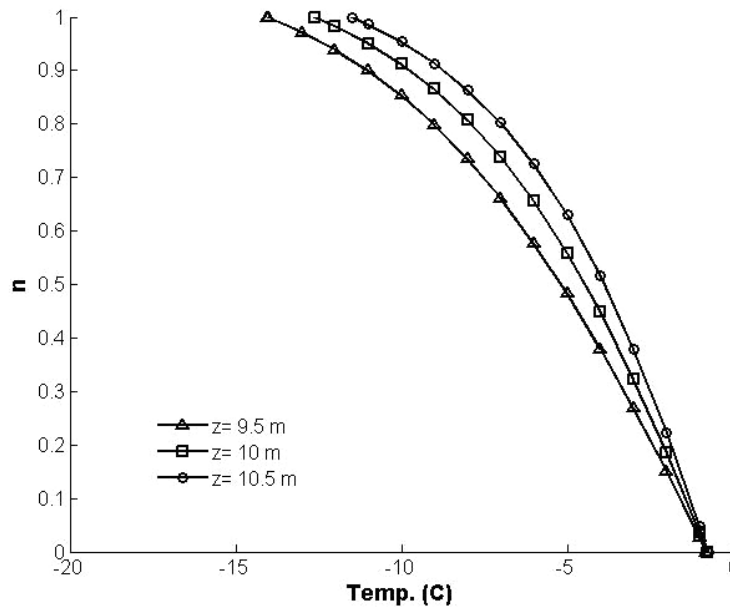


Fig. 5.8: Changes in freezing fraction versus air temperature for different heights at

$$v_s = 12.9 \text{ m/s}, U = 20.6 \text{ m/s}, S_w = 34\text{‰}, RH = 80\%, L = 1 \text{ m and } \alpha = 0^\circ$$

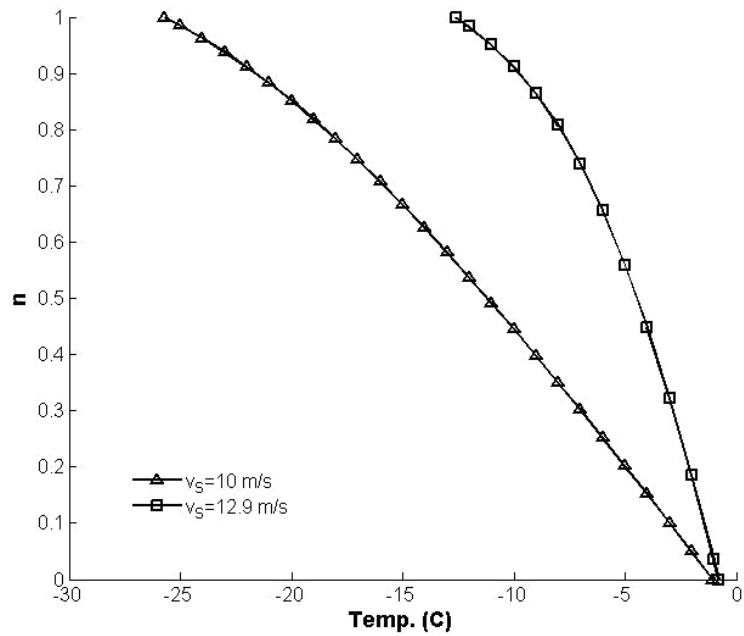


Fig. 5.9: Changes in freezing fraction versus air temperature for different vessel speeds at

$$U = 20.6 \text{ m/s}, S_w = 34\%, RH = 80\%, L = 1\text{m} \text{ and } \alpha = 0^\circ$$

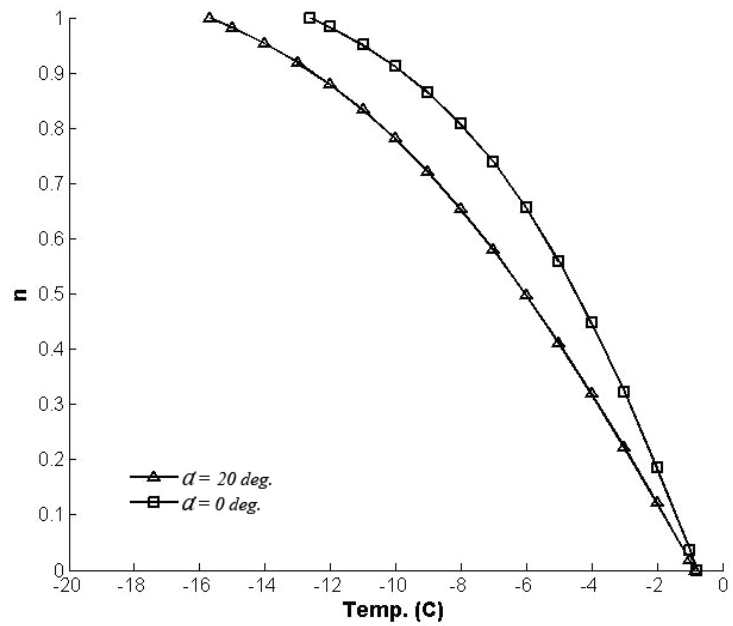


Fig. 5.10: Changes in freezing fraction versus air temperature for different heading angles

$$\text{at } v_s = 12.9 \text{ m/s}, U = 20.6 \text{ m/s}, S_w = 34\%, RH = 80\% \text{ and } L = 1\text{m}$$

According to Figs. 5.6 to 5.10, the following results can be observed. Wind velocity, U , affects two main parameters: (1) the total flux of seawater spray and (2) the convection heat transfer coefficient, so that the total flux of seawater spray is a function of the LWC of the wind spray, wave spray, wave height and wave period. In addition, the convection heat transfer coefficient is a function of the Reynolds number. Thus, by increasing the wind velocity, dry-growth icing (rime) occurs at a lower air temperature (Fig. 5.6).

The salinity of the water spray, S_w , has an impact on the water film temperature; when the salinity rises, the freezing fraction decreases (Fig. 5.7). Using salt can decrease the amount of ice accretion on marine vessels and structures. The effect of the height from the water's surface on the freezing fraction is significant (Fig. 5.8) because both the LWC of the wind spray and the wave spray are functions of height. Furthermore, most sea spray occurs up to 15-20 m above the sea surface and forms about 50% to 90% of the icing on ships (Cammaert, 2013). Vessel speed, v_s , has a significant effect on the total flux of seawater spray and the convection heat transfer coefficient. According to Fig. 5.9, by decreasing vessel speed, the freezing fraction equal to 1 occurs at lower air temperatures. As mentioned, the vessel heading, α , is the angle between the vessel heading and the wind/wave direction (Fig. 5.11). Since α is equal to 0° , the vessel goes into the waves directly and when α is 180° , the vessel passes from the waves. The freezing fraction equal to 1 occurs at higher air temperatures when the vessel moves directly into the waves (Fig. 5.10).

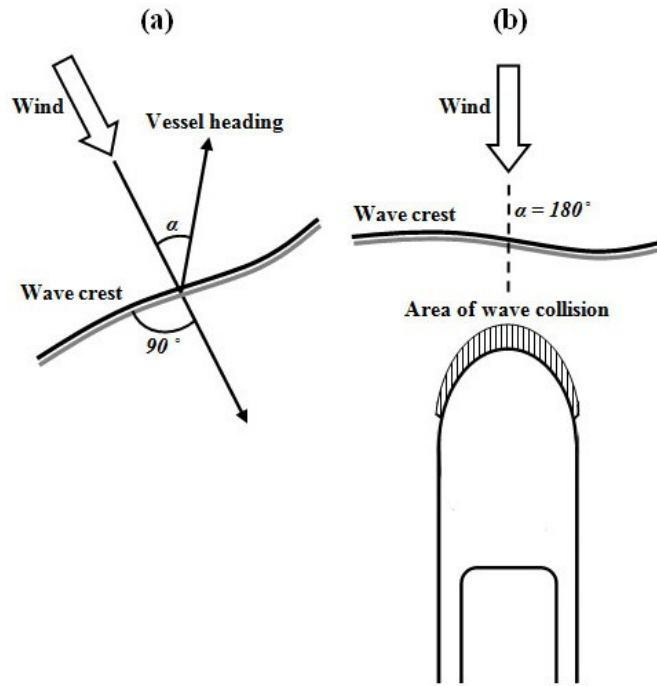


Fig. 5.11: Schematic representation of (a) the angle between the vessel heading and the wind/wave direction and (b) the seawater spray flight over a marine vessel

5.1.4 Horizontal Plate with Consideration of Heat Conduction in the Ice Layer

5.1.4.1 Heat Transfer Formulation

According to Fig. 5.1, to predict the phenomenon of marine icing and the quantity of ice accumulation on a horizontal icing surface, in this section, conduction heat transfer inside the ice formation layer is considered. Hence, the one-dimensional Stefan problem will be analyzed.

The governing equations for the water film and ice layer are expressed, respectively, by:

$$\frac{\partial}{\partial y} \left(k_b \frac{\partial T_w}{\partial y} \right) = \rho_b c_b \frac{\partial T_w}{\partial t}, \quad b \leq y \leq b + \eta \quad (5.10)$$

$$\frac{\partial}{\partial y} \left(k_i \frac{\partial T_i}{\partial y} \right) = \rho_i c_i \frac{\partial T_i}{\partial t}, \quad 0 \leq y \leq b \quad (5.11)$$

where T_w is the temperature in the water film, T_i is the temperature in the ice layer, k_b is the thermal conductivity of brine, k_i is the thermal conductivity of ice, ρ_b is the density of brine, ρ_i is the density of ice formation, c_b is the specific heat capacity of brine and c_i is the specific heat capacity of ice accretion.

The ice accumulation layer contains pure ice, brine pockets and air bubbles (Blackmore et al., 2002; Makkonen, 1987). In reality, the volume and distribution of the brine pockets and air bubbles, as well as the concentration of brine pockets in the ice layer are not uniform. As a result, the thermal conductivity, density and specific heat capacity of ice accretion are a function of time, position and temperature. The ice formation can be called “spongy ice” (Makkonen, 1987). In this study, it is assumed that the volume and distribution of brine pockets and air bubbles as well as the concentration of the brine pockets within the accumulated ice are uniform. Thus, Eqs. (5.10) and (5.11) can be written as follows:

$$\frac{\partial T_w}{\partial t} = \alpha_b \frac{\partial^2 T_w}{\partial y^2}, \quad \alpha_b = \frac{k_b}{\rho_b c_b}, \quad b \leq y \leq b + \eta \quad (5.12)$$

$$\frac{\partial T_i}{\partial t} = \alpha_i \frac{\partial^2 T_i}{\partial y^2}, \quad \alpha_i = \frac{k_i}{\rho_i c_i}, \quad 0 \leq y \leq b \quad (5.13)$$

where α_i and α_b are the thermal diffusivity of ice formation and brine, respectively. By using a phase change or Stefan condition at the ice-water interface, the following equation can be obtained:

$$\rho_i l_f (1 - \beta) \frac{db}{dt} = k_i \frac{\partial T_i}{\partial y} - k_b \frac{\partial T_w}{\partial y} \quad (5.14)$$

The above equation illustrates that the velocity of the interface is commensurate with the heat flux across it. To solve the problem, several boundary and initial conditions are needed, which are expressed as follows.

By applying the heat balance at the air-water interface, $b + \eta$, the equation below can be written as:

$$Q_{a,w} = Q_c + Q_e + Q_d + Q_r \quad (5.15)$$

where $Q_{a,w}$ is the heat conduction in the water film. By substituting Eqs. (2.61), (2.66), (2.68) and (2.72) into the above equation, the following relationship can be obtained.

$$\frac{dT_w}{dy} = A_w - B_w T_w(y, t), \quad y = b + \eta \quad (5.16)$$

where A_w and B_w are coefficients independent of the water film temperature. They are determined as:

$$A_w = \frac{[(h_c + C e_0 RH + \dot{M}_{w,wind} c_w + \sigma a) T_a + C E_0 (RH - 1) + \dot{M}_{w,wave} c_w T_{d,wave}]}{k_b} \quad (5.17)$$

$$B_w = \frac{[h_c + C e_0 + \dot{M}_{w,t} c_w + \sigma a]}{k_b} \quad (5.18)$$

For the ice-water interface, b , the ice accretion and brine are at the freezing temperature, T_f . Thus,

$$T_w(b, t) = T_i(b, t) = T_f \quad (5.19)$$

Also, at the surface between the ice and substrate, a constant temperature is assumed. Therefore,

$$T_i(0, t) = T_{sub} \quad (5.20)$$

The initial conditions are given by:

$$\eta(0) = b(0) = 0, \quad t = 0 \quad (5.21)$$

By considering a constant temperature below freezing at the substrate, the process of icing happens in two separate phases. In the first phase, all the impinged water droplets will freeze immediately, but in the second phase, both the water film and the ice layer will increase at the same time. During the first phase, when only ice accumulation is increasing, since the freezing fraction, n , is equal to 1, the thickness of the ice layer can be obtained by the following relationship:

$$b(t) = \frac{\dot{M}_{w,t}}{\rho_i} t \quad (5.22)$$

Non-dimensionalization of the heat equation for the ice layer is performed by taking the time-scale from Eq. (5.22), thereby yielding:

$$\frac{\partial^2 T_i^*}{\partial y^{*2}} = \lambda_i \frac{\partial T_i^*}{\partial t^*} \quad (5.23)$$

where

$$T^* = \frac{T - T_a}{T_f - T_a}, \quad y^* = \frac{y}{b}, \quad t^* = \left(\frac{\dot{M}_{w,t}}{\rho_i b} \right), \quad \lambda_i = \frac{c_i b^* \dot{M}_{w,t}}{k_i} \quad (5.24)$$

and

$$b^* \ll \frac{k_i}{c_i \dot{M}_{w,t}} \quad (5.25)$$

Here b^* is the non-dimensional height-scale. The right hand side of Eq. (5.23) is very small ($\lambda_i \ll 1$). Thus,

$$\frac{\partial^2 T_i^*}{\partial y^{*2}} \approx 0 \quad (5.26)$$

The dimensional form of the above equation can be written as:

$$\frac{\partial^2 T_i}{\partial y^2} \approx 0 \quad (5.27)$$

To solve Eq. (5.27) and obtain the temperature distribution in the ice layer, two boundary conditions are required. One of them is Eq. (5.20) and another, by employing the heat balance at the air-ice interface, is given by:

$$Q_{a,i} = Q_c + Q_e + Q_d + Q_r \quad (5.28)$$

where $Q_{a,i}$ is the heat conduction term in the ice layer. By substituting Eqs. (2.61), (2.66), (2.68) and (2.72) in Eq. (5.28), the following relationship can be obtained.

$$\frac{\partial T_i}{\partial y} = A_i - B_i T_i(y, t), \quad y = b \quad (5.29)$$

where the coefficients of A_i and B_i are defined as:

$$A_i = \frac{[(h_c + C e_0 RH + \dot{M}_{w,wind} c_w + \sigma a) T_a + C E_0 (RH - 1) + \dot{M}_{w,wave} c_w T_{d,wave}]}{k_i} \quad (5.30)$$

$$B_i = \frac{[h_c + C e_0 + \dot{M}_{w,t} c_w + \sigma a]}{k_i} \quad (5.31)$$

Then the temperature distribution in the ice layer is written as follows:

$$T_i = G y + T_{sub} \quad (5.32)$$

where G is a constant coefficient. Eq. (5.32) illustrates that the temperature profile is linear in y . These problems are called “quasi or pseudo-steady” (Myers and Hammond,

1999). Time enters the equation through the moving boundary conditions, exerted at $y=b(t)$.

In the second phase, a water film increases on the surface of the ice layer. As in the previous phase, the energy equations, (5.12) and (5.13), can be simplified to quasi-steady forms. Thus,

$$\frac{d^2 T_i}{dy^2} \approx 0 \quad , \quad \frac{d^2 T_w}{dy^2} \approx 0 \quad (5.33)$$

while

$$b^* \ll \frac{k_i}{(1-\psi) c_i \dot{M}_{w,t}} \quad \& \quad \eta^* \ll \frac{k_b}{\psi c_b \dot{M}_{w,t}} \quad (5.34)$$

where ψ is the fraction of brine that stays liquid. The water film has to remain thin, unless there is a slow growth of water, $\psi \ll 1$, which permits time for the temperature to adjust.

The temperature distribution in the ice layer is given as follows:

$$T_i = \left(\frac{T_f - T_{sub}}{b} \right) y + T_{sub} \quad (5.35)$$

Also, the temperature distribution in the water film is equal to:

$$T_w = \left(\frac{A_w - B_w T_f}{1 + B_w \eta} \right) (y - b) + T_f \quad (5.36)$$

In the water film, there is a temperature gradient. The temperature gradient will be large when the freezing fraction, n , is near 0, and will be small when the freezing fraction, n , is near 1. Note that during the icing conditions, there will be a turbulent mixture of the water film, so by considering the average value of the water film temperature, Eq. (5.36) will be more accurate.

By taking the derivative of Eqs. (5.35) and (5.36) and substituting these equations in the Stefan condition (Eq. (5.14)), the equation below will be obtained:

$$\rho_i l_f (1 - \beta) \frac{db}{dt} = k_i \left(\frac{T_f - T_{sub}}{b} \right) - k_b \left(\frac{A_w - B_w T_f}{1 + B_w \eta} \right) \quad (5.37)$$

By substituting Eq. (2.55) in Eq. (5.37), the following equation can be obtained:

$$l_f (1 - \beta) n \dot{M}_{w,t} - k_i \left(\frac{T_f - T_{sub}}{b} \right) + k_b \left(\frac{A_w - B_w T_f}{1 + B_w \eta} \right) = 0 \quad (5.38)$$

By solving the above equation, the freezing fraction, n , will be determined. For this purpose, the parameters of b , η , T_f and T_{sub} should be replaced in Eq. (5.38). The parameters of b and η are defined by integrating Eqs. (2.55) and (2.56), respectively. Also, the freezing temperature of water film, T_f , can be calculated by Eq. (5.1). According to Myers and Charpin (2004), T_{sub} will usually be equal to the ambient temperature, T_a .

5.1.4.2 Results and Discussion

To solve the algebraic equations and obtain the freezing fraction and the ice layer thickness, several parameters and properties will be used. According to Cox and Weeks (1983) and Horjen (2013), the density of ice can be approximated by Eq. (4.61). Also, the density of brine, ρ_b , is given by Eq. (2.96). The thermal conductivity of brine, k_b , can be calculated by Eq. (3.33). The Prandtl number, Pr , and the Schmidt number, Sc , respectively, are given by Eqs. (3.13) and (3.17). Pringle et al. (2007) developed a model for estimating the thermal conductivity of ice by considering the first-order temperature dependence of the individual conductivities in the ice. Additionally, they neglected the conductivity of the air bubbles. This formula is written as follows:

$$k_i = \left(\frac{\rho_i}{\rho_{i,p}} \right) \left[2.11 - 0.011T + 0.09 \frac{S_i}{T} - \frac{(\rho_i - \rho_{i,p})}{1000} \right] \quad (5.39)$$

where S_i is the salinity of ice formation, T is the temperature in degrees Celsius and the thermal conductivity is in units of W/mK. The above formula is based on a geometrical configuration of bubbly brine inclusions. Note that Fichfet and Maqueda (1997) considered a constant thermal conductivity of sea ice equal to 2.03 W/mK. The specific heat capacity of ice formation, c_i , can be determined by (Ono, 1967):

$$c_i = 0.505 + 0.0018T + 4.3115 \frac{S_i}{T^2} \quad (5.40)$$

In this relation, c_i , is in units of Cal/gr°C. To estimate the temperature in Eqs. (5.39) and (5.40), a temperature equal to T_f was assumed. Other parameters in the modeling of the horizontal icing process are illustrated in Table 5.1.

Figure 5.12 indicates the freezing fraction changes with air temperature at three different times. As can be seen in this figure, when the air temperature goes below -1.85°C (271.3 K), ice accumulation begins. Tabata et al. (1963), Tabata (1969), Lundqvist and Udin (1977) as well as Cammaert (2013) reported that ice accretion will form on marine platforms once the air temperature is approximately -2°C (271.15 K). As a result from Fig. 5.12, with increasing time, freezing occurs at lower air temperatures; for instance, there is a lower air temperature for the freezing fraction equal to 1 when time increases. Thus, the freezing fraction is a strong function of time. Figure 5.13 illustrates the changes in the freezing fraction over time for several air temperatures. At initial times, water droplets will freeze quickly because the droplet collision adapts to the sub-zero substrate temperature, such that there is nearly dry-growth icing at air temperatures of 266

K and 264 K. By increasing time, both the ice layer and water film will grow simultaneously; however, with increasing time at a constant air temperature, the growth rate of ice accumulation is less than the water film. Additionally, Fig. 5.13 shows that the amount of the freezing fraction at lower air temperatures is greater compared to higher air temperatures. Therefore, the air temperature is an important factor in increasing icing rates.

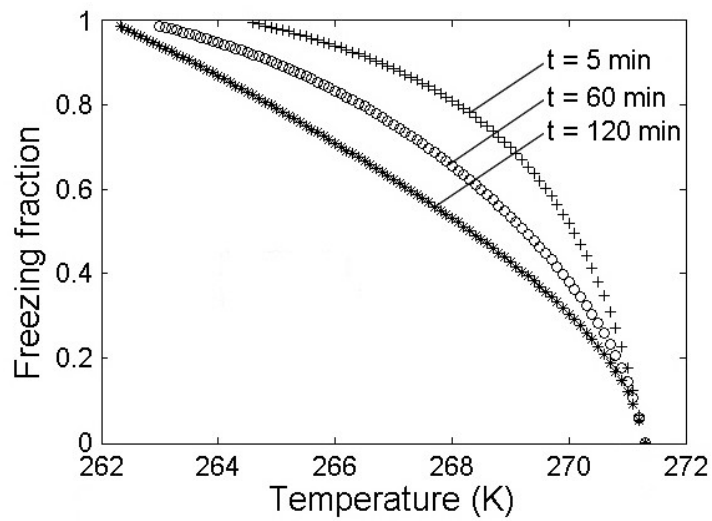


Fig. 5.12: Variations of the freezing fraction versus air temperature at three different times

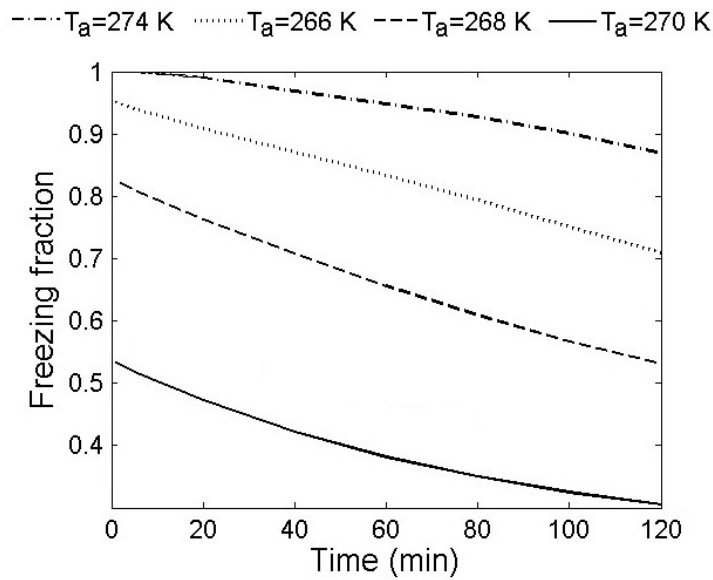


Fig. 5.13: Variations of the freezing fraction versus time for several air temperatures

Figure 5.14 shows the changes in ice formation thickness with time for different air temperatures. As observed in this figure, with increasing time and decreasing air temperature, the thickness of ice accumulation will increase despite the change of salinity in the ice layer. There is a feedback mechanism between the icing intensity and the water film salinity, such that with increasing icing intensity, the water film salinity will increase (Horjen, 2015); then, due to the increased salinity over time, the icing intensity will decrease. Additionally, salinity has a smaller impact on the freezing fraction at lower air temperatures. In other words, the icing intensity will increase at lower air temperatures. As described in Figs. 5.12 to 5.14, the parameters of time, air temperature and salinity can play a significant role in the growth rate of ice on vessels and marine platforms.

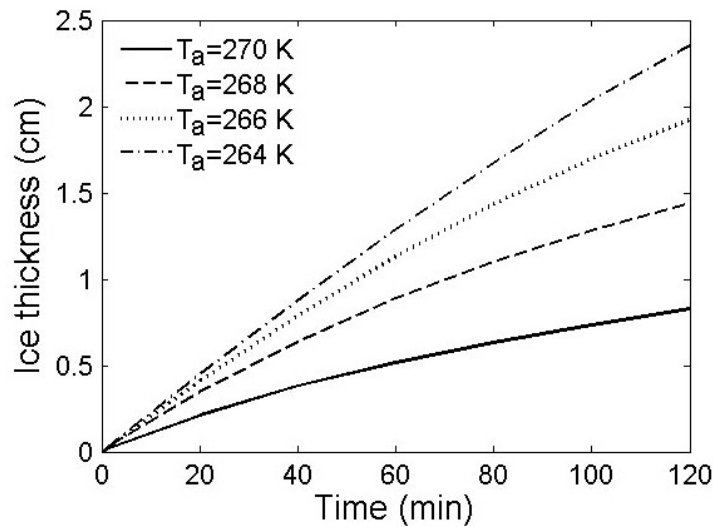


Fig. 5.14: Variations of the ice formation thickness versus time at different air temperatures

Table 5.2 indicates the changes in air temperature and the thickness of ice accumulation at different times for dry-growth icing. Also, Table 5.3 displays the changes in the freezing fraction and the thicknesses of ice layer and water film for wet-growth icing at $T_a = 266.1$ K. Figure 5.15 shows and compares the changes of the ice layer and water film thicknesses over time for two distinct conditions, which are expressed in Tables 5.2 and 5.3. According to Fig. 5.15 and Table 5.3, the thicknesses of the ice layer and water film, when time is equal to 5 min, are 1.057 mm and 0.064 mm, respectively. In other words, after impinging on the surface, the water droplets will freeze immediately at initial times (approximately less than 5 min); this is called the first phase. However, for the second phase, both the water film and ice layer increase at the same time, but the growth rate of these layers varies over time.

Table 5.2: Variations of air temperature and thickness of ice layer at different times for dry-growth icing

Time (min)	Air temperature (K)	Ice layer thickness (mm)
5	264.4	1.13
15	263.9	3.39
30	263.3	6.79
45	262.9	10.18
60	262.6	13.57
90	262.2	20.35
120	261.9	27.16

Table 5.3: Variations of the freezing fraction and ice layer and water film thicknesses for glaze icing at $T_a = 266.1$ K

Time (min)	Freezing fraction	Ice layer thickness (mm)	Water film thickness (mm)
5	0.9354	1.057	0.064
15	0.9129	3.094	0.259
30	0.8836	5.991	0.691
45	0.8557	8.702	1.286
60	0.8268	11.21	2.058
90	0.7644	15.55	4.200
120	0.7006	19	7.114

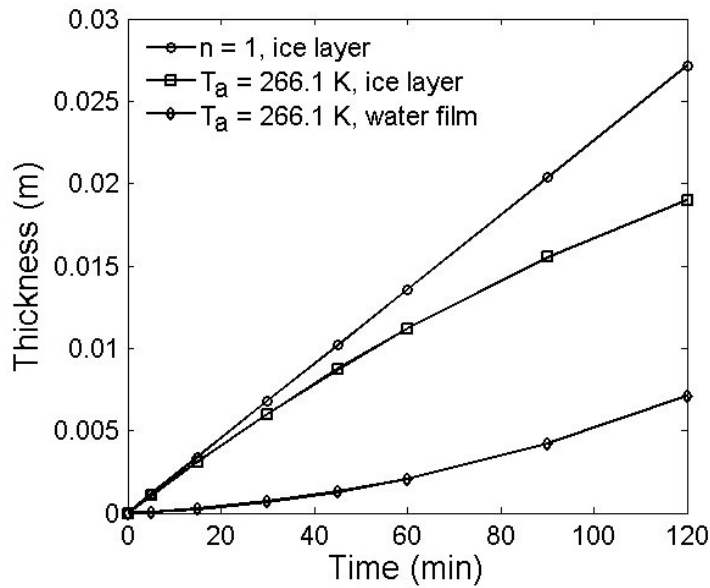


Fig. 5.15: Variations of the ice layer and water film thicknesses for rime and glaze icing

Figures 5.16 and 5.17 represent the influence of the seawater spray salinity and wind velocity, respectively, when the time is equal to 1 h. In these figures, it is assumed that one parameter is variable, while the other parameters are kept constant. According to Fig. 5.16, by decreasing the salinity, the freezing fraction is equal to 1 below higher air temperatures. As a result, the salinity affects several parameters, such as density, specific heat capacity and freezing temperature. When the wind velocity increases, the freezing fraction drops (Fig. 5.17), because the wind velocity has a significant effect on the total flux of seawater spray and convection, evaporation as well as on the heat capacity of the impinging droplets.

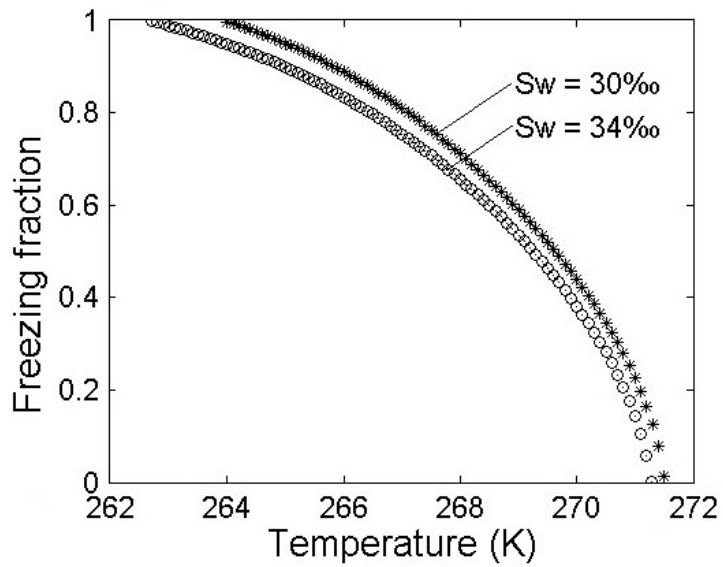


Fig. 5.16: Variations of freezing fraction versus air temperature at two different salinities

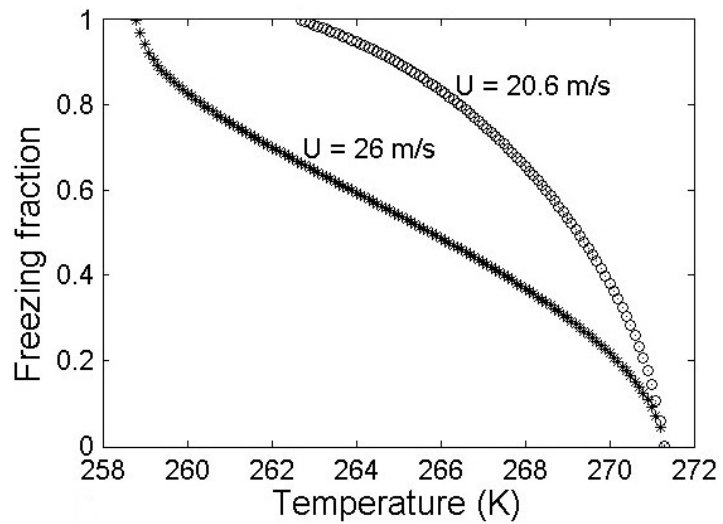


Fig. 5.17: Variations of freezing fraction versus air temperature at two different wind velocities

Figure 5.18 shows and compares the thicknesses of ice formation and water film for two different approaches with identical parameters. As illustrated in this figure, in the case that heat conduction is considered within the ice layer (solid line), by increasing time

at a constant air temperature (266.1 K), the rates of growth of ice formation and brine film are different. For comparison purposes, when the heat conduction is assumed negligible in the ice accretion (dash lines), and time increases at a constant air temperature, the rates of growth of both the ice layer and brine film are the same. As a result, the conductive heat flux inside the ice accumulation layer has a considerable effect on the growth rate of icing because of the changes of the water film salinity and the icing intensity over time.

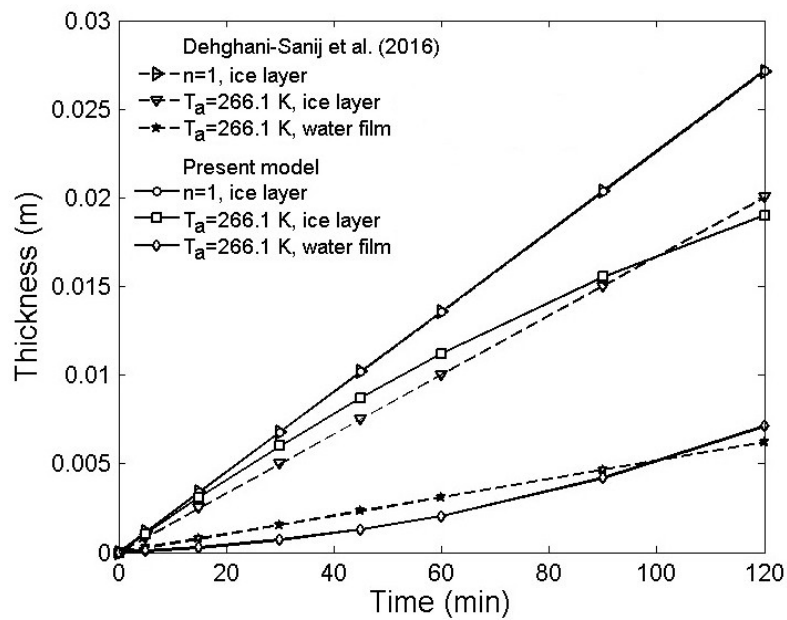


Fig. 5.18: Comparison of ice layer and water film thicknesses for different models

5.2 Model Description for Vertical Surfaces

The formulation of vertical plates during the sea spray icing event is similar to the formulation of horizontal plates but with some differences, when it is assumed that the heat conduction inside the ice formation layer is negligible. Figure 2.4 illustrates the model configuration for a typical vertical plate with associated heat and mass fluxes. To

calculate the total mass flux of seawater spray ($\dot{M}_{w,t}$) during a spray event, Eq. (2.1) is used. For a vertical plate, the collision efficiency and U_{rs} can be determined from Eqs. (2.28) and (2.32), respectively. According to Fig. 2.4, by using a mass balance for the vertical plate, the mass flux of ice accumulation on the plate (\dot{M}_{ice}) can be estimated from Eq. (2.53). All details and formulae required to compute $\dot{M}_{w,t}$ and \dot{M}_{ice} are reported in chapter 2.

The icing rate can be predicted from the thermodynamic process. The water droplets after impingement at the surface of the vertical plate freeze due to several heat fluxes at the air-water interface (Fig. 2.4). These heat fluxes are explained in all details in section 2.3. By neglecting conduction heat transfer in the ice layer, using the heat balances at the air-water and the ice-water interfaces, and combining them (the same procedure as in section 5.1.3), the freezing fraction, n , for a stationary icing model, can be calculated by:

$$l_f (1 - \beta) \frac{n \dot{M}_{w,t}}{\rho_i} = -k_w (A_r - B_r T_s) \quad (5.41)$$

In the above relationship, the coefficients of A_r and B_r are given by Eqs. (5.6) and (5.7), respectively. Also, the thickness of ice formation, b , can be computed by integrating Eq. (2.55).

The parameters used to predict the seawater spray icing phenomenon on vertical plate are displayed in Table 5.1. Figure 5.19 shows the changes in the freezing fraction with air temperature. As illustrated in this figure, the ice layer starts to freeze when the air temperature goes down to -1.05°C . Afterwards, when decreasing the air temperature, the ice accumulation grows. The most growth rate of icing occurs between -17°C and -18°C

(Fig. 5.20), then the icing rate decreases. Furthermore, the variations of freezing fraction are not linear, so that two different parts can be distinguished in the freezing fraction distribution between $T_a = -1.05^\circ\text{C}$ and $T_a = -26.9^\circ\text{C}$. A main part of the distribution, beginning from -1.05°C to -15°C is almost linear; while, in the other part between -15°C and -26.9°C , the freezing fraction varies exponentially. Finally, the freezing fraction is equal to 1 at $T_a = -26.9^\circ\text{C}$.

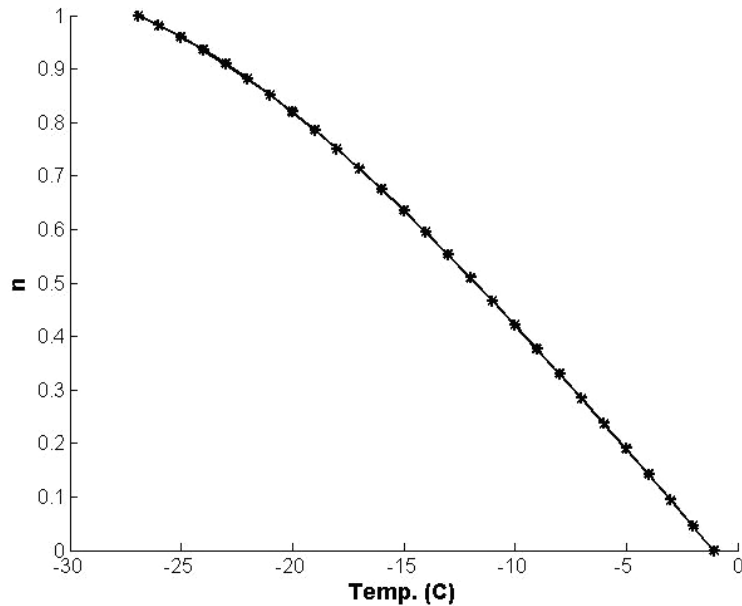


Fig. 5.19: Variations of the freezing fraction versus air temperature

at $v_s = 12.9 \text{ m/s}$, $U = 20.6 \text{ m/s}$, $S_w = 34\%$ and $\alpha = 0^\circ$

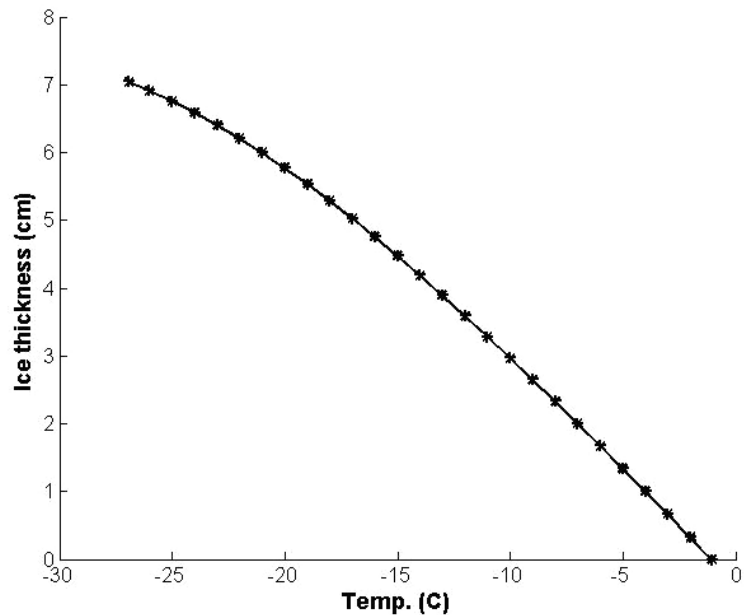


Fig. 5.20: Variations of the ice layer thickness versus air temperature

$$\text{at } v_s = 12.9 \text{ m/s}, U = 20.6 \text{ m/s}, S_w = 34\text{‰} \text{ and } \alpha = 0^\circ$$

The predicted results are similar to the previously published results by other researchers. Tabata et al. (1963) and Tabata (1969) reported that ice accretion starts at an air temperature of -2°C , and the icing intensity is most strong at $T_a = -17^\circ\text{C}$, then after that the icing intensity decreases. Kulyakhtin and Tsarau (2014) explained that the water freezes with all salt contained in it when the temperature is below -23°C . Additionally, Lundqvist and Udin (1977) expressed that the air temperature is below -2°C for icing to occur in ocean water. Cammaert (2013) reported that for sea spray, ice accretion occurs when the air temperature is below the freezing point of seawater (approximately -2°C) and air-borne brine droplets impact a structure and partially freeze. The differences between the results are due to a different relative humidity, salinity of the spray water, air temperature, air velocity and vessel speed.

Chapter 6

Experimental Arrangement and Procedure for Measurement of Ice Accumulation on Vertical Marine Platform Surfaces

In this chapter, the experimental setup and procedure to measure ice accumulation on vertical plates of marine platforms during spray icing in a cold room are reported. To conduct various experiments, testing equipment and measuring instrumentation were employed. This equipment and instrumentation are described in the following sections. Figure 6.1 shows a schematic of the experiment with all components.

6.1 Equipment

To perform the experiments, a cold room was used to create cold and freezing conditions. The temperature of this cold room can reach as low as -30°C . A vertical plate was selected to measure the weight and thickness of ice formation during the spray icing event. The details of the plate are shown schematically in Fig. 6.2. The vertical plate was made of aluminum as this is commonly used on ship superstructures. Soares and Garbatov (2015) reported that aluminum structures have different uses in marine

applications, such as the construction of ship superstructures. Aluminum can decrease the structural weight and fuel consumption, as well as increase the payload and speed.

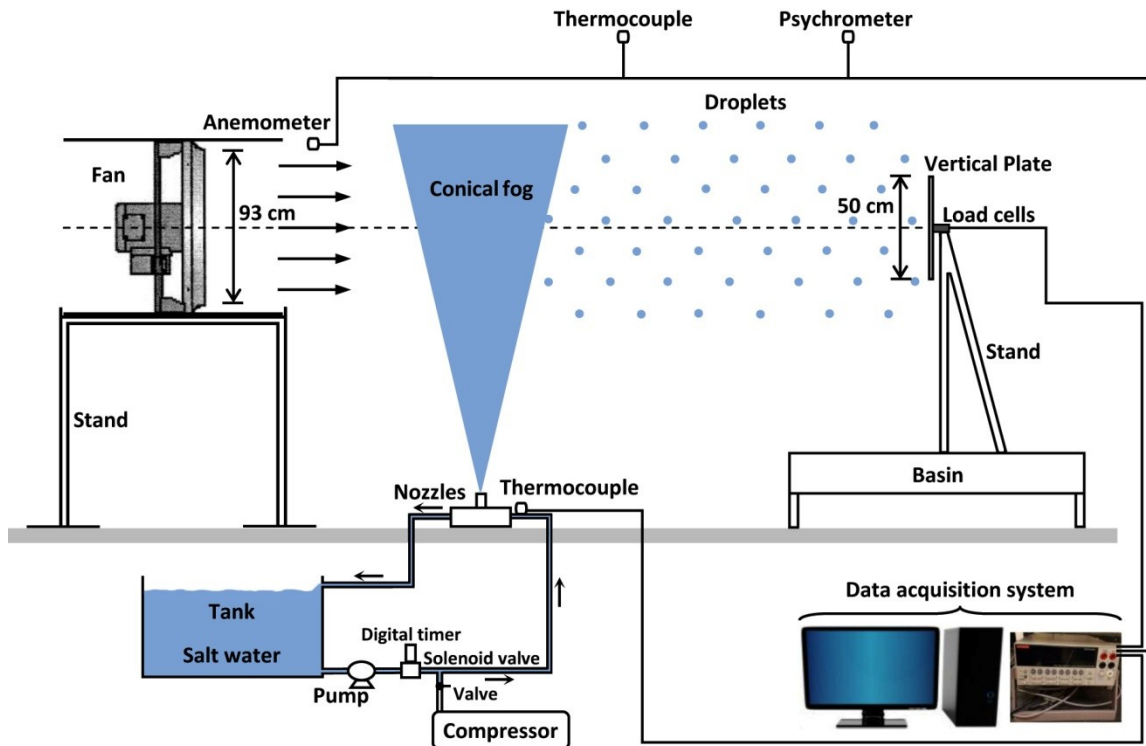


Fig. 6.1: Schematic illustration of the experiment with all components

In Fig. 6.2, the thickness of the vertical plate is 6 mm. According to ship classification standards, the minimum thickness for side plating on superstructures is 5 mm (Soares and Garbatov, 2015). The actual calculation for the required thickness depends on the ship size, the extent of the deck structure and the spacing of the framing members. Soares and Garbatov (2015) reported that the thickness of the plate can be in the range of 5 mm to 20 mm.

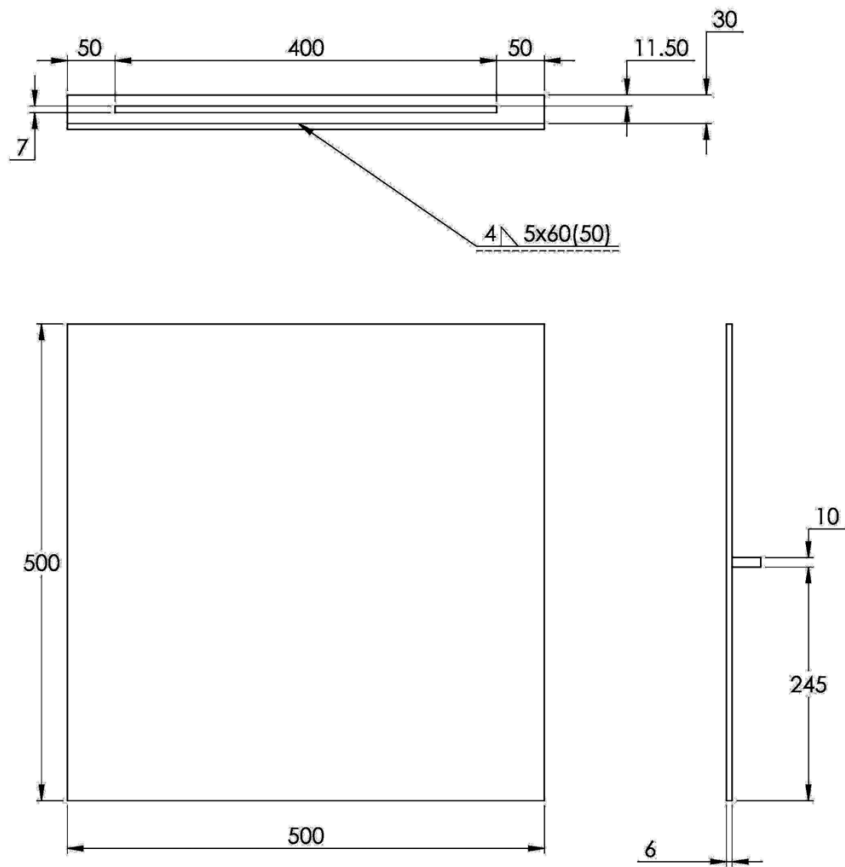


Fig. 6.2: Schematic illustration of the vertical plate.

Note: all sizes in this figure are in mm

As shown in Fig. 6.3, the vertical plate was installed on a stand via two load cells. The load cells allow the real-time monitoring of ice accretion on the plate during the entire experiment. Figure 6.4 indicates the schematic design of the stand for the vertical plate at different views. The stand was made of aluminum. Aluminum was selected for the stand because there was a salt water spray.



Fig. 6.3: Installation of the load cells for measuring ice accretion rates on a vertical plate

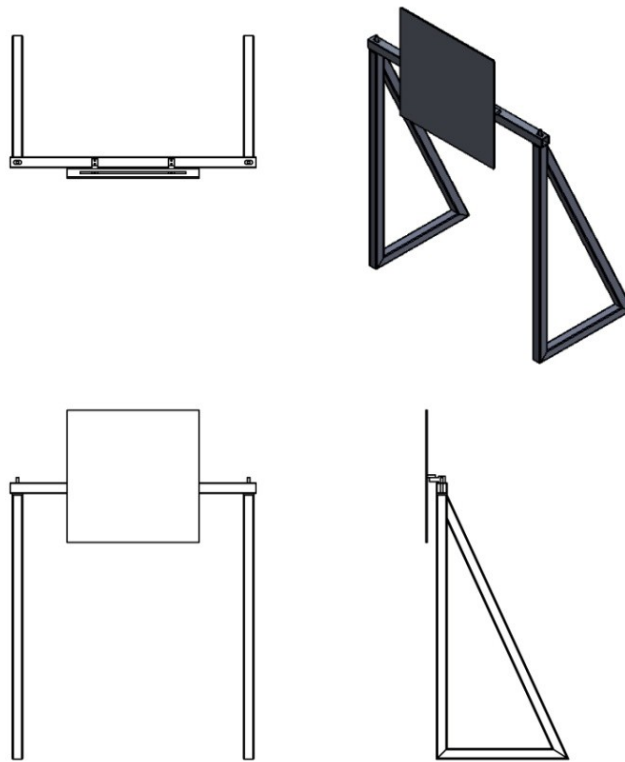


Fig. 6.4: Schematic illustration of the stand for the vertical plate at different views

Two nozzles were used for the formation of the saline water mist spray inside the cold room. The nozzles are stainless steel type 316, which is effective to resist corrosion. The spray pattern shape of these nozzles is a full cone. The droplet size distribution in the spray created by the nozzles depends on different factors, such as nozzle type, spray pattern type, liquid properties, nozzle capacity, spray pressure and spray angle. The model of nozzles which was selected for this experiment is 1/8GG-316SS3, where the inlet connection is 1/8, the nozzle type is GG, the material code is 316SS and the capacity size is 3. According to the droplet size specifications at two different pressures (Fig. 6.5), the Volume Median Diameters ($Dv0.5$)¹ at pressures of 40 PSI and 100 PSI are 1,250 μm and 700 μm , respectively. In addition, between these two situations, a linear relationship can be considered: $Dv0.5 = -9.1667P + 1616.7$.

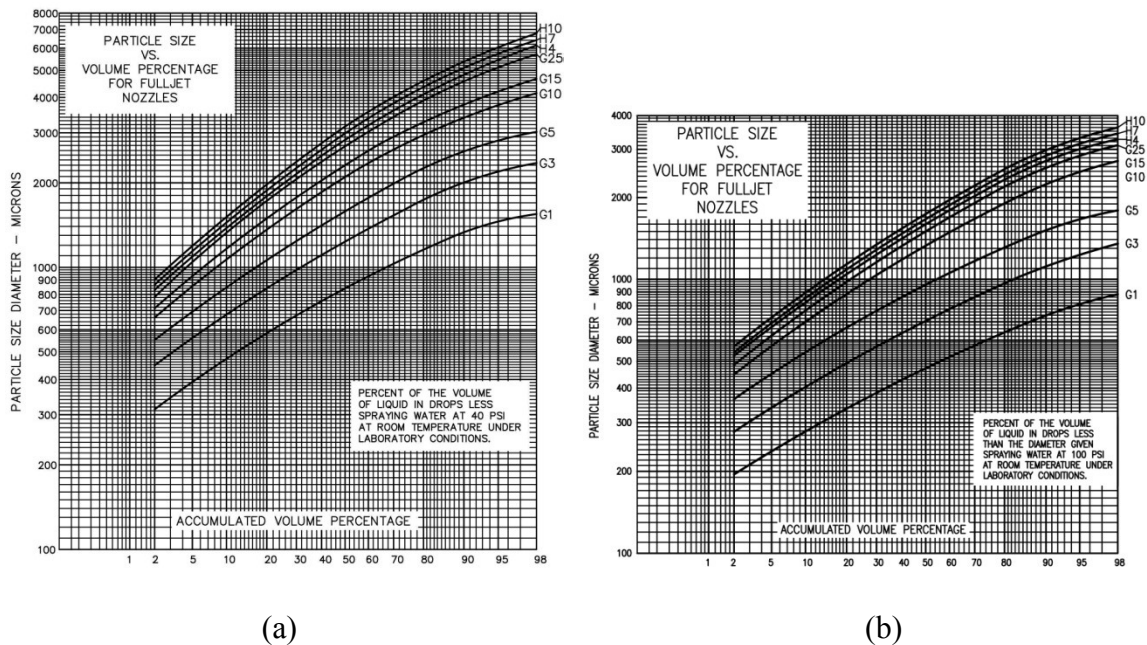


Fig. 6.5: Droplet size characteristics at (a) P = 40 PSI and (b) P = 100 PSI

1. Volume Median Diameters divide the droplet spectrum so half of the total volume of the spray has a smaller diameter and half of the larger diameter.

A fan with a diameter of 93.98 cm was employed in this experiment to produce airflow inside the cold room and to move the water spray. Figure 6.6 shows the characteristics of this fan in detail. All components of the fan, including blades and walls, have an epoxy coating to resist corrosion. Additionally, the speed of the fan was controlled using a Variable-Frequency Drive (VFD). In consideration of the wind loading on the vertical plate, the center of the fan and center of the plate were situated on an identical level to avoid any error in measuring the weight of ice formation.

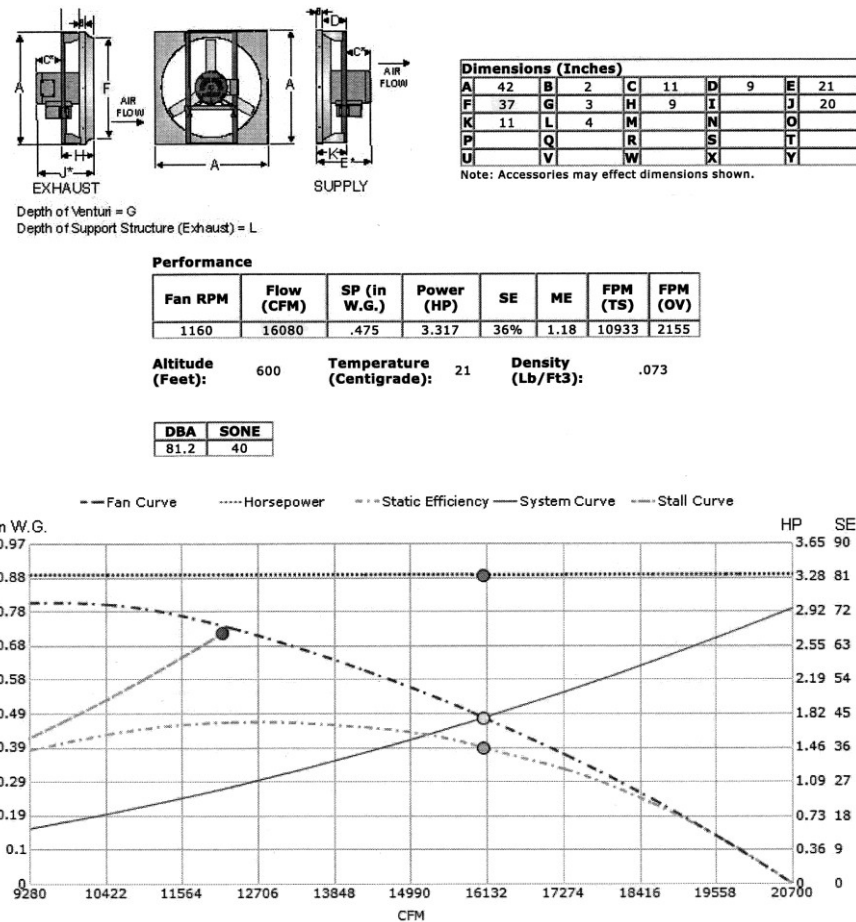


Fig. 6.6: Characteristics of the fan

The stand with four legs, which was made of aluminum, was placed under the fan (Fig. 6.7). To reduce fan vibrations, four floor pads were situated underneath the legs of the fan's stand, and a piece of rubber was added to each of the upper four corners (Fig. 6.7).



Fig. 6.7: Stand used underneath the fan

A 2-way solenoid valve and a digital timer were used to create the periodic spray during the icing event in the cold room. Table 6.1 illustrates the relevant specifications of the solenoid valve and digital timer used in this experiment. It should be noted that the digital timer can be adjusted to any time period for generation of the spray.

A large basin was used to install the stand of the vertical plate and collect excess water from the spray during tests in the cold room. Foam insulation was wrapped around the pipe to prevent the freezing of water inside the pipe in the cold room. After conducting each test, it was necessary to purge the water inside the pipe because the temperature

within the cold room was low (between -10 and -30°C). For this purpose, a compressor was used.

Table 6.1: Relevant characteristics of the solenoid valve and digital timer

Instrument	Description
Burkert Zero Differential Pressure 2-Way Solenoid Valve	2/2-way valve, 6213 EV series solenoid valve, ¼" NPT, working pressure: 0-145 PSI, Cv: 4.2, seal material: FKM, body: stainless steel, volt: 120-60, normally closed: UL/UR
Burkert 1078-2 Series Digital Timer	Timing range: 0.2 s to 9999 h, continuous, switch status: LED, supply: 110-230V/50, four switching functions, mounting: DIN 43650 form A (standard coil plug)

6.2 Measuring Instruments

Several measuring instruments were utilized to obtain the experimental results during the spray icing event. These measuring instruments are described in the following subsections.

i) Weight Measurement

To record the weight of ice formation on the vertical plate during the spray icing event, two load cells were used (Fig. 6.3). The model of the interface sealed beam load cells was SSB-AJ-100. Table 6.2 displays the relevant specifications of the load cells. To calibrate these load cells, different scales of weight up to 100 lb_f were used. For this purpose, the amount of each known weight scale was measured by the load cells. Then, the difference between the measured quantity and the real value was corrected by changing the settings of the load cells. Moreover, the amounts obtained via the load cells for various weights were drawn on a diagram to determine the best fitted line between the measured points.

Table 6.2: Relevant characteristics of the load cells

Instrument	Description
Interface sealed beam load cell	Capacity: 100 lb _f Tension and compression Rated output (nominal): 3.0 mV/V Thermal compensation: -15 to 65°C Operation range: -55 to 90°C Effect on zero- % RO/°F - Max: ±0.0015 Safe overload- % CAP: ±150

ii) Airflow Measurement

To determine the airflow velocity produced by the fan inside the cold room, an anemometer (AVT 55/65/75 model) with a velocity range from 0 to 50 m/s was employed. To obtain the airflow profile and also the average velocity of the airflow for different fan speeds, several locations in front of the fan at a distance of 40 cm from the blades were selected. In these locations, the velocity of the airflow was measured by the anemometer for the 1 min at the identical fan speed. These measurements were repeated several time to find the more accurate results.

iii) Humidity Measurement

To measure the relative humidity during tests, a multifunctional environmental meter (REED LM-8000) was used. The humidity range of this instrument is between 0 and 95% RH, and its humidity resolution is equal to 0.1% RH. To examine the accuracy of the results obtained from the REED LM-8000 device, three different devices were used to measure the relative humidity for the same conditions. The measured results indicated that this device had a good accuracy.

iv) Temperature Measurement

A thermocouple measured the water temperature inside the pipe during the icing event. The relevant characteristics of this thermocouple are displayed in Table 6.3. To survey the accuracy of the results obtained by this thermocouple, the measured results were compared with the results obtained from another thermocouple for the identical conditions. The results showed that the accuracy of this thermocouple is high.

Table 6.3: Relevant specifications of the thermocouple used to record the water temperature inside the pipe

Instrument	Description
Pipe plug thermocouple probe Model: TC-K-NPT-U-72	Rugged 304 SS design with strain relief spring Probe temperature range to 650°C ¼” NPT mounting thread

Two thermocouple sensors were used to measure the temperature of the front and back of the vertical plate for the duration of the test. The accuracy of these thermocouple sensors was examined by a comparison of the measured results from these sensors and another temperature measuring device. The results illustrated that thermocouple sensors had good accuracy.

v) Salinity Measurement

To determine the salinity of water, a conductivity portable meter (Orion Star A222) was utilized. The salinity range of this device is between 0.06 to 80.00 PSU, and its salinity resolution is equal to 0.01 PSU minimum.

vi) Thickness Measurement

A digital caliper (Mitutoyo Absolute 500-196-20) with ± 0.001 " accuracy and 0.0005" resolution was used to measure the average thickness of ice formation on the vertical plate.

vii) Data Collection

To record and collect the data measured from various experiments during the spray icing events, a Model 2700 multimeter/data acquisition system was used.

6.3 Design Factors and Measurements

To obtain the experimental results, a wide range of tests for various conditions was carried out as follows.

- (1) Two different distances between the fan and the plate were tested. (a) The distance between the fan and the vertical plate was 2.5 m. The nozzles were located between the fan and plate, and the distance between the fan and nozzles was 1.2 m. (b) The distance between the fan and the vertical plate was 1.65 m. The nozzles were located between the fan and plate, and the distance between the fan and nozzles was 0.85 m.
- (2) Two different temperatures inside the cold room were tested. (a) $T_C = -10^\circ\text{C}$ and (b) $T_C = -20^\circ\text{C}$. It should be noted that the temperature inside the cold room was not constant at -10°C or -20°C during tests. Due to the refrigeration system of the cold room, the temperature varied between -8°C and -12°C for the adjusted temperature at -10°C or between -18°C and -22°C for the adjusted temperature at -20°C .
- (3) Two different salinities were tested. (a) $S_w = 0\text{‰}$, fresh water and (b) $S_w = 35\text{‰}$, saline water.

- (4) Three different fan speeds were studied. (a) $V_{ave,1} \approx 7.85$ m/s ($V_{max} \approx 13$ m/s and $V_{min} \approx 2.7$ m/s), (b) $V_{ave,2} \approx 6$ m/s ($V_{max} \approx 10.2$ m/s and $V_{min} \approx 1.8$ m/s), and (c) $V_{ave,3} \approx 2.65$ m/s ($V_{max} \approx 4.1$ m/s and $V_{min} \approx 1.2$ m/s). Note that the distribution of air velocity inside the cold room was not uniform because (a) two fans were installed on the inside of the cold room ceiling for adjustment of the temperature, and (b) the internal space of the cold room was a limiting factor of a uniform airflow.
- (5) Two different times for the spray events were tested. (a) The duration of each spray event was equal to 5 s and the period between spray events equal to 30 s. (b) The duration of each spray event was equal to 3 s and the period between spray events equal to 1 min.

The time period of each test was 3 hr. Figure 6.8 shows an overall classification of the experiments in various conditions. According to this classification, a specific code was given for each test, like (x_1, x_2, x_3) where x_1 is for the adjusted temperature inside the cold room, x_2 is for the salinity, and x_3 is for the average fan speed. For example, test (1-2-3) is for the temperature of -10°C , the salinity of 35‰, and the fan velocity of 7.85 m/s. Experiments were repeated several times in the same conditions. For the first repetition, the symbol “a” was assigned. Also, for the second, third and fourth repetitions, the symbols “b”, “c” and “d” were used, respectively.

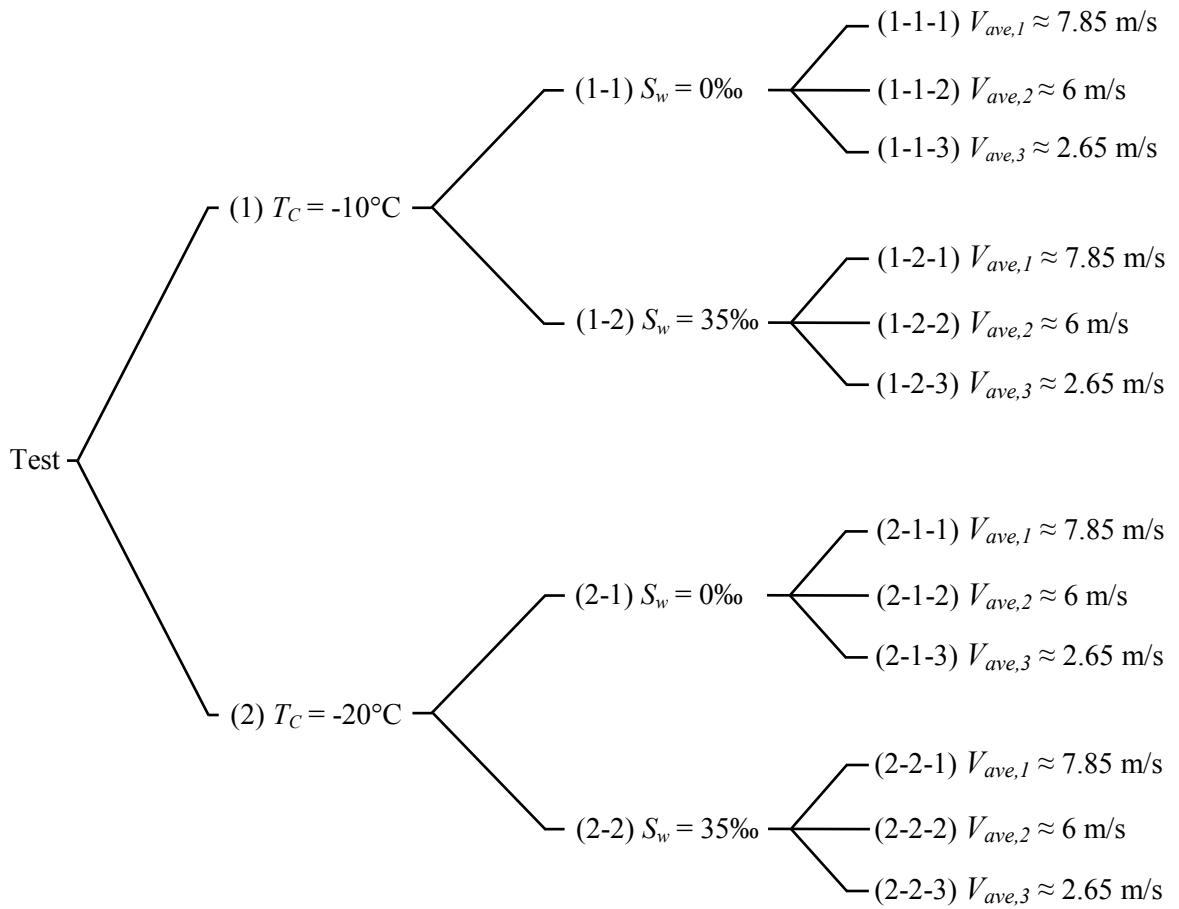


Fig. 6.8: Classification of the experiments for various conditions

After conducting each test, seven different specified points around the vertical plate were selected to compute the average thickness of formed ice on the plate with a caliper. To estimate the average thickness of ice layer using theoretical methods, the following formula was employed:

$$\bar{\delta}_t = \frac{\dot{W}_i (kg_f)}{\rho_i A_{eff}} \quad (6.1)$$

where \dot{W}_i is the weight of ice, A_{eff} is the effective area, and ρ_i is the ice density for pure ice equal to 917 kg/m^3 (Pringle et al., 2007; Brakel et al., 2007) and for saline ice it can be calculated by Eq. (4.61). Kulyakhtin et al. (2013) reported that the volume fraction of air in the ice, v'_a , changes from 3% to 7% on a vertical structure. By considering $S_w = 35\%$, $v'_a = 5\%$, and $\beta = 1/3$ (Horjen, 2013, 2015), the density of saline ice is equal to 903.675 kg/m^3 . The percent of error is given by:

$$\%error = \left| \frac{A_{experimental} - A_{theoretical}}{A_{theoretical}} \right| \times 100 \quad (6.2)$$

6.4 Spray Mass Flux Measurement

To measure the amount of mass flux of water spray that impacts on the vertical plate for the duration of the spray event, a narrow trapezoidal funnel and a small container to collect water, which was connected at the bottom of the funnel, were employed (Fig. 6.9). At three different fan speeds, the quantity of spray mass flux every hour was measured. After turning off the fan, all water around the container was removed. Then, after 5 min from turning off the fan, the weight of container with the water content inside it was measured by a high accuracy scale.

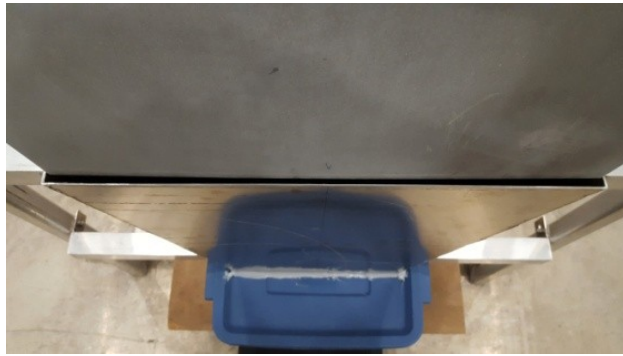


Fig. 6.9: View of a narrow trapezoidal funnel and a small container

Chapter 7

Analysis of Experimental Measurements of Ice Accumulation on Vertical Marine Platform Surfaces

In this chapter, the ice accumulation that was created on a vertical plate of marine platforms during spray icing in a cold room is investigated and analyzed experimentally. Several parameters, such as the weight and thickness of ice formation on the plate at two different approaches, the temperature at the front and back of the vertical plate, and the water temperature inside the pipe during the spray icing event, in various conditions is reported and discussed in the following sections.

7.1 Experimental Results

Figure 7.1 shows the distribution of ice formation on the vertical plate from different views at $V_{ave,t} \approx 7.85$ m/s, $T_C = -10^\circ\text{C}$, $S_w = 0\%$, $RH_{ave} = 72.2\%$ and the distance of 1.65 m between the fan and the plate, as well as 5 s for the duration of each spray event and 30 s for the period between spray events. According to this figure, the ice weight after the 3 hr test was 8.727 kg_f and the maximum height of icicle was 58.6 cm. The average

measured ice thickness was 33.15 mm. Also, the average ice thickness obtained by Eq. (6.1) was 28.84 mm. Therefore, the percent error was equal to 15%.

After performing several experiments at a distance of 1.65 m between the fan and the plate, as shown in Fig. 7.1, it was observed that there were a number of icicles with large dimensions and a non-uniform distribution of ice on the plate. Hence, for other tests the distance of 2.5 m between the fan and the vertical plate was considered. In the following section, all tests were carried out for this duration of the spray event: 5 s for the duration of each spray event and 30 s for the period between spray events.



Fig. 7.1: Views of ice formation on the vertical plate at $V_{ave,l} \approx 7.85$ m/s, $T_C = -10^\circ\text{C}$, $S_w = 0\%$, $RH_{ave} = 72.2\%$, and the distance of 1.65 m between the fan and the plate

Figure 1.A shows the distribution of ice accretion on the vertical plate from different views for test (1-1-1-a), (1-1-1-b), (1-1-2-a), (1-1-2-b), (1-1-3-a), (1-1-3-b) and (1-1-3-c), respectively. Figure 2.A illustrates the ice weight changes over time for test (1-1-1-a), (1-1-1-b), (1-1-2-a), (1-1-2-b), (1-1-3-a), (1-1-3-b) and (1-1-3-c), respectively. Figure 3.A indicates the temperature changes at the front and back of the vertical plate over time for test (1-1-1-a), (1-1-1-b), (1-1-2-a), (1-1-2-b), (1-1-3-a), (1-1-3-b) and (1-1-3-c), respectively. These figures are presented in Appendix A.

Test (1-1-1-a): The ice weight after the 3 hr test was 3.446 kg_f and the maximum height of icicle was 3.9 cm. The average measured ice thickness was 15.45 mm. Also, the average ice thickness obtained by Eq. (6.1) was 14.73 mm. Therefore, the percent error was equal to 4.9%. The average relative humidity during the test was 73.7%.

Test (1-1-1-b): The ice weight after the 3 hr test was 2.964 kg_f and the maximum height of icicle was 1.4 cm. The average measured ice thickness was 13.65 mm. Also, the average ice thickness obtained by Eq. (6.1) was 12.67 mm. Therefore, the percent error was equal to 7.7%. The average relative humidity during the test was 69.6%.

Test (1-1-2-a): The ice weight after the 3 hr test was 2.170 kg_f and the maximum height of icicle was 0.3 cm. The average measured ice thickness was 10.35 mm. Also, the average ice thickness obtained by Eq. (6.1) was 9.46 mm. Therefore, the percent error was equal to 9.4%. The average relative humidity during the test was 71.9%.

Test (1-1-2-b): The ice weight after the 3 hr test was 2.955 kg_f and the maximum height of icicle was 1.8 cm. The average measured ice thickness was 13.58 mm. Also, the average ice thickness obtained by Eq. (6.1) was 12.63 mm. Therefore, the percent error was equal to 7.5%. The average relative humidity during the test was 72.8%.

Test (1-1-3-a): The ice weight after the 3 hr test was 2.858 kg_f and the maximum height of icicle was 1.5 cm. The average measured ice thickness was 13.26 mm. Also, the average ice thickness obtained by Eq. (6.1) was 11.98 mm. Therefore, the percent error was equal to 10.7%. The average relative humidity during the test was 71.5%.

Test (1-1-3-b): The ice weight after the 3 hr test was 1.700 kg_f and there were no icicles. The average measured ice thickness was 8.10 mm. Also, the average ice thickness obtained by Eq. (6.1) was 7.27 mm. Therefore, the percent error was equal to 11.4%. The average relative humidity during the test was 73.5%.

Test (1-1-3-c): The ice weight after the 3 hr test was 1.447 kg_f and there were no icicles. The average measured ice thickness was 7.04 mm. Also, the average ice thickness obtained by Eq. (6.1) was 6.12 mm. Therefore, the percent error was equal to 15%. The average relative humidity during the test was 68.1%.

Figure 4.A shows the distribution of ice accretion on the vertical plate from different views for test (1-2-1-a), (1-2-1-b), (1-2-1-c), (1-2-1-d), (1-2-2-a), (1-2-2-b), (1-2-3-a) and (1-2-3-b), respectively. Figure 5.A illustrates the ice weight changes over time for test (1-2-1-a), (1-2-1-b), (1-2-1-c), (1-2-1-d), (1-2-2-a), (1-2-2-b), (1-2-3-a) and (1-2-3-b), respectively. Figure 6.A indicates the temperature changes at the front and back of the vertical plate over time for test (1-2-1-a), (1-2-1-b), (1-2-1-c), (1-2-1-d), (1-2-2-a), (1-2-2-b), (1-2-3-a) and (1-2-3-b), respectively. These figures are presented in Appendix A.

Test (1-2-1-a): The ice weight after the 3 hr test was 3.794 kg_f and the maximum height of icicle was 16.1 cm. The average measured ice thickness was 16.74 mm. Also, the average ice thickness obtained by Eq. (6.1) was 15.53 mm. Therefore, the percent error was equal to 7.8%. The average relative humidity during the test was 73.2%.

Test (1-2-1-b): The ice weight after the 3 hr test was 2.820 kg_f and the maximum height of icicle was 13.6 cm. The average measured ice thickness was 12.53 mm. Also, the average ice thickness obtained by Eq. (6.1) was 11.44 mm. Therefore, the percent error was equal to 9.5%. The average relative humidity during the test was 72.5%. Note that after 1 hr from the start of the test, the temperature inside the cold room was approximately -7°C until the end of the test.

Test (1-2-1-c): The ice weight after the 3 hr test was 3.145 kg_f and the maximum height of icicle was 19.2 cm. The average measured ice thickness was 15.16 mm. Also, the average ice thickness obtained by Eq. (6.1) was 13.86 mm. Therefore, the percent error was equal to 9.4%. The average relative humidity during the test was 69.2%. Note that after one and a half hours from the start of the test, the temperature inside the cold room was approximately -7°C until the end of the test.

Test (1-2-1-d): The ice weight after the 3 hr test was 3.311 kg_f and the maximum height of icicle was 14.1 cm. The average measured ice thickness was 15.09 mm. Also, the average ice thickness obtained by Eq. (6.1) was 13.95 mm. Therefore, the percent error was equal to 8.2%. The average relative humidity during the test was 70.5%.

Test (1-2-2-a): The ice weight after the 3 hr test was 3.353 kg_f and the maximum height of icicle was 15.6 cm. The average measured ice thickness was 14.95 mm. Also, the average ice thickness obtained by Eq. (6.1) was 13.73 mm. Therefore, the percent error was equal to 8.9%. The average relative humidity during the test was 68.2%.

Test (1-2-2-b): The ice weight after the 3 hr test was 3.435 kg_f and the maximum height of icicle was 13.3 cm. The average measured ice thickness was 15.44 mm. Also, the

average ice thickness obtained by Eq. (6.1) was 14.33 mm. Therefore, the percent error was equal to 7.7%. The average relative humidity during the test was 73%.

Test (1-2-3-a): The ice weight after the 3 hr test was 0.721 kg_f and the maximum height of icicle was 3.4 cm. The average measured ice thickness was 3.77 mm. Also, the average ice thickness obtained by Eq. (6.1) was 3.14 mm. Therefore, the percent error was equal to 20%. The average relative humidity during the test was 67.1%.

Test (1-2-3-b): The ice weight after the 3 hr test was 3.621 kg_f and the maximum height of icicle was 19.4 cm. The average measured ice thickness was 15.66 mm. Also, the average ice thickness obtained by Eq. (6.1) was 14.42 mm. Therefore, the percent error was equal to 8.6%. The average relative humidity during the test was 68.7%. Note that the door between the two cold rooms was opened during this experiment.

Figure 7.A shows the distribution of ice accretion on the vertical plate from different views for test (2-1-1), (2-1-2) and (2-1-3), respectively. Figure 8.A illustrates the ice weight changes over time for test (2-1-1), (2-1-2) and (2-1-3), respectively. Figure 9.A indicates the temperature changes at the front and back of the vertical plate over time for test (2-1-1), (2-1-2) and (2-1-3), respectively. These figures are presented in Appendix A.

Test (2-1-1): The ice weight after the 3 hr test was 4.810 kg_f and the maximum height of icicle was 5.7 cm. The average measured ice thickness was 21.99 mm. Also, the average ice thickness obtained by Eq. (6.1) was 20.37 mm. Therefore, the percent error was equal to 7.9%. The average relative humidity during the test was 62.7%.

Test (2-1-2): The ice weight after the 3 hr test was 1.874 kg_f and there were no icicles. The average measured ice thickness was 8.93 mm. Also, the average ice thickness

obtained by Eq. (6.1) was 8.01 mm. Therefore, the percent error was equal to 11.5%. The average relative humidity during the test was 62.9%.

Test (2-1-3): The ice weight after the 3 hr test was 0.595 kg_f and there were no icicles. The average measured ice thickness was 3.33 mm. Also, the average ice thickness obtained by Eq. (6.1) was 2.55 mm. Therefore, the percent error was equal to 30%. The average relative humidity during the test was 63.9%.

Figure 10.A shows the distribution of ice accretion on the vertical plate from different views for test (2-2-1), (2-2-2-a), (2-2-2-b) and (2-2-3), respectively. Figure 11.A illustrates the ice weight changes over time for test (2-2-1), (2-2-2-a), (2-2-2-b) and (2-2-3), respectively. Figure 12.A indicates the temperature changes at the front and back of the vertical plate over time for test (2-2-1), (2-2-2-a), (2-2-2-b) and (2-2-3), respectively. These figures are presented in Appendix A.

Test (2-2-1): The ice weight after the 3 hr test was 4.054 kg_f and the maximum height of icicle was 15.9 cm. The average measured ice thickness was 18.45 mm. Also, the average ice thickness obtained by Eq. (6.1) was 17.35 mm. Therefore, the percent error was equal to 6.3%. The average relative humidity during the test was 62.4%.

Test (2-2-2-a): The ice weight after the 3 hr test was 1.000 kg_f and the maximum height of icicle was 0.6 cm. The average measured ice thickness was 5.28 mm. Also, the average ice thickness obtained by Eq. (6.1) was 4.30 mm. Therefore, the percent error was equal to 22%. The average relative humidity during the test was 63.5%.

Test (2-2-2-b): The ice weight after the 3 hr test was 1.650 kg_f and the maximum height of icicle was 4.4 cm. The average measured ice thickness was 8.04 mm. Also, the average

ice thickness obtained by Eq. (6.1) was 7.19 mm. Therefore, the percent error was equal to 11.8%. The average relative humidity during the test was 63.1%.

Test (2-2-3): The ice weight after the 3 hr test was 0.539 kg_f and there were no icicles. The average measured ice thickness was 3.05 mm. Also, the average ice thickness obtained by Eq. (6.1) was 2.35 mm. Therefore, the percent error was equal to 29.8%. The average relative humidity during the test was 63.6%.

Table 7.1 shows an overall summary of the ice weight obtained from the load cells in various conditions during the spray icing experiments when the distance between the fan and the vertical plate was 2.5 m. Table 7.2 illustrates the average thickness of ice accretion from theoretical and experimental methods in different conditions after a 3 hr test for a distance of 2.5 m between the fan and the plate.

Table 7.1: Comparison of the ice weight for two different salinities and temperatures and including at three air velocities

Temperature (°C)	Salinity (‰)	Ice weight (kg _f)								
		V _{ave,1} (m/s)			V _{ave,2} (m/s)			V _{ave,3} (m/s)		
		1 hr	2 hr	3 hr	1 hr	2 hr	3 hr	1 hr	2 hr	3 hr
-10	0	1.384	2.567	3.446	0.952	1.746	2.170	0.941	2.212	2.858
								0.572	1.206	1.700
		0.940	1.817	2.964	0.946	1.766	2.955	0.576	1.212	1.447
	35	1.183	2.375	3.794	1.135	2.176	3.353	0.415	0.638	0.721
		1.179	2.031 ^a	2.820 ^a						
		1.375	2.386 ^b	3.145 ^b	1.145	2.184	3.435	1.291 ^c	2.419 ^c	3.621 ^c
-20	0	0.968	2.073	3.311						
		1.283	3.070	4.810	0.518	1.233	1.874	0.378	0.539	0.595
		1.549	2.918	4.054	0.488	0.794	1.00	0.265	0.418	0.539
	35				0.738	1.183	1.650			

^a After 1 hr from the start of the test, the temperature inside the cold room was approximately -7°C until the end of the test.

^b After one and a half hours from the start of the test, the temperature inside the cold room was approximately -7°C until the end of the test.

^c The door between the two cold rooms was opened during the experiment.

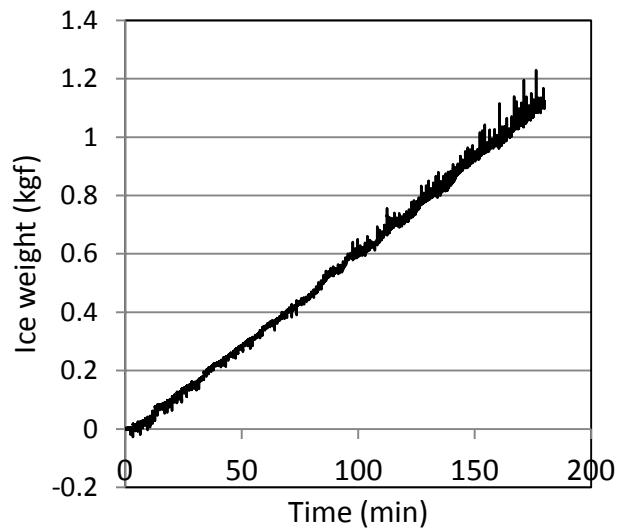
Table 7.2: Comparison of the average thickness of ice formation for two different salinities and temperatures and including three air velocities for a 3 hr test

Temperature (°C)	Salinity (‰)	Ice thickness (mm)					
		Theoretical method			Experimental method		
		V _{ave,1} (m/s)	V _{ave,2} (m/s)	V _{ave,3} (m/s)	V _{ave,1} (m/s)	V _{ave,2} (m/s)	V _{ave,3} (m/s)
-10	0	14.73	9.46	11.98	15.45	10.35	13.26
				7.27			8.10
		12.67	12.63	6.12	13.65	13.58	7.04
	35	15.53	13.73	3.14	16.74	14.95	3.77
		11.44			12.53		
		13.86	14.33	14.42	15.16	15.44	15.66
		13.95		15.09			
-20	0	20.37	8.01	2.55	21.99	8.93	3.33
	35	17.35	4.30	2.35	18.45	5.28	3.05
			7.19			8.04	

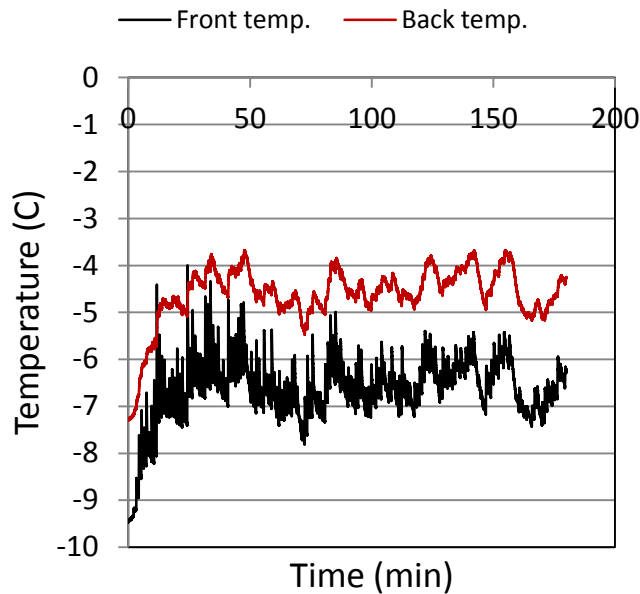
To study the effect of spray time on the weight and thickness of ice accretion on the vertical plate, another time for the spray experiments was considered: 3 s for the duration of each spray event and 1 min for the period between spray events. Figure 7.2 displays the distribution of ice formation on the vertical plate from two views at $V_{ave,3} \approx 2.65$ m/s, $T_C = -10^\circ\text{C}$, $S_w = 0\text{‰}$, $RH_{ave} = 68.4\%$, as well as 3 s for the duration of each spray event and 1 min for the period between spray events. Figure 7.3 illustrates the variations of the ice weight and the temperature at the front and back of the vertical plate over time at $V_{ave,3} \approx 2.65$ m/s, $T_C = -10^\circ\text{C}$, $S_w = 0\text{‰}$, $RH_{ave} = 68.4\%$, and including 3 s for the duration of each spray event and 1 min for the period between spray events, respectively. From these figures, the ice weight after the 3 hr test was 1.115 kg_f and there were no icicles. The average measured ice thickness was 5.58 mm. Also, the average ice thickness obtained by Eq. (6.1) was 4.78 mm. Therefore, the percent error was equal to 16.7%.



Fig. 7.2: Two views of ice accretion on the vertical plate at $V_{ave,3} \approx 2.65$ m/s, $T_C = -10^\circ\text{C}$,
 $S_w = 0\%$, $RH_{ave} = 68.4\%$, including 3 s for the duration of each spray event and
1 min for the period between spray events



(a)



(b)

Fig. 7.3: Changes in (a) the ice weight and (b) temperature at the front and back of the vertical plate versus time at $V_{ave,3} \approx 2.65$ m/s, $T_C = -10^\circ\text{C}$, $S_w = 0\%$, $RH_{ave} = 68.4\%$, including 3 s for the duration of each spray event and 1 min for the period between spray events

Figure 7.4 displays the distribution of ice formation on the vertical plate from two views at $V_{ave,3} \approx 2.65$ m/s, $T_C = -10^\circ\text{C}$, $S_w = 35\%$, $RH_{ave} = 69.6\%$, including 3 s for the duration of each spray event and 1 min for the period between spray events. Figure 7.5 illustrates the variations of ice weight and temperature at the front and back of the vertical plate over time at $V_{ave,3} \approx 2.65$ m/s, $T_C = -10^\circ\text{C}$, $S_w = 35\%$, $RH_{ave} = 69.6\%$, including 3 s for the duration of each spray event and 1 min for the period between spray events, respectively. From these figures, the ice weight after the 3 hr test was 1.104 kg_f and the

maximum height of icicle was 2.9 cm. The average measured ice thickness was 5.21 mm. Also, the average ice thickness obtained by Eq. (6.1) was 4.79 mm. Therefore, the percent error was equal to 8.8%.

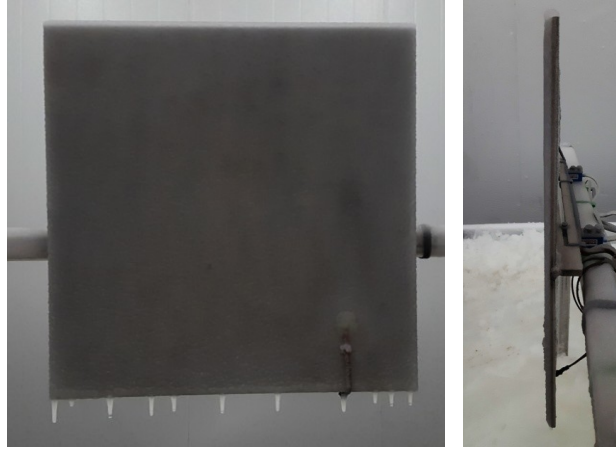
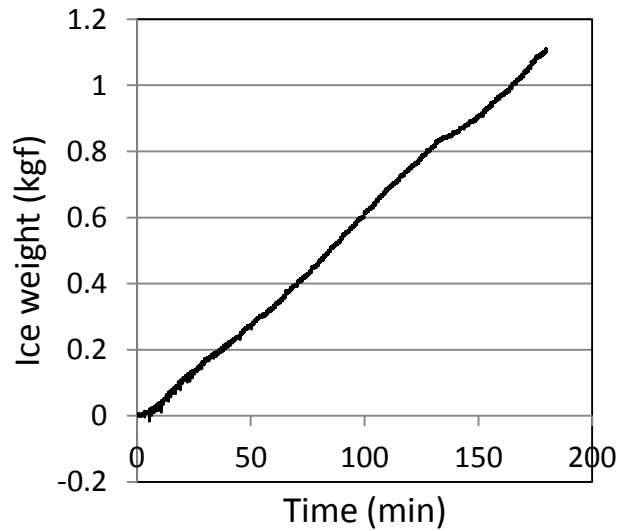


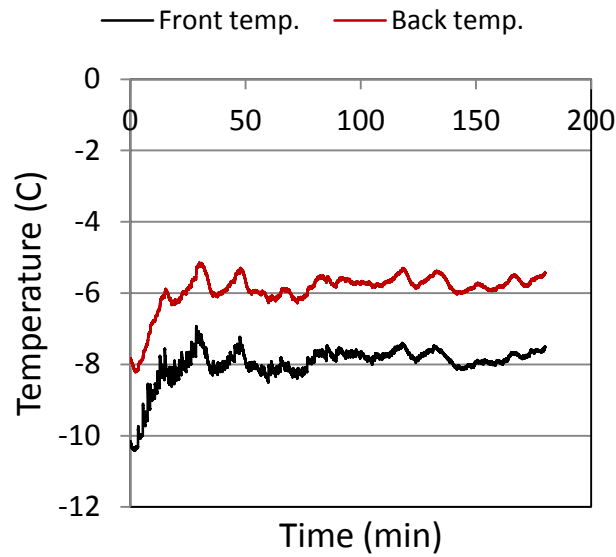
Fig. 7.4: Two views of ice accretion on the vertical plate at $V_{ave,3} \approx 2.65$ m/s, $T_C = -10^\circ\text{C}$,

$S_w = 35\%$, $RH_{ave} = 69.6\%$, including 3 s for the duration of each spray event and

1 min for the period between spray events



(a)



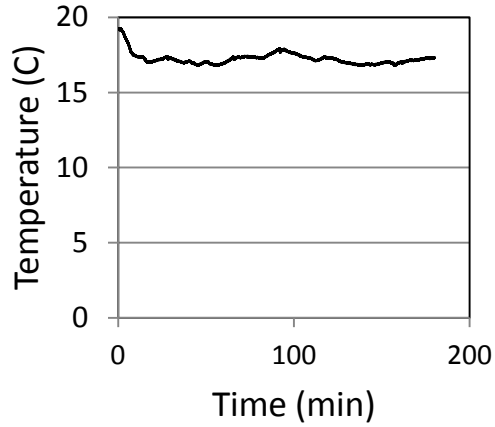
(b)

Fig. 7.5: Changes in (a) the ice weight and (b) temperature at the front and back of the vertical plate versus time at $V_{ave,3} \approx 2.65$ m/s, $T_C = -10^\circ\text{C}$, $S_w = 35\%$, $RH_{ave} = 69.6\%$, including 3 s for the duration of each spray event and 1 min for the period between spray events

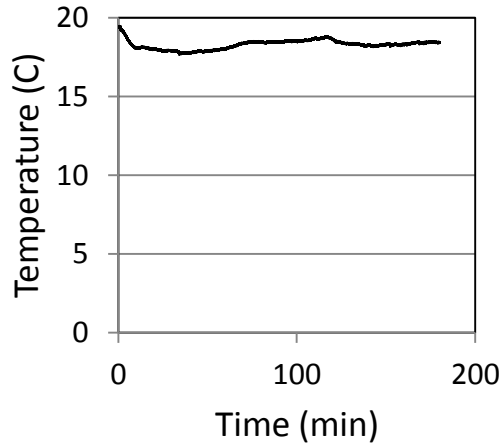
Table 7.3 shows a summary of the ice weight obtained from the load cells for two different conditions with a distance of 2.5 m between the fan and the vertical plate, 3 s for the duration of each spray event and 1 min for the period between spray events. Figure 7.6 indicates the changes in the water temperature inside the pipe before exposure to the spray system over time for tests (1-1-2-b) and (1-2-1-b), respectively. It should be noted that the water temperature inside the tank was 20.9°C for both tests.

Table 7.3: Comparison of the ice weight at $V_{ave,3} \approx 2.65$ m/s, $T_C = -10^\circ\text{C}$, two different salinities and 3 s for the duration of each spray event and 1 min for the period between spray events

Temperature ($^\circ\text{C}$)	Salinity (‰)	Ice weight (kg_f)		
		$V_{ave,3}$ (m/s)		
		1 hr	2 hr	3 hr
-10	0	0.346	0.717	1.115
	35	0.329	0.749	1.104



(a)



(b)

Fig. 7.6: Variations of the water temperature inside the pipe versus time for (a) test (1-1-2-b) and (b) (1-2-1-b)

Table 7.4 demonstrates the amount of mass flux of water spray that impacts on the vertical plate for the duration of the spray event at three fan speeds. These results are for the distance of 2.5 m between the fan and the plate, 5 s for the duration of each spray event and 30 s for the period between spray events.

Table 7.4: Mass flux of water spray that strikes on the vertical plate for the duration of the spray event at three fan speeds

Time	Speed		
	$V_{ave,1}$ (m/s)	$V_{ave,2}$ (m/s)	$V_{ave,3}$ (m/s)
1 hr	1.867 kg	1.340 kg	0.899 kg
2 hr	3.409 kg	2.804 kg	1.515 kg
3 hr	5.320 kg	4.658 kg	2.162 kg

7.2 Discussion

According to the empirical measurements that were reported in the previous section, the following can be concluded.

Due to the experimental measurements, the relative humidity for the adjusted temperature at -10°C was between 67.1% and 73.7%, with an average amount of 70.9% for fifteen tests. Also, the relative humidity for the adjusted temperature at -20°C was between 62.4% and 63.9%, so that the average value for seven tests was 63.1%. As a result, the average amount of relative humidity for the adjusted temperature at -20°C was lower than for the adjusted temperature at -10°C .

The empirical measurements indicate that the fluctuations of temperature inside the cold room during the icing event had a significant influence on the icing intensity and

growth trends. Figure 7.7 shows the ice weight variations over time for tests (1-1-1-a) and (1-1-1-b). As illustrated in this figure, the quantity and growth trends of accumulated ice on the vertical plate were not same while the conditions of both tests, such as fan speed, salinity and the adjusted temperature of the cold room at -10°C were identical, except for the temperature fluctuations during the spray icing event.

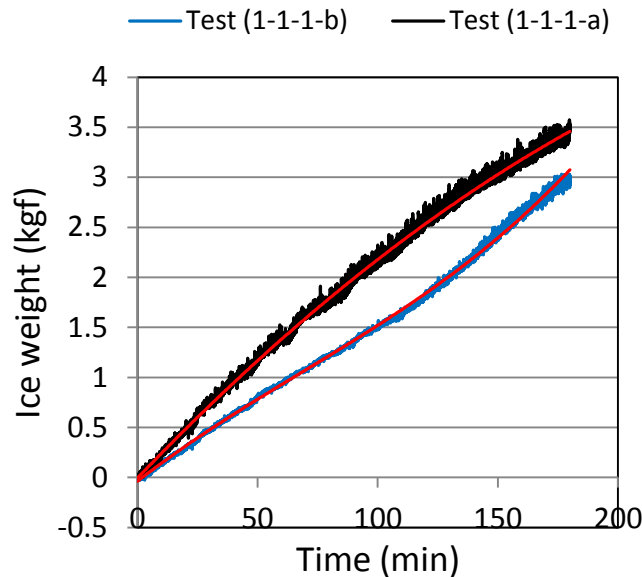


Fig. 7.7: Changes in the ice weight versus time for tests (1-1-1-a) and (1-1-1-b)

The ambient temperature plays an important role in the icing intensity and the amount of ice accumulation on the vertical plate. Figure 7.8 indicates the ice weight variations over time for tests (1-1-1-a) and (2-1-1). Adjusted temperatures inside the cold room were -10°C and -20°C , respectively, but other conditions such as the fan speed, salinity and the time period of the spray event were the same. As observed in this figure, the amount of accumulated ice on the plate at a temperature of -20°C is approximately 1.4 times more

than the temperature of -10°C after the 3 hr test. This result illustrates that there is a good agreement between the data measured and the theoretical predictions.

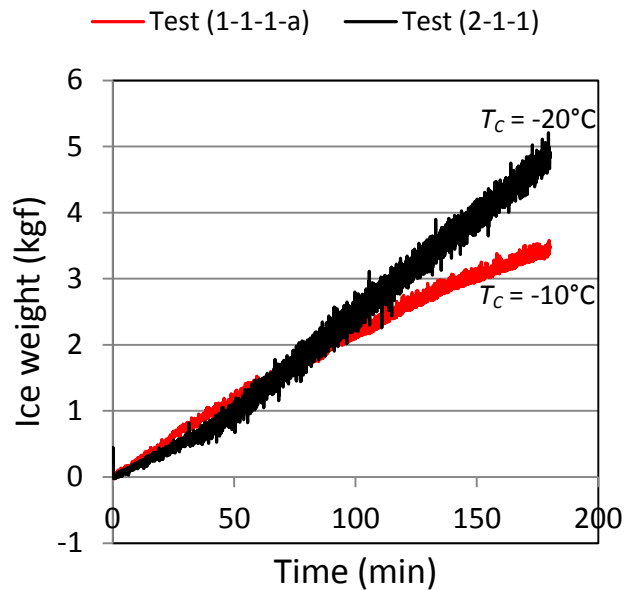


Fig. 7.8: Changes in the ice weight versus time for tests (1-1-1-a) and (2-1-1)

The experimental results show that the distance between the fan and the vertical plate has a substantial impact on the quantity of formed ice on the plate. For instance, for the conditions of $V_{ave,1} \approx 7.85$ m/s, $T_c = -10^{\circ}\text{C}$, $S_w = 0\%$, and the distance of 1.65 m between the fan and the plate, the thickness of ice formation on the plate was 33.15 mm after the 3 hr test, whereas for the same conditions and the distance of 2.5 m between the fan and the vertical plate, the accumulated ice thickness was 15.45 mm (test (1-1-1-a)). Additionally, the amount of runoff for the distance of 1.65 m was higher than that for the distance of 2.5 m.

According to the empirical measurements, the effect of airflow velocity on icing intensity and the amount of ice accretion on the vertical plate was significant. Figure 7.9 displays the weight ice variations over time for three different fan speeds, $T_C = -20^\circ\text{C}$, $S_w = 35\%$, and the distance of 2.5 m between the fan and the plate. As illustrated in this figure, the quantity of ice accumulation on the vertical plate at a higher velocity is much greater compared to lower velocity. This result indicates that the empirical results have a good agreement with the theoretical predictions.

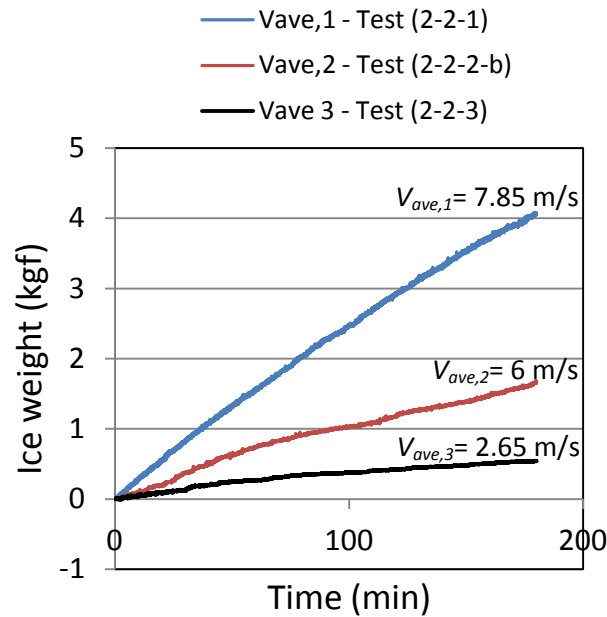


Fig. 7.9: Changes in the ice weight versus time for three different fan speeds, $T_C = -20^\circ\text{C}$, $S_w = 35\%$, and the distance of 2.5 m between the fan and the plate

As mentioned in the previous chapter, the velocity distribution inside the cold room was non-uniform because (a) two fans were installed on the inside of the cold room ceiling for adjustment of the temperature, and (b) the internal space of the cold room was

a limiting factor of a uniform airflow. For test (1-2-3-b), the door between the two cold rooms was open. It was observed that the amount of ice formation on the vertical plate for test (1-2-3-b) was higher than for test (1-2-3-a), while other conditions such as the fan speed, salinity, the temperature inside the cold room, distance between the fan and the plate, and the time period for the spray event were the same. As a result, a more uniform distribution of velocity can create more accumulated ice on the vertical plate. Thus, using a wind tunnel inside the cold room is a suitable approach to generate uniform air velocity.

The results show that errors between the average ice thicknesses obtained from the empirical measurements and the theoretical methods were between 5% and 20% except for three tests. For tests (2-2-2-a), (2-2-3) and (2-1-3), the percentage error was 22%, 29.8% and 30%, respectively, because of the low thickness of accumulated ice. For example, for test (2-1-3), the average ice thicknesses obtained from the experimental and theoretical methods were 3.33 mm and 2.55 mm, respectively.

The time of spray event has a significant effect in the icing intensity and the quantity of ice accretion on the vertical plate during the icing events. Figure 7.10 shows the weight of ice variations over time for two different times of a spray event. As illustrated in this figure, the amount of ice formation on the plate at 5 s for the duration of each spray event and 30 s for the period between spray events was higher than 3 s for the duration of each spray event and 1 min for the period between spray events while other conditions were the same. This is due to an increased mass flux during the spray event.

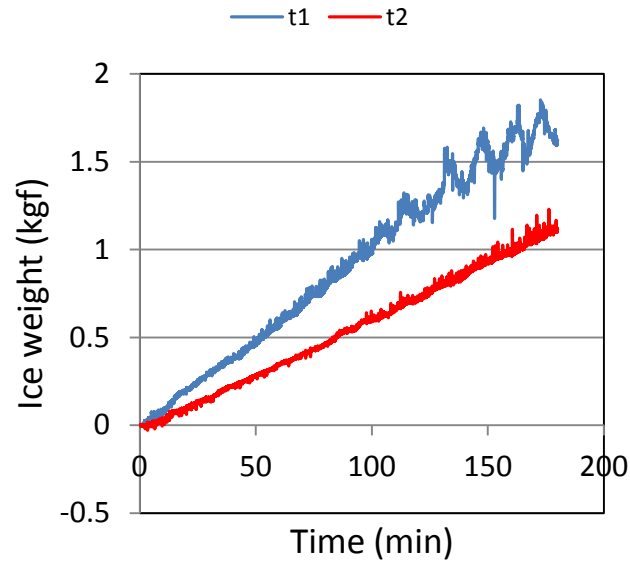


Fig. 7.10: Changes in the ice weight versus time for two different times of spray event, $T_C = -10^\circ\text{C}$, $S_w = 0\text{‰}$, $V_{ave,3} = 2.65 \text{ m/s}$ and the distance of 2.5 m between the fan and the plate. Note: In the above figure, t_1 refers to 5 s for the duration of each spray event and 30 s for the period between spray events and t_2 refers to 3 s for the duration of each spray event and 1 min for the period between spray events

Figure 7.11 indicates the temperature variations at the front and back of the vertical plate over time for tests (1-1-1-b) and (1-2-1-b), where all conditions were the same except the salinity of water spray. As illustrated in this figure, for the formation of saline ice the temperature difference between the front and back of the plate was greater compared to the pure ice formation during the spray icing event. This occurs because (a) the thermal conductivity of saline ice is smaller than the thermal conductivity of pure ice and (b) the temperature gradient has an inverse relation with the thermal conductivity.

The empirical results show that the fluctuations of temperature at the front and back of the vertical plate for saline ice were lower than for pure ice. In other words, for saline ice the temperature changes at the front and back of the vertical plate during spray icing events were smoother. As shown in Fig. 7.11, the temperature of the vertical plate during the spray icing for the both saline ice and pure ice was higher than the adjusted temperature inside the cold room (for both tests $T_C = -10^\circ\text{C}$).

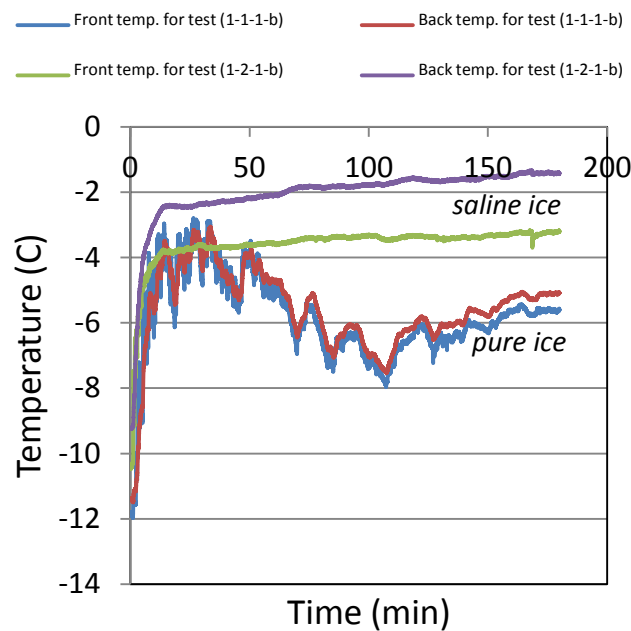


Fig. 7.11: Temperature changes at the front and back of the vertical plate versus time for tests (1-1-1-b) and (1-2-1-b)

The amount of mass flux out (runoff) and the freezing fraction during the spray icing event for each test can be calculated using Eqs. (2.53) and (2.55), respectively. Firstly, the amount of accumulated ice on the vertical plate without any icicles must be computed. By considering the area of the vertical plate (0.25 m^2) instead of the effective area and a

proportion, the quantity of accumulated ice on the plate is obtained. The freezing fraction, n , for each experiment can be determined by:

$$n = \frac{\dot{M}_{ice}}{\dot{M}_{w,t}} \quad (7.1)$$

Also, the amount of runoff is determined by neglecting the mass flux of evaporation (Schröder Hansen, 2012; Myers et al., 2002; Myers and Charpin, 2004):

$$\dot{M}_{runoff,w} = \dot{M}_{w,t} - \dot{M}_{ice} \quad (7.2)$$

Table 7.5 shows the amount of ice accumulation and runoff, as well as the freezing fraction at two different salinities and temperatures inside the cold room, while the fan speed was constant at 7.85 m/s for all tests. As illustrated in this table, at $T_C = -10^\circ\text{C}$ and $S_w = 35\text{‰}$, the lowest amount of ice accumulation and freezing fraction occur as well as the highest amount of runoff. By decreasing the temperature and salinity, the quantity of ice accumulation and freezing fraction will increase. As a result, salinity has an impact on the freezing fraction, such that with increasing salinity the amount of runoff and the number of icicles will increase. This result shows that the experimental measurements agree with the theoretical predictions.

Table 7.5: Comparison of the quantity of ice accumulation and runoff, as well as the freezing fraction for different conditions and tests

Temperature ($^\circ\text{C}$)	Salinity (‰)	\dot{M}_{ice} (kg)	$\dot{M}_{runoff,w}$ (kg)	n	Test code
-10	0	3.378	1.942	0.63	test (1-1-1-a)
	35	3.152	2.168	0.59	test (1-2-1-d)
-20	0	4.669	0.651	0.88	test (2-1-1)
	35	3.919	1.401	0.74	test (2-2-1)

Figure 7.12 shows the changes of collided water mass and accumulated ice on the vertical plate over time for various conditions, while the fan speed was constant at 7.85 m/s for all tests. As illustrated in this figure, the quantity of ice formation on the plate for lower temperature and salinity was higher compared to other conditions. This means that the temperature and salinity have a significant impact in the icing intensity and amount of ice accumulation on the vertical plate.

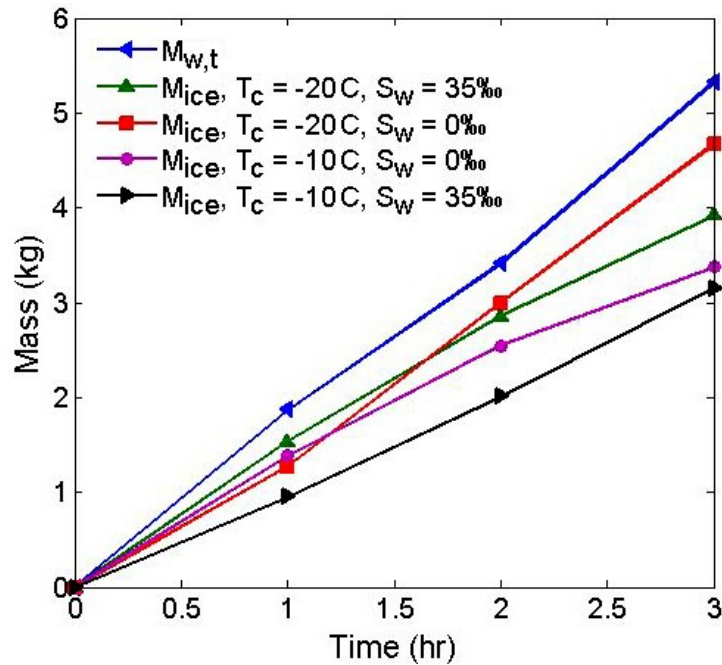


Fig. 7.12: Comparison of the amount of collided water mass and ice accretion on the vertical plate versus time for different conditions

Chapter 8

Summary and Recommendations for Future Research

The phenomenon of icing in cold seas and ocean regions is a significant challenge to marine operations, especially for the extraction and transportation of oil and gas. It can seriously threaten the stability of marine vessels and structures, as well as the safety of the crew. Previous studies illustrated that sea spray icing, or marine icing, is a primary reason in the formation of ice accumulation on marine vessels and offshore structures. An overall survey showed that past results were obtained for field observations and followed by empirical correlations. Theoretical investigations correlated the experimental results. Also, numerical simulations have led to predictions of icing phenomena.

The trajectories and cooling process of droplets during flight over the MFV in cold seas and ocean regions were predicted and analyzed theoretically. The model considered: (1) a uniform temperature within the droplet and (2) convection, evaporation and radiation heat transfer from the droplet's surface to the ambient air. The theoretical results indicated that the water droplets with medium sizes can attain maximum heights and positions at the moment of impact on the deck in the flight duration over the MFV. Additionally, for small water droplets (about 1.1 mm), the assumption of a uniform

temperature inside the droplet was a reasonable approximation. The temperature gradient within the droplet was small for larger droplets, because the Biot number was lower than 0.5. The sensitivity analysis showed that the wind velocity has a significant impact on the droplet trajectories. In addition, the droplet size, initial droplet temperature, air temperature, and the droplet flight time have a considerable effect on the droplet cooling process, although the size of marine platforms is an important factor. The theoretical prediction showed that the assumption of a single droplet for estimation of the amount of ice accumulation on marine platforms is inaccurate because the water droplets have different trajectories and cooling processes. The distribution of the droplets must be considered.

The thermal behaviour and freezing process of a saline water droplet in cold weather conditions were investigated and analyzed using semi-analytical techniques. Three stages with different conditions were analyzed: a liquid cooling stage, a solidification stage, and a solid cooling stage. A new semi-analytical technique was developed to solve an inward moving boundary problem. The results showed that the liquid cooling stage was short and the temperature at the center of the water droplet was close to the initial temperature of the droplet. In addition, the temperature changes during this stage were non-linear. During the solidification stage, the velocity of inward freezing within the droplet was approximately constant, and also the variations of temperature were nearly linear when the temperature inside the droplet reached the freezing temperature. The solid cooling stage occurred much longer compared to other stages, and the temperature variations in this stage were non-linear. For the case study, theoretical predictions found that the droplet temperature with a diameter of 1 mm at the moment of impact on the deck was

approximately -2.1°C . Moreover, there was an ice shell with a thickness of 0.07 mm on the surface of the water droplet at the moment of impact on the deck.

To analyze the icing process on horizontal surfaces of marine vessels and offshore structures in cold seas and ocean regions, another new predictive model was developed. In this study, conduction heat transfer within the ice layer was considered. It was assumed that the volume and distribution of brine pockets and air bubbles inside the ice accumulation were uniform. The freezing fraction and ice layer thickness were predicted using heat and mass balances as well as phase change equations. The results showed that the variations of air temperature, wind velocity, time, and salinity affect the growth rate of ice formation on vessels and marine platforms. With a change of time, the water film salinity and icing intensity will vary. By decreasing the air temperature, the icing intensity will increase. Moreover, the variations of water film salinity affect the thermal conductivity, specific heat capacity of ice accumulation, and the freezing temperature. As a result, heat conduction within the accumulated ice layer has a substantial impact on the growth rate of icing of marine vessels and structures during the freezing conditions in cold seas and ocean regions.

The process of ice accumulation on a vertical plate of marine platforms during spray icing was investigated experimentally in a cold room for various conditions. The empirical measurements showed that: (a) The ambient temperature plays an important role in the icing intensity and the quantity of ice formation on the vertical plate, such that the amount of accumulated ice on the plate at a temperature of -20°C was higher than the temperature of -10°C . (b) The temperature fluctuations inside the cold room during the icing event had a significant influence on the icing intensity and growth trends. (c) The

average amount of relative humidity for the adjusted temperature at -20°C was less than that for the adjusted temperature at -10°C . (d) The distance between the fan and the vertical plate had a substantial impact on the quantity of formed ice on the plate. (e) The effect of airflow velocity on icing intensity and the amount of ice accretion on the vertical plate was significant, so that the quantity of accumulated ice on the plate at a higher velocity was much higher compared to the lower velocity case. (f) The errors between the average ice thicknesses obtained from the experimental and theoretical methods were from 5% to 20% except for three tests where the errors were between 20% and 30%. (g) The time of spray event had a significant effect in the icing intensity and the quantity of ice accretion on the vertical plate during the icing events. (h) For the saline ice formation, the temperature difference between the front and back of the plate was greater compared to the pure ice formation during the spray icing event. Also, the fluctuations of temperature at the front and back of the vertical plate for saline ice were less than for pure ice. (i) The salinity had an impact on the freezing fraction, so that with increasing salinity the amount of runoff and number of icicles increased. (j) There was good agreement between the data measured and the theoretical predictions.

Further future research is recommended as follows. It is recommended to further develop more accurate modeling and analysis of the cooling and freezing processes of water droplets using numerical methods. More detailed analysis of the thermal behaviour and particle image velocimetry (PIV) of saline spray flow inside the cold room using high speed and thermal cameras is also suggested. It is recommended to conduct more testing inside the cold room to obtain additional experimental data and the quantity of accumulated ice on horizontal and inclined marine platform surfaces under various

conditions. Lastly, to produce uniform air velocity inside the cold room, using a wind tunnel is suggested.

References

- Achenbach, E., 1977. The Effect of Surface Roughness on the Heat Transfer from a Circular Cylinder to the Cross Flow of Air. *Int. J. Heat Mass Transfer*, 20, 359-369.
- Aksyutin, L.R., 1979. Icing of Ships. Sudostroeyne Publishing House, Leningrad, (126 p). (in Russian)
- Andreas, E.L., 1990. Time Constants for the Evolution of Sea Spray Droplets. *Tellus B*, 42(5), 481-497.
- Andreas, E.L., Persson, P.O.G., Hare, J.E., 2008. A Bulk Turbulent Air-sea Flux Algorithm for High-Wind, spray conditions. *J. Phys. Oceanogr.*, 38(7), 1581-1596.
- Ashcroft, J., 1985. Potential ice and snow accretion on North Sea rigs and platforms. Marine Technical Note no. 1, British Meteorological Office, Bracknell.
- ASHRAE Handbook of Fundamental, 1977. American Society of Heating, Refrigerating and Air Conditioning Engineers, Inc., New York, NY, USA.
- Assur, A., 1958. Composition of Sea Ice and its Tensile Strength, Arctic Sea Ice. US National Academic Sciences-National Research Council Pub., 598, 106-138.
- Brakel, T.W., Charpin, J.P.F., Myers, T.G., 2007. One-Dimensional Ice Growth Due to Incoming Supercooled Droplets Impacting on a Thin Conducting Substrate. *Int. J. Heat Mass Transfer*, 50, 1694–1705.

- Berenbeim, D.Y., 1969. Hydro-meteorological conditions of vessel icing. *Meteorology and Hydrology*, No. 5.
- Bergman, T.L., Lavine, A.S., Incropera, F.P., DeWitt, D.P., 2011. *Introduction to Heat Transfer*. 6th Edition, John Wiley & Sons, Inc.
- Blackmore, R.Z., Lozowski, E.P., 1994. An Heuristic Freezing Spray Model of Vessel Icing. *Int. J. Offshore and Polar Engineering*, 4(2), 119-126.
- Blackmore, R.Z., Lozowski, E.P., 1998. A theoretical spongy spray icing model with surficial structure. *Atmos. Res.* 49, 267–288.
- Blackmore, R.Z., Makkonen, L., Lozowski, E.P., 2002. A new model of spongy icing from first principles. *Journal of Geophysical Research*, 107 (D21).
- Bodaghkhani, A., Dehghani, S.R., Muzychka, Y.S., Colbourne, B., 2016. Understanding spray cloud formation by wave impact on marine objects. *Cold Regi. Sci. Tech.*, 129, 114–136.
- Bonacina, A., 1973. Numerical Solution of Phase-Change Problems. *Int. J. Heat Mass Transfer*, 16, 1825–1832.
- Borisenkov, E.P., Panov, V.V., 1972. Fundamental Results and Perspectives into the Hydro-Meteorological Aspects of Ships Icing. Leningrad, *Arkt. Autarkt. Nauc-Issled Inst.* T298, 5-33.
- Borisenkov, Y.P., Zablokiy, G.A., Makshtas, A.P., Migulin, A.I., Panov, V.V., 1975. On the Approximation of the Spray Cloud Dimensions. In: *Arkticheskii i Antarkticheskii Nauchno-Issledovatel'skii Institut, Trudy* 317, Gidrometeoizdat, Leningrad, 121-126. (in Russian)

- Bottyan, Z., 2011. Estimation of Structural Icing Intensity and Geometry of Aircrafts during Different Conditions: a Fixed-wing Approach. Quarterly J. Hungarian Meteorological service, 115(4), 275-288.
- Brakel, T.W., Charpin, J.P.F., Myers, T.G., 2007. One-dimensional Ice Growth due to Incoming Supercooled Droplets Impacting on a Thin Conducting Substrate. Int. J. Heat Mass Transfer, 50, 1694-1705.
- Brown, R.D., Roebber, P., 1985. The Scope of the Ice Accretion Problem in Canadian Waters Related to Offshore Energy and Transportation. Canadian Climate Centre, Report No. 85.13, Downsview, Ont., (295 p).
- Brown, R.D., Mitten, P., 1988. Ice Accretion on Drilling Platforms off the East Coast of Canada. In: Hansen, A., Storm, J.F. (Eds.), Proceedings of the International Conference on Technology for Polar Areas, Tapir Publishers, Trondheim, Norway, 2, 409-421.
- Brown, R.D., Horjen, I., Jørgensen, T., Roebber, P., 1988. Evaluation of state of the art drilling platform ice accretion models. 4th Int. Workshop on Atmospheric Icing of Structures, Paris, pp. 208–213.
- Brown, R.D., Horjen, I., 1989. Evaluation of state of the art drilling platform icing models. Canadian Climate Centre, Report No. 89-10. Atmospheric Environment Service, Ontario (80 p).
- Caldwell, J., Chan, C., 2000. Spherical Solidification by the Enthalpy Method and the Heat Balance Integral Method. Appl. Math. Model., 24, 45–53.
- Cammaert, G., 2013. Impact of Marine Icing on Arctic Offshore Operations. Arctic Marine Operations Challenges & Recommendations, Vol. 5, Pilot Project.

- Cansdale, J.T., McNaughton, I.I., 1977. Calculation of Surface Temperature and Ice Accretion Rate in a Mixed Water Droplet Ice Crystal Cloud. Royal Aircraft Establishment Technical Report 77090, Farnborough, Hants, UK.
- Carslaw, H.S., Jaeger, J.G., 1959. Conduction of Heat in Solids, 2nd edition. Oxford University Press, p. 285.
- Chaine, P.M., Skeates, P., 1974. Wind and Ice Loading Criteria Selection. Canadian Climate Centre Internal Report, Industrial Meteorology-Study III, Atmospheric Environment Service, Downsview, Ontario, Canada.
- Chan, C.W., Tan, F.L., 2006. Solidification inside a Sphere - an Experimental Study. *Int. Comm. Heat Mass Transfer*, 33, 335–341.
- Chung, K.K., Lozowski, E.P., 2010. On the Growth of Marine Icicles. *Atmosphere-Ocean*, 28(4), pp. 393-408.
- Clift, R., Grace, J.R., Weber, M.E., 1978. Bubbles, Drops and Particles. San Diego, Calif.: Academic Press.
- Comiskey, A., 1976. Vessel Icing-Know When to Expect It. *Alaska Seas and Coasts*, 4(5), 6-7.
- Cox, G.F.N., Weeks, W.F., 1983. Equations for Determining the Gas and Brine Volumes of Sea-Ice Samples. *J. Glaciol.*, 29 (102), 306–316.
- Dehghani, S.R., Muzychka, Y.S., Naterer, G.F., 2016a. Droplet trajectories of wave-impact sea spray on a marine vessel. *Cold Regi. Sci. Tech.* 127, 1–9.
- Dehghani, S.R., Naterer, G.F., Muzychka, Y.S., 2016b. Droplet size and velocity distributions of wave-impact sea spray over a marine vessel. *Cold Regi. Sci. Tech.* 132, 60–67.

- Dehghani, S.R., Muzychka, Y.S., Naterer, G.F., 2017a. Water breakup phenomena in wave-impact sea spray on a vessel. *Ocean Eng.*, 134, 50–61.
- Dehghani, S.R., Naterer, G.F., Muzychka, Y.S., 2017b. Transient heat conduction through a substrate of brine-spongy ice. *Heat and Mass Transfer*. 53 (8), 2719–2729.
- Dehghani-Sanij, A.R., Muzychka, Y.S., Naterer, G.F., 2015. Analysis of Ice Accretion on Vertical Surfaces of Marine Vessels and Structures in Arctic Conditions. The ASME 2015 34th International Conference on Ocean, Offshore and Arctic Engineering (OMAE2015), OMAE2015-41306, St. John's, Newfoundland, Canada.
- Dehghani-Sanij, A.R., Muzychka, Y.S., Naterer, G.F., 2016. Predicted Ice Accretion on Horizontal Surfaces of Marine Vessels and Offshore Structures in Arctic Regions. The ASME 2015 35th International Conference on Ocean, Offshore and Arctic Engineering (OMAE2016), OMAE2016-54054, Busan, South Korea.
- Dehghani-Sanij, A.R., Dehghani, S.R., Naterer, G.F., Muzychka, Y.S., 2017a. Sea Spray Icing Phenomena on Marine Vessels and Offshore Structures: Review and Formulation, *Ocean Engineering*, 132, 25–39.
- Dehghani-Sanij, A.R., Dehghani, S.R., Naterer, G.F., Muzychka, Y.S., 2017b. Marine Icing Phenomena on Vessels and Offshore Structures: Prediction and Analysis, *Ocean Engineering*, 143, 1-23.
- Dehghani-Sanij, A.R., Naterer, G.F., Muzychka, Y.S., 2017c. Heat Transfer of Impinging Seawater Spray and Ice Accumulation on Marine Vessel Surfaces, *Heat Transfer Research*, 48 (17), 1599-1624.
- Dehghani-Sanij, A.R., Naterer, G.F., Muzychka, Y.S., Pope, K., 2017d. Thermal Analysis of Saline Droplet Motion with Cooling in Cold Regions. The ASME 2017 36th

- International Conference on Ocean, Offshore and Arctic Engineering (OMAEE2017), OMAEE2017-61097, Trondheim, Norway.
- Efimov, Y.O., 2012. Vessel Icing on the Shtokman FPSO. MS thesis, Faculty of Science and Technology, University of Stavanger, Norway.
- Engineering Toolbox, 2017. Retrieved from: <http://www.engineeringtoolbox.com>
- Environment and Climate Change, Canada, Met 101. <http://www.ec.gc.ca/meteo-weather/default.asp?lang=En&n=279AC7ED-1&offset=6&toc=show>
- Fazelpour, A., Dehghani, S.R., Masek, V., Muzychka, Y.S., 2016a. Infrared Image Analysis for Estimation of Ice Load on Structures, in: Arctic Technology Conference. Offshore Technology Conference.
- Fazelpour, A., Dehghani, S.R., Masek, V., Muzychka, Y.S., 2016b. Effect of Ambient Conditions on Infrared Ice Thickness Measurement, in: IEEE Conference, Newfoundland and Labrador Section.
- Feit, D.M., 1987. Forecasting of Superstructure Icing for Alaskan Waters. Natl. Wea. Dig., 12(2), 5-10.
- Fichefet, T., Maqueda, M.M., 1997. Sensitivity of a Global Sea Ice Model to the Treatment of Ice Thermodynamics and Dynamics. J. Geophys. Res., 102 (12), 609–646.
- Finstad, K.J., Lozowski, E.P., Gates, E.M., 1988. A computational investigation of water droplet trajectories. J. Atmos. Oceanic Technol., 5, 160-170.
- Feuillebois, F., Lasek, A., Creismas, P., Pigeonneau, F., Szaniawski, A., 1995. Freezing of a Subcooled Liquid Droplet. J. Colloid Interface Sci., 169, 90–102.

- Forest, T., Lozowski, E., Gagnon, R., 2005. Estimating Marine Icing on Offshore Structures Using RIGICE04. International Workshop on Atmospheric Icing on Structures (IWAIS), Montreal, Canada.
- Fu, P., Farzaneh, M., Bouchard, G., 2006. Two-Dimensional Modelling of the Ice Accretion Process on Transmission Line Wires and Conductors. *Cold Reg. Sci. Tech.*, 46, 132–146.
- Fukusako, Sh., Horibe, A., Tago, M., 1989. Ice Accretion Characteristics along a Circular Cylinder Immersed in a Cold Air Stream with Seawater Spray. *Experimental Thermal and Fluid Science*, 2, 81-90.
- Gaches, R., Eik, K., Mathlesen, M., 2013. Skrugard Field Metocean Design Basis. PTM MMG MGE RA 58. Statoil, Norway.
- Gao, W., Smith, D.W., SeGO, D.C., 2000. Freezing behavior of freely suspended industrial wastewater droplets. *Cold Reg. Sci. Tech.* 31, 13–26.
- Gautier, D.L., Bird, K.J., Charpentier, R.R., Grantz, A., Houseknecht, D.W., Klett, T.R., Moore, T.E., Pitman, J.K., Schenk, C.J., Schuenemeyer, J.H., Sørensen, K., Tennyson, M.E., Valin, Z.C., Wandrey, C.J., 2009. Assessment of Undiscovered Oil and Gas in the Arctic. *Science*, 324(5931), 1175-1179.
- Green, D.W., Perry, R.H., 2008. *Perry's Chemical Engineers' Handbook*. 8th Edition, McGraw-Hill, New York, USA.
- Guest, P., 2005. Vessel Icing. *Mariners Weather Log*, 49(3).
- Guglielmini, G., Pisoni, C., 2001. *Introduzione Alla Trasmissione Del Calore*. Casa Editrice Ambrosiana, Milano. (in Italian)

- Gupta, S.C., 1987. Analytical and numerical solutions of radially symmetric inward solidification problems in spherical geometry. *Int. J. Heat Mass Transfer*, 30(12), 2611–2616.
- Gupta, S.C., Arora, P.R., 1992. Analytical and numerical solutions of inward spherical solidification of a superheated melt with radiative-convective heat transfer and density jump at freezing front. *Warme-und Stoffubertr.*, 27, 377–384.
- Hay, R.F.M., 1956a. Meteorological Aspects of the Loss of Lorella and Roderigo. *Marine Observer.*, 26, 89-94.
- Hay, R.F.M., 1956b. Ice Accumulation upon Trawlers in Northern Waters. *Meteor. Mag.*, 85(1010), 225.
- Hill, J.M., Kucera, A., 1983. Freezing a saturated liquid inside a sphere. *Int. J. Heat Mass Transfer*, 26(11), 1631–1637.
- Hindmarsh, J.P., Russell, A.B., Chen, X.D., 2003. Experimental and Numerical Analysis of the Temperature Transition of a Suspended Freezing Water Droplet. *Int. J. Heat Mass Transf.*, 46, 1199–1213.
- Hindmarsh, J.P., Russell, A.B., Chen, X.D., 2004. Experimental and Numerical Analysis of the Temperature Transition of a Freezing Food Solution Droplet. *Chem. Eng. Sci.*, 59, 2503–2515.
- Horjen, I., 1983a. Mobile Platform Stability. MOPS Subproject 02-Icing, MOPS Report No.7, Norwegian Hydro-dynamic Laboratories, NHL 283021.
- Horjen, I., 1983b. Icing on Offshore Structures, Atmospheric Icing. *Norwegian Maritime research*, 3, 9-22.

- Horjen, I., 1990. Numerical Modeling of Time-dependent Marine Icing, Anti-icing and Deicing. Doctoral thesis, Norges Tekniske Høgskole (NTH), Trondheim, Norway.
- Horjen, I., 2013. Numerical Modeling of Two-dimensional Sea Spray Icing on Vessel-mounted Cylinders. *Cold Regi. Sci. Tech.*, 93, 20-35.
- Horjen, I., 2015. Offshore Drilling Rig Ice Accretion Modeling Including a Surficial Brine Film. *Cold Regi. Sci. Tech.*, 119, 84-110.
- Horjen, I., Vefsnmo, S., 1984. Mobile Platform Stability (MOPS) Subproject 02-icing. MOPS Report No. 15, Norwegian Hydrodynamic Laboratories, STF60 A 284002, (56 p).
- Horjen, I., Vefsnmo, S., 1985. A Kinematic and Thermodynamic Analysis of Sea Spray, Offshore Icing-Phase II. STF60 F85014, Norwegian Hydrodynamic Laboratory (NHL), Norway. (in Norwegian)
- Horjen, I., Vefsnmo, S., 1986a. Computer modelling of sea spray icing on marine structures. In *Proc. Symp. On Automation for Safety in Shipping and Offshore Operations*, Trondheim, Norway (ed. G. Kuo et al.), pp. 315-323.
- Horjen, I., Vefsnmo, S., 1986b. Calibration of ICEMOD – extension to a time-dependent model. Norwegian Hydrodynamic Laboratories Report STF60 F86040.
- Horjen, I., Løset, S., Vefsnmo, S., 1986. Icing hazards on supply vessels and stand-by boats. Technical Report, Norwegian Hydrotechnical Laboratory.
- Horjen, I., Vefsnmo, S., 1987. Time-dependent sea spray icing on ships and drilling rigs – a theoretical analysis. Norwegian Hydrodynamic Laboratories Report STF60 F87130.

- Horjen, I., Vefsnmo, S., Bjerke, P.L., 1988. Sea spray icing on rigs and supply vessels. ESARC Report no. 15, Norwegian Hydrodynamic Laboratories Report STF60 F88137.
- Horjen, I., Carstens, T., 1990. Numerical Modelling of the Sea Spray Icing on Vessels. In Proc. 10th Int. POAC Conf, Lulea, Sweden, 3, 694-704.
- Huang, C.L., Shih, Y.P., 1975. A perturbation method for spherical and cylindrical solidification. Chem. Eng. Sci., 30, 897–906.
- IMO. 2016. International code of safety for ships operating in polar waters (polar code). London: International Maritime Organization, 2016 edition.
- Incropera, F.P., DeWitt, D.P., 1985. Fundamentals of Heat and Mass Transfer. New York, John Wiley and Sons.
- Incropera, F.P., DeWitt, D.P., Bergman, T.L., Lavine, A.S., 2006. Introduction to Heat Transfer., 5 edition, Wiley.
- Itagaki, K., 1979. Icing on Ships and Stationary Structures under Marine Conditions, A Preliminary Literature Survey of Japanese Sources. US Army Corps of Engineers, Cold Regions Research & Engineering Laboratory, CRREL Special Report 77-27, (26 p).
- Itagaki, K., 1984. Icing Rate on Stationary Structures under Marine Conditions. US Army Corps of Engineers, Cold Regions Research & Engineering Laboratory, CRREL REPORT 84-12, (9 p).
- Jessup, R.G., 1985. Forecast techniques for ice accretion on different types of marine structures, including ships, platforms and coastal facilities, Marine Meteorological

- and Related Oceanographic Activities. Report No. 15, WMO/TD-No. 70, Geneva, WMO Secretariat, 90 pp.
- Jørgensen, T.S., 1982. Influence of Ice Accretion on Activity in the Northern Part of the Norwegian Continental Shelf. Offshore Technology Testing and Research report No. F82016, Trondheim, Norway: Continental Shelf Institute, Norwegian Hydrodynamic Laboratories.
- Jørgensen, T.S., 1985. Impacts on Safety and Operation of Marine Units due to Ice Accretion. J. Bull. Norwegian Hydrotech. Lab., 79-84.
- Jones, K.F., 1996. Ice Accretion in Freezing Rain. US Army Corps of Engineers, Cold Regions Research & Engineering Laboratory, CRREL REPORT 96-2 (31 p).
- Jones, K.F., Andreas, E.L., 2009. Technology Assessment and Research Program. Safety and engineering research: sea spray icing of drilling and production platforms, US Army Engineer Research and Development Center, Cold Regions Research and Engineering Laboratory, ERDC/CRREL TR-09-3, (63 p).
- Jones, K.F., Andreas E.L., 2012. Sea Spray Concentrations and the Icing of Fixed Offshore Structures. Q. J. R. Meteorol. Soc., 138, 131-144.
- Kachurin, L.G., Gashin, L.I., Smirnov, I.A., 1974. Icing rate of small displacement fishing boats under various hydrometeorological conditions. Meteorologiya i Gidrologiya, Moscow, 3, 50-60.
- Karlekar, B.V., Desmond, R.M., 1977. Engineering Heat Transfer. West Publishing Co., New York, USA.

- Kato, R., 2012. Modeling of Ship Superstructure Icing: Application to Ice Bridge Simulators. MS thesis, Department of Marine Technology, Norwegian University of Science and Technology, Norway.
- Kreith, F., Krumdieck, S., 2013. Principles of Sustainable Energy Systems. Second Edition, Boca Raton: CRC Press, Taylor and Francis Group.
- Krzewinski, T.G., Tart, R.G., 1985. Thermal Design Considerations in Frozen Ground Engineering: A State of the Practice Report. American Society of Civil Engineers (ASCE), New York, USA.
- Kulyakhtin, A., Løset, S., 2011. Sea Spray Icing: In-cloud Evaporation, Semi-analytical and Numerical Investigations. The 14th International Workshop on Atmospheric Icing of Structures, Chongqing, China, p. 5.
- Kulyakhtin, A., Shipilova, O., Libby, B., Løset, S., 2012. Full-scale 3D CFD Simulation of Spray Impingement on a Vessel Produced by Ship-wave Interaction. The 21st IAHR International Symposium on Ice, Dalian, China, 1129-1141.
- Kulyakhtin, A., Kulyakhtin, S., Løset, S., 2013. Marine Icing Field Experiment 2012. 2013-1776, Det Norske Veritas.
- Kulyakhtin, A., 2014. Numerical Modelling and Experiments on Sea Spray Icing. Doctoral thesis, Department of Civil and Transport Engineering, Norwegian University of Science and Technology (NTNU), Norway.
- Kulyakhtin, A., Tsarau, A., 2014. A Time-dependent Model of Marine Icing with Application of Computational Fluid Dynamics. Cold Regi. Sci. Tech., 104-105, 33-44.

- Kulyakhtin, A., Shipilova, O., Muskulus, M., 2014. Numerical Simulation of Droplet Impingement and Flow around a Cylinder Using RANS and LES. *J. Fluids Structure*, 48, 280–294.
- Kulyakhtin, A., Kulyakhtin, S., Løset, S., 2016. The role of the ice heat conduction in the ice growth caused by periodic sea spray. *Cold Regi. Sci. Technol.* 127, 93–108.
- Kuwahara, S., 1938. Velocity of Sound in Sea Water and Calculation of the Velocity for Use in Sonic Sounding. *Japanese J. Astronomy and Geophys.* 16, 1–17.
- Lackenby, H., 1960. Formation of Ice on Trawlers. *Fishing Boats of the World*, Vol. 2-Sea Behaviour, 511-514.
- Lange, N.A., Forke, G.M., 1952. *Handbook of Chemistry*. 8th ed., Handbook Publ., Sandusky, Ohio, USA.
- Langmuir, I., Blodgett, K., 1946. A Mathematical Investigation of Droplet Trajectories. General Electric Res. Lab., Report RL-224, Reprinted in “Collected Works of I. Langmuir”, Pergamon Press, 335-393.
- Lewis, E.R., Schwartz, S.E., 2004. *Sea Salt Aerosol Production: Mechanisms, Methods, Measurements, and Models – A Critical Review*. Geophysical Monograph 152, AGU: Washington, DC.
- Li, Nai-Yi, Barber, J.R., 1989. Sinusoidal Perturbation Solutions for Planar Solidification. *Int. J. Heat Mass Transfer*, 32(5), 935–941.
- Livingood, J.N.B., Hrycak, P., 1973. Impingement Heat Transfer from Turbulent Air Jets to Flat Plates. A literature survey, National Aeronautics and Space Administration Washington, D.C. 20546, NASA TM X-2778.

- Lock, G.S.H., 1972. Some Aspects of Ice Formation with Special Reference to the Marine Environment. *North East Coast Inst of Engineers & Shipbuilders*, 88(6), 175-184.
- London, A.L., Seban, R.A., 1943. Rate of ice formation. *Transactions of the American Society of Mechanical Engineers*, 65(7), 771–779.
- Lorenzini, G., Saro, O., 2013. Thermal Fluid Dynamic Modelling of Water Droplet Evaporation in Air. *Int. J. Heat Mass Transfer*, 62, 323–335.
- Lozowski, E.P., 2017. Sea Spray Icing of Ships and Offshore Structures. *Encyclopedia of Life Support Systems*, 31 pp. In Press, United Nations Educational Scientific and Cultural Organization (UNESCO).
- Lozowski, E.P., Stallabrass, J.R., Hearty, P.F., 1983. The Icing of an Unheated, Non-rotating Cylinder, Part I: A Simulation Model. *J. Climate Appl. Meteorology*, 22, 2053-2062.
- Lozowski, E.P., Gates, M.E., 1985. An Overview of Marine Icing Research. *Proceeding of the International Offshore Mechanics and Arctic Engineering Symposium*, 2, 6-15.
- Lozowski, E.P., Blackmore, R.Z., Forest, T.W., Shi, J., 1996. Spongy icing in the marine environment. *American Society of Mechanical Engineers*, New York, NY, USA.
- Lozowski, E.P., Szilder, K., Makkonen, L., 2000. Computer Simulation of Marine Ice Accretion. *Royal Society of London Philosophical Transactions Series A*, 358, 2811-2845.
- Lundqvist, J.E., Udin, I., 1977. Ice Accretion on Ships with Special Emphasis on Baltic Conditions. *Winter Navigation Research Board, Swedish Administration of Shipping and Navigation, Finnish Board of Navigation, Research Report, No. 23.*

- Macdonald, O.C., McCartney, H.A., 1987. Calculation of splash droplet trajectories. *Agric. For. Meteorol.*, 39, 95-110.
- Makkonen, L., 1984a. Atmospheric Icing on Sea Structures. US Army Cold Regions Research and Engineering Laboratory, monograph 84-2, 102.
- Makkonen, L., 1984b. Modeling of Ice Accretion on Wires. *J. Climate Appl. Meteor.*, 23, 929-939.
- Makkonen, L., 1985. Heat transfer and icing of a rough cylinder. *Cold Regi. Sci. Tech.*, 10(2), 105-116.
- Makkonen, L., 1986. The Effect of Conductor Diameter on Iceload as Determined by a Numerical Icing Model. In *Proc. 3rd Int. Workshop on Atmospheric Icing of Structures*, 81-89.
- Makkonen, L., 1987. Salinity and growth of ice formed by sea spray. *Cold Reg. Sci. Tech.*, 14, 163-171.
- Makkonen, L., 1989. Formation of spray ice on offshore structures. US Army Cold Regions Research & Engineering Laboratory, IAHR State-of-the-Art Report on Ice Forces: CRREL Special Report, 89-5, 277-309.
- Makkonen, L., 2000. Models for the Growth of Rime, Glaze, Icicles and Wet Snow on Structures. *Phil. Trans. R. Soc. Lond. A*, 358, 2913-2939.
- Makkonen, L., 2010. Solid Fraction in Dendritic Solidification of a Liquid. *Appl. Phys. Letters*, 96(9), 091910-1- 091910-3.
- Marine Log Website. http://www.marinelog.com/index.php?option=com_k2&view=item&id=7630:dnv-gl-launches-sea-spray-icing-project&Itemid=230
- Matlab version R14. The MathWorks Inc., USA.

- McDonald, J.E., 1954. The shape and aerodynamics of large rain drops. *J. Meteorol.* 11, 478–494.
- Mertins, H.O., 1968. Icing on Fishing Vessels due to Spray. *Marine Observer.*, London, 38(221), 128-130.
- Mezhericher, M., Levy, A., Borde, I., 2008. Heat and Mass Transfer of Single Droplet/Wet Particle Drying. *Chem. Eng. Sci.*, 63(1), 12–23.
- Milanez, L.F., Boldrini, J.L., 1988. Perturbation solution for spherical solidification by convective cooling. *J. Thermophysics Heat Transfer*, 2, 88–91.
- Minsk, L.D., 1977. Ice accumulation on ocean structure. US Army Corps of Engineers, Cold Regions Research & Engineering Laboratory, CRREL Report 77-17.
- Minsk, L.D., 1984a. Ice Observation Program on the Semisubmersible Drilling Vessel SEDCO 708. US Army Corps of Engineers, Cold Regions Research & Engineering Laboratory, Special Report 84-2.
- Minsk, L.D., 1984b. Assessment of Ice Accretion on Offshore Structures. US Army Cold Regions Research and Engineering Laboratory, Hanover, New Hampshire, CRREL Special Report 84-4, (12 p).
- Mitten, P., 1994. Measurement and modelling of spray icing on offshore structures. Final Report to Atmospheric Environment Service of Canada, Contract no. 07SE. KM169-8-7439.
- Monahan, E.C., Fairall, C.W., Davidson, K.L., Boyle, P.J., 1983. Observed Interrelations between 10 m Winds, Ocean Whitecaps and Marine Aerosols. *Q.J.R. Meteorol. Soc.*, 109, 379-392.

- Monahan, E.C., 1986. The Ocean as a Source for Atmospheric Particles. In *The role of air-sea exchange in geochemical cycling*, ed. P. Buat-Ménard, 129-163, Dordrecht, The Netherlands: D. Reidel Publishing.
- Murray, W.D., Landis, F., 1959. Numerical and Machine Solutions of Transient Heat-Conduction Problems Involving Melting or Freezing. *Trans. ASME J. Heat Transfer*, 81, 106–112.
- Myers, T.G., 1998. Thin Films with High Surface Tension. *Siam Rev.*, 40(3), 441-462.
- Myers, T.G., Hammond, D.W., 1999. Ice and Water Film Growth from Incoming Supercooled Droplets. *Int. J. Heat Mass Transfer*, 42, 2233-2242.
- Myers, T.G., 2001. Extension to the Messinger Model for Aircraft Icing. *AIAA J.*, 39(2), 211-218.
- Myers, T.G., Charpin, J.P.F., Chapman, S.J., 2002. The Flow and Solidification of a Thin Fluid Film on an Arbitrary Three Dimensional Surface. *Phys. Fluids*, 14(8), 2788-2803.
- Myers, T.G., Charpin, J.P., 2004. A Mathematical Model for Atmospheric Ice Accretion and Water Flow on a Cold Surface. *Int. J. Heat Mass Transfer*, 47(25), 5483-5500.
- Maykut, G., Untersteiner, N., 1971. Some Results from a Time-Dependent Thermodynamic Model of Sea Ice. *J. Geophys. Res.*, 76, 1550–1576.
- Nakakita, K., Nadarajah, S., Habashi, W., 2010. Toward Real-time Aero-icing Simulation of Complete Aircraft via FENSAP-ICE. *J. Aircr.*, 47(1), 96-109.
- Naterer, G.F., 2011. Multiphase Transport Processes of Droplet Impact and Ice Accretion on Surfaces. *Cold Regi. Sci. Tech.*, 65, 5-12.

- Nauman, J.W., Tyagi, R., 1985. Sea spray icing and freezing conditions on offshore oil rigs-Alaska experience and regulatory implications. Proceedings International Workshop on Offshore Winds and Icing, Halifax, Nova Scotia, 313-328.
- Nicolis, G., Maes, D., Rice, S.A., Dinner, A.R. (Editors), 2010. Advances in Chemical Physics. Volume 151: Kinetics and Thermodynamics of Multistep Nucleation and Self-Assembly in Nanoscale Materials. John Wiley & Sons.
- Ono, N., 1964. Studies of Ice Accumulation, Part II: Condition of Icing and Accreted Ice Weights. Low Temperature Science, Series A 22. (Translated by Hope, E.R., Def. Res. Bd., Dir. Sci. Inf. Serv. T94 J, Ottawa, 1967)
- Ono, N., 1967. Specific Heat and Fusion of Sea Ice, in Physics of Snow and Ice: International Conference on Low Temperature Science, edited by H. Oura, Inst. of Low Temp. Sci., Hokkaido Univ., Sapporo, Japan, 1 (1), 599–610.
- Overland, J.E., Pease, C.H., Preisendorfer, R.W., Comiskey, A.L., 1986. Prediction of Vessel Icing. J. Climate Appl. Meteor., 25(12), 1793-1806.
- Overland, J.E., 1990. Prediction of Vessel Icing for Near-freezing Sea Temperatures. Weather and Climate, 5, 62-77.
- Ozisik, M.N., 2000. Heat Conduction. John Wiley, New York.
- Panov, V.V., 1971. On the Frequency of Splashing a Medium-sized Fishing Vessel with Sea Spray. In: Theoretical and Experimental Investigations of the Conditions of Icing of Ships, Gidrometeoizdat, Leningrad, 87-90. (in Russian)
- Panov, V.V., 1976. Icing of Ships. Arkticheskii i Antarkticheskii Nauchno-Issledovatel'skii Institut, Trudy 334, Gidrometeoizdat, Leningrad, (263 p). (in Russian)

- Panov, V.V., Moltjanov, V.N., 1972. Spray and Icing on Fishing Vessels of Type SRT and SRTM. Trudy, 298, Arctic and Antarctic Research Institute, Leningrad.
- Parang, M., Crocker, D.S., Haynes, B.D., 1990 .Perturbation solution for spherical and cylindrical solidification by combined convective and radiative cooling. Int. J. Heat Fluid Flow, 11 (2), 142–1486.
- Paulin, M.V., 2008. Arctic Offshore Technology Assessment of Exploration and Production Options for Cold Regions of the US Outer Continental Shelf. IMV Projects Atlantic, US Minerals Management Service, St. John's, Newfoundland, Canada.
- Pearcey, T., Hill, G.W., 1956. The accelerated motion of droplets and bubbles. Australian Journal of Physics, 9, 19-30.
- Pedroso, R.I., Domoto, G.A., 1973a. Inward spherical solidification-solution by the method of strained coordinates. Int. J. Heat Mass Transfer, 16, 1037–1043.
- Pedroso, R.I., Domoto, G.A., 1973b. Perturbation solutions for spherical solidification of saturated liquids, ASME J. Heat Transfer, 95, 42–46.
- Pringle, D.J., Eicken, H., Trodahl, H.J., Backstrom, L.G.E., 2007. Thermal Conductivity of Landfast Antarctic and Arctic Sea Ice. J. Geoph. Research C04017, 112, 1–13.
- Preobrazhenskii, L.Y., 1973. Estimate of the Content of Spray Drops in the Near-water Layer of the Atmosphere. Fluid Mechanics-Soviet Research, 2(2), 95-100.
- Rashid, T., Khawaja, H.A., Edvardsen, K., 2016. Review of marine icing and anti-/de-icing systems. Journal of Marine Engineering & Technology, 15(2), 79-87.
- Ranz, W.E., Marshall, W.R., 1952. Evaporation from Drops. Chem. Eng. Prog., 48(3), 141–146.

- Riley, D.S., Smith, F.T., Poots, G., 1974. The inward solidification of spheres and circular cylinders. *Int. J. Heat Mass Transfer*, 17, 1507–1516.
- Roebber, P., Mitten, P., 1987. Modelling and measurement of icing in Canadian waters. Canadian Climate Centre Report 87-15.
- Rohsenow, W.M., Choi, H.Y., 1961. *Heat, Mass, and Momentum Transfer*. Prentice-Hall, Inc.
- Romagnoli, R., 1988. Ice growth modeling for icing control purposes of offshore marine units employed by the petroleum industry. In *Proc. Int. Association for Hydraulic Research Symposium on Ice*, Sapporo, Japan, pp. 486-497.
- Ryerson, C., 1995. Superstructure Spray and Ice Accretion on a Large US Coast Guard Cutter. *Atmos. Res.*, 36, 321-337.
- Ryerson, C.C., 2008. Assessment of Superstructure Ice Protection as Applied to Offshore Oil Operations Safety: Problems, Hazards, Needs, and Potential Transfer Technologies. US Army Cold Regions Research and Engineering Laboratory, ERDC/CRREL TR-08-14, (156 p).
- Ryerson, C.C., 2009. Assessment of Superstructure Ice Protection as Applied to Offshore Oil Operations Safety: Ice Protection Technologies, Safety Enhancements, and Development Needs. US Army Cold Regions Research and Engineering Laboratory, ERDC/CRREL TR-09-4, (342 p).
- Ryerson, C.C., 2011. Ice Protection of Offshore Platforms. *Cold Regi. Sci. Tech.*, 65(1), 97-110.
- Ryerson, C.C., Gow, A.J., 2000a. Crystalline Structure and Physical Properties of Ship Superstructure Spray Ice. *Phil. Trans. R. Soc. Lond. A*, 358, 2847-2871.

- Ryerson, C.C., Gow, A.J., 2000b. Ship Superstructure Icing: Crystalline and Physical Properties. US Army Cold Regions Research and Engineering Laboratory, ERDC/CRREL TR-00-11, Hanover, NH.
- Sadafi, M.H., Jahn, I., Stilgoe, A.B., Hooman K., 2014. A Theoretical Model with Experimental Verification for Heat and Mass Transfer of Saline Water Droplets. *Int. J. Heat Mass Transf.* 81, 1–9.
- Sadafi, M.H., Jahn, I., Stilgoe, A.B., Hooman, K., 2015. Theoretical and Experimental Studies on a Solid Containing Water Droplet. *Int. J. Heat Mass Transf.*, 78, 25–33.
- Saha, D., Dehghani, S.R., Pope, K., Muzychka, Y., 2016a. Temperature Distribution during Solidification of Saline and Fresh Water Droplets after Striking a Super-Cooled Surface, in: Arctic Technology Conference. Offshore Technology Conference.
- Saha, D., Dehghani, S.R., Pope, K., Muzychka, Y., 2016b. The Extent of Water Sheet Breakup on a Vertical Surface, in: Arctic Technology Conference. Offshore Technology Conference.
- Samuelsen, E.M., Edvardsena, K., Graversena, R.G., 2017. Modelled and observed sea-spray icing in Arctic-Norwegian waters. *Cold Regions Science and Technology*, 134, 54-81.
- Sawada, T., 1966. A Method of Forecasting Ice Accretion in the Waters off the Kuril Islands. Tokyo, Japan. Met. Agency, *J. Met. Res.*, 18, 15-23, 1967. Also, in *Bull. Hakodate Mar. Obs'y*, No. 14, 1969.

- Schulze, H.J., Beckett, P.M., Howarth, J.A., Poots, G., 1983. Analytical and Numerical Solutions to Two-Dimensional Moving Interface Problems with Applications to the Solidification of Killed Steel Ingots. *Proc. R. Soc. A*, 383, 313–343.
- Schröder Hansen, E., 2012. Numerical Modeling of Marine Icing on Offshore Structures and Vessels. MS thesis, Department of Physics, Norwegian University of Science and Technology, Norway.
- Schwerdtfeger, P., 1963. The Thermal Properties of Sea Ice. *J. Glaciol.*, 4 (36), 789–807.
- Seban, R.A., 1960. The Influence of Free Stream Turbulence on the Local Heat Transfer from Cylinders. *J. Heat Transfer*, 82, 101-107.
- Seeniraj, R.V., Bose, T.K., 1982. Planar solidification of a warm flowing liquid under different boundary conditions, *Warme-und Stoffubertr.*, 16, 105–111.
- Sharapov, A.V., 1971. On the Intensity of Superstructure Icing of Small Vessels (MFV Type). In *Theoretical and Experimental Investigations of the Conditions of Ship Icing*, Gidrometeoizdat, Leningrad, pp. 95-97. (in Russian)
- Shekhtman, A.N., 1968. The Probability and Intensity of the Icing Up of Ocean Going Vessels, *Moskow Nauk-Issled Inst. Aeroklim, T. Vyp 50*, 55-65.
- Shellard, H.C., 1974. The Meteorological Aspects of Ice Accretion on Ships. World Meteorological Organization, Marine Science Affairs Report No. 10 (WMO-0No. 397), (34 p).
- Shipilova, O., Kulyakhtin, A., Tsarau, A., Libby, B., Moslet, P.O., Loset, S., 2012. Mechanism and Dynamics of Marine Ice Accretion on Vessel Archetypes. Offshore Technology Conference, OTC-23762-MS, OTC Arctic Technology Conference, 3-5 December, Houston, Texas, USA.

- Silveira, R.A., Maliska, C.R., Estivam, D.A., Mendes, R., 2003. Evaluation of Collection Efficiency Methods for Icing Analysis. Proceedings of COBEM 2003, 17th International Congress of Mechanical Engineering, São Paulo, SP.
- Soares, C.G., Garbatov, Y. (editors), 2015. Ships and Offshore Structures XIX. CRC Press, USA.
- Stallabrass, J.R., 1980. Trawler Icing. A Compilation of Work Done at N.R.C. Mechanical Engineering Report MD-56, N.R.C. No. 19372.
- Sutherby, F.S., 1951. Symposium on the Deposition of Ice on Exposed Surfaces: Icing problems on ships. *Journal of Glaciology*, 1(10), 546–548.
- Szilder, K., Lozowski, E.P., Gates, E.M., 1988. Some Applications of a New, Time-dependent Cylinder Ice Accretion Model. *Atmospheric Research*, 22, 41-59.
- Szilder, K., Lozowski, E.P., 1995. Experimental Verification of a Pendant Ice Formation Model. In Proc. 5th Int. Offshore and Polar Engineering Conf., II, 469-475.
- Tabakova, S., Feuillebois, F., Radev, S., 2010. Freezing of a Supercooled Spherical Droplet with Mixed Boundary Conditions. *Proc. R. Soc. A*, 466, 1117–1134.
- Tabata, T., Iwata, S., Ono, N., 1963. Studies on the Ice Accumulation on Ships I. Low Temperature Science, Series A, Physical Sciences, 21, 173-221.
- Tabata, T., 1969. Studies on the Ice Accumulation on Ships III. Low Temperature Science, Series A, Physical Sciences, 27, 339-349.
- Terwilliger, J.P., Dizon, S.F., 1970. Salt rejection phenomena in the freezing of saline solutions. *Chem. Eng. Sci.*, 25 (8), 1331–1349.

- Tagami, M., Hamai, M., Mogi, I., Watanabe, K., Motokawa, M., 1999. Solidification of Levitating Water in a Gradient Strong Magnetic Field. *J. Cryst. Growth*, 203, 594–598.
- Tracy, C.R., Welch, W.R., Porter, W.P., 1980. *Properties of Air, a Manual for Use in Biophysical Ecology*. 3rd edition, Technical report No. 1, University of Wisconsin.
- US Navy, 1988. *Cold Weather Handbook for Surface Ships*. OPNAV P-03C-01-89, Chief of Naval Operations, Washington DC.
- Vasileva, G.V., 1971. Hydro meteorological conditions of sea vessels icing. *Proceedings of Hydro meteorological Research Institute of the USSR*. Leningrad, 87, 82-92.
- Voller, V., 1985. Implicit Finite-Difference Solutions of the Enthalpy Formulation of Stefan Problems, *J. Numer. Anal.*, 5, 201–214.
- Wang, G., Matthys, E., 1992. Numerical Modeling of Phase Change and Heat Transfer Rapid Solidification Processes: Use of Control Volume Integrals with Element Subdivision. *Int. J. Heat Mass Transfer*, 35, 141–153.
- Weinbaum, S., Jiji, L.M., 1977. Singular perturbation theory for melting or freezing in finite domains initially not at the fusion temperature. *J. Appl. Mech.*, 44, 25–30.
- Wheeler, A., Ahmad, N., 1995. Recent Developments in Phase Field Models of Solidification. *Adv. Space Res.*, 16 (7), 163–172.
- Wiersema, E., Lange, F., Cammaert, G., Sliggers, F., Jolles, W., Van Der Nat, C., 2014. *Arctic operations handbook JIP*. OTC Arctic Technology conference. Offshore Technology Conference.
- Yan, M.M., Huang, P.N.S., 1974. Perturbation solutions to phase change problems subjected to convection and radiation. *Trans. ASME J. Heat Transfer*, 96, 95–100.

- Yao, S., Schrock, V., 1976. Heat and mass transfer from freely falling drops. *J. Heat Transfer, Trans. ASME Ser. C* 98 (1), 120–126.
- Yoon, B., Ettema, R., 1993. Droplet Trajectories and Icing-collision Efficiencies for Cylinders Determined Using LDV. *Cold Regi. Sci. Tech.*, 21, 381-397.
- Young, I.R., Zieger, S., Babnin, A.V., 2011. Global Trends in Wind Speed and Wave Height. *Science*, 332, 451-455.
- Zarling, J.P., 1980. Heat and Mass Transfer from Freely Falling Drops at Low Temperatures. US Army Cold Regions Research and Engineering Laboratory, CRREL Report BO-1B.
- Zakrzewski, W.P., 1986a. Icing of Ships, Part I: Splashing a Ship with Spray. NOAA Technical Memorandum, ERL PMEL-66, Seattle, (74 p).
- Zakrzewski, W.P., 1986b. Icing of Fishing Vessels, Part I: Splashing a Ship with Spray. 8th IAHR Symposium on Ice, Iowa, USA.
- Zakrzewski, W.P., 1987. Splashing a Ship with Collision-generated Spray. *Cold Regi. Sci. Tech.*, 14(1), 65-83.
- Zakrzewski, W.P., Lozowski, E.P., Muggeridge, D., 1988. Estimating the Extent of the Spraying Zone on a Sea-going Ship. *Ocean Eng.*, 15(5), 413-429.
- Zakrzewski, W.P., Lozowski, E.P., 1989a. Modelling and forecasting vessel icing. In: *Freezing and Melting Heat Transfer in Engineering*, Cheng K.C. and Seki N., Eds., Hemisphere, New York, 661-706.
- Zakrzewski, W.P., Lozowski, E.P., 1989b. Soviet Marine Icing Data. Canadian Climate Centre Rept 89-2.

Appendix A: Figures Obtained from Experiments



(a)



(b)



(c)



(d)



(e)

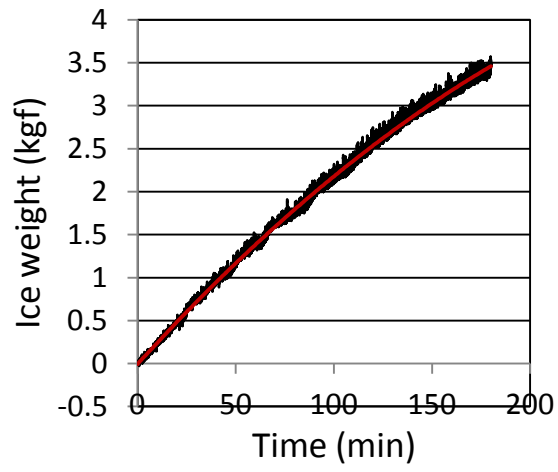


(f)

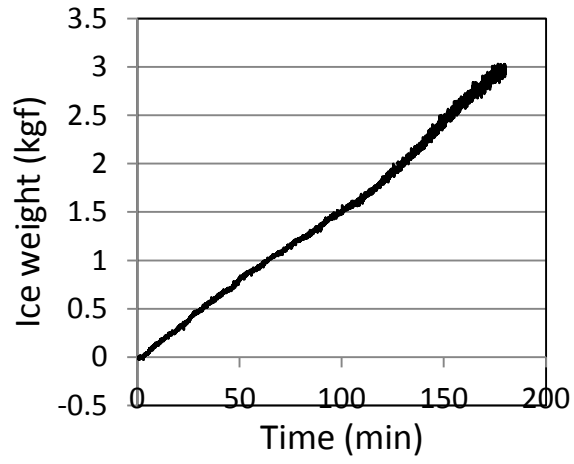


(g)

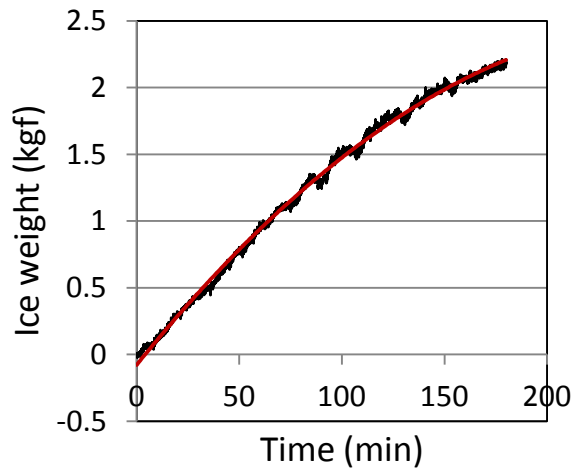
Fig. 1.A: Views of ice accretion on the vertical plate for (a) test (1-1-1-a),
(b) (1-1-1-b), (c) (1-1-2-a), (d) (1-1-2-b), (e) (1-1-3-a),
(f) (1-1-3-b) and (g) (1-1-3-c)



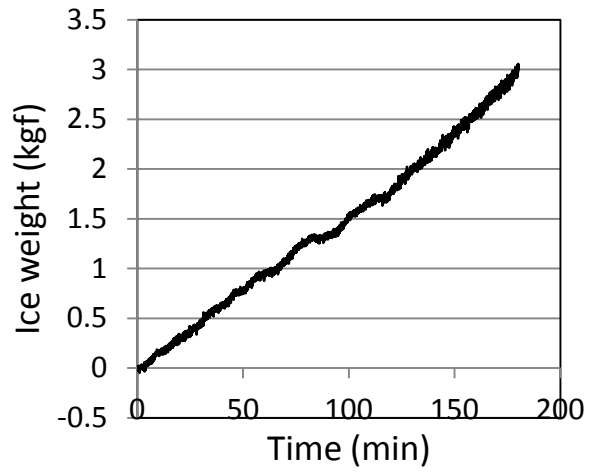
(a)



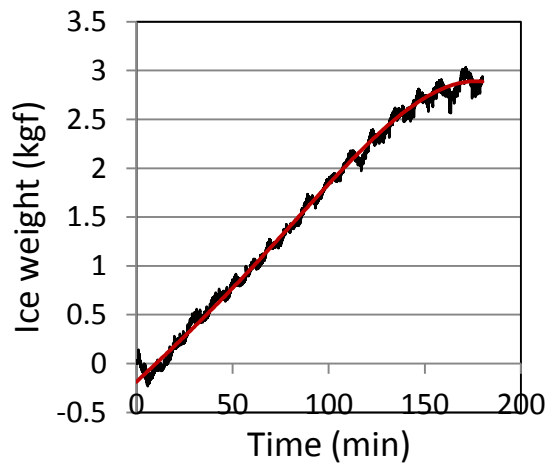
(b)



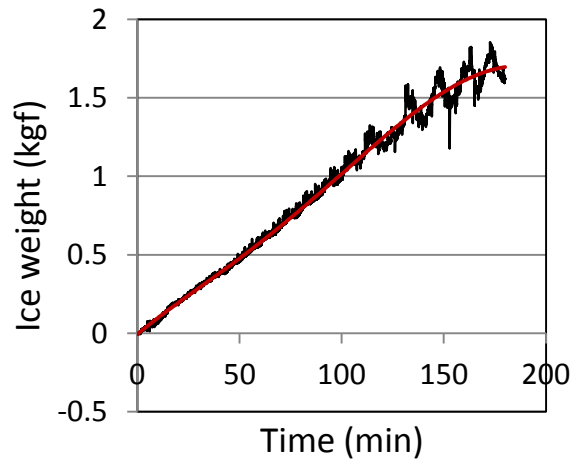
(c)



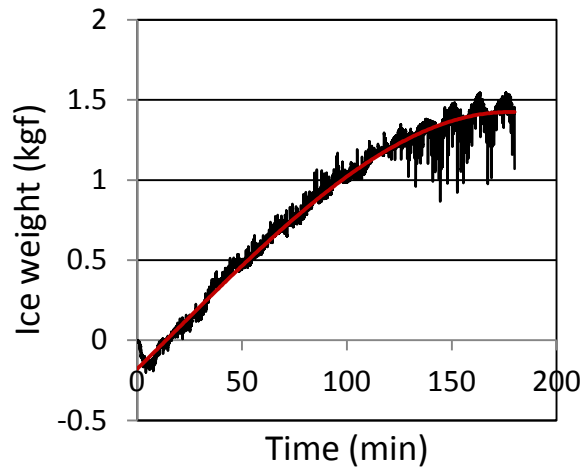
(d)



(e)

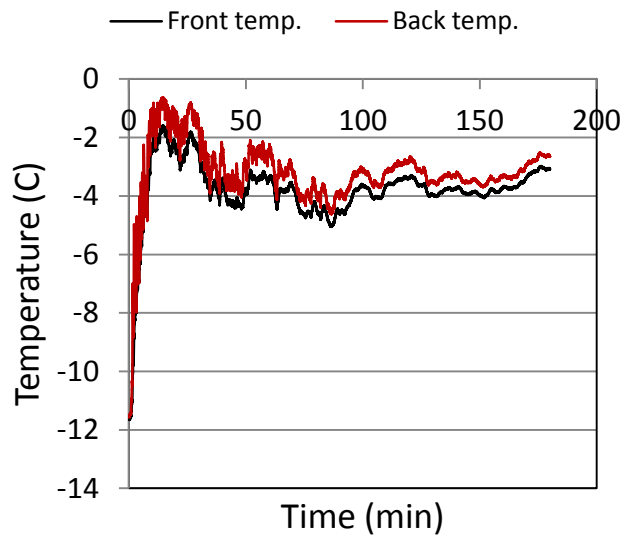


(f)

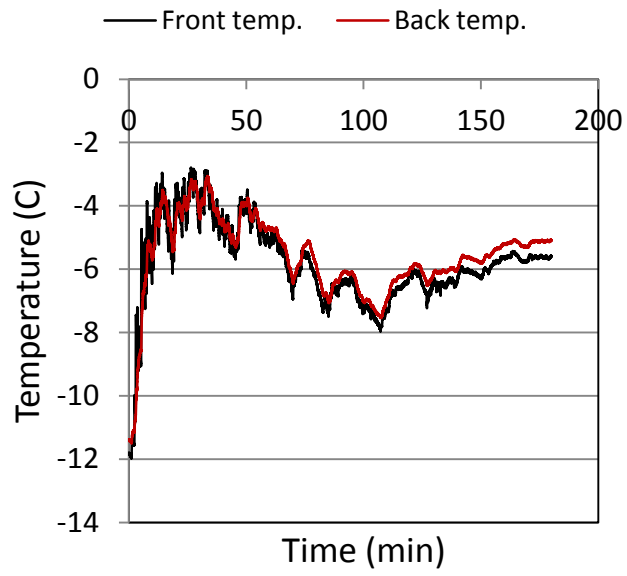


(g)

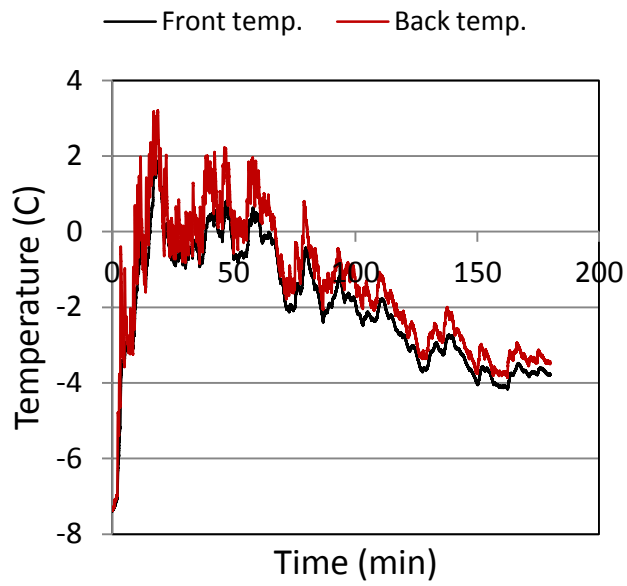
Fig. 2.A: Variations of the ice weight versus time on the vertical plate for (a) test (1-1-1-a), (b) (1-1-1-b), (c) (1-1-2-a), (d) (1-1-2-b), (e) (1-1-3-a), (f) (1-1-3-b) and (g) (1-1-3-c)



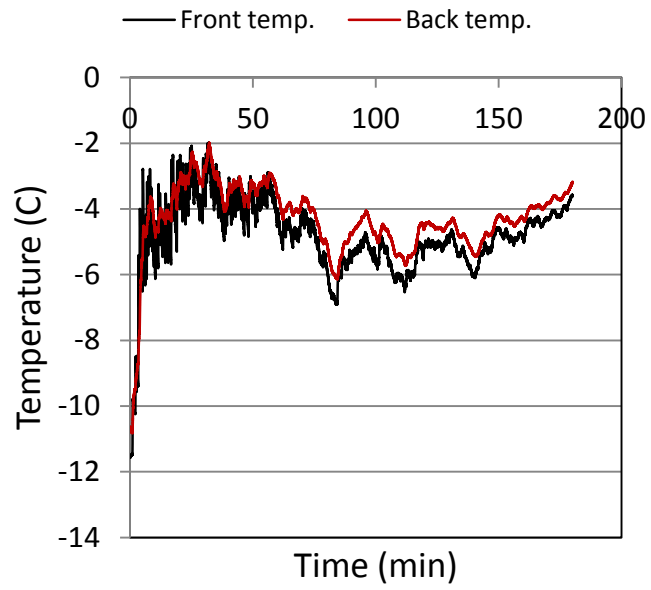
(a)



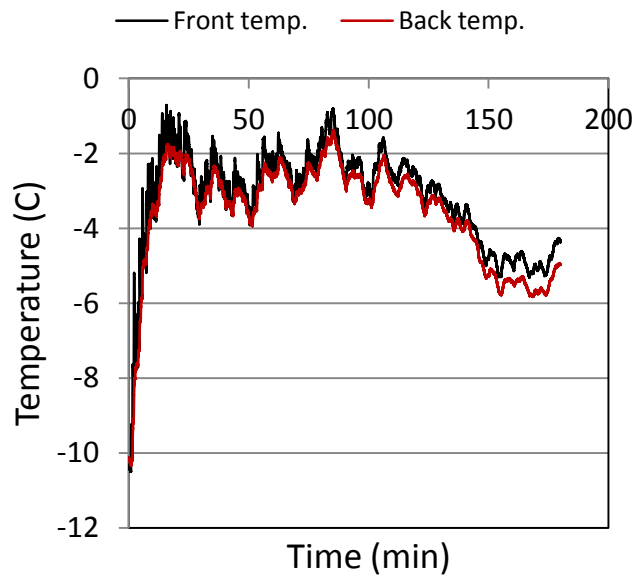
(b)



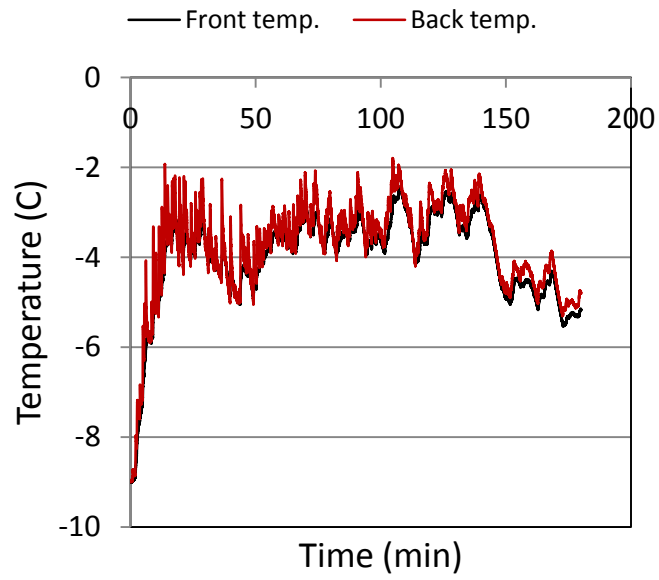
(c)



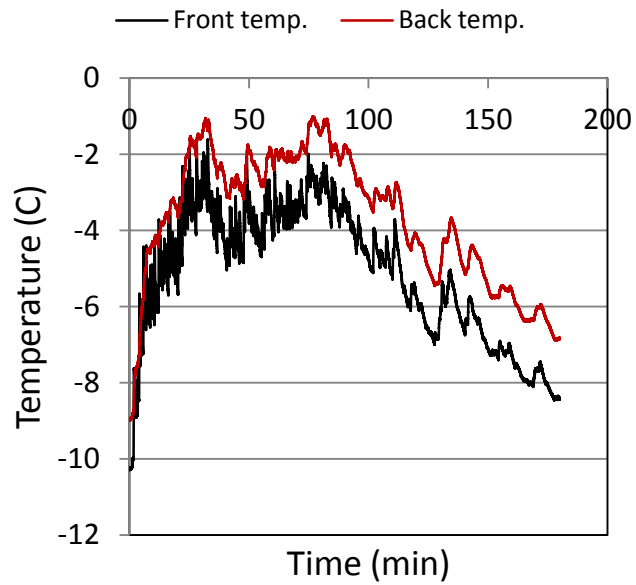
(d)



(e)

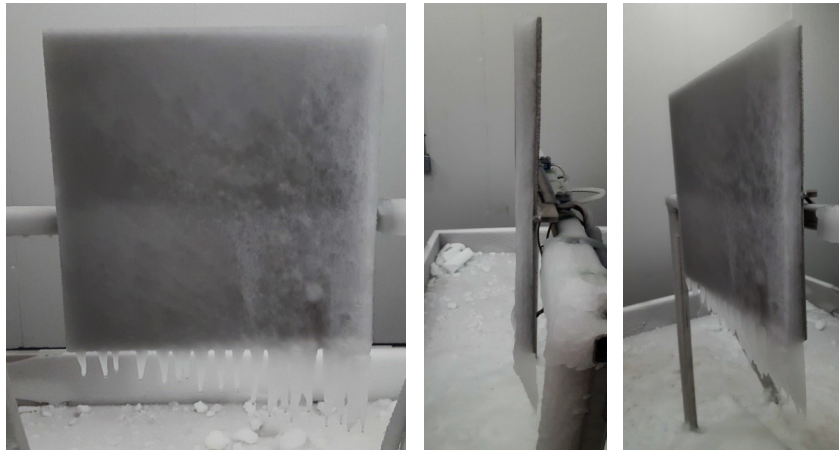


(f)

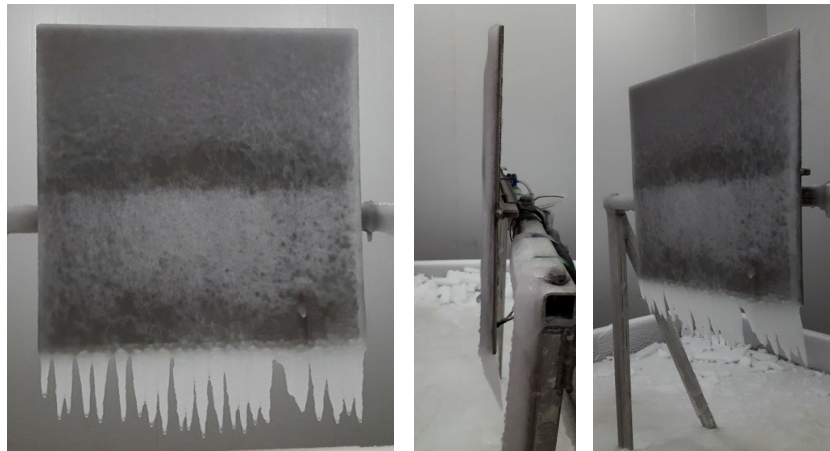


(g)

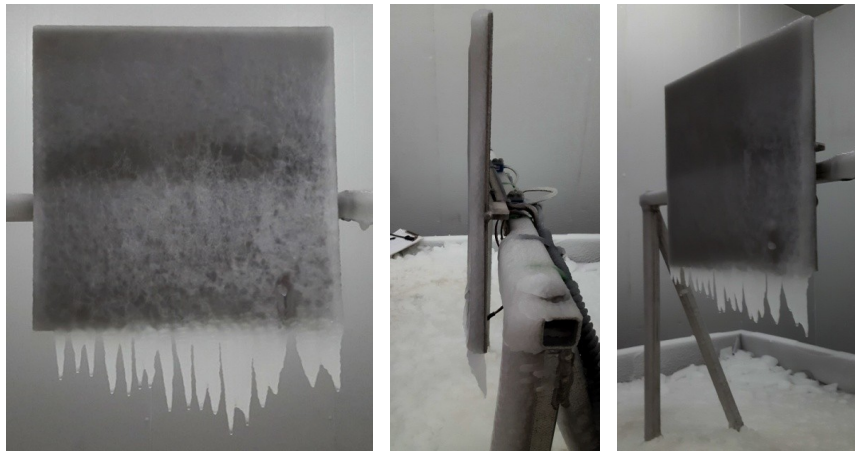
Fig. 3.A: Variations of the temperature at the front and back of the vertical plate versus time for (a) test (1-1-1-a), (b) (1-1-1-b), (c) (1-1-2-a), (d) (1-1-2-b), (e) (1-1-3-a), (f) (1-1-3-b) and (g) (1-1-3-c)



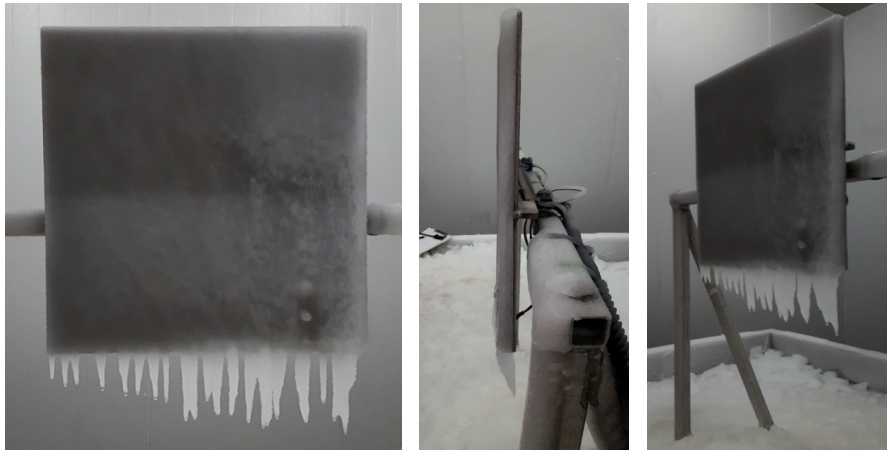
(a)



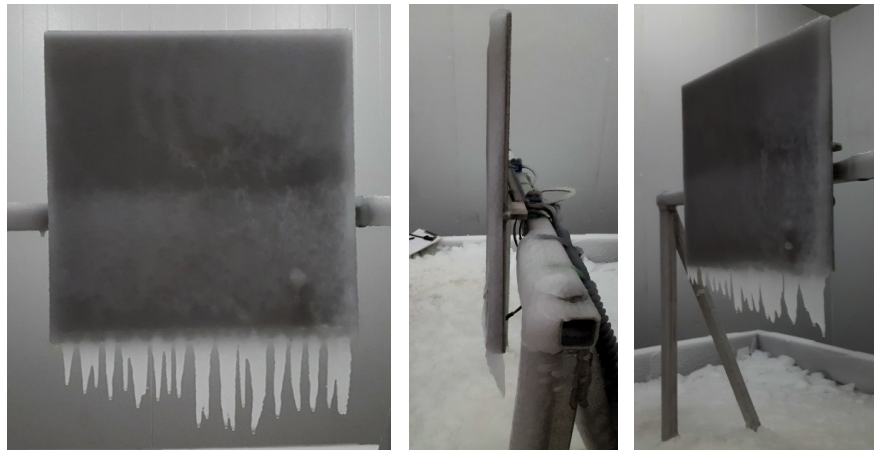
(b)



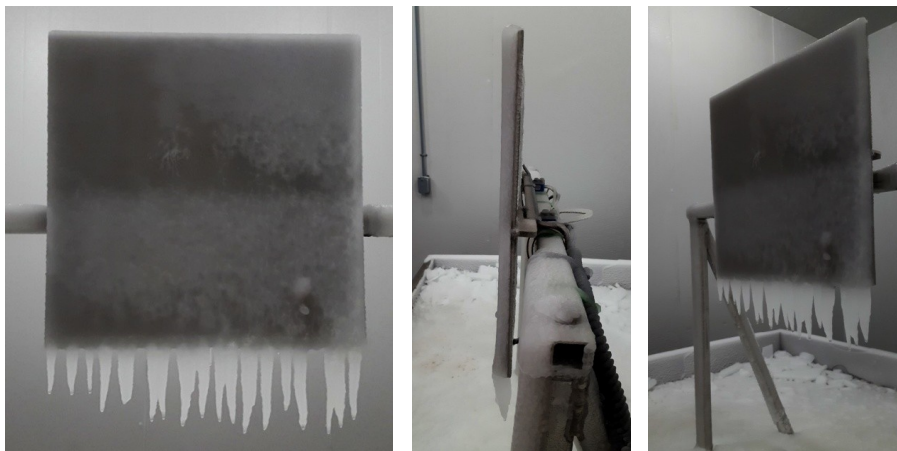
(c)



(d)



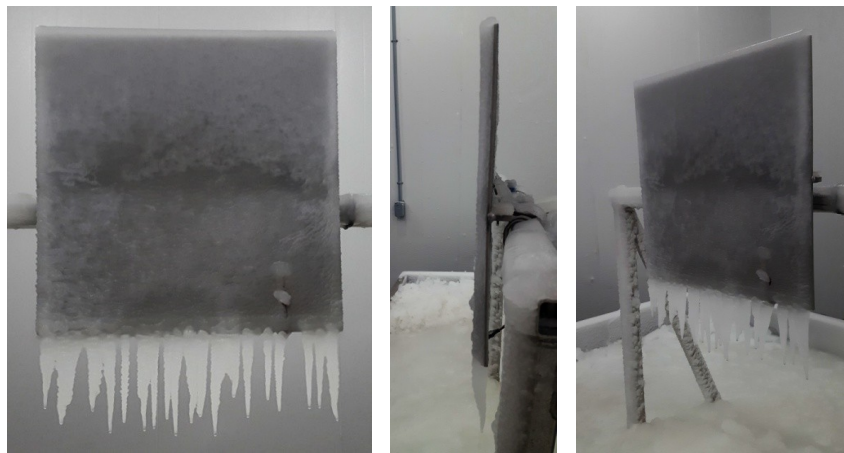
(e)



(f)

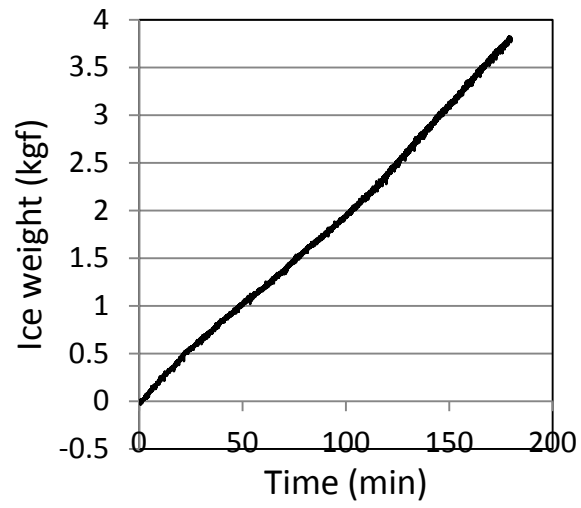


(g)

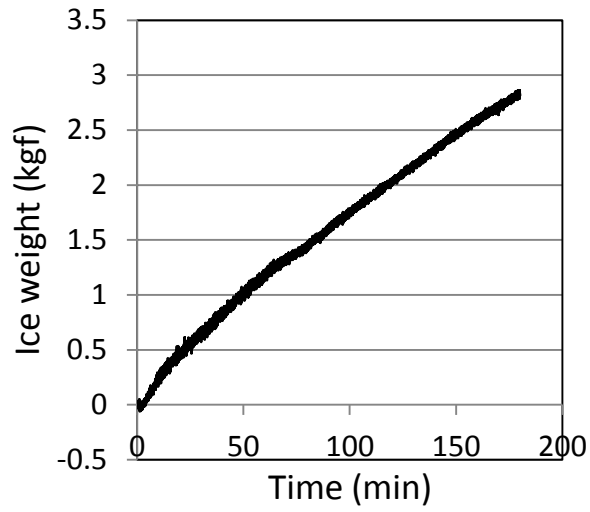


(h)

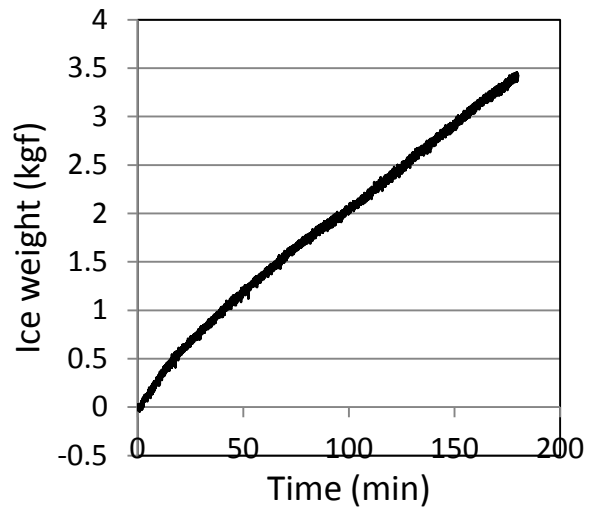
Fig. 4.A: Views of ice accretion on the vertical plate for (a) test (1-2-1-a),
(b) (1-2-1-b), (c) (1-2-1-c), (d) (1-2-1-d), (e) (1-2-2-a),
(f) (1-2-2-b), (g) (1-2-3-a) and (h) (1-2-3-b)



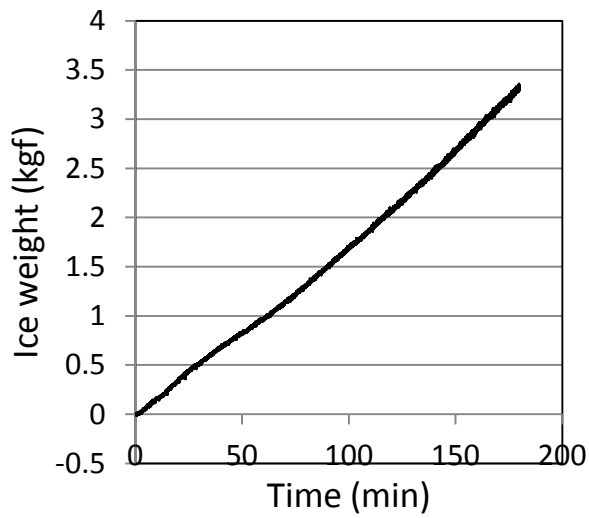
(a)



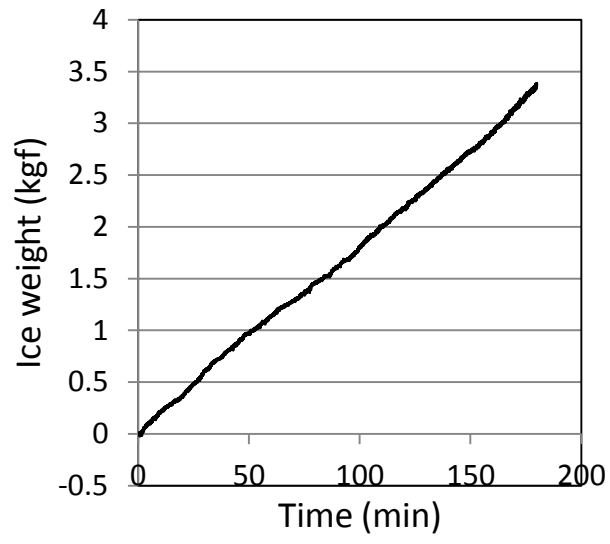
(b)



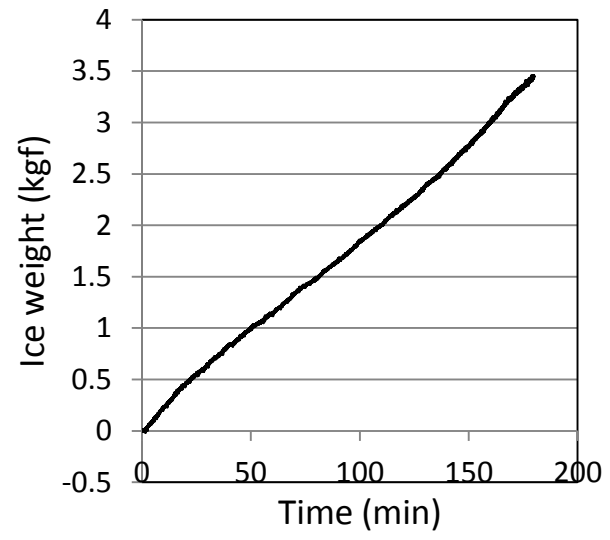
(c)



(d)



(e)



(f)

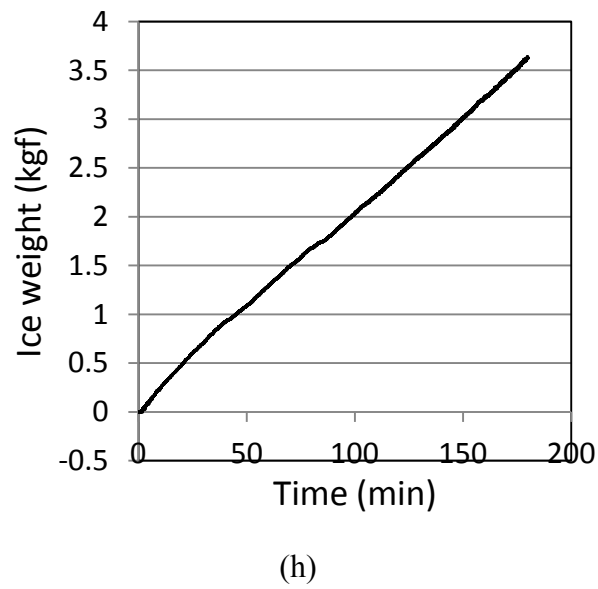
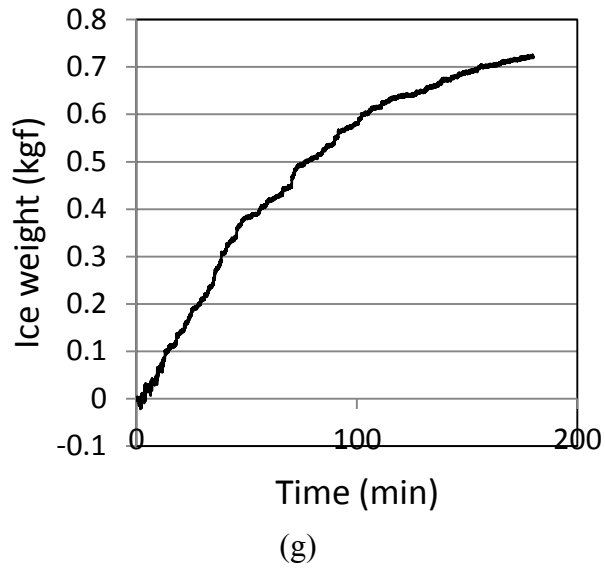
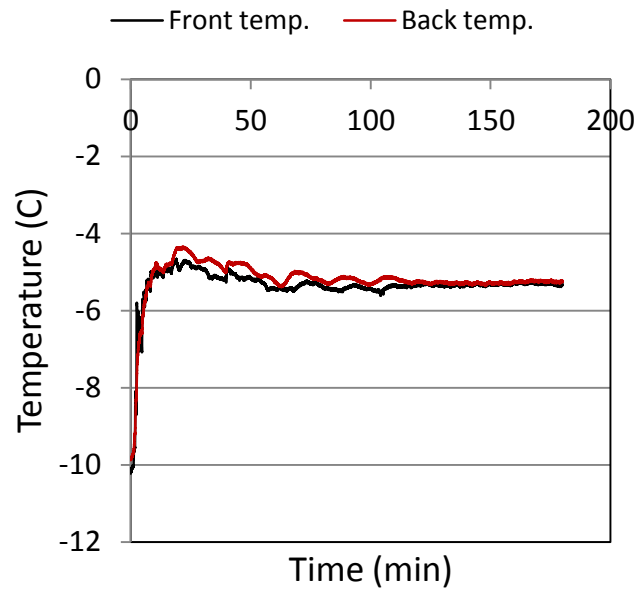
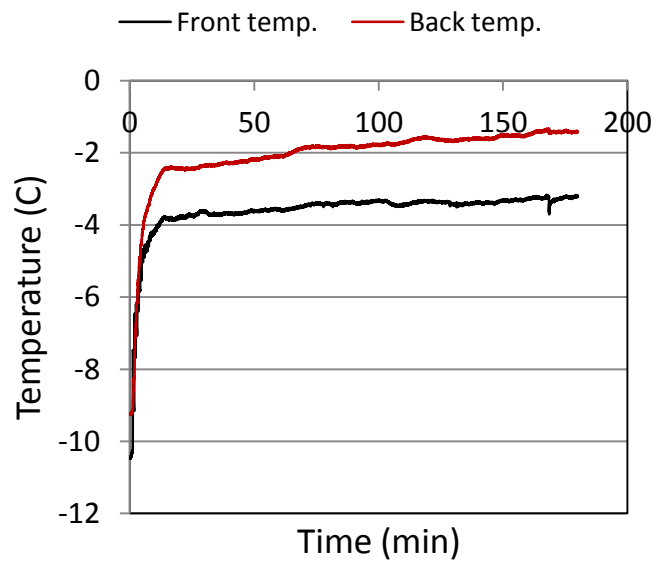


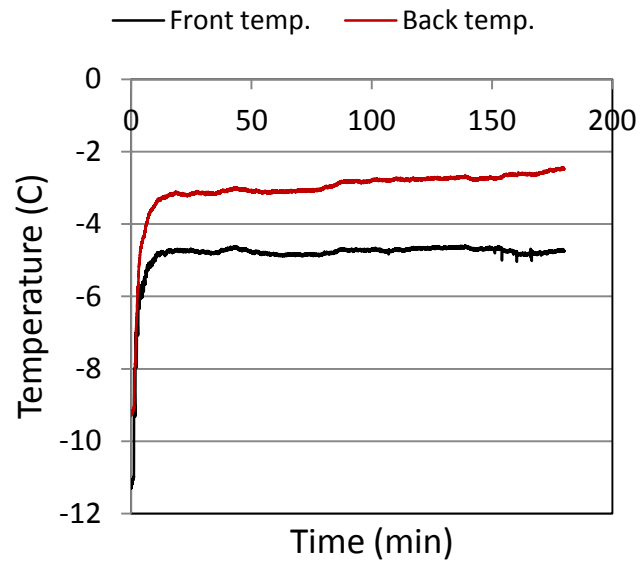
Fig. 5.A: Variations of the ice weight versus time on the vertical plate for
 (a) test (1-2-1-a), (b) (1-2-1-b), (c) (1-2-1-c), (d) (1-2-1-d),
 (e) (1-2-2-a), (f) (1-2-2-b), (g) (1-2-3-a) and (h) (1-2-3-b)



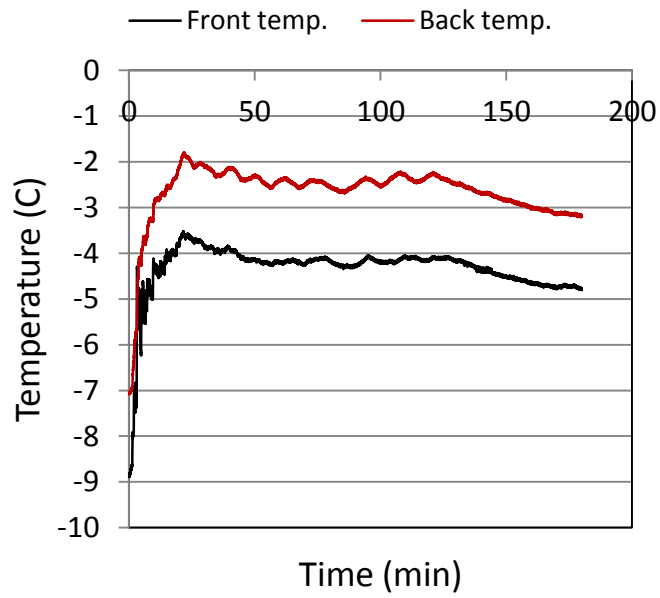
(a)



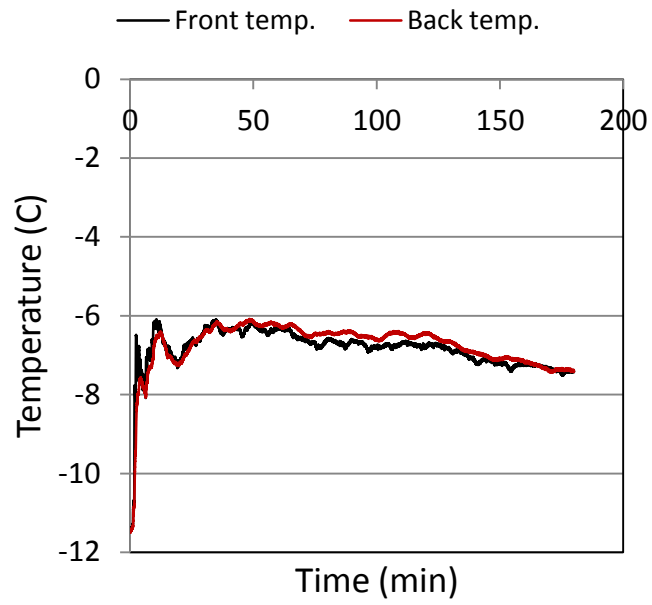
(b)



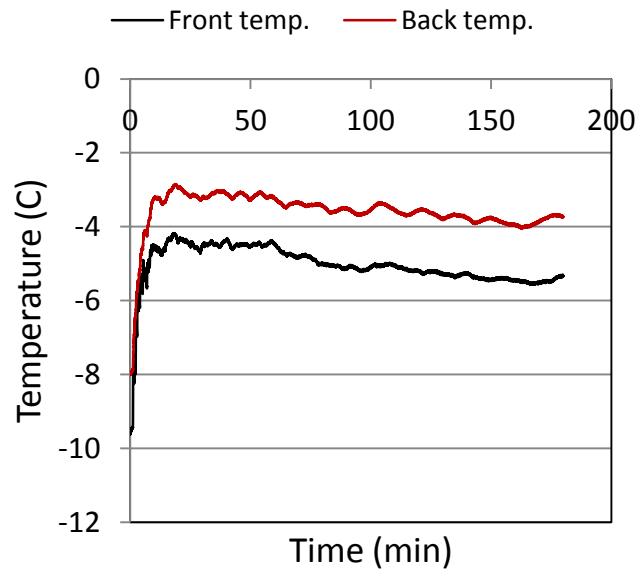
(c)



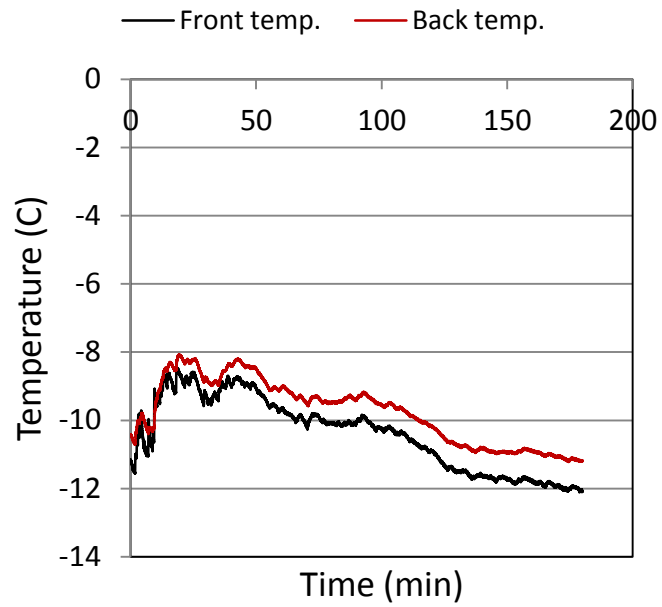
(d)



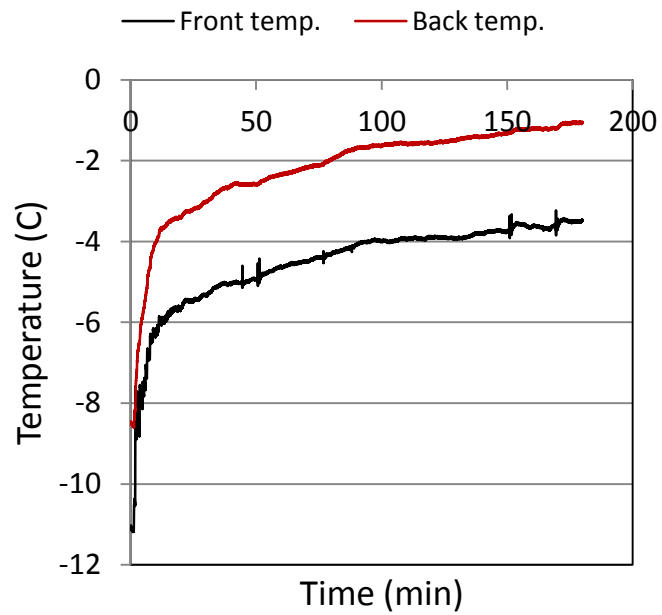
(e)



(f)

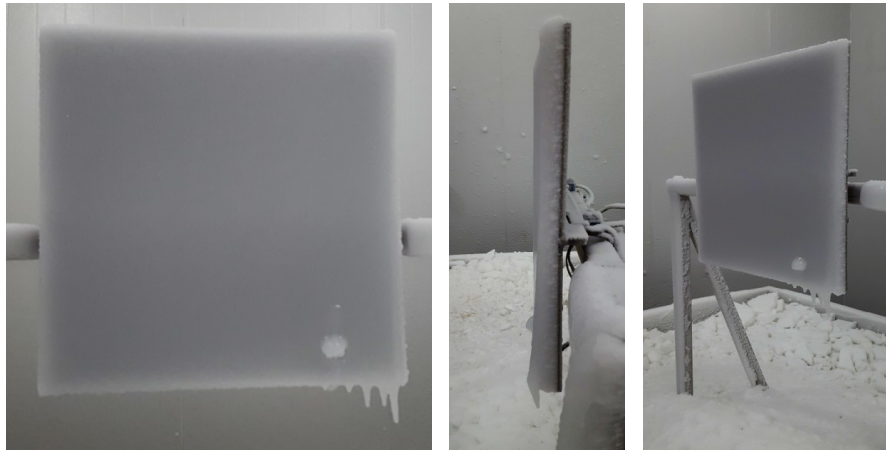


(g)

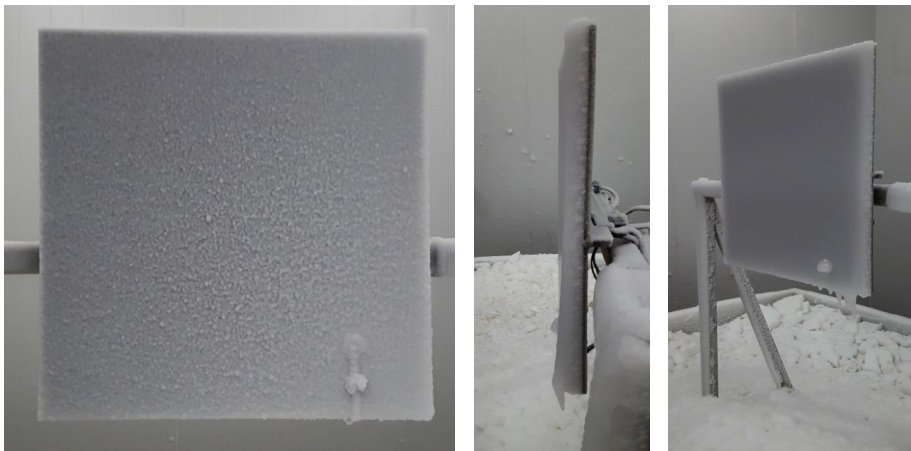


(h)

Fig. 6.A: Variations of the temperature at the front and back of the vertical plate versus time for (a) test (1-2-1-a), (b) (1-2-1-b), (c) (1-2-1-c), (d) (1-2-1-d), (e) (1-2-2-a), (f) (1-2-2-b), (g) (1-2-3-a) and (h) (1-2-3-b)



(a)

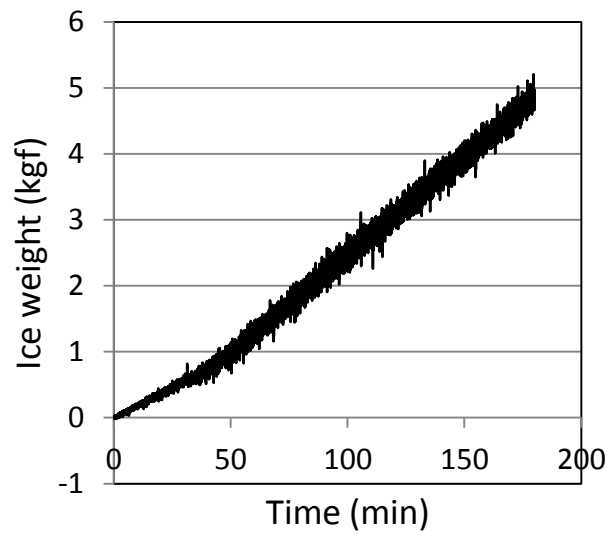


(b)

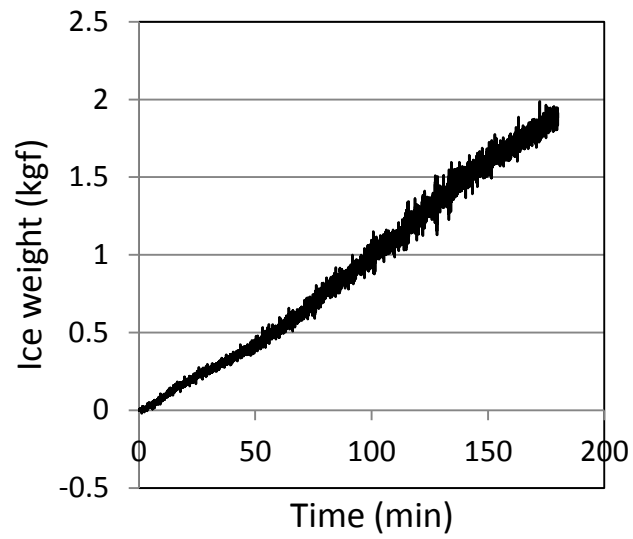


(c)

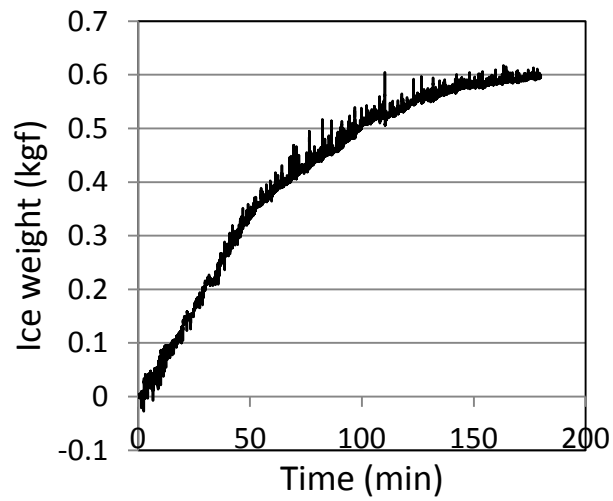
Fig. 7.A: Views of ice accretion on the vertical plate for
(a) test (2-1-1), (b) (2-1-2) and (c) (2-1-3)



(a)



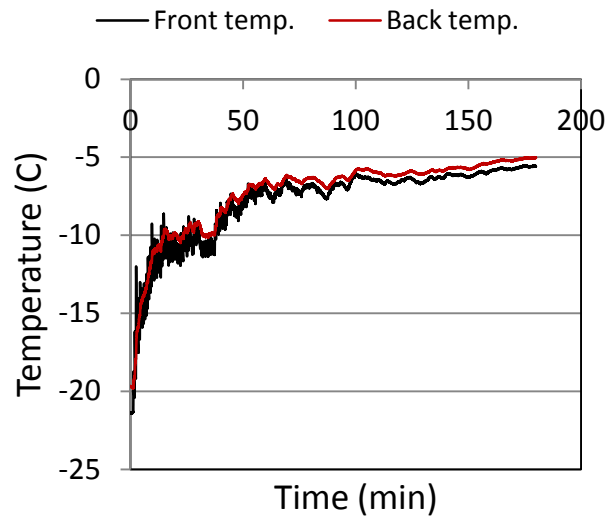
(b)



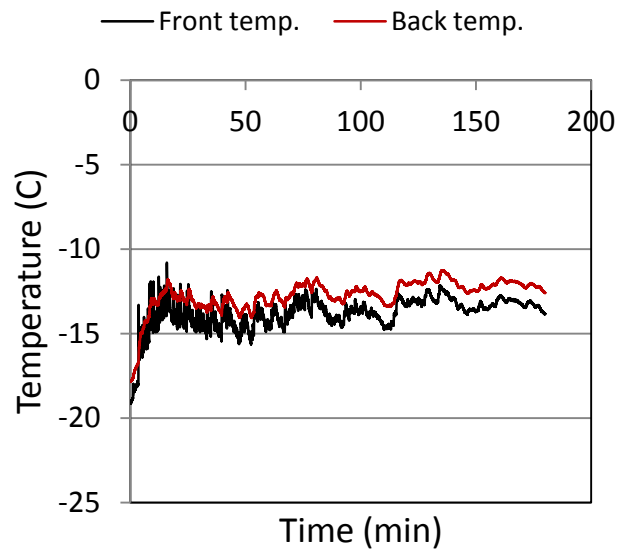
(c)

Fig. 8.A: Variations of the ice weight versus time on the vertical plate for

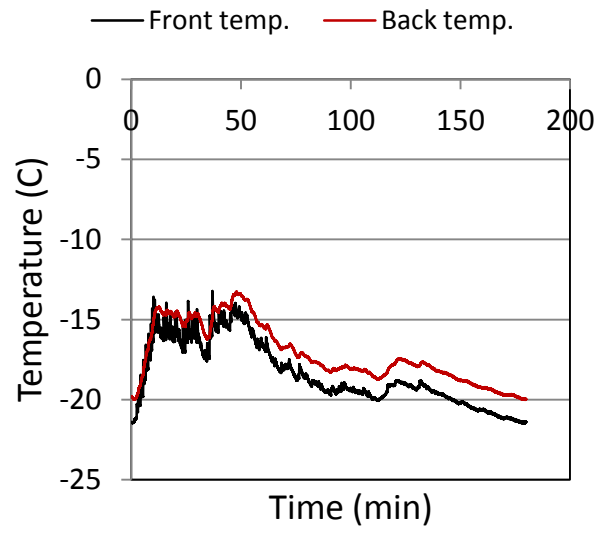
(a) test (2-1-1), (b) (2-1-2) and (c) (2-1-3)



(a)

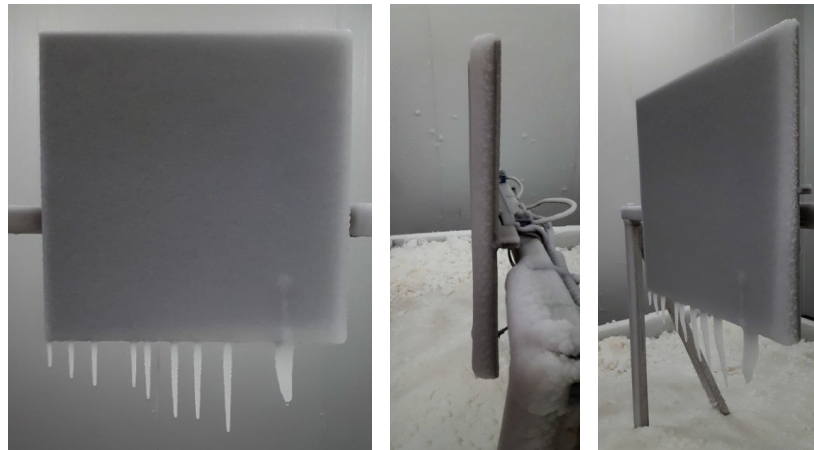


(b)



(c)

Fig. 9.A: Variations of the temperature at the front and back of the vertical plate versus time for (a) test (2-1-1), (b) (2-1-2) and (c) (2-1-3)



(a)



(b)



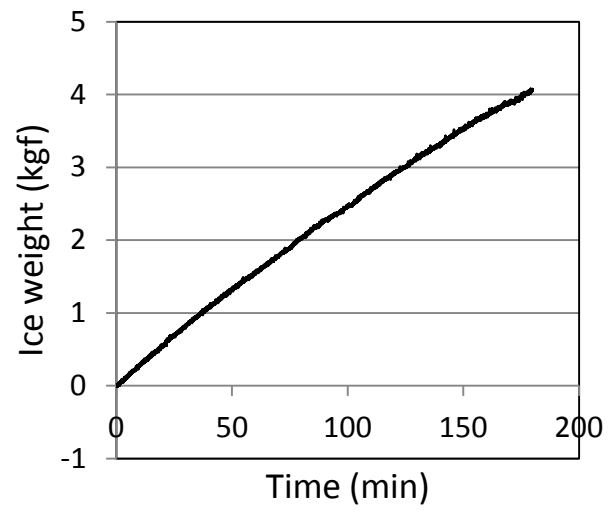
(c)



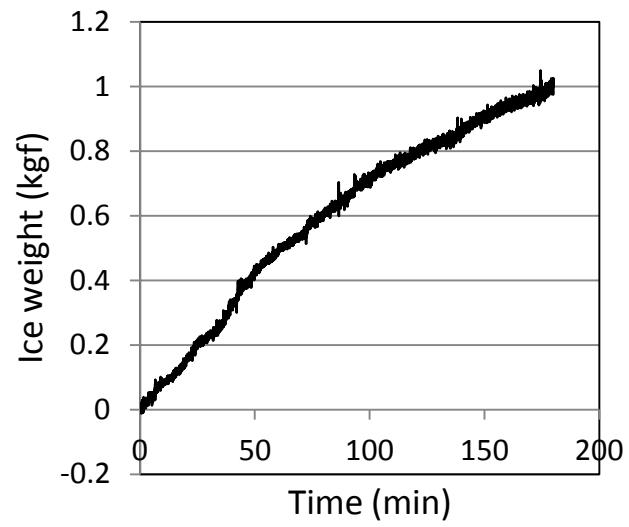
(d)

Fig. 10.A: Views of ice accretion on the vertical plate for (a) test (2-2-1),

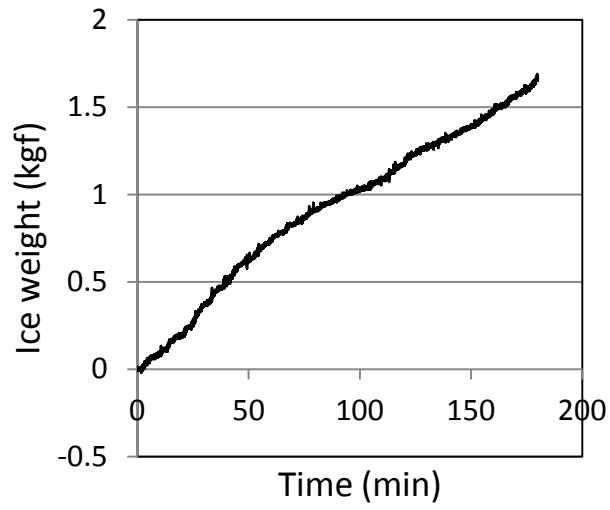
(b) (2-2-2-a), (c) (2-2-2-b) and (d) (2-2-3)



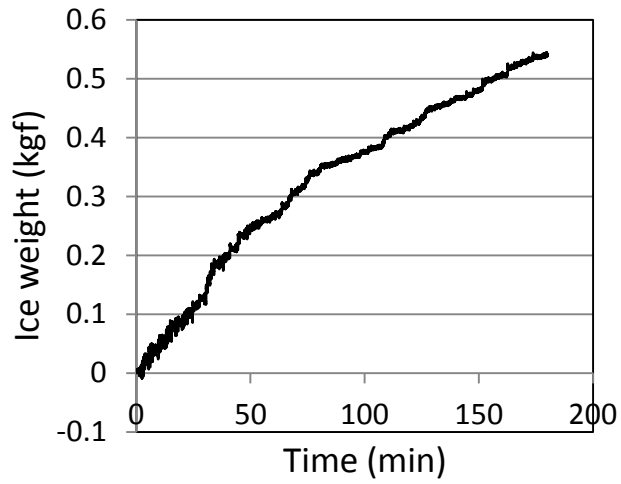
(a)



(b)



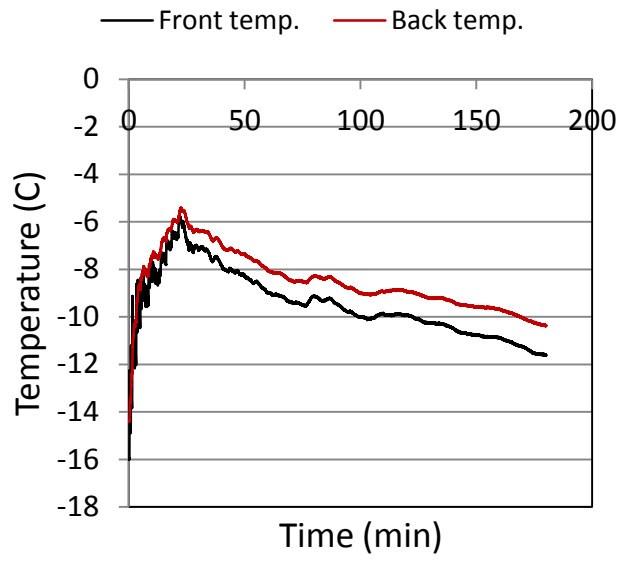
(c)



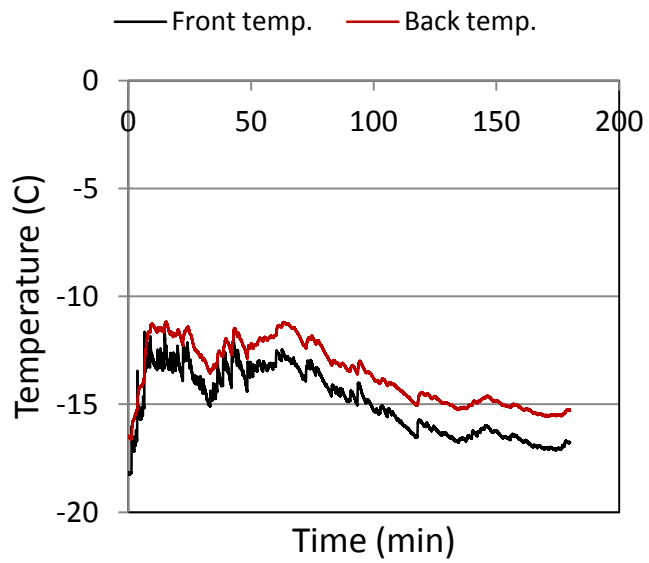
(d)

Fig. 11.A: Variations of the ice weight versus time on the vertical plate for

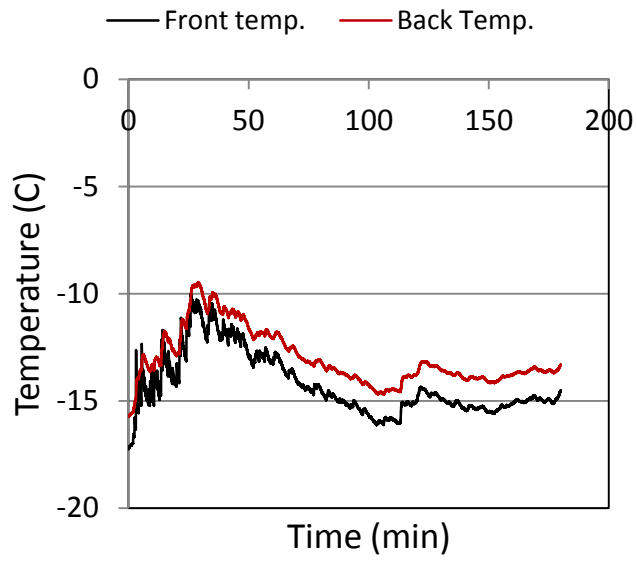
(a) test (2-2-1), (b) (2-2-2-a), (c) (2-2-2-b) and (d) (2-2-3)



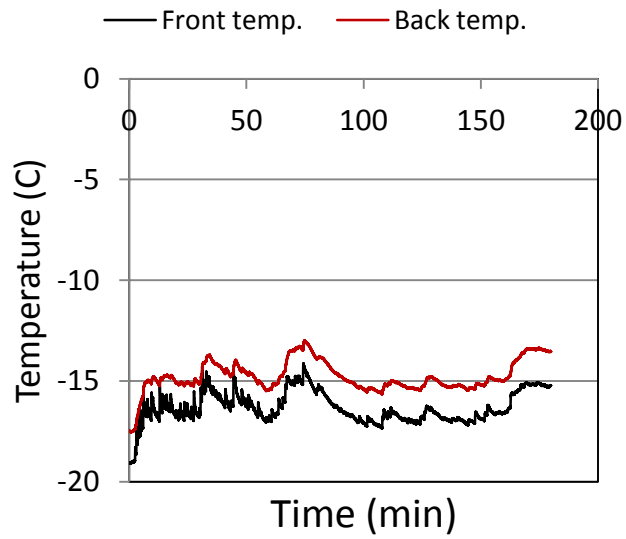
(a)



(b)



(c)



(d)

Fig. 12.A: Variations of the temperature at the front and back of the vertical plate versus time for (a) test (2-2-1), (b) (2-2-2-a), (c) (2-2-2-b) and (d) (2-2-3)